NUMERICAL MODELLING OF SUPERHEATED JET ATOMISATION

Konstantinos Lyras

Department of Mechanical and Automotive Engineering
Kingston University London

This dissertation is submitted for the degree of
Doctor of Philosophy

March 2018

To Katerina

Declaration

I hereby declare that except where specific reference is made to the work of others, the contents of this dissertation are original and have not been submitted in whole or in part for consideration for any other degree or qualification in this, or any other university. This dissertation is my own work and contains nothing which is the outcome of work done in collaboration with others, except as specified in the text and Acknowledgements. This dissertation contains fewer than 40,000 words including appendices, bibliography, footnotes, tables and equations and has fewer than 150 figures.

Konstantinos Lyras
March 2018

Acknowledgements

I am very grateful to all people who supported me during this PhD project. I would like to thank my supervisors Professor Jennifer Wen and Professor Siaka Dembele for giving me the chance to be part of the SafeLNG project and for their support during my PhD. This research was benefited immensely from the Innovative Doctoral Programme (IDP) funded by the Marie Curie Action of the 7th Framework Programme of the European Union for the Numerical characterisation and simulation of the complex physics underpinning the Safe handling of Liquefied Natural Gas (SafeLNG) (2014-2018) which I am also thankful.

I would like to thank Professor David Schmidt from the University of Massachusetts Amherst for his contribution and help in coding and knowledge he shared with me. I am also thankful to Dr. Simon Jallais and Dr. Elena Vyazmina for welcoming me in AirLiquide's research centre and for the discussions we had during my secondment. I truly appreciate the discussions and support of Dr. Chandra Madhav Rao Vendra in the University of Warwick.

I would like to express my gratitude to my colleagues in Kingston University for the pleasant working atmosphere during our studies and their support and help in coding, data visualisation and many others. Especially, I would like to thank Antoine Hubert, Dinesh Bhatia, Liam Griggs, Marco Macchi and Reza Khodadadi Azadboni.

Very special thanks go to my family for all their love and support during my time in England and France. In particular, my mother Stavroula and father Georgios, Anna-Maria, Evridiki and Panagiotis.

My final and most heartfelt thanks go to Katerina who supported and advised me over the years and has always believed in me.

Abstract

The aim of this research project is to provide the academic and industrial community with a numerical tool that can be used for describing extreme flow cavitation scenarios and the atomisation process of these multiphase jets in a low-pressure environment. The research lies in the intersection of Numerical Analysis, Applied Physics and programming. From the physical point of view, the project has two different strands: The first is developing a methodology for channel flows due to a rapid pressure drop which is possible to result into various flow regimes inside the channel. The second step is to track the liquid fragmentation of the liquid jet downstream the channel exit and describing the atomisation process to liquid ligaments and blobs to droplets.

Using a fully Eulerian approach, this research aims towards a holistic approach that addresses some of the major challenges that govern superheated jets atomisation. The finite volumes method in a compressible framework is used utilising various models for modelling the underpinning physics of flashing jets. Flashing occurs either if a liquid follows an isothermal depressurisation or isobaric heating. In both cases, the fluid fails to adjust to the local changes in pressure and temperature admitting a metastable state which makes the process more challenging to understand. The Homogeneous-Relaxation-Model (HRM) is used for modelling the heat transfer under sudden depressurisation conditions accounting for the non-equilibrium vapour generation. A new pressure equation is proposed which employs the continuity equation indirectly. The pressure responds to compressibility and density changes due to the rapid phase change and includes the surface tension contribution in the pressure-velocity coupling algorithm. The coupling of the continuity and momentum equation with the HRM and the interface tracking method is thoroughly described. The result of this coupling is a conserved numerical method that is capable of characterising the flow regimes and the impact of bubble nucleation on the mass flow rate.

The present study presents a numerical approach for simulating the atomisation of flashing liquids accounting for the distinct stages, from primary atomisation to secondary break-up to small droplets Following the Eulerian-Lagrangian-Spray-Atomisation approach, the concept of the surface density Σ is introduced into the methodology for the spray dynamics. The proposed approach has the advantage of avoiding the unrealistic common assumption of

pure liquid at the nozzle exit. It models the change in the regime inside the nozzle treating flashing in a unified approach simulating the metastable jet both inside and outside the nozzle. Important mechanisms such as thermal non-equilibrium, aerodynamic break-up, droplet collisions and evaporation are modelled in a novel atomisation model. The modified Σ-equation employed a new source term proposed for cryogenic jets. A wide range of numerical tests is presented for validation and obtaining insights for the underlying physics. Short and long nozzle geometries are tested for both low and high-pressure releases for flashing water, R134A, liquid nitrogen and LNG. Results for turbulent flows for both sub-cooled and superheated liquids are presented showing that the proposed approach can accurately simulate the primary atomisation.

Table of contents

List of figures

List of tables

Nomenclature

Roman Symbols

A	area [m^2]
$A()$	matrix of momentum equation
a_P	diagonal coefficient matrix of the discretised momentum equation at the central cell
a_{acc}	particle acceleration [m/s^2]
a_{eff}	sum of laminar and turbulent thermal diffusivities [m^2/s]
a_{nb}	diagonal coefficient matrix of the discretised momentum equation at the neighboring cells
B_0	non-dimensional impact parameter [-]
B_M	Spalding number [-]
$C_{1\varepsilon}$	constant in the production component in $k-\varepsilon$ model
$C_{2\varepsilon}$	constant in the destruction term of the $k-\varepsilon$ model
C_D	drag coefficient
C_F	constant in TAB model, C_F=1.3
C_b	constant in TAB model, C_b=0.5
C_d	constant in TAB model, C_d=5.0
C_f	discharge coefficient
C_k	constant in TAB model, C_k=8.0
$C(t)$	curve changing through time

c_A constant of the original form of ELSA model [-]

c_Ξ constant of the original form of ELSA model [-]

c_k speed of sound in phase k, $k = l, v$ $[m/s]$

C_μ constant of turbulence model, C_μ=0.09

c_{pl} specific heat of liquid $[m^2/Ks^2]$

$\mathfrak{D}$ diffusion coefficient of the droplet in the carrier fluid $[m^2/s]$

D nozzle diameter $[m]$

d diameter $[m]$

d_m spring-mass constant

d_{max} maximum diameter $[m]$

D_{10} average mean diameter $[m]$

D_{32} Sauter mean diameter, SMD $[m]$

D_{mn} generalised mean diameter $[m]$

e energy $[m^2/s^2]$

$\mathbf{F}$ forces on particle $[kgm/s^2]$

$F()$ cummulative distribution function

$F(\vec{x},t)$ geometrical constraint for surface representation

$\mathbf{F_D}$ drag force $[kgm/s^2]$

F_{spring} restoring force $[kgm/s^2]$

F_{damp} damping force $[kgm/s^2]$

F_σ surface tension force $[kgm/s^2]$

$f()$ probability density function

f_0 parameter in homogeneous nucleation theory

f_v, s mass flux at the surface $[kg/sm^2]$

G,G^* Gibbs free energy, critical Gibbs free energy $[kgm^2/s^2]$

H Heaviside step function

$H()$ matrix coefficient for all the neighbours of a cell with all the source terms expept for pressure

h specific enthalpy $[m^2/s^2]$

h_{fg} enthalpy of vaporisation $[m^2/s^2]$

I unit matrix

J nucleation flux density $[1/m^3]$

Ja Jacob number, $c_{pl}\Delta T_{sh}/h_{fg}\frac{\rho_l}{\rho_g}$ [-]

K model constant for vaporisation source term in ELSA, $K = \mathfrak{D}Sh^*/6$ $[m^2/s]$

K_{br} ETAB model constant

k kinetic energy $[m^2/s^2]$

k_B Boltzmann constant, 1.38064852 10^{-23} $[m^2kg/s^2K]$

k_m spring-mass constant $[kg/s^2]$

L length of nozzle $[m]$

L_{coll} mean free path $[m]$

l length scale $[m]$

l_t turbulent length scale $[m]$

m random natural number

m_d droplet mass[kg]

m_p mass flux in particles $[kg/s]$

m_v mass vaporisation rate $[kg/s]$

M, or Ma Mach number [-]

N normal vector

N_f number of cell faces

N_i number of particles (or number of moles) composing the i-th chemical component

N_{nb} number of neighboring cells

N_p number of particles

N_s parameter in homogeneous nucleation theory

$\vec{n}$ normal vector

$n(t)$ droplet number through time t []

n_f normal face vector in discretised equations [-]

Oh Ohnesorge number, $\mu_l/\rho_l D_{32}\sigma_l$

p pressure $[kg/ms^2]$

Q_p source term in discretised momentum equation [-]

q heat flux $[kg/s^3]$

R, r radius $[m]$

R_g gas constant $[kgm^2/s^2Kmol]$

R_{ij} Reynolds stresses $[kg/ms^2]$

R_p dimensionless pressure [-]

Re Reynolds number, $\rho u_{slip} d/\mu$ [-]

$\mathscr{S}$ velocity ratio

s entropy per mass $[m^2/s^2K]$

$S(\theta)$ function for homogeneous nuleation theory

S generic expression for source terms in ELSA

S_f face area vector [-]

S_{eff} cross-section of collision $[m^2]$

S_{ij} components of strain rate tensor [-]

S_{init} minimum liquid/gas interface production $[1/ms]$

S_{turb} source term for interface production/destruction due to turbulence $[1/ms]$

S_{coll} interface density source term due to collisions $[1/ms]$

S_{2ndBU} interface density source term due to secondary break-up $[1/ms]$

$S_{vap,den}$ interface density source term due to evaporation in dense spray region $[1/ms]$

$S_{vap,dil}$ interface density source term due to evaporation in dilute spray region $[1/ms]$

S_e energy source term

S_m mass source term

S_M momentum source term

Sc Schmidt number [-]

Sc_t turbulent Schmidt number, $\mu/\rho D_m$ [-], where D_m =mass diffusivity $[m^2/s]$

t time $[s]$

T temperture $[K]$

Ta Taylor number, $Oh\sqrt{We_g}$ [-]

T_{2ndBU} total dimensionless characteristic time for drop break-up [-]

T_c critical temperture $[K]$

Sh Sherwood number [-]

$\mathbf{u}$ velocity vector in lagrangian framework $[m/s]$

U specific internal energy $[m^2/s^2]$

u, u_j velocity $[m/s]$

$\tilde{u}_i$ mass weighted Favre averaged velocity $[m/s]$

u_{coll} characteristic collision velocity $[m/s]$

V volume $[m^3]$

$\mathbf{v}$ particle velocity $[m/s]$

$\vec{w}$ surface velocity at the liquid/gas interface $[m/s]$

$\vec{w}_\perp$ tangential component of surface velocity at the liquid/gas interface $[m/s]$

Greek Symbols

A production term due to streching and velocity gradients in surface density equation $[s^{-1}]$

α void fraction [-]

Γ interfacial mass transfer in the HRM $[kg/m^3 s]$

γ sum of liquid and vapour mass fractions [-]

γ_p polytropic constant [-]

Δ filter in Large Eddy Simulations

$\Delta G, \Delta G^*$ difference in Gibbs free energy/critical Gibbs free energy $[kgm^2/s^2]$

Δh difference in enthalpy $[m^2/s^2 kg]$

Δp pressure difference $[kPa]$

ΔV finite volume $[m^3]$

$\Delta x, \Delta y, \Delta z$ grid spacing in directions x,y,z $[m]$

δ_I local instantaneous interfacial area concentration [-]

δ_{ij} Dirac function [-]

ε specific turbulent dissipation $[m^2/s^3]$

Θ relaxation time scale $[s]$

Θ_0 constant in the HRM $[s]$

θ angle [degrees]

η Kolmogorov scale $[m]$

λ_Φ under-relaxation factor [-]

Λ maximum wavelength $[m]$

λ	wavelength $[m]$
μ, μ_t	dynamic viscosity, dynamic turbulent viscosity $[kg/ms]$
μ_i	chemical potential of the i-th chemical component $[J/\text{particle}]$
ν, ν_t	kinematic eddy viscosity $[m^2/s]$
Ξ	production surface term due to turbulence $[1/s]$
ρ	density $[kg/m^3]$
σ	surface tension $[kg/s^2]$
Σ	liquid/gas interface density $[1/m]$
Σ^*	equilibrium interface density $[1/m]$
Stk	Stokes number [-]
τ	characteristic time of a process $[s]$
τ_{bu}	characteristic time of break-up $[s]$
τ_d	frictious time in re-initialisation process in Level Set method $[s]$
τ_{dep}	departure time $[s]$
τ_f	characteristic time of the flow field $[s]$
τ_l	integral time-scale $[s]$
τ_v	momentum responce time $[s]$
τ_{ij}	viscous stress tensor $[kg/ms^2]$
τ_Σ	equilibrium time-scale corresponding to a process in ELSA $[s]$
Υ	destruction term of surface $[ms^{-1}]$
υ	specific volume $[m^3/kg]$
$\tilde{\Phi}$	mass weighted Favre averaged of a variable Φ
Φ	correction fuction [-]
ϕ	liquid volume fraction [-]

χ distance function [m]

χ_d corrected distance function [m]

Ψ phase indicator function [-]

ψ compressibility [s^2/m^2]

Ω growth rate of most unstable wave [s^{-1}]

ω turbulence frequency calculated by the turbulence model [s^{-1}]

Superscripts

$*$ predicted value index

$**$ corrected value index

0 initial state index

corr corrected value

j superscript index

N neighboring cell

n current time-step

$n+1$ next time-step

pred predicted value

sat saturation conditions index

sgs sub-grid scale

$()_f^{\perp}$ normal at the face of the cell

Subscripts

∞ farfield

0 subscript index

1,2 initial and final conditions index

2*ndBU* secondary break-up

$bu, break-up$ related to break-up

$crit$ Critical state

$child$ child droplet

$coll$ collisions

dep departure

f calculation at the cell face

g gas phase

in inlet conditions at nozzle

inj injection state

k Kolmogorov

l liquid phase

max maximum

min minimum

n normal

nb neighboring cell

out outlet conditions at nozzle

p particle index

P centre cell

$parent$ parent droplet

ref reference state

sat saturation state

sh superheat index

$slip$ refererring to slip between the two phases index

sub sub-cooling index

t turbulent property

$turb$ turbulent source term

v vapour state

Other Symbols

$\oint_\gamma$ integration around a curve γ

$\oint$ surface integral

∇ gradient of a scalar or vector, $\partial_j a_i$ rank of a quantity a increases by one

$\nabla\cdot$ divergence of a vector, $\partial_i a_i$ rank of a quantity a decreases by one

∇_s surface divergence

$()_f$ interpolation at cell face

D/Dt material derivative, $\partial/\partial t + u\cdot\partial/\partial x_i$

$sgn(\ )$ the sign function

$\dot{(\ )}, \ddot{(\ )}$ first and second time derivatives

$|\ |$ norm of rank 0 or 1 quantities

$\|\ \|$ norm of rank 0 or 1 quantities

$()_{h,x}$ calculaation of the expression included in parenthesis for constant h,x

$()_{p,x}$ calculaation of the expression included in parenthesis for constant p,x

$()_{p,h}$ calculaation of the expression included in parenthesis for constant p,h

$<>$ statistical average

$\bar{()}$ average of the included expression

$'$ fluctuating part of the quantity included in Reynolds averaging

$''$ fluctuating part of the quantity included in Favre averaging

$\tilde{()}$ Favre average of the included expression

$:$ double inner product of tensors

$\check{()}$ normalised quantity

$\sim$ approximatelly equal

$\mathscr{O}()$ of the order

Acronyms / Abbreviations

ALE Arbitrary Lagrangian Eulerian method

BI Boundary Integral method

CFD Computational Fluid Dynamics

CFL Courant–Friedrichs–Lewy

CSF Continouus Surface Force model

CLSVOF Coupled Level-Set-Volume-of-Fluid

DEM Discrete Element Method

DNS Direct Numerical Simulation

ELSA Eulerian-Lagrangian-Spray-Atomisation

FVM Finite Volume Method

HEM Homogeneous Equilibrium Model

HRM Homogeneous Relaxation Model

HSE Health and Safety Executive

IBM Immersed Boundary Method

IC Internal Combustion

KH Kelvin-Helmholtz

LS Level Set

LES Large Eddy Simulation

LHS Left Hand Side

LNG Liquefied Natural Gas

NS Navier-Stokes

NIST National Institute of Standards and Technology

SIMPLE Semi-Implicit Method for Pressure-Linked Equations

SLIC Simple Line Interface Calculation

SPH Smoothed Particle Hydrodynamics

TAB Taylor Analogy Break-up model

TVD Total Variation Diminishing

PISO Pressure implicit with splitting of operator

PLIC Piecewise Linear Interface Calculation

R134A 1,1,1,2 – Tetrafluoroethane: $CF_3 - CH_2F$

RANS Reynolds Averaged Navier Stokes

RHS Right Hand Side

RT Rayleigh-Taylor

SGS Subgrid Scale

VOF Volume of Fluid

Chapter 1

Introduction

Flash-boiling atomisation is a process that transforms bulk liquid into a spray due to mechanical and thermodynamic effects. This process plays an important role in process industries, aeronautics, automotive engineering and power generation.

This complex phenomenon is the result of two major mechanisms: flash-boiling and liquid atomisation. The fundamentals of these phenomena are widely studied since the twentieth century and both are extremely important in health and safety, in the controlling of the efficiency, and the study of the nature of many systems which involve a sudden pressure drop. The characteristics of the spray produced in case of an accidental pressurised release are still poorly predicted. In cases of LNG sprays, no detailed numerical or experimental studies are reported in the literature regarding the jet structure.

Moreover, the prediction of the spray dynamics and dispersion is of critical importance to predict the behaviour of the vapour cloud that cryogenic liquids produce, and is now part of an upheaval in the global energy industries for generating numerical tools to model the process.

This study is part of a research program that aims at providing academia and industry with a modelling tool to simulate and investigate the complex multi-facet phenomenon of flash-boiling atomisation.

1.1 Background

Flash boiling is the rapid phase change of a fluid that discharges to ambient conditions below the vapour pressure leading to nucleate boiling. Usually, this occurs when a fluid is initially stored under high pressure and high temperatures. Flash boiling jets have numerous applications in industry and can be either dangerous, leading to disastrous releases for the human body and infrastructure, or be beneficial. In terms of safety, typical industrial scenarios

involve accidental releases in cracks at pipeline systems, for instance in CO_2 transferring, or storage vessels of cryogenic liquids like liquefied natural gas (LNG). Other applications are the loss of coolant accidents (LOCA) in nuclear power plants where pressurised water flashes emanating from a fracture into the ambient conditions. In aerosol industry, flashing can be an efficient method to produce fine sprays reducing the mean droplet size of the liquid drops. This can be advantageous in droplet impingement on solid surfaces, medical and paint sprays. In combustion, flashing can enhance the combustion of the fuel spray and increase the efficiency. In all these cases, the release results in a spray at the nozzle exit which disperses, following turbulent mixing and aerodynamic break up, producing either a hazardous and potentially explosive two-phase cloud or a fine spray surrounded by vapour. The whole process is not fully understood experimentally, however in all the above scenarios the physics of the jet is the same. Differences occur depending on the fluid. For instance, in cases of water jets, the spray morphology is inherently different than in cryogenic liquids such as LNG, which is subject to enhanced evaporation. In general, the stages that flash-atomisation consists of, are nucleation, bubble growth, and atomisation. Flashing can occur either inside or outside the nozzle depending on the local pressure and geometry among others, and the vapour generation leads to interfacial interactions that influence the spray properties. Critical flow and choking are of major importance in chemical process industry and are also related to flashing and cavitation. A precise knowledge of critical flow behaviour is related to the efficiency and level of safety of the system. Hence, cavitation and flashing form a challenging problem from academic point of view and a major topic in industry. The study of these processes is an integral part of on/off-shore facilities and consequently is directly associated to the energy market.

Especially for LNG, technologies for storing and handling liquefied natural gas have matured rapidly and have now established it in as a popular energy source. The LNG trade has quadrupled over the last two decades and is set to double over the next two. In the upcoming years, the growth in LNG supply and the liquefaction plants already under construction, is forecast to create a long market.

1.2 Motivations

Flashing occurs, like cavitation, when the liquid becomes locally superheated. The liquid usually flows though channels whose geometry is a major parameter for the study of the jet hydrodynamics. The non-zero length of the channel is not a necessary condition, which means that flashing can occur with liquids flowing through orifices as well.

The phase change is manifested by bubbles forming within the liquid, changing progressively the regime of the flow. The definition of the exact time and position of the bubble generation is not a trivial task, especially in the presence of turbulence. The flow is strongly dependent on the initial pressure and superheat or sub-cooling degree. The flow characteristics dominantly affect the subsequent atomisation upstream the nozzle exit. Atomisation of a liquid jet is the process of the progressive fragmentation of the jet from a liquid core to ligaments and blob gradually producing a spray. This liquid fragmentation is the outcome of either mechanical or thermodynamics effects. In superheated jets atomisation, both mechanisms are acting in a competing manner Figure 1.1. The rapid phase change along the jet and bubble nucleation within the liquid core influences the spray formation. Insights drawn from scholarly literature suggest that flashing inception might start either inside or outside the channel. Consequently, flash-boiling atomisation of superheated jets is a two-fold problem: both internal flow patterns and the spray dynamics downstream the channel must be studied to fully describe the underline physics of the phenomenon. Cavitating and flashing jets atomisation are commonly studied experimentally. Analytical models from the 1960's (Fauske, 1962; Henry, 1970; Moody, 1965) and experimental studies for the internal flows have provided engineers useful knowledge in a first pragmatic approach. Detailed experiments in the 1990's (Park and Lee, 1994; Park et al., 1997; Reitz, 1990) gave new insights for the spray characteristics of these jets. The phenomenological nature of the developed analytical models and the limitations of the experiments which arise from the intrusive techniques for data collection, the limitation in resolution and cost has led engineers to other approaches such as CFD. This study illustrates the importance of using Computational Fluid Dynamics to simulate the flashing phenomenon and its impact on the atomisation. CFD is proven to be a useful and reliable tool for modelling complex flow phenomena, such as cavitation and liquid atomisation, for academic and industrial purposes. One the of the most attractive advantages of CFD simulations is that there are no limitations in the scales of the problem. Although this is not entirely true due to CPU limitations, in practice numerical modelling has to do with a trade-off in terms of accuracy and computational cost. Other restrictions such as near-nozzle region spray data which is a major challenge in experiments are overcome with CFD. Here, CFD techniques are used to model the complex flow patterns of the jet starting from the flow inside channels, moving on to the investigation of the major traits in the dense and dilute regions of the generated sprays.

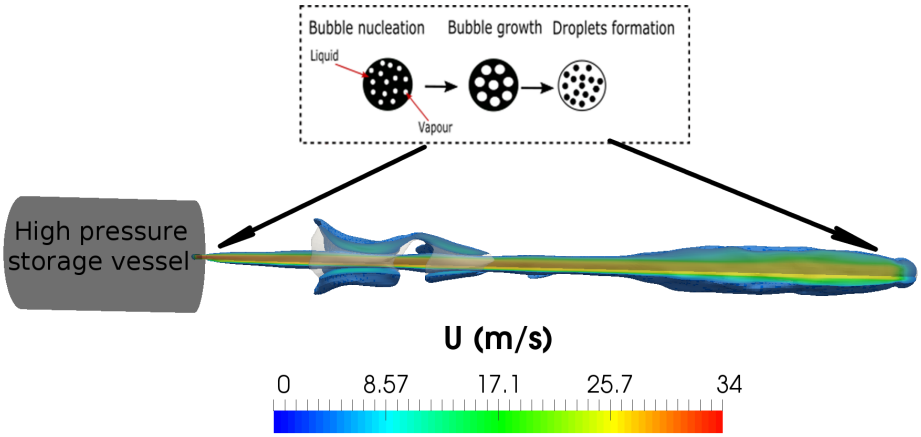

Fig. 1.1 Graphical illustration of an R134A jet emerging to a low pressure region through a channel (velocity magnitude is shown). The resulting two-phase jet has higher velocity at the centreline. The atomisation process is the result of both fluid flow instabilities (Kelvin-Helmholtz) and the boiling process which changes the regime ((Lyras et al., 2017b)).

1.3 Approaches for modelling flash-boiling

This research builds on existing knowledge in the fields of Numerical Analysis and Physics involving models and techniques established the last decades. A careful study of the basic concepts and notions is essential in order to understand the fundamental mechanisms of flashing and the atomisation process. Lord Rayleigh was one of the first that studied the bubble growth proposing 1892 the first equation for bubble radius evolution decades before meticulous experiments shed some light regarding bubble nucleation and parametric studies that identified the parameters that influence the bubble formation. Plesset later, in 1953, expanded Rayleigh's equation including viscosity utilising the basic equation for bubble evolution which is used till today in both analytical modelling and CFD codes for modelling cavitation. Unfortunately, the Rayleigh-Plesset equation only predicts the behaviour of one single bubble. The complex flows within channels demand an investigation across the entire liquid jet considering the possibility of bubble interactions, geometry influence e.t.c.

Similarly, the first attempts to investigate the fundamentals of liquid jet atomisation date back to the works of Savart (1833), Plateau (1853) and Rayleigh (1892). The growing waves on the jet surface have been studied and gave boost ever since to understand when primary atomisation occurs. Researchers have classified the growing instabilities which fragment a liquid jet. In this thesis, Kelvin-Helmholtz and Rayleigh-Taylor instabilities are notably studied. CFD methods have the capability to capture these instabilities in the frame of Navier-Stokes equations and these capabilities are illustrated in the developed methodology here. The majority of the numerical models for simulating the properties of the two-phase

mixture during flash-boiling uses various assumptions. These assumptions aim to simplify the problem for evaluating the properties of interest in a more straightforward way than detailed CFD approaches. They might have their basis on a zero or one-dimensional thinking and are usually induced from experimental observations. A successful model should be able to simulate the two-phase flow characteristics such as the velocity, pressure, mass fractions and densities. Analytical models usually exist for the internal flow properties considering the stagnation conditions. Such analytical models emerged since the 1960s and assume either thermodynamic equilibrium or they are frozen flow models in a sense that no mass transfer is considered between the two phases. Later, models considering thermodynamic non-equilibrium were developed employing empirical correlations. In the same direction, empirical correlations have been developed based on experiments for the spray properties of flashing and cavitating jets of water or hydrocarbon fuels. These models are divided to those that assume that the jet has constant enthapy during the release process (isenthalpic conditions) and those that assume that the entropy of the jet is constant (isentropic conditions) for the expansion region. There is an uncertainty in the literature regarding which assumption is more reasonable since both induce errors. Correlations for important parameters like the Sauter mean diameter (SMD) are proposed taking into account the inertia and viscous forces, the pressure drop the liquid jet experiences and the superheat degree. The result is the SMD to be a function of the non-dimensioned numbers (Reynolds, Weber, Ohnesorge e.t.c.). The range of validity of such empirical formulations is generally limited and dictated by cut-off values of these dimensionless numbers and geometry constraints. Three-dimensional CFD approaches have been developed from the 1980s with the increasing computer capabilities. CFD methods in CFD software, commercial or open-source, are usually developed in a Eulerian or Lagrangian framework. Additional numerical techniques such as interface tracking methods or models for particle motion and interactions are needed for closure. Turbulence models for multiphase flows have matured the last decades, and both RANS and LES are employed here. For the applications considered here (sub-sonic/sonic releases) the pressure-based approaches are proven to be efficient enough for all the stages of the process. A pressure-velocity algorithm is needed to correct the numerical solution and its importance is particularly discussed in this study.

1.4 Aim of the present work

Flashing occurs either if a liquid follows an isothermal depressurisation or an isobaric heating. In both cases, the fluid fails to adjust to the local changes in pressure and temperature, admitting a metastable state which makes the process more challenging to understand. The

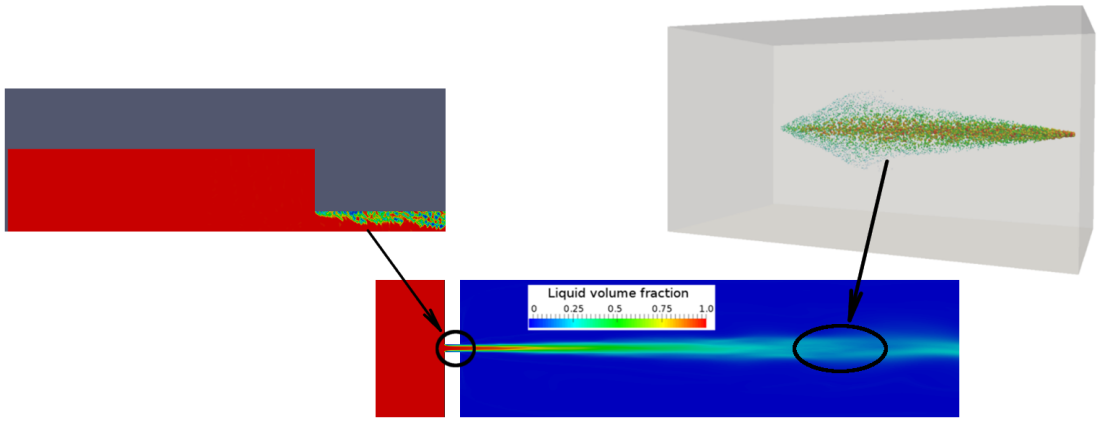

Fig. 1.2 Graphical illustration of the jet emerging to a low pressure region through a channel. The atomisation process is the result of both fluid flow instabilities (Kelvin-Helmholtz e.t.c.) and the boiling process which changes the regime (Lyras et al. (2017a)).

research here aims to overcome the limitations of zero-dimensional empirical correlations performing simulations in two and three dimensions, elucidating the impact of geometry and the nozzle length-to-diameter ratio, the degree of superheat or sub-cooling, the storage and ambient conditions on the atomisation process. Owing to the complexity of the two-phase flow, a unified multi-scale and multi-dimensional approach is developed as shown in Figure 1.2.

One of the major challenges for modelling the atomisation of superheated jets regarding physics is the metastable two-phase mixture that occurs during depressurisation. The Homogeneous Relaxation Model (HRM) is a reliable model able to capture mass transfer under these conditions, accounting for the non-equilibrium vapour generation. This approach uses a relaxation term in the transport equation for the vapour. On the basis of the generic compressible flow solver within the open source computational fluid dynamics (CFD) code OpenFOAM, the HRM has been implemented in the current PhD thesis to create a dedicated new solver. An algorithm that links the standard pressure-velocity coupling algorithm to the HRM is used. In this method, a pressure equation is derived which employs the continuity equation including compressibility effects. The pressure equation is based on the methodology of Schmidt et al. (2010) and some new extensions are proposed. A relaxation term has been defined such that the instantaneous quality would relax to the equilibrium value over a given time-scale. Although it is possible to consider this time-scale constant, it is calculated via an empirical correlation in the present study.

This study presents a numerical approach for simulating the atomisation of flashing liquids accounting for the distinct stages, from primary atomisation to secondary break-up to small droplets using the Eulerian-Lagrangian-Spray-Atomisation model coupled with the

homogeneous relaxation model. The surface density equation (Σ-equation) is implemented in the code and solved in a fully Eulerian approach for tracking liquid structures of any shape, and computes the spray characteristics. A modified version for the transport equation of the surface density is used and new source terms accounting for the changes in Σ due to evaporation in both dense and dilute spray regions are added.

The proposed approach has the advantage of avoiding the unrealistic common assumption of pure liquid rather than a mixture at the nozzle exit. It models the change in the regime inside the nozzle treating flashing in a unified approach, simulating the metastable jet both inside and outside the nozzle. Important mechanisms such as thermal non-equilibrium, aerodynamic break-up, droplet collisions and evaporation are modelled in a novel atomisation model. Results for turbulent flows for both sub-cooled and superheated liquids are presented showing that the proposed approach can accurately simulate the primary atomisation.

1.5 Outline of the thesis

This thesis is organised into two main parts. In the first part, the thesis includes the necessary background on the physics of cavitation and flash-boiling of liquids (chapter 2). The fundamentals of the physics of primary atomisation of liquid jets are included in chapter 3. Chapters 2 and 3 include detailed reviews of the existing numerical models for simulating cavitation and flashing in nozzles and liquid atomisation and secondary break-up. Discussions for the capabilities and the limitations of the currently popular approaches in the literature are also added. Some results for a Lagrangian approach for flashing jets are presented in Chapter 3. The importance of simulating the internal flow as an integral part of the liquid jet atomisation is highlighted many times in this document and in particular in chapters 2, 3 and 6. In chapter 4 the basic background on the numerical framework for turbulence modelling, pressure-velocity algorithms and OpenFOAM is given. The novelties of this research are included in two different Chapters. In chapter 5 a novel pressure equation for flash-boiling including the coupling of HRM and interface tracking methods. A detailed description of this coupling for the development of a conservative finite volume method is presented. Chapter 6 describes an ELSA method for modelling atomisation using a new modified surface density equation. This novel coupling illustrates the first numerical 3D approach in the literature for simulating cavitating and flashing jets in a holistic approach that considers the internal flow effect in the spray dynamics. Results for validation and obtaining new insights are presented in the RANS/LES framework and for various liquids including water, liquid nitrogen, R134A and LNG.

Chapter 2

Flash-boiling and cavitation

The basic principles that trigger the mechanisms of cavitation and flashing are contextualised at this chapter. The flash-boiling process is directly linked to the bubble nucleation, bubble growth and atomisation. Bubble growth has been studied theoretically since the nineteenth century with a starting point the pioneering work of Lord Rayleigh and a brief discussion of his work is included in Section 2.3. The result of bubble nucleation is the bubbles to growth and disperse through the carrier fluid. The studies in this chapter are limited to two-phase flows of liquid and gas only. Bubble nucleation gives rise to a wide range of flow regimes which are listed in the last Section. The most important of these regimes related to flashing jets are discussed.

2.1 Physics of flashing and cavitation

The mechanisms of Flash-boiling and cavitation

The disintegration of liquid jets from a high pressure region to a small pressure environment is an interesting topic in multiphase flows. Depending on the application, this pressure drop may occur when the liquid flows through a nozzle or a pipe. If the pressure drops below the vapour pressure, a rapid phase change begins which is generally termed flashing. In case of pure cavitation, the pressure recovers above the limit of the vapour pressure unlike the extreme case of flashing in which pressure remains below the saturation pressure. Both of these processes occur in various industrial scenarios such as fuel spray injection systems, accidental releases through cracks in pipes and loss of coolant accidents (LOCA) in nuclear industry to name a few. Prior research from Ishii (1975); Oza (1984) has suggested that flash boiling is associated to three different processes, which are, bubble nucleation, bubble growth

and atomisation. In order to establish a modelling strategy for flashing we have to give an illustration of the factors that contribute to this multi-facet problem. Flashing of a liquid can occur when the fluid, initially being either sub-cooled or saturated, follows an isothermal pressure drop or an isobaric heating path respectively as shown in Figure 2.1. As long as the liquid moves towards the low pressure region, the pressure drops and upon reaching the liquid saturation curve it becomes superheated. In cases of a liquid flowing within a channel, the fluid might be superheated inside or outside the channel depending the geometry and the thermodynamic conditions.

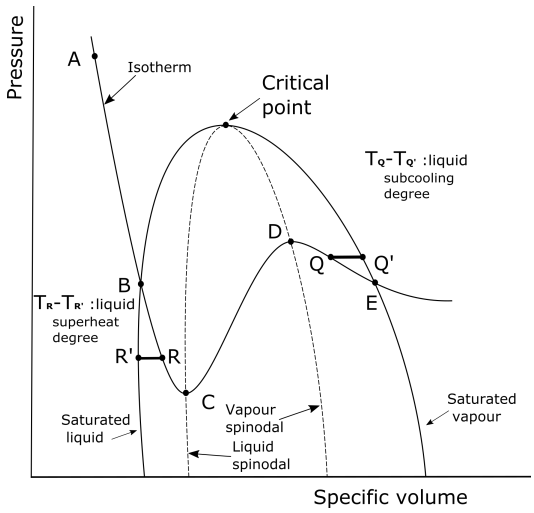

Fig. 2.1 Graphical explanation of the stages of flashing process explained in the pressure-specific volume diagram.

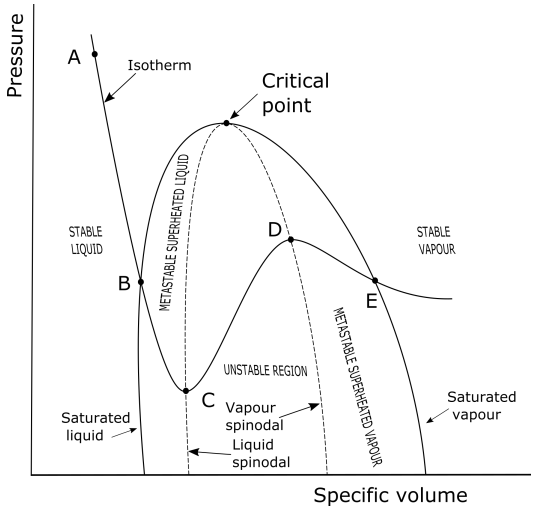

Fig. 2.2 Stable, metastable and unstable regions in flashing process. Reproduced by Sher et al. (2008)

Bubbles form and grow following the isotherm inside the saturation dome until the limiting point of the $\partial p/\partial \upsilon = 0$ (spinodal line). At that point, the isothermal compressibility K (equal to $-\rho(\partial p/\partial \upsilon)^{-1}$) becomes infinite. When the liquid is superheated enough to cross this threshold, the liquid cannot exist, in theory, in a superheated state and separates spontaneously into two phases. This phase transition from the metastable to a stable state is associated to the bubble formation at an initial stage and the bubble growth and the final stable liquid-vapour equilibrium later on.

Figure 2.1 illustrates the difference between boiling and cavitation. Assuming that a saturated liquid (point B) rapidly depressurises following the isotherm, cavitation takes place. Cavitation is the process of liquid rupturing when the pressure falls below the vapour pressure in nearly constant temperature (bubble nucleation). Upon reaching point B and if there exit sufficient nucleation sites of a certain size the state will move from point to B to C and liquid will become vapour. The state will then come to equilibrium beyond the point E. In the scenario that not enough nucleation cites are present, the fluid will not follow the same path BC as before but state down the theoretical isotherm to a metastable state. For a random point R at the metastable liquid region the process of cavitation is denoted with the path $(B-R)$. In case of boiling, the process of nucleation takes place when temperature raises above the saturation value and corresponds to the path $(R^{'}-R)$ in the same graph. The degree of superheat, ΔT_{sup} of the liquid can be defined as the difference between these two last temperatures e.g. $\Delta T_{sup} = T_R - T_{R'}$. The liquid sub-cooling degree is defined as the temperature difference of a liminal state Q between the vapour spinodal (point D) and the theoretical isotherm (point E) at the metastable vapour region, with the vapour temperature, e.g. $\Delta T_{sub} = T_Q - T_{Q'}$. Both of these degrees are some of the parameters that influence the phase transition from the metastable to stable state, manifesting different physics and thus they have significant impact on the spray morphology. The probability for the vapour to form, increases with increasing the superheat. Flashing jets usually have an enhanced and faster evaporation rate than non-flashing jets.

Basic principles of flashing

Regarding the sub-critical releases the liquid spinodal curve defines the extent to which the liquid can reach without any vaporisation and divides the region inside the saturation dome in two regions, the metastable (superheated) liquid region and the unstable one. In exactly the same way, the vapour spinodal curve, separates the unstable and the metastable (supercooled) vapour region. The schematics is shown in Figure 2.2. It is clear that the two spinodals meet

at the critical point. Denoting the internal energy and entropy with U and s respectively we have the following criteria for the stability of the system

$$\left(\frac{\partial^2 U}{\partial s^2} \leq 0\right) \quad \text{and} \quad \left(\frac{\partial^2 U}{\partial \upsilon^2} \leq 0\right) \tag{2.1}$$

$$\frac{\partial^2 U}{\partial s^2}\frac{\partial^2 U}{\partial \upsilon^2} - \left(\frac{\partial^2 U}{\partial s \partial \upsilon}\right)^2 \leq 0 \tag{2.2}$$

Hence the following stand inside the saturation dome

$$\frac{\partial^2 U}{\partial s^2} = \frac{\partial U}{\partial s}\left(\frac{\partial U}{\partial s}\right) \rightarrow \frac{\partial T}{\partial s} \leq 0 \tag{2.3}$$

$$\frac{\partial^2 U}{\partial \upsilon^2} = \frac{\partial U}{\partial \upsilon}\left(\frac{\partial U}{\partial \upsilon}\right) = \frac{\partial}{\partial \upsilon}(-p) \rightarrow \frac{\partial p}{\partial \upsilon} \geq 0 \tag{2.4}$$

The last inequalities are derived using the definition of temperature $T = (\partial U/\partial s)$ and pressure $p = (\partial U/\partial \upsilon)$ for constant volume and entropy (and other state variables) respectively (Kovev (2011)). The last part of Equation 2.4 is the basic principle of flashing. As an example of an equation of state that respects this together with the critical point condition $\partial p/\partial \upsilon = \partial^2 p/\partial \upsilon^2 = 0$ is the Van der Waals equation of state. A description of this equation of state is out of the scope of this research, although it is important to mention that it generally fails to predict the actual properties in the liquid/gas transition region.

2.2 Bubble nucleation

During the depressurisation process, the pressure might drop enough initiating an early flashing event (Sher et al. (2008)). This might be enhanced by other parameters such as turbulence or the changes at the nozzle geometry. Iciek (1980) has pointed out this impact of turbulence on the jet dynamics and observed that for long nozzles, the developed turbulence attenuates the effect of the nozzle length. Moreover, in typical channel geometries, sharp inlet corners usually exist forming high pressure gradient areas in their vicinity. Pressure fluctuations may trigger phase transition where the local pressure falls below the saturation value. There are two types of nucleation

- The homogeneous nucleation
- The heterogeneous nucleation

Additional subdivisions include, bulk-homogeneous, bulk-heterogeneous ad wall nucleation. Homogeneous nucleation is inherently associated with the existence of metastable gas cavities in micro-scale level. According to Brennen (2013): *The thermal motions within the liquid form temporary, microscopic voids that can constitute the nuclei necessary for rupture and growth to macroscopic bubbles*. This describes homogeneous nucleation. Homogeneous nucleation occurs when no impurities of pre-existing interfaces exist in the flow. The pressure variation gives a non-zero Gibbs free energy G characteristic of the energy content of the fluid. The change in G equals to the work exchanged by the system with its surroundings and is proportional to the pressure change[1], $\Delta G = V\Delta p$. Following the homogeneous nucleation theory, the nucleation flux density J can be calculated as follows:

$$J = f_0 N_s exp\left(-\frac{\Delta G^*}{k_B T}\right) \tag{2.5}$$

where J is the critical nuclei formed per unit of time and unit of volume, k_B is the Boltzmann constant, T is the temperature and f_0, N_s are parameters related to the nuclei rate of change. The constant f_0 can be considered as a product of the rate of incoming matter with the probability that a nuclei in its critical size will continue to grow (the so-called Zeldovich factor). The factor ΔG^* is the free energy barrier to nucleation. This is the maximum value of the free energy which is a function of the characteristic scale of the nucleus e.g. the radius r assuming spherical configuration. The maximum is then calculated for $\partial G/\partial r = 0$ which gives

$$\Delta G^* = \frac{16\pi\sigma^3}{3(\Delta g)^2} \tag{2.6}$$

where σ is the surface tension of the liquid and Δg is the difference in chemical potential between the liquid and vapour phases and is proportional to the inverse of the square of temperature difference.

In the heterogeneous nucleation, the solid boundaries influence the nucleation rate resulting into a reduced critical free energy

$$\Delta G^* = \frac{16\pi\sigma^3}{3(\Delta g)^2} S(\theta) \tag{2.7}$$

where $S(\theta)$ is function of the angle θ of the solid with the nozzle wall (nucleating agent) and $S(\theta) < 1$. Equation2.5 describes the initial stage during the formation of a new phase. For a bubble with pressure p_b and uniform temperature distribution T, the pressure difference

[1] Using the Legendre transformation of internal energy, $dU = -pdV + TdS + \sum_i \mu_i dN_i$, from the Gibbs free energy definition $G = pdV + U - TdS$ and after some algebraic manipulations one gets $dG = Vdp - sdT - \sum_i \mu_i dN_i$.

between with the ambient pressure p is related to the surface tension with

$$p_b - p = \frac{2\sigma}{R} \tag{2.8}$$

The bubble radius will continue grow until the exterior pressure $p = p_{sat} - 2\sigma/R$ in the limiting case of pure vapour inside the bubble (critical radius R_{crit}). The tensile strength of the liquid is then $\Delta p_{crit} = 2\sigma/R_{crit}$. Gibbs (1961) correlated this tensile strength with the energy burier for nucleation to be equal to $\Delta G^* = 16\pi\sigma^3/3(\Delta p_{crit})^2$, which is similar to equation 2.6.

Experimental investigations on the nucleation kinetics report a different response of the liquids in the temperature variations which corresponds to different nucleation rates. For instance, for flashing water and for moderate superheat ($T < 0.7T_c$, T_c is the critical temperature), J is in the range between $10^2 - 10^4 cm^{-3}s^{-1}$ whereas for higher superheat the nucleation rate grows within $10^8 - 10^{13} cm^{-3}s^{-1}$ (Pavlov (1988)). The intensity of the bubble nucleation rate generally leads to an enhanced boiling and is a primary cause of change in the flow regime which can be combined with shattering of the jet attributing explosive characteristics to the process. Previous studies have shown that even small changes in temperature may alter the jet structure (Park and Lee (1994)). In light of this, it is likely to have a two-phase jet inside the nozzle with a variety of possible regimes (Sher et al. (2008), Park and Lee (1994)). A paradigm of the most crucial parameters for bubble nucleation is the geometry of the nozzle the fluid flows through (Park et al. (1997)). Many studies have been carried out regarding the expected regimes in industrial depressurisations applications (Benajes et al. (2004); Cleary (2008); Yellow book (2005); Yildiz (2005)). Usually, phenomenological approaches induced from experiments consider the length-to-diameter of the nozzle to be the integral geometry parameter that influences the flow regime, although other studies suggest that the use of the length of the nozzle might be also adequate (Yellow book (2005)). Notwithstanding with the choice of the description of the geometric factor, the resulting jet can be thought as the outcome of two mechanisms, which is the fluid instabilities (i.e. Kelvin-Helmholtz) on one side, and the boiling conditions together with thermal non-equilibrium on the other side. These mechanisms act in and on the jet in a competing way and give rise to a violent disintegration, characteristic of the flashing process. Flashing continues until the generated vapour has enough energy to achieve equilibrium.

2.3 Bubble growth - Rayleigh-Plesset equation

The starting point of the bubble growth study is the Rayleigh equation. Assuming the ideal case of a spherical bubble that increases in a large uniform superheated liquid domain of density ρ_l and neglecting the effect viscosity and surface tension, Rayleigh (1917) calculated the radius R of a bubble from

$$R\ddot{R} + \frac{3}{2}\dot{R}^2 = \frac{p_v - p_\infty}{\rho_l} \tag{2.9}$$

Where p_v, p_∞ are the vapour pressure and the ambient pressure. The bubble will continue to grow until it reaches the critical value R_{crit} (Blake critical radius) which is calculated with respect to the bubble temperature T_g and mass m_g according to Brennen (2013); Crowe (2005)

$$R_{crit} = \sqrt{\frac{9\gamma_p m_g T_g R_g}{8\pi\sigma}} \tag{2.10}$$

At that point every fluctuation in pressure might lead the bubble to collapse. The effect of surface tension and viscosity μ was included in the work of Plesset. The surface tension can be interpreted as the macroscopic representation of the intermolecular forces that tend to hold molecules together and viscosity the resistance of the liquid in deformation by either shear stress or tensile stress. The resulting Rayleigh-Plesset equation for the bubble growth reads

$$R\ddot{R} + \frac{3}{2}\dot{R}^2 = \frac{1}{\rho_l}\left(p_v - p_\infty - \frac{2\sigma}{R} - \frac{4\mu}{R}\dot{R}\right) \tag{2.11}$$

Initially, the radius growth of the small bubble that forms is dominated by the surface tension. Depending on the superheat degree of the liquid, the bubble grows and reaches the value that corresponds to an equal liquid and vapour pressure. After this point, the surrounding liquid cools down due to the heat that is released due to evaporation. The vapour pressure drops and thermal diffusion and inertia control the bubble growth rate. Thermal diffusion prevails over the inertia when the bubble growth rate further decreases (Plesset and Prosperetti (1977)).

2.4 Flow regimes in two-phase flows

There are different regimes of two-phase flows. We limit our study in this thesis in immiscible fluids which are either in liquid or gas state. The two-phase flow patterns have been categorised by various researchers in the past (Hewitt and Hall-Taylor, 1970; Ishii, 1975; Wallis, 1969;). Here we choose to follow the classification of Ishii (1975). The two-phase flow can be divided in three different classes:

1. Separated
2. Mixed or transitional
3. Dispersed

The annular and jet flow are the two cases of separated flow that are going to be investigated in this research. The annular regime was proven to be quite common for a vast majority of channel flows we investigated for lower and higher pressure and short and small nozzles. The role of the pressure gradients in the sharp inlet corners is discussed in Chapter 5. The flow inside the nozzle is inherently connected with flashing/cavitating sprays and full details of the associated parameters is discussed in Chapter 3. The dispersed-flow regime includes droplet and bubbly flows. The bubbly flow is also possible for the change in the regime in the depressurisation scenarios presented here and is evident in the density change along the flow. The droplet-flow regime is studied together with the jet flows and a dedicated method for the characterisation of the atomisation of flashing jets is proposed in Chapter 6. The transitional regimes can also be present along the pressure drop direction and depend on a wide range of parameters like the thermo-physical properties of the fluid and the channel geometry. The overview of the regime classification is shown in Figure 2.3.

Experimental studies for pressure and mass flow rates in cavitation/flashing

Studies in cavitation within nozzles have shown that it has a key role in spray dynamics and atomisation efficiency (Schmidt and Corradini (2001)). The geometry, initial conditions and the composition of the mixture are mainly responsible for preserving or damping the transient phenomena. In case of sharp nozzle inlets the fluid flows towards a smaller cross section and accelerates. The fluid reaches its maximum velocity at a short distance from the nozzle inlet. The result is flow separation in the vicinity of the nozzle walls with the stream diameter becoming minimum (vena contracta). Winklhofer et al. (2001) studied diesel fuel cavitation at high pressures and illustrated how the pressure drops inside a nozzle for different nozzle geometries. Two regions with a high-pressure gradient are identified: one at the inlet and another one at the outlet of the nozzle. Similarly, the same trend for pressure drop inside nozzles are reported from Park et al. (1997); Tikhonenko et al. (1978) for flashing water experiments.

Park et al. (1997) has studied internal flashing for water using nozzles with different lengths. They noticed that the flashing inception starts inside the nozzle and that pressure

Class	Regimes	Description
Separated flows	Film flow	Liquid film in gas Gas film in liquid
	Annular flow	Liquid core and gas film Gas core and liquid film
	Jet flow	Liquid jet in gas Gas jet in liquid
Mixed or transitional flows	Cap, Slug or Churn-turbulent flow	Gas pocket in liquid
	Bubbly annular flow	Gas bubbles in liquid film with gas core
	Droplet annular flow	Gas core with droplets and liquid film
	Bubbly droplet annular flow	Gas core with droplets and liquid film with gas bubbles
Dispersed	Bubbly flow	Gas bubbles in liquid
	Droplet flow	Liquid droplets in gas
	Particulate flow	Solid particles in gas or liquid

Fig. 2.3 Graphical illustration of the two-phase flow regimes reproduced from Ishii (1975).

distribution has similar patterns across the channel for different storage conditions. The effect of flashing on the mass flow rate was also studied. The authors showed that the initial pressure has a strong impact on the mass flow rate for both sub-cooled and superheated water. The impact of initial temperature on the mass flow rate was studied by Reitz (1990) who observed that increasing the temperature, the mass flow rate decreases. This decrease was attributed to the bubble nucleation: Increasing the temperature, liquid density drops, and the generated vapour reduces the total (mixture) density. Different inlet pressures and sub-cooling degrees were studied by Xu et al. (1995) in order to determine their effect on the mass flow rate of flowing sub-cooled and saturated water. Importantly, then authors showed that the mass flow rate is less sensitive for short nozzles compared to long ones. Moreover, the initial pressure proved to be a catalytic parameter for all the geometries. Regarding mass flow rate experiments for cryogenic liquids, Simoneau (1975) has studied flashing liquid nitrogen jets through orifices and for a wide range of pressures indicating the existence of a metastable jet at the orifice. Similar behaviour for the mass flow rate regarding the temperature changes is also reported for liquid oxygen flashing jets flowing through converging-diverging nozzles (Hendricks et. al. (1976)). The mass flow rate of liquid Nitrogen and the profile of important quantities such as density and velocity are discussed in Chapter 6. Recently, Wang et al. (2017) studied the impact of pressure increment in bubble nucleation in cryogenic fluids. They examined internal flashing R134A discharging through long nozzles ($43 < L/D \leq 60$) for pressure less than 15 bar. They observed that bubble nucleation happens in random positions inside the channel. For small pressure difference bubbles formed in the vicinity of the inlet whereas upon increasing the pressure bubbles formed along the channel or close to the exit for higher values. Large bubbles were also observed and the bubbly regime tended to be stable increasing the pressure.

Modelling flashing and cavitating flows

Some of the most commonly used numerical models for cavitation and flashing are illustrated in this chapter. These approaches are applicable for superheated liquids flowing through nozzles and channels. The thermal non-equilibrium and the compressibility effects are two major challenges in modelling flashing, previous studies have addressed. Generally accepted numerical models for flash boiling flows are of limited number. The pressure change is of high-priority for updating the thermo-physical properties of the mixture and is discussed.

2.5 Modelling critical flow rates

Flashing is a complex process involving multiphase flows that usually occurs during the sudden depressurisation of a fluid stored under high pressure and high temperatures. Although the whole process of flashing is not entirely understood experimentally, its stages can be divided into nucleation, bubble growth, and atomisation Oza (1984). Flashing can occur either inside or outside the nozzle depending on the local pressure and geometry among others, and the vapour generation leads to interfacial interactions that eventually influence the spray properties. A key aspect of flashing is bubble nucleation. The flashing phenomenon may happen in the case of a superheated or a sub-cooled liquid following either an isothermal or an isobaric process which corresponds to a metastable state where liquid and vapour co-exist. Flashing inception starts when, inside the saturation dome, the liquid exists in a metastable state. In this situation the liquid is in tension and will follow the thermodynamic path described above.

Bubble formation and growth in two-phase mixtures within nozzles have a significant impact on the atomisation process and spray dynamics. Depending on the vaporisation rate and conditions the flow pattern might be bubbly, slug or annular. The regime of the flow has a significant impact on the flow characteristics and the mass flow rate. Increasing pressure, the mass flow rate increases due to the mass conservation principle. At the limiting point at which the mass flow rate is not increasing, the flow is described as choked (Figure 2.4). In this occasion the mass flow rate is maximum. Decreasing downstream pressure the mass flow rate does not change for constant upstream pressure. Another associated term is the critical flow which is used to characterise the locally sonic flow at the channel exit. It is common that the terms "choked" and "critical" are used interchangeably in various texts in literature, but they should not be confused. According to Kovev (2011), the formal definition of critical flow is when the Mach number inside the channel becomes equal to one. Choking differs from critical flow phenomenon in that it is due to the rapid expansion of the superheated fluid that pushes back the flow. It is possible that choking occurs at a sub-sonic speed (w.r.t. frozen acoustic speed). Calculation of the critical mass flow rate is extremely important in industry typical applications of which, require prior knowledge of the mass flow rate for safety and design purposes. Critical flow for a single-phase gas occurs when the flow is sonic (Mach number is one) at the smallest cross-section. The molecular relaxation phenomena are rapid enough so that the thermodynamic equilibrium is achieved. In cases of two-phase flows, the relaxation time-scales of heat and mass transfer are comparable to the residence time of the fluid at the choking region. The definition of a critical location cannot be easily established as in single-phase flows making the two-phase flow more complex.

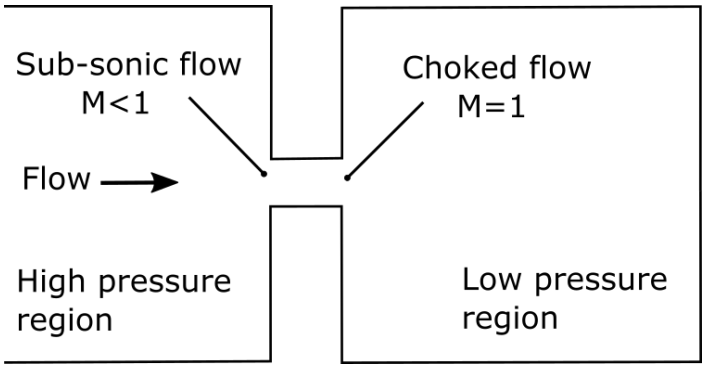

Fig. 2.4 Flow at choking conditions with respect to the Mach number, M. The sub-sonic flow ($M < 1$) becomes sonic at the nozzle throttle ($M = 1$).

Frozen flow model and Bernoulli equation

Different modelling strategies have been developed for simulating flashing flows inside pipes and giving an approximation of the critical mass flow rate, m_{crit}. One of the most widely known and among the oldest models for thermal non-equilibrium in two-phase critical discharges was proposed by Henry (1970) who considered the flow as frozen and hence no phase change occurs, a concept that could be valid for small flow time-scales. Flows within short nozzles and orifices are a typical paradigm. If the liquid at the nozzle exit is sub-cooled then m_{crit} can be calculated by the Bernoulli equation. Assuming incompressible flow the Bernoulli equation between the upstream and downstream positions of the nozzle gives

$$m_{crit} = AC_f\sqrt{2\Delta p/\upsilon} \tag{2.12}$$

This equation is when the pressure difference between the high and low pressure are known and is used in chemical process industry for a fast and straightforward solution. It assumes a single-phase jet at the nozzle exit which is not always valid. Usually the RHS part of the above equation includes a discharge coefficient, C_f which depends on the flow. For non-choked lows, most researchers suggest C_f to be around 0.6 to account for the vena-contracta and changes with respect to Re. In general, Bernoulli equation tends to over-predict m_{crit} and hence it may lead to significant errors.

Homogeneous Equilibrium Model (HEM)

If the bubble distribution is such that there is no or very little relative velocity between the two phases (slip velocity), then the flow can be considered homogeneous and if the slip velocity cannot be ignored the flow is called separated. Homogeneous Equilibrium Model

(HEM) is the most common critical flow model which assumes zero slip velocity. It assumes that mass, momentum and energy transfer between the phases happens rapidly enough so that both mechanical and thermodynamic equilibrium is established. HEM is predicated on the ideal case of interphase equilibrium and the two-phase flow is treated in a one-fluid thinking (single equations for the two phases). In the case of an isentropic flow the critical mass flow rate can be calculated as

$$m_{crit} = AC_f\sqrt{2\Delta h}/\upsilon \tag{2.13}$$

The HEM model seems to work very well in non-isentropic liquid expansion cases and long pipes where the flow has sufficient time to reach equilibrium (Salvador et al., 2017). However, the predicted mass flow rates can be very large compared to experiments and in cases of short nozzles where there is not sufficient time for vapour generation to reach equilibrium, the difference between the prediction and the exact value can be 25 percent according to Schröder and Vuxuan (1987). Various three-dimensional CFD approaches employed the HEM model to calculate the critical mass flow rates (Janet et al., 2015; Liao and Lucas, 2015a; Liao et al., 2015b) proving that it can provide reasonable results for long nozzles.

Slip flow models

In cases of annular or dispersed flows, HEM cannot reproduce the strong kinetic and thermodynamic non-equilibrium effects and further adjustments are needed. An improvement was proposed by Fauske (1962) taking into account the velocity ratio $\mathscr{S}$, ($\mathscr{S}$ is the ratio of the vapour and liquid velocities). Fauske estimated that the maximum mass flow rate is achieved at $\mathscr{S} = (\upsilon_g/\upsilon_l)^{1/2}$ using momentum balance at the nozzle exit. In the same direction, Moody (1965), using an energy balance for determining the conditions at the nozzle exit, proposed that the maxima of mass flow rate occur at $\mathscr{S} = (\upsilon_g/\upsilon_l)^{1/3}$. Deviations with the actual experimental critical mass flow rates exist using these models, with the calculated values being usually higher than in HEM, and with non-physical values for $\mathscr{S}$. In the models of Fauske and Moody, mass flow rate estimation is treated in the same way for short and long nozzles e.g. by extracting from a formulation that includes only the thermo-physical properties of the fluid which are usually stagnation pressure and degree of superheat (or sub-cooling). Zaloudek (1964) and Xu et al. (1995) among others showed that the geometry could play an important role in the case of depressurisation inside pipes. In such cases, the above-mentioned models fail to predict the experimental mass flow rates resulting in under-predictions, which can be attributed to the underlying assumption of thermodynamic

equilibrium. The latter is a convenient approach that leads to a set of equations that under certain circumstances can be successful for some multiphase flow cases across nozzles. For example, in HEM one might obtain a one-fluid formulation suitable for small-scale cavitating flows. The latter is commonly used in some open source CFD codes (Karrholm, 2008).

Homogeneous Relaxation Model (HRM)

One major hypothesis of the HEM is the thermal equilibrium for the two-phase flow. Downar-Zapolski et al. (1996) proposed the Homogeneous Relaxation Model (HRM) which accounts for the non-equilibrium vapour generation. The Homogeneous relaxation model considers that the two-phase flow no longer evolves instantaneously at thermodynamic equilibrium, but only at mechanical equilibrium. The model estimates the rate of change of the local vapour quality. The mathematical expression of the HRM is

$$\frac{Dx}{Dt} = -\rho \left(\frac{x - x_{eq}}{\Theta} \right) \tag{2.14}$$

The concept of the relaxation term which has its origin back to Einstein (1920)'s work for sound propagation in dissociated gases and others, expresses a physical reality, i.e. the instant vapour mass fraction would relax to the equilibrium value over a proposed time-scale. The values of the time-scale are linked to the interphase mass transfer in a way that will be described in Chapter 5. The model might have a behaviour similar to the frozen flow model or the HEM depending on whether the relaxation time-scale is high or low. Although older modelling approaches were based on a one-dimensional thinking, when moving to multi-dimensional modelling, the HEM and HRM are in reality only homogeneous on the sub-grid scale level, which is less restrictive than 1-D.

2.6 HEM and HRM in CFD codes

There are two families of numerical methods to simulate dispersed flows with various advantages and disadvantages: the ones that consider one set of equations treating the mixture as a pseudo-fluid (one-fluid approach) and others that employ two sets of equations, one for each phase (two-fluid approach). Other approaches such as Eulerian-Lagrangian are also possible in simulating flashing flows using the thermal-equilibrium assumption (see (Coldrick, 2016). In the two-fluid approach, each phase has its velocity, and the continuity equation is solved for the liquid and vapour phase, whereas in the one-fluid approach the flow characteristics are averaged between the two phases offering a simpler

formulation. Maksic and Mewes (2002) used a four-equation model to simulate flashing in converging-diverging geometries employing a scalar transport equation for the bubble number density (number of bubbles per unit volume) assuming that vapour remained always in saturation conditions, over-predicting the void fraction. Other two-fluid models choose to drop the initial bubble formation, presuming a size and distribution of the bubbles which can be attributed as a major constraint Rusche (2002). However, bubble nucleation can be random across the flow direction, and there is insufficient evidence to support such a simplification, at least for the majority of flash boiling flows where the pronounced stochastic nature of flashing inception inside the channel indicates that this assumption might fail to model the underpinning physics properly. Liao and Lucas (2015a) have modelled flashing water flowing through vertical circular converging-diverging nozzles using a two-fluid model which incorporated thermal non-equilibrium effects in the calculations. The results for pressure and vapour mass fraction were in good agreement with the experiments although only initially sub-cooled water was simulated. Wang et al. (2014) simulated cavitating liquid jets using a compressible and equilibrium two-phase flow solver but did not provide mass flow rate results.

Regarding the one-fluid approaches, Bianchi et al. (2008) developed a one-dimensional model for flash evaporation. A one-dimensional mixture model formulation was employed to predict the influence of the superheat degree and geometry in flashing and atomisation. The authors considered the thermal non-equilibrium via the HRM. The relaxation time-scale was calculated by considering the temperature change in the vapour phase. The model showed that when increasing the superheat degree, bubble nucleation was enhanced with atomisation following possibly the same mechanism described by Senda et al. (1994). Lu et al. (2014) assumed equilibrium conditions for simulating two-phase flashing jets in both inside and outside nozzle. The results presented from Lu et al. (2014) regarded qualitative predictions for the liquid volume fraction but did not provide discussions for the influence of the equilibrium assumption on the results. The impact of the nozzle geometry, regarding the boiling process will be discussed in the results section (Chapters 5-6).

An attempt to make use of the efficiency of the HRM in two-dimension simulations was made by Lee et al. (2009). They used a fully Eulerian approach using the Pressure-Implicit-Split-Operator (PISO) algorithm. Given the fact that the pressure evaluation is associated to the rapid phase change, a relaxation term is included in the PISO algorithm. The model was validated for superheated water flowing within nozzles with relatively small length-to-diameter ratios, L/D and constant pressure cases. Results showed that by combining HRM with one-fluid compressible two-phase solvers, high fidelity simulations can be performed. Additional work has been conducted by Schmidt et al. (2010) who included one more term

to account for the compressibility effects. Simulations were performed for flashing water, initially saturated, for $L/D = 4$ and 10. These were the first multi-dimensional approaches to use HRM in CFD codes for simulating non-equilibrium flows inside pipes and nozzles. A few years later, Wen et al. (2013, 2016) used the same model to model carbon-dioxide releases using a constant relaxation time of 0.1 ms. Brusiani et al. (2013) have employed the HRM to study the effect of the rapid phase change in the internal flow characteristics providing results for the critical flow rate and choking which were in good agreement with experiments. Moulai et al. (2015) and Duke et. al (2015) have also employed the HRM for considering the non-equilibrium effects in the internal flow but do not provide comparisons with experiments for the critical flow rates. (Salvador et al., 2017) have used HEM to simulate the internal flow in convergent-divergent diesel nozzles using a one-fluid approach investigating the nozzle geometry on the discharge coefficient and flow properties.

2.7 Pressure update in flashing/cavitation

In this research, we are interested in both sub-sonic and sonic releases. There are regions with large density variations where the incompressible assumption is not valid. From a mathematical point of view, a cavitating flow within a throttle is a three-dimensional problem with initial conditions at the inlet and outlet that may vary significantly (in pressure, density, temperature e.t.c.). The incompressible assumption in not valid since the density has large variations across the domain. The typical approaches for solving the compressible equations have to make the assumption that the Mach number is constant in time and space. In cases of cavitation and flashing, the boundary conditions variate the Mach number Brennen (2013). In addition to the phase change, the channel geometry might also cause this variation. The result is that the pressure-density coupling weakens in this low Mach regime (no reference Mach number can be defined).

Moreover, expansion waves might propagate into the superheated region (low entropy region) and compression waves might travel towards the mixture region (high entropy region). These waves have been experimentally and numerically observed for small (up to 5 bar) and moderate pressure drops (15 bar) (Alekseev et al., 2016; Edwards and O'Brien, 1970; Simoes-Moreira and Shepherd, 1999). The formation of such compression waves is substantially connected to superheated liquid jets and induces some additional challenges regarding the downstream thermodynamic properties for the liquid-vapour mixture. Attempts to tackle this, are proposed in the past using appropriate correlations or suitable equations of state for the thermodynamic parameters (Saurel et al., 2008; Simoes-Moreira and Shepherd, 1999). The latter is the core of some previous numerical works in flows with cavitation. For

instance Karrholm (2008) used a barotropic equation of state in a compressible framework:

$$\frac{D\rho}{Dt} = \psi \frac{Dp}{Dt} \tag{2.15}$$

This equation is not an equilibrium equation of state hence the pressure obtained from this equation does not satisfy the equation of state of the liquid and vapour phases. The barotropic equation is integrated to form a pressure equation Schmidt (1997). The mixture's equation of state reads:

$$\rho = (1-\alpha)\rho_l^0 + (\alpha\psi_v + (1-\alpha)\psi_l)p^{sat} + \psi(p - p^{sat}) \tag{2.16}$$

The pressure is updated in the PISO loop as:

$$\frac{\partial \psi p}{\partial t} + (\rho_l + \psi_l - \psi_v)p_{sat}\frac{\partial \alpha}{\partial t} - p_{sat}\frac{\partial \psi}{\partial t} + \frac{\partial \rho u_j}{\partial x_j} = 0 \tag{2.17}$$

where α is the void fraction (see also Chapter 3) and ψ, ψ_l, ψ_v are the compressibility of the mixture, liquid and vapour respectively. This approach gives the mixture density via the saturation and a reference state 0 and is implemented within OpenFOAM. It preserves the assumption of thermal equilibrium of the phases (HEM) which means that cases of thermal non-equilibrium cannot be dealt properly with this methodology. Following the same logic, in Chapter 5 a pressure equation equivalent to an equation of state is developed that encapsulates thermal non-equilibrium and is thoroughly described.

2.8 Concluding remarks

The basics of cavitation and flash-boiling are discussed in this chapter. The process of flash-boiling is described in a mathematical way first, before moving to the numerical modelling of superheated jets. The process can be divided into three different stages, e.g. bubble nucleation, bubble growth and atomisation. These three stages are described since they are integral parts of flashing jets. The different possible regimes that are possible to exist in cases of sudden depressurisation. Annular, bubbly and dispersed flow regimes will be thoroughly investigated in this thesis and are briefly discussed.

In this chapter, some of the most important modelling approaches for cavitation and flashing are presented. These models emerged in an attempt to describe the underpinning physics of these processes allowing the calculation of the critical mass flow rate by usually making simplifications or using phenomenological approaches. The limitations of these models such as the thermal equilibrium or slip velocity are also discussed here. Most of

the old modelling approaches are derived in a one-dimensional thinking which makes the Homogeneous-Equilibrium-Model and the Homogeneous-Relaxation-Model the only three-dimensional models for CFD codes. The discussions focus on the HRM which is used here in the developed methodology for modelling the thermal non-equilibrium which is associated with the flashing process.

Chapter 3

Atomisation and sprays

This chapter describes the fundamentals of the physics underpinning liquid atomisation. The process of atomisation can be divided to the primary atomisation and the secondary break-up. Both of these mechanisms have their own aetiology in terms of physics. Different regime classifications are discussed as a first step to understand the mechanisms of liquid fragmentation. Detailed studies of the regimes for flashing studies started in the 1980s considering the initial thermodynamics conditions and the impact of the geometry on the jet dynamics. In flash-boiling atomisation both the thermodynamic and the mechanical effects act on the jet antagonising each other augmenting the complexity of flashing jets. Consequently, the physical aspects of some flashing regimes are not yet fully understood despite the existing experimental works. Some of the most important experiments are discussed in the last section.

3.1 Primary atomisation

Liquid atomisation is the process wherein a liquid bulk is converted to a collection of droplets leading to the formation of a spray and has numerous applications in engineering and science. Upon atomisation, the bulk liquid is fragmented to a spray system where the droplets disperse interacting with each other and the gaseous ambient environment. Thus, atomisation can be considered as the result of the inertia and the external forces acting on the jet surface. Atomisation modelling supplies the initial conditions for spray computations i.e. the droplet size, velocity, temperature e.t.c. Understanding the fragmentation process is a challenging task since there are still many uncertainties about the fundamental mechanisms of the liquid disintegration. Atomisation depends on the complex interactions between the aerodynamic and capillary forces. Turbulence and shear layers deform the liquid-gas interface while the surface tension can amplify instabilities (Navarro-Martinez (2014)). Savart in 1833

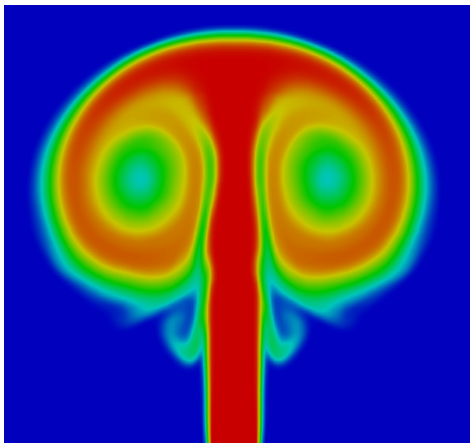

Fig. 3.1 Rayleigh-Taylor instability in a two-dimensional jet with the characteristic mushroom shape using OpenFOAM.

was the first who realised that the break-up of a jet is directly related by the jet dynamics considering a non-linear analysis of the jet break-up. In his work Savart (1833) estimated a characteristic wavelength which is associated to the frequency of the vibrations on the jet surface. This wavelength λ_{crit} is $\propto \frac{1}{d}$ and $\propto \sqrt{\Delta p}$ and was calculated by Plateau (1850) to be $\lambda_{crit} = 2\pi d$. The perturbations in the liquid surface that have a wavelength less than the critical value are not stable. Rayleigh (1892) calculated the most unstable wavelength to be $\lambda = 9.01d$. More discussion about Rayleigh's work is provided later when more details about the modelling concepts will be discussed. Instabilities that occur at the liquid-gas interface are mainly caused from the velocity difference between the two phases (Kelvin-Helmholtz instabilites, Lee and Park (2002); Reitz (1987)) or from their density difference (the so-called Rayleigh-Taylor instabilities). In cases of supersonic flows, Richmayer-Meshkov instabilities are also possible to be observed (Khodadadi et al. (2017)) but is usually less reported in the literature for flashing jets. The Rayleigh-Taylor instability (Figure 3.1) is distinct from the Rayleigh-Plateau type of instabilities which occur in cylindrical jets which break-up into small droplets having the same volume with each other but lower surface density. Break-up regimes are usually classified in terms of non-dimensional analysis based on characteristic numbers. The most important of these dimensionless numbers are: Reynolds number (Re), Weber number (We) and Ohnesorge number (Oh). Reynolds number is the ratio of the inertia to viscous forces, Weber number is the ratio of the aerodynamic forces to the inertia (surface tension forces) and the Ohnesorge number is the ratio of the viscous to the surface tension forces. Reynolds, Weber number for each phase k and Ohnesorge are defined as

$$Re = \frac{\rho_l u_{slip} d}{\mu_l} \tag{3.1}$$

$$We_k = \frac{\rho_k u_{slip}^2 d}{\sigma} \tag{3.2}$$

$$Oh = \frac{\sqrt{We}}{Re} = \frac{\mu}{\sqrt{\rho_l \sigma d}} \tag{3.3}$$

where the magnitude of the slip velocity u_{slip} is used for Weber number and is equal to the difference of the liquid and gas velocities. Here, the dispersed Reynolds number is defined using a characteristic length scale d (usually the droplet diameter).

Following Lin and Reitz (1998) the following break-up cases can be identified (Figure 3.2)

- **Rayleigh break-up**

  Initially no jet exists, and the flow drips off. At low jet velocities the axi-symmetric perturbations caused by the inertia and surface forces impact on break-up. At this stage, the droplet sizes are greater than the nozzle diameter the jet is injected from.

- **First wind-induced break-up**

  The gas Weber number describes the influence of the gas surrounding the jet. Increasing Weber number (for example increasing the relative jet velocity) the aerodynamic forces on the surface of the liquid gain on influence. The enhanced wave growth rate contributes to the break-up process. The resulting droplets have the same scale (diameter) with the jet diameter.

- **Second wind-induced break-up**

  With further increase of *We* the process of the first wind-induced break-up still occurs but in a larger extent. The gas inertia effect in this case is more intense. The flow inside the nozzle is now turbulent and the unstable growth of short wavelength surface waves causes the jet to break-up. In this case, the produced droplets have diameter which is smaller than the diameter of the jet Reitz and Bracco (1986)).

- **Atomisation** The small droplets separating from the jet surface manifest the jet disintegration. This process stops when the jet completely fragments into droplets. The intact surface length is the associated spatial scale describing the initiation of the surface disintegration. When this length becomes small enough, the regime is in the atomisation mode. The dense part of the spray consists of a liquid-core surrounded by a developing multiphase mixing layer. In this case the resulting droplets are much smaller than the jet diameter. This regime is much more complicated and difficult to understand than the others. The atomisation regime depends not only on the ambient

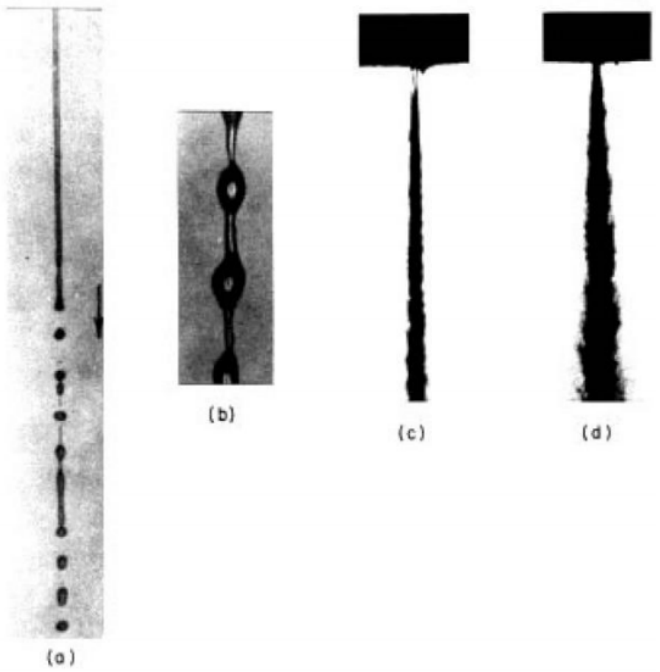

Fig. 3.2 Regime classification according to Lin and Reitz (1998).(a) Rayleigh break-up, (b)First wind-induced break-up, (c) Second wind-induced break-up and (d) Atomisation.

environment but also on the flow characteristics inside the nozzle, the turbulence and the nozzle design. For flashing jets, the thermodynamic state has also significant impact on atomisation. Experimental investigations are still limited and usually apply intrusive methods and cannot offer detailed information for the whole jet. That is to say, experiments cannot argue in which extent the combination of the aerodynamic forces acting on the jet with the effects stemming from the internal nozzle flow due to turbulence and cavitation, affect the liquid atomisation. Particularly in the first stages of atomisation experimentally measured data are scarce. The scope of this thesis is to give some insights regarding the metastable nature of superheated jets and investigate their primary atomisation.

3.2 Secondary break-up

The process described in the previous section concerned the first stage of the atomisation when large droplets and ligaments form during the primary atomisation process. These large ligaments are usually not stable and hence they are subject to further break-up. This

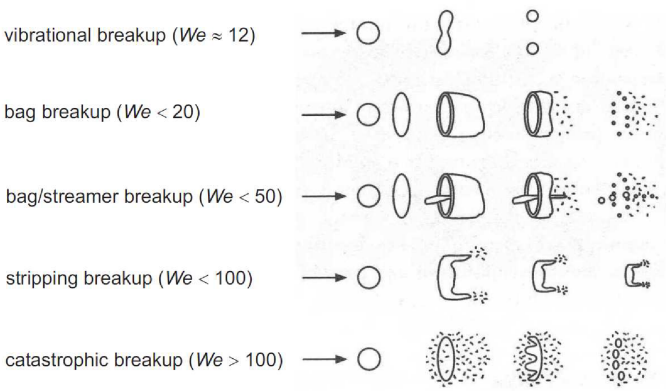

Fig. 3.3 Break-up regimes correlated to Weber number according to Pilch and Erdman (1987); Weirzba (1993).

subsequent break-up of these large liquid structures is generally referred to as secondary break-up. The secondary break-up occurs mainly due to relative velocity, turbulence or in cases of supersonic flows shock interactions. Therefore, the relative velocity of the droplets with the ambient gas plays an key role in the break-up mechanism. The transition from the dense to dilute region of the spray signals a reduce in liquid volume fraction with subsequent round drops formation. There are various kinds of secondary break-up depending on the Weber number based on the aerodynamically induced wave growth on the liquid surface. Either for liquid-gas flows Pilch (1981) or for liquid-liquid interactions (O'Brien (1961)) the break-up regimes tend to follow similar trends with respect to We. In Figure 3.3 a classification regarding the different break-up regimes is shown which are:

1. Vibrational break-up, $We \leq 12$
2. Bag break-up, $12 < We \leq 50$
3. Bag-and-stamen break-up, $50 < We \leq 100$
4. Sheet stripping, $100 < We \leq 350$
5. Wave crest stripping (catastrophic break-up), $350 < We$

These regimes consider a liquid droplet that is suddenly exposed to a high-velocity flow field with less density (either liquid or gas). The droplet deforms due to the relative high velocities and responds in a different way for each case. For very low relative velocities the droplet remains stable. Vibrational break-up happens when the droplet oscillations intensify since surface tension acts as a counter force against the developed surface oscillations. When the break-up occurs, only few fragments (droplets) are produced. During the bag break-up

the droplet deforms taking a bag-like shape which gives a small number (more than before) of new droplets when it breaks-up. In the bag-and-stamen break-up regimes, the droplet again is deformed taking a toroid rim shape alongside with a stamen at the centre of the bag. In the sheet stripping regime, the droplet takes the shape of a thin sheet which fragments at both sides giving new droplets until it becomes small enough. In the wave crest striping mode, the small-wavelength waves on the droplet surface, alter the surface progressively. At higher Weber numbers, the long-wavelength waves penetrate the liquid surface and fragment the droplet to smaller ones (catastrophic break-up).

The critical Weber number We_{crit} is defined as the Weber number below which no break-up occurs. The critical Weber number depends on the viscosity effects as reported in previous studies by Faeth (2002); Hsiang and Faeth (1995). The effect of viscosity on the droplet is described from the Ohnesorge number. The following result stands for the We_{crit}

$$We_{crit} = \begin{cases} \text{constant} & \text{if} \quad Oh < 0.1 \\ \sim Oh^2 & \text{for} \quad Oh > 0.1 \end{cases} \tag{3.4}$$

For constant ambient (gaseous) properties the $Oh - Re$ relationship can be contextualised in a way that one pair (Oh, Re) to correspond to one the four jet break-up regimes described earlier (Rayleigh, first wind induced, second wind induced, atomisation). Reitz (1978) expanded this regime classification considering the gaseous properties. For lower Re and for the same conditions, increasing Oh aerodynamic forces might play the dominant role in disintegration or the jet might disintegrate at the nozzle exit thus the regime progressively changes from Rayleigh type towards the wind-induced and atomisation regime. The transition limit from the Rayleigh regime to the aerodynamic mode is identified for $We_l = 1.7410^4/Re^{0.5}$ and the transition limit between aerodynamic disintegration and the atomization regime is observed for $We_l = 9.410^5/Re^{0.5}$ (Crowe (2005); Reitz (1978)). For higher Reynolds numbers, ($Re \geq 10^5$) a clear atomisation regime is expected that does not depend on Oh.

3.3 Atomisation of flashing jets

Regimes in flashing jets

In cases of flashing jets, the flow is much more complex due to the heat and mass exchange between the liquid and the gas phases. Except for the aerodynamic and capillary forces which are present and effect the jet, the thermodynamic instabilities also play a major role in atomisation. Significantly, turbulent effects which occur across the jet, influence the flow

patterns. The impact of the channel geometry the jet emerges from is usually ignored in the literature employing assumptions for the internal flow (single flow, uniform velocity at the nozzle exit e.t.c). This lack of information for the internal flow is integral for accurate predictions of the spray properties as will be illustrated in Chapter 6 in the numerical results.

In cavitating and flashing jets the flow may change rapidly where the geometry changes, for instance in sharp inlet/outlet corners. This gives rise to cavities that form and disperse through the liquid medium. These vapour pockets might collapse or interact with each other before they reach the channel exit. As pointed out by Sher et al. (2008), Henry (1970) and Ramamurthi and Nandakumar (1999) the flow can be either separated or re-attached due to geometry changes in the nozzle. A classification of cavitating flows regimes is shown in Figure 3.4. The flow cases of non-re-attached cavitation (patterns (d) and (e)) is observed in the test cases studied here for a wide range of pressure differences and will be thoroughly investigated in Chapters 5 and 6. A key point to remember is that flashing regimes cannot be classified in a straightforward way including the impact of the flow properties, thermodynamics and geometry, e.g. there are no diagrams or formulations correlating $Re, Oh, \Delta T_{sh}$ and L/D. For instance, for nozzle length-to-diameter (L/D) less than five, the flow is more likely to be separated. Ramamurthi and Nandakumar (1999) showed that increasing Re for $L/D = 5$ causes the flow to separate. For short nozzles with small L/D it still remains uncertain if turbulence effects are important. For long nozzles turbulence has time to fully develop and dominates the flow according to Iciek (1980). The flow in these long nozzles is more likely to reattach to the nozzle walls (Sher et al. (2008)). Regarding short nozzles, Henry (1970) showed that for $3 \leq L/D \leq 12$ the flow starts to become bubbly and for the case where $L/D = 12$ bubble nucleation in enhanced. Oza (1984) proposed classifying flashing jets depending of the flashing location, e.g. whether they flash inside (internal flashing) or outside the nozzle (external flashing). The jet mode significantly depends on the storage conditions. The intact surface length corresponds to the time delay in bubble nucleation and bubble growth which result to the liquid fragmentation. In their work Lamanna et al. (2014) proposed a classification of flashing jets with respect to the dimensionless pressure $R_p = p_{sat}/p_\infty$ where p_{sat}, p_∞ are the pressure in saturation and ambient conditions (Figure 3.5). The pressure difference is a crucial parameter since the flashing inception starts when pressure drops below p_{sat}. For lower pressures the jet will have larger intact length and external flashing is more likely (b-d regimes). Increasing the pressure, flashing is more likely to occur earlier and inside the nozzle. The bubbles formed, collide to each and the resulting atomisation starts earlier giving sprays with droplet sizes generally smaller than before (e-g regimes).

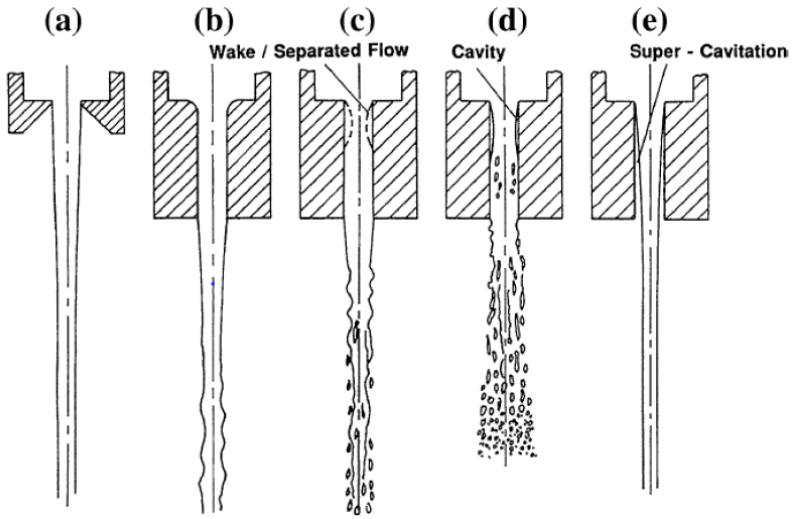

Fig. 3.4 Regimes in cavitating jets according to Hiroyasu (1991)

.

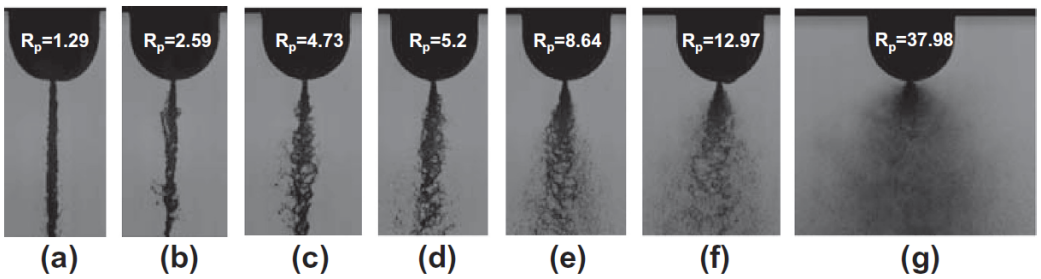

Fig. 3.5 Regimes in flashing jets according to Lamanna et al. (2014).

As mentioned before, there are two break-up mechanisms that are responsible for the liquid disintegration: mechanical due to aerodynamic forces and thermodynamic due to flashing. The mechanical break-up mechanism dominates the atomisation of sub-cooled jets. Increasing the superheat degree, the flow has more chances to become more bubbly and the relationship of the two mechanisms starts to be more competitive. In higher superheat degrees flashing prevails the atomisation process which predicates flash atomisation (or flashing break-up mode). Kitamura et al. (1986) studied the transition from mechanical to flashing break-up for long nozzles ($50 < L/D < 110$) for flashing water and ethanol jets. According to the authors the transition occurs at a critical superheat where bubble growth overrules flashing. The Jacob number (Ja) is usually employed to elucidate the transition between break-up mechanisms and represents the non-dimensioned superheat degree.

$$Ja = \frac{c_{pl}\Delta T_{sh}}{h_{fg}} \frac{\rho_l}{\rho_g} \tag{3.5}$$

where c_{pl} is the specific heat of liquid and h_{fg} is the enthalpy of vaporisation. Cleary (2008) extended the idea of the transition location in the work of Kitamura et al. (1986) using a transition region between which the mechanical and flashing break-up are separated from. Two thresholds are proposed by the author for the transition zone. The first one is the mechanical break-up threshold which corresponds to the upper limit for the atomisation due to mechanical effects (regime b in Figure 3.5). The second threshold is the flashing limit which corresponds to the end of the transition region. These limits depend on the fluid flow and are calculated experimentally. Cleary (2008) proposed the modified limits based on measurements for flashing water jets for a various range of nozzle diameters, $0.85 < L/D < 3.4$ and temperatures up to 180^oC for the flashing cases and $1.7 < L/D < 50$ and pressures up to 24 bar for the sub-cooled cases. The following limits were proposed:

$$Ja\Phi = 55We_v^{-1/7} \qquad \text{Mechanical break-up limit} \tag{3.6}$$

$$Ja\Phi = 150We_v^{-1/7} \qquad \text{Flashing break-up limit} \tag{3.7}$$

where We_v is the gaseous Weber number (vapour phase). The correction factor Φ was an emperical factor for the bubble growth rate based on Kitamura et al. (1986). This factor is a function of the densities ratio and corresponds to the bubble growth rate due to nucleation.

$$\Phi = 1 - e^{-2300\frac{\rho_v}{\rho_l}} \tag{3.8}$$

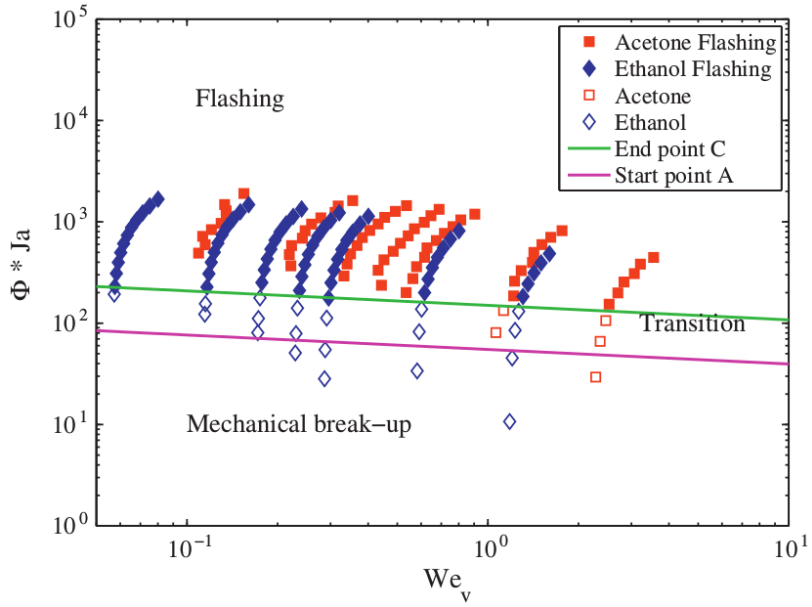

Fig. 3.6 Transition criteria for flashing according to Lamanna et al. (2014).

This formulation is derived for various liquids included water, methanol and pentane. An example of this theory and how it can be employed to elucidate the break-up mechanisms is shown in Figure 3.6. The lower $Ja\Phi$-limit represents the maximum limit for mechanical breakup. The higher $Ja\Phi$-limit denotes the fully flashing regime were bubble impact on the spray is evident. The back-pressure along the liquid curves remained constant. Moving from lower to higher superheat the Ja increases leading to a transitional regime. Further increase in Ja or in superheat degree results to a fully flashing break-up. The proper contextualisation relies on experiments since the process depends on the liquid properties and the limits for the transitional region are subject to change as shown in Figure 3.6.

The work of Cleary (2008) and Lamanna et al. (2014) is a good starting point for correlative comparisons of the superheat jets atomisation. In general, they propose that in high degrees of superheat the external flashing is more likely to occur whereas for small superheat degrees, where at some point the mechanical effects will dominate the atomisation, the internal flashing is more likely. The internal flashing mode is the most catastrophic and is fundamentally associated to the regime change within the nozzle. Extensions of the regime transition in other fluids such as cryogens or investigations in the limit of the thermodynamic critical point are pending, therefore, more study for extending the transition conditions is needed.

As mentioned before, one of the novelties of this research is that the internal flow is considered and modelled. The flow patterns prior to the atomisation are studied since they

are inherently connected to the atomisation process. Notably, the developed methodology in this study does not require a prior regime characterisation or assumptions for the internal flow or the spray dynamics.

Additional challenges in the physics of flashing and cavitation

Due to the sudden pressure drop, it is very likely that waves travel along the fluid. Following similar thinking with Simoes-Moreira and Shepherd (1999) depending on the pressure drop, the flow is divided into two regions, separated by the transition front e.g. the superheated liquid region and the liquid-vapour mixture region (Figure 3.7). Under certain conditions, expansion waves might propagate into the superheated region (low entropy region) and compression waves might travel towards the mixture region (high entropy region). The evaporation waves are adiabatic rapid phase change processes which occur in metastable and superheated liquids. These moving fronts transform the superheated liquid to a two-phase mixture with high velocity and act in a similar way as the deflagration fronts in deflagration-to-detonation (Simoes-Moreira and Shepherd, 1999; Simoes-Moreira, 2000; Simoes-Moreira and Bullard, 2003). The occurrence of these waves happens in specific degrees of superheat and pressure difference. A key thing to remember is that one characteristic of this phenomenon is large pressure jump across the front. The pressure drop is the driving force of the flashing process. Simoes-Moreira and Shepherd (1999) take this pressure drop across the evaporation front to be equal to

$$\frac{p_2}{p_1} \approx \frac{1}{1+\gamma_p} \tag{3.9}$$

where p_1, p_2 are the upstream and downstream pressure in the channel the liquid flows in, and γ_p is the ratio of the specific heats. The proper calculation of pressure inside and outside the channel plays a significant role in the properties of the jet. The algorithm developed for updating pressure for flash-boiling is discussed in details in Chapter 5.

Some important spray characteristics

Thermodynamic and mechanical effects act inside the jet and on the jet surface altering the jet shape and dynamics. The pressure drops rapidly leading to a phase transition in cases of cavitation and flashing. The rest of the thermodynamic quantities, for instance enthalpy and vapour quality, also change across the jet. During flashing bubbles form and grow from

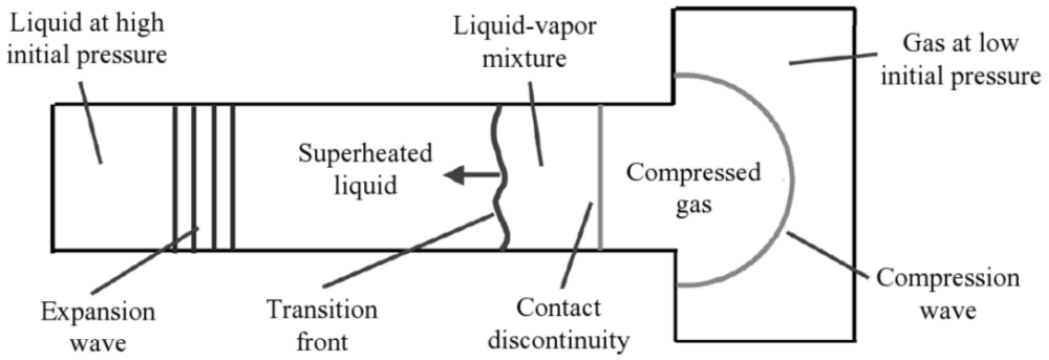

Fig. 3.7 Regimes in flashing jets according to Simoes-Moreira and Shepherd (1999).

the vapour clusters. The changes that happen in a microscopic level vary locally in time and space and is hard to define a characteristic spatial scale for the liquid structures.

From an experimental point of view the liquid break-up gives droplets with a wide range of sizes. The aerodynamic forces cannot exceed the surface tension forces which increase as the droplet size decreases. The new droplets have sizes that vary between the parental droplet size (d_{max}) and a minimum size. Since the exact droplet size spectrum cannot be precisely determined, the next reasonable step is to assume that droplet sizes d follow a distribution $f(d)$ which satisfies some minimum requirements imposed by the underlying physics which are

$$\lim_{d\to 0}\int_0^{d_{max}} f(d)\mathrm{d}d = \lim_{d\to\infty}\int_0^{d_{max}} f(d)\mathrm{d}d = 0 \tag{3.10}$$

$$\int_0^{d_{max}} f(d)\mathrm{d}d = 1 \tag{3.11}$$

The different sizes are expressed from the following formula for the generalised mean diameter (Mugele and Evans (1951))

$$D_{mn} = \left(\frac{\int_0^{d_{max}} d^m f(x)\mathrm{d}x}{\int_0^{d_{max}} d^n f(x)\mathrm{d}x}\right)^{\frac{1}{m-n}} \tag{3.12}$$

where m,n are integers. Some of the mean diameters that are commonly used are the arithmetic mean diameter D_{10} and the Sauter Mean Diameter (SMD or D_{32}). SMD is the most common diameter that is used to characterise sprays and atomisation systems. It is a fictitious diameter which can be considered as the ratio of the particle volume to its surface area.

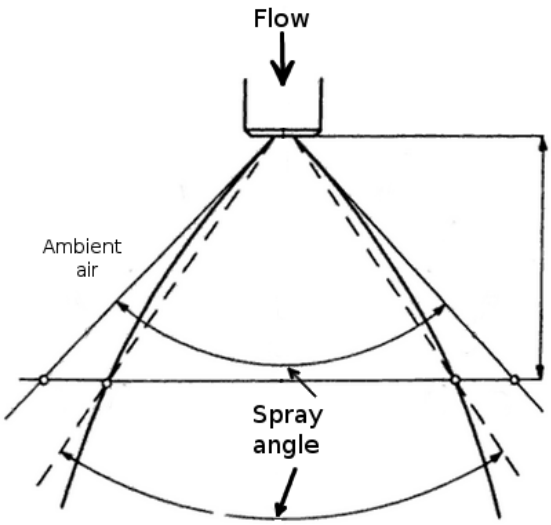

Fig. 3.8 Spray angle definition according to Bayvel and Orzechowski (1993). Both definitions can be used for the spray angle.

Another quantity to characterise the spray shape is the spray angle. The spray angle can be calculated using the liquid characteristics such as density and velocity. Generally, this is the (smallest) angle that is formed from two lines that include the spray core and start from the discharge point and end at the point the at which the influence of the ambient gas becomes important (Figure 3.8).

Past experimental studies in flashing jets

By contrast to the computational studies which are scarce, various experimental works have been conducted the last three decades for unravelling the mysteries of the liquid atomisation of flashing jets. Typically, experiments are carried out for non-hazardous liquids such as water measuring the spray characteristics e.g. velocity, D_{32}, spray angle e.t.c. Reitz (1990) studied flash boiling atomisation of water under relatively small pressure (p_{inj}) and different initial temperatures (T_{inj}). The jet was well atomised giving small sized droplets that dispersed downstream the nozzle exit. The majority of the droplet sizes was measured to be around $100\mu m$ (Figure 3.9). The flow was bubbly with a two-phase jet observed outside the nozzle with minimum and maximum droplet diameters varying around two orders of magnitude. A key thing to remember is that droplet diameter decreased along the radial direction by contrast to the trend at the axial direction.

Similar scales for the drop diameter were reported by Allen (1998) for flashing propane jets. The diameters measured, were within the range of some microns up to $500\mu m$ for a storage pressure of 6 bar. Some insights for the velocity profiles across the jet were obtained. The velocity had a characteristic bell shape with a maximum at the jet centreline (Figure 3.10). The velocity decreased moving further away the nozzle exit while preserving the same shape. The change in the regime of the jet was observed. The change in the measured drop sizes was attributed to the bubbles that burst each other giving new drops with smaller diameter.

Park and Lee (1994) using flashing water provided some interesting details regarding the anatomy of flashing jets. The droplet sizes were measured at various locations at the radial direction (Figure 3.11). The higher size at the jet centreline indicated an intact liquid core which progressively disintegrated across the radial and axial directions.

Similar velocity profiles at different locations are also reported in the literature in the work of Yildiz (2005) for flashing R134A jets with high degrees of superheat. Although the velocities at the radial direction of flashing jets tend to follow the same trend as non-flashing jets (for instance as illustrated in Abramovich (1963)), the axial behaviour of velocity is expected to change regarding if flashing happens inside or outside the nozzle.

Hervieu and Veneau (1996) provided some results for the jet shape of flashing jets for propane releases but did not include details for the spray angles. Park and Lee (1994) illustrated the spray angle and how it changes with respect to the initial flow conditions. They showed that the spray angle increased while increasing the initial temperature with values smaller to 90^oC. Recently, Wang et al. (2017) studied the effect of the internal flow patterns in the spray dynamics. In their study for flashing R134A jets the flow was bubbly for relatively small storage pressure ($p \leq 15bar$) with nucleation occurring at random locations and the spray angle increasing for higher pressure.

Ju et al. (2015) also investigated the internal flow patterns and the impact on the spray characteristics for flashing R134A jets observing a sudden gas-liquid transition for low orifice ratios and a pressure of 6.0MPa. Gunther and Wirth (1986) investigated the atomisation of superheated jets and also found that the internal flow patterns influence the quality of the two-phase jet that emerges to the lower pressure region. They also observed that the droplet velocity is generally lower for lower temperatures. Zhang et al. (2015) investigated the impact of the superheat degree on the bubble nucleation concluding that it plays a dominating role in the regime change of the jet.

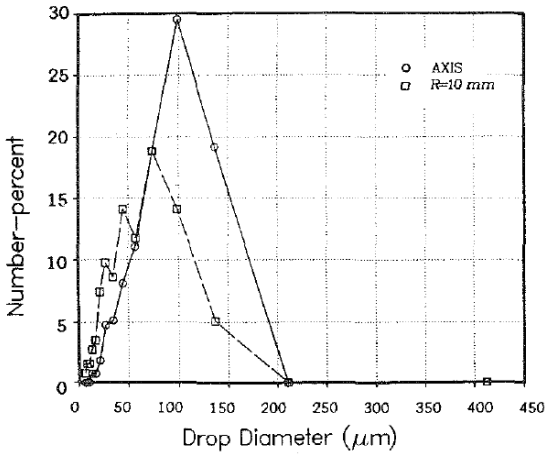

Fig. 3.9 Drop size distribution (number-percent) for flashing water measured by Reitz (1990) 60 mm form the nozzle exit at the jet axis and 10 mm from the jet axis, $p_{inj} = 7.87bar$, $T_{inj} = 419K$ and $L/D = 72$.

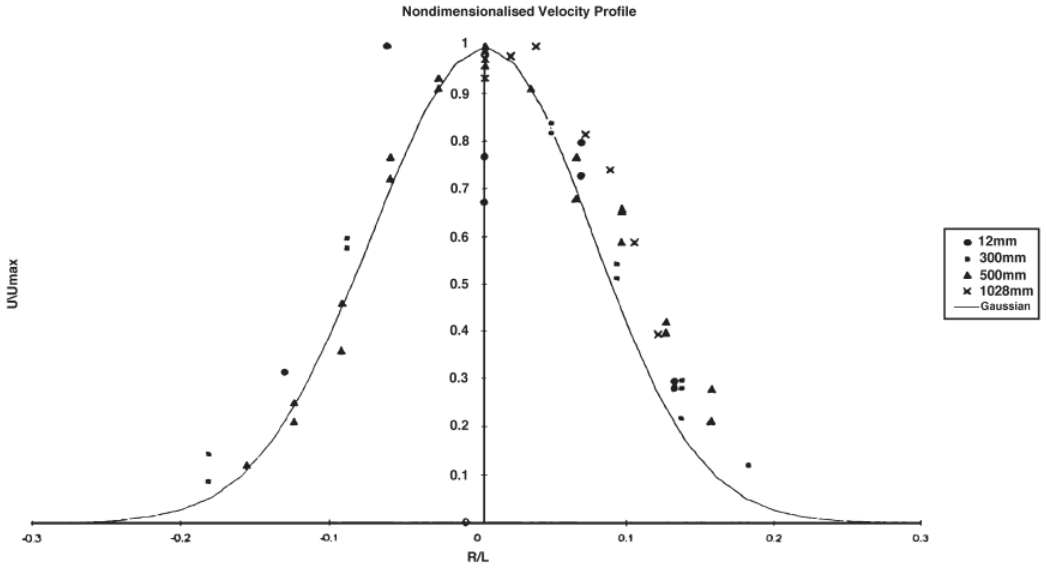

Fig. 3.10 Normalised velocities measured by Allen (1998) at different locations downstream the nozzle exit, $p_{inj} = 6bar$, $T_{inj} = 16.1°C$ and $L/D = 4.03$.

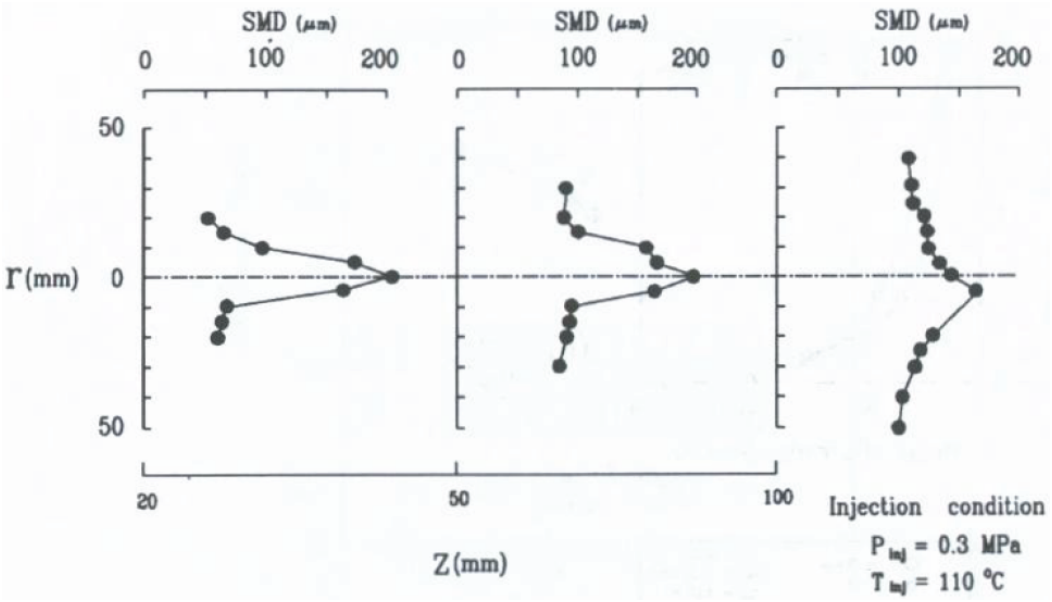

Fig. 3.11 Spatial distribution of D_{32} measured by Park and Lee (1994) at various locations downstream the nozzle exit, $p_{inj} = 3bar$, $T_{inj} = 110°C$ and $L/D = 72$.

Modelling atomisation and sprays

The fundamentals of spray modelling are discussed here. Starting from the basic definitions, the parameters that are used to describe the physics of atomisation in a Lagrangian point of view are illustrated. Lagrangian descriptions have managed to overcome the multi-scale problem of atomisation employing concepts predicated to experimental observations. The key idea in this approach is to divide atomisation into various sub-processes and use specific models for describing their physics. Primary and secondary break-up, droplets collisions and coalescence and evaporation are studied here for liquid parcels exiting nozzles, emphasising on the first two. Their contribution to the gaseous set of equations is discussed here and a paradigm of the Eulerian-Lagrangian is illustrated, as implemented in standard OpenFOAM. Finally, preliminary results for a realistic flashing propane jet are shown in the last Section.

3.4 Modelling approaches for sprays

The biggest challenge of modelling multiphase sprays is the large range of spatial scales in the process. Due to atomisation the liquid core fragments to ligaments and blobs which break-up and form liquid droplets (Figure 3.12). There are mainly two different ways for representing liquid jets in two-phase spray flows in CFD. These two approaches are: the

Eulerian method, where the spray is considered as a continuum across the whole flow domain, and the Lagrangian method, where the motion of clusters of droplets are tracked through the domain. In the Lagrangian particle tracking approach, the gas phase is represented using the Eulerian grid but the liquid phase is represented by a number of discrete computational particles. Individual particles are tracked through the flow domain from their injection point until they escape the domain or until they become small enough to be negligible (for instance due to evaporation). Each fluid particle typically represents a large number of droplets with a given size distribution and transport properties. The spray, in this case, consists of a cloud of a large number of particles providing a reasonable representation of the liquid morphology. One of the advantages of the Lagrangian approach is that, depending on the application, an accurate representation of the droplet distribution can be obtained at a lower cost compared with the Eulerian approaches such as the volume of fluid and level set methods. The latter offer a detailed representation for the dense parts of the spray but tracking the interface might require high grid resolution ($\Delta x \sim O(10^{-6})$) to capture the droplet-droplet interactions and small time-steps are usually required for a stable solution ($\Delta t \sim O(10^{-7})$), increasing the computational cost.

For droplets transported by the gas flow, spatial particle scale could be significant for determining the turbulence generation and dissipation. The effects caused by the mass exchange at the surface of the droplet and consequently the movement (or distortion as described later on) of the droplet surface can have a considerable impact on the main properties of the carrier phase. This is the challenge of all Lagrangian methods. For example Irannejad and Jaberi (2014) modelled the physical properties of the spray by calculating the SGS kinetic energy fluctuations caused by the evaporating mass. Same idea was used by Navarro-Martinez (2014) using a stochastic method to calculate the sub-grid fluctuations of the surface and liquid volume. Modelling approaches typically used in modern CFD software, contextualise usually in purely Eulerian (or Eulerian-Eulerian) and in the hybrid Eulerian-Lagrangian. Purely Lagrangian methods or Lattice-Boltzmann-Methods are beyond the scope of this study. In both approaches, the carrier gas is considered to be a continuum phase and is solved in the Eulerian frame. In the Eulerian-Eulerian approach, equations are derived for drops using a variety of methods such as interface capturing. In the Eulerian-Lagrangian the drops are treated in the Lagrangian frame and the properties between two phases are coupled with proper source terms in the governing equations. In this Chapter, a detailed discussion of the Eulerian-Lagrangian approach is discussed together with the additional sub-models typically derived for simulating sprays.

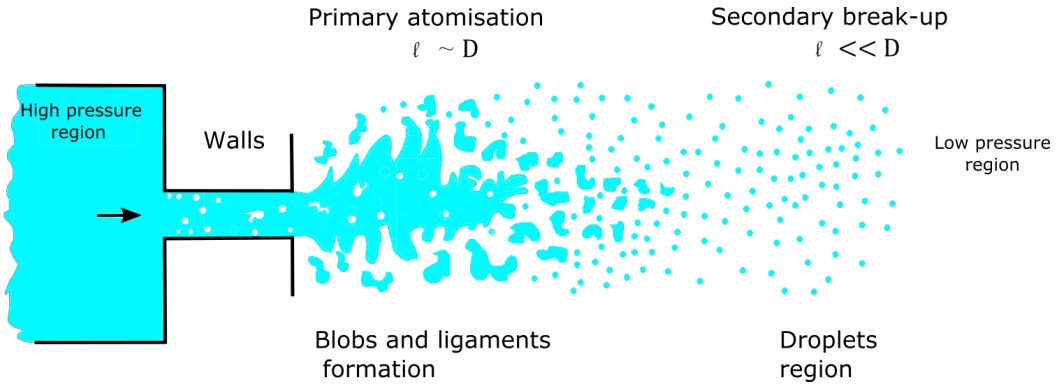

Fig. 3.12 An overview of the spatial scales in the liquid atomisation process.

3.5 Dispersed phase description

Assuming that the density ratio between the liquid and the gas is large enough, only the drag force affects the momentum of the droplet. Considering a droplet at the position $\mathbf{x}$ having velocity $\mathbf{v}(\mathbf{x})$ it is possible to write

$$\frac{\mathrm{d}\mathbf{x}}{\mathrm{d}t} = \mathbf{v} \tag{3.13}$$

By definition the force equation for the droplet is

$$\frac{\mathrm{d}\mathbf{v}}{\mathrm{d}t} = \frac{\mathbf{F}}{m_p} \tag{3.14}$$

where $\mathbf{F}$ contains the effect of various forces acting on the droplet with mass m_p. This is a simplified version of Basset-Boussinesq-Oseen equation Crowe (2005). The forces acting on the droplet motion are primarily due to drag, gravity, lift and added mass (Crowe, 2005; Jiang et al., 2010; Prosperetti and Tryggvason, 2009). Moreover, Prosperetti and Tryggvason (2009) includes the history forces and any other additional force particular to each process individually. The forces considered here are due to drag and all the rest are omitted due to the high density ratio (ρ_l/ρ_g 10) between the phases and other forces such as Magnus effects are also dropped since droplet rotation is not considered important which is in accordance with Crowe (2005). That is, if the material density of the dispersed phase is much greater than the density of the fluid phase (as in the atomisation region) the body forces are neglected and the Stokes drag force is assumed to become the dominate force on the particles. The drag force, $\mathbf{F_D}$ is calculated using the drag force coefficient

$$C_D = \frac{\mathbf{F_D}}{\frac{\rho}{2}|\mathbf{u}-\mathbf{v}|(\mathbf{u}-\mathbf{v})A_p} \tag{3.15}$$

where $A_p = \pi d^2/4$ is the frontal area the droplet and $\mathbf{u}, \rho$ denote the velocity and density of the gaseous phase. The drag coefficient is calculated with respect to the particle Reynolds number Re_p, $Re_p = d|\mathbf{u}-\mathbf{v}|/\nu$ and is evaluated as

$$C_D = \begin{cases} \frac{24}{Re_p} & \text{if} \quad Re_p < 0.5 \\ \frac{24}{Re_p}(1+0.15Re_p^{0.687}) & \text{if} \quad 0.5 < Re_p < 1000 \\ 0.44 & \text{if} \quad 1000 < Re_p < Re_{crit} \end{cases} \tag{3.16}$$

The first regime corresponds to the Stokes flow. The second one is due to Schiller and Nauman (1933) and is valid for describing the drag on spherical drops. For higher Reynolds numbers up to the critical value $Re_{crit} = 3.5 \cdot 10^5$ the drag coefficient is constant (Newton's regime).

The equation of motion for the particles is usually written in a more convenient way using the particle response time, τ_p which is the time-scale over which the droplet velocity becomes zero because of drag. Following Crowe (2005), $\rho_p \mathbf{v}/\tau_p \sim \mathbf{F_D}$ and the response time is

$$\tau_p = \frac{4}{3}\frac{\rho_p}{\rho}\frac{d}{C_D}\frac{1}{|\mathbf{u}-\mathbf{v}|} \tag{3.17}$$

Following Schiller and Nauman (1933) and Prosperetti and Tryggvason (2009) the expression for C_D is written

$$\tau_p = \frac{\rho_p}{\rho}\frac{d^2}{18\nu}\frac{1}{Re_p}(1+0.15Re^{0.687}) \tag{3.18}$$

The equation of droplet motion following Prosperetti and Tryggvason (2009) is now

$$\frac{\mathrm{d}\mathbf{v}}{\mathrm{d}t} = \frac{\mathbf{u}-\mathbf{v}}{\tau_p} \tag{3.19}$$

Here $\mathbf{u}$ is the fluid velocity. In the limiting case of negligible Re_p the particle response time reduces to Stokes response time and the velocity (momentum) response time, τ_v can be used in the droplet motion equation.

The Stokes number is very important for dispersed flows and is formally defined (Crowe, 2005) as the ratio of the momentum response time τ_v, $\tau_v = \rho_p d^2/18\mu$ and the time-scale τ_f which is the characteristic time of the flow field, $Stk = \tau_v/\tau_f$. If $Stk << 1$, the response time of the particles is much less than the characteristic time associated with the flow field. In this case the particles will have sufficient time to respond to velocity changes in flow and the particle velocity will be nearly equal to the gaseous one. On the other hand, if $Stk >> 1$, the particle will have no adequate time to respond to the fluid velocity changes, and the

particle velocity will be little affected. In the limiting case of $Stk \rightarrow \infty$ the particle velocity approaches to zero.

For droplets dispersing through turbulent flows, the choice of the appropriate fluid time-scale τ_f to use in the Stokes number ratio introduces some extra complexities. The time-scales vary from the integral τ_l to the Kolmogorov τ_k scale and since the ratio of the two time-scales, τ_k / τ_l, is analogous with $Re_t^{1/2}$, where Re_t is the turbulence Reynolds number, a wide variation of Stk is possible. The literature lacks on data for the Stokes number of droplets in flashing sprays. HSE (2002) suggest that for small droplets of $20\mu m$ it is $Stk \sim 1$ which is more of an intuitive approximation rather than a detailed work based on experiments.

3.6 Gas phase evolution

The three-dimensional Eulerian gas flow and Lagrangian particle trajectory equations are solved on a fixed grid. The equations for continuity, momentum, energy and species mass fraction in case of evaporating sprays in Eulerian-Lagrangian framework are written according to Miller and Bellan (1999). Source terms accounting for the Lagrangian impact on the gaseous phase are included on the RHS.

$$\frac{\partial \rho}{\partial t} + \frac{\partial \rho u_j}{\partial x_j} = S_m \tag{3.20}$$

$$\frac{\partial \rho u_j}{\partial t} + \frac{\partial}{\partial x_j}\left[\rho u_j u_i + p\delta_{ij} - \tau_{ij}\right] = S_M \tag{3.21}$$

$$\frac{\partial \rho e}{\partial t} + \frac{\partial}{\partial x_j}\left[(\rho e + p)u_j - q_j - u_i\tau_{ij}\right] = S_e \tag{3.22}$$

$$\frac{\partial \rho a}{\partial t} + \frac{\partial}{\partial x_j}(\rho u a + J) = S_a \tag{3.23}$$

Viscous stress tensor, heat flux and mass diffusion are calculated as

$$\tau_{ij} = 2\mu S_{ij} - \frac{2}{3}\mu\delta_{ij}S_{kk} \tag{3.24}$$

$$q = -k\frac{\partial T}{\partial x_j} \tag{3.25}$$

$$J = -D_m\frac{\partial \rho a}{\partial x_j} \tag{3.26}$$

The source terms are calculated at each computational cell by volumetric averaging and interpolation of the Lagrangian variables from all droplets Np in each cell as

$$S_m = -\sum_{Np} \frac{w_p}{\Delta V} \dot{m}_p \tag{3.27}$$

$$S_M = -\sum_{Np} \frac{w_p}{\Delta V} \left[m_p \frac{\mathrm{d}\mathbf{v}}{\mathrm{d}t} + \dot{m}_p \mathbf{v} \right] \tag{3.28}$$

$$S_e = -\sum_{Np} \frac{w_p}{\Delta V} \left[\frac{\mathrm{d}(me)_p}{\mathrm{d}t} + \frac{1}{2} \dot{m}_p \mathbf{v}^2 + \dot{m}_p \mathbf{v} \frac{\mathrm{d}\mathbf{v}}{\mathrm{d}t} \right] \tag{3.29}$$

In case of a multi-component fluid

$$S_a = -\sum_{Np} \frac{w_p}{\Delta V} \dot{m}_{species} \tag{3.30}$$

The mass flux, $\dot{m}_p$ stands for the evaporation at the drop interface, typically evaluated by a droplet evaporation model as it will be illustrated in Chapter 4. Similar equations are solved in Lagrangian solvers within OpenFOAM. More details for the spray source terms are included in Karrholm (2008).

Discrete element method

The equations above correspond to a two-way coupling, where there is a mutual effect between the flows of both phases with including particle motion effects in the continuous-fluid motion. For unsteady dense flows where particle-particle interactions are important, a more general discrete element method is required that considers the droplet-droplet interactions, the so-called four-way coupling. A classification of phase-coupling mechanisms according to the void fraction and particle time-scales is available from the classical $\alpha - \tau_p/\tau_K$ diagram proposed by Elghobashi (1994). In general, for $\alpha \leq 10^{-6}$ the particles have a negligible effect on turbulence (one-way coupling region). For void fraction values higher than 10^{-3} in the dense suspension zone, the particle interactions are enhanced, and the interaction between the particles and turbulence is termed four-way coupling. In the intermediate zone $10^{-6} \leq \alpha \leq 10^{-3}$ the effects of the particles on the turbulence vary significantly as a function of the ratio τ_p/τ_K. In all these approaches, the motion and position (as well as other properties) of individual particles, or representative particles, are tracked with time. Having in mind that the order of the number of particles in a typical industrial application are $\mathcal{O}(10^9)$, tracking each particle individually is impossible due to the huge computational cost required. CFD engineers have overcome this barrier using a smaller number of computational particles to represent the actual particles. These computational particles are regarded as a

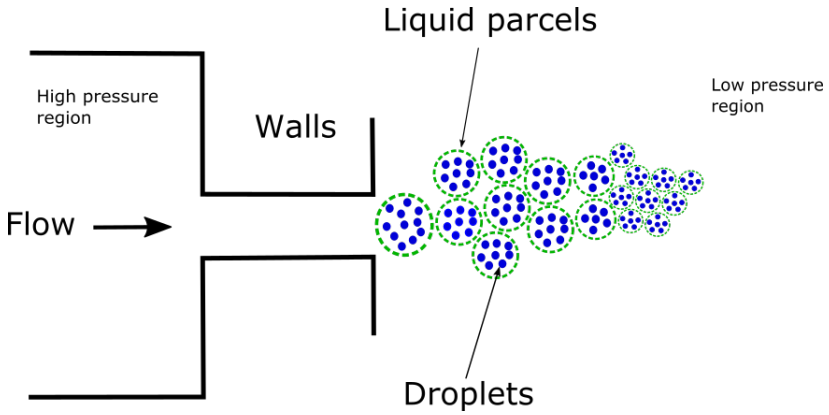

Fig. 3.13 Parcels concept for modelling spray motion. Droplets are grouped in families of droplets with the same properties.

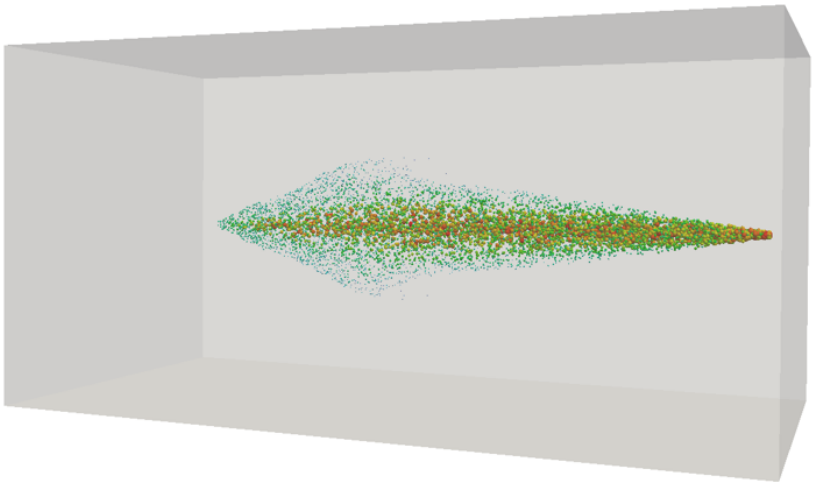

Fig. 3.14 Spray representation in Lagrangian particle tracking. Larger droplets break-up giving smaller droplets which disperse and interact with each other.

parcels of particles as shown in Figure 3.13. Under this assumption, the parcel of particles moves through the carrier fluid with the same velocity and temperature, as a single physical particle. The parcel is identified as a discrete element. Additionally, size distribution effects can be included by specifying parcels with a specific particle size. The result of the DEM method a large collection of parcels with a wide spectrum of sizes like in Figure 3.14.

3.7 Sub-models for primary atomisation and secondary break-up

There are only a few detailed models for the simulation of the primary break-up of high-pressure sprays. Some of the challenges in the experimental investigation of sprays arise from the small size of the generated droplets and the limitations of the experimental methods. Some of the limitations in measuring high-pressure sprays are acknowledged in Yildiz (2005) who reported difficulties in the characterisation of non-spherical ligaments in the vicinity of the nozzle exit (x/D<30) in PDA measurements for flashing water. Thus, it is difficult to understand the relevant processes that take place and verify proper primary break-up models.

3.7.1 Primary atomisation

Primary atomization modelling can be utilised by two types of methods as mentioned before: Lagrangian or Eulerian. The most popular Lagrangian approach is the Blob Model (Reitz and Diwakar, 1987) which treats the liquid core as families of droplets in the form of blobs that initially have a characteristic size equal to the nozzle hole diameter. It uses the idea that primary and secondary break-up within the dense spray near the nozzle is indistinguishable processes, and that a detailed simulation can be replaced by the injection of big spherical droplets with uniform size, which are then subject to secondary aerodynamic induced break-up (Jiang et al., 2010).

The diameter of these blobs equals the nozzle hole diameter D (mono-disperse injection) and the number of drops injected per unit time is determined from the mass flow rate. Although the blobs break up due to their interaction with the gas, there is a region of large discrete liquid particles near the nozzle, which is conceptually equivalent to a dense core. The injection velocity can be calculated as

$$u_{inj} = \frac{\dot{m}}{A \cdot \rho} \tag{3.31}$$

if we assume a known mass flow rate at the nozzle exit (inj stands for the injection properties). In case of a known pressure inside the storage tank, the Bernoulli equation for frictionless flow can be used to calculate an upper limit of the initial velocity,

$$u_{inj}^{max} = \sqrt{\frac{2\Delta p}{\rho}} \tag{3.32}$$

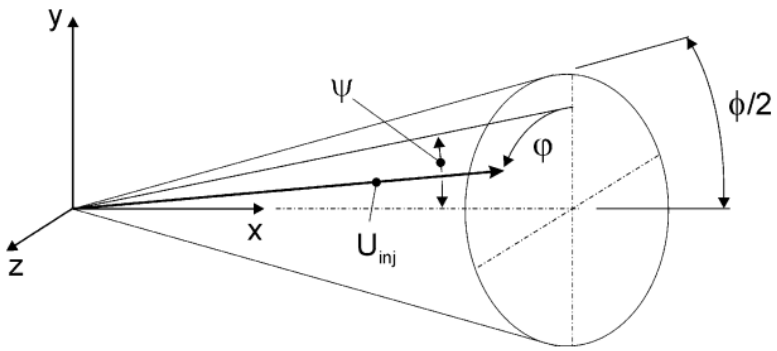

Fig. 3.15 Spray cone angle according to Baumgarten (2006).

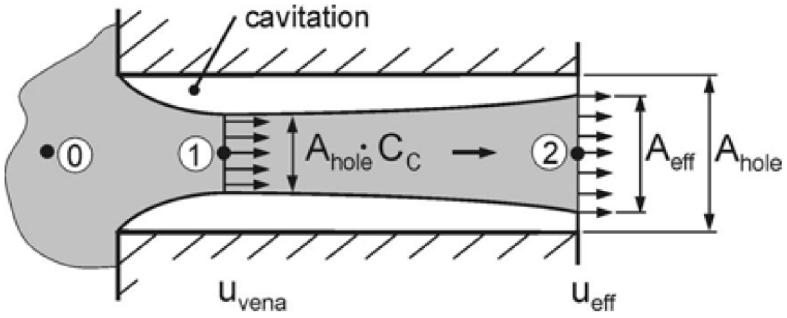

Fig. 3.16 Cavitating flow scenario in enhanced blob method, Baumgarten (2006).

where Δp is the pressure difference between the storage tank and ambient conditions. According to experiments in nozzles, the flow velocity at the nozzle hole exit is about 70–90 percent of the Bernoulli velocity (Baumgarten, 2006). In order to define the velocity components of each blob, the spray cone angle must be known from measurements or has to be estimated using semi-empirical relations. The velocity u_{inj} of the primary blob in the spray cone has a direction which is estimated by choosing two arbitrary numbers β_1, β_2 within the range of [0,1]. The azimuthal angle is $\phi = 2\pi\beta_1$ and the polar angle is $\psi = \phi\beta_2/2$ in the spherical coordinate system, Figure 3.15.

Applications with the Blob Model are reported for instance in Irannejad and Jaberi (2014). An extension of the Blob method is the Enhanced Blob method of von Kuensberg Sarre et al. (1999). This method was proposed as an alternative to the Blob method in cases of cavitating flows upstream the nozzle exit. In case of large injection lengths, the main flow is possibly cavitating meaning that the jet is not uniform prior to the injection (Figure 3.16). In this case, the effective area of mass flow rate is different from the nozzle area (analytical formulation is reported in Baumgarten (2006)).

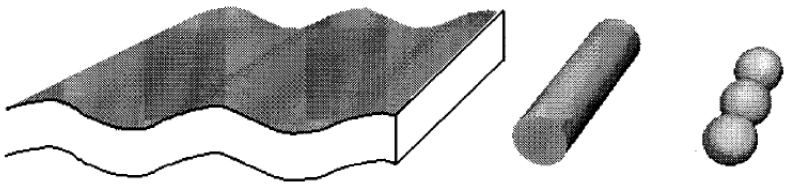

Fig. 3.17 Break-up of a liquid sheet, Senecal et al. (1999).

The Blob Model is suggested in cases where neither detailed information about the composition of the spray nor prior knowledge about the spray cone angle are available but might not be able to represent precisely the underpinning physics and model properly the associated processes during the primary break-up. The most important disadvantage of this model is that the impact of the geometry of the exit hole on the spray angle and the drop size distribution cannot be mapped and that the promotion of primary break-up by turbulence and implosions of cavitation bubbles outside the nozzle is not regarded at all (Baumgarten, 2006). Senecal et al. (1999) developed another primary atomisation model, the linearised instability sheet atomisation model (LISA model) for the atomisation of liquid sheets that includes the effects of the surrounding gas, surface tension and the liquid viscosity on the wave growth process. The idea of the LISA model is that the droplet sizes may be correlated with the wavelengths of the waves that grow on the surface of the sheet. A dispersion relation for the growth rate of long waves with infinitesimal amplitude, including the effects of surface tension, aerodynamic forces, and liquid viscosity was developed from the authors. They identified the wavelength with the largest growth rate and assumed that this wave breaks up the sheet at half wavelength intervals into ligaments. The ligaments then break up into droplets, according to Weber's theory for a cylindrical liquid column. The modelling idea is shown in (Figure 3.17). LISA model was validated by Senecal et al. (1999) for pressure-swirl atomisers and is proven to be able to model primary and secondary break-up as well. The disadvantage of this model is that the liquid sheet idea could lead to limitations in some cases.

Cavitation-induced atomisation models have also been developed the last decades allowing to simulate specific cases where cavitation plays a major role in the atomisation process. Arcoumanis et al. (1997) have developed a primary break-up model for full-cone diesel sprays that considers cavitation and turbulence. The internal flow and the spray motion are connected by considering the effective hole area. The diameter of the droplet exiting the nozzle is equal to the nozzle diameter, and the first break-up is assumed to occur due to the Kelvin-Helmholtz instabilities. One of the assumptions of this model is the single virtual

bubble for calculating the bubble collapse time. The cavitation bubbles are grouped into a single big artificial bubble which occupies the same area as all the small ones together. The collapse and burst time are calculated using the turbulent velocity obtained by the turbulence model and the force acting on the jet is finally estimated. The model takes all the important processes into account and has been validated by the authors but the use of one-dimensional sub-model for the effective area or the artificial single bubble hypothesis, generally not valid, reduces the model's applicability.

Distribution function methods

These methods apply when the flow inside the nozzle and its effects on the spray are negligible. The liquid is assumed that is entirely atomised at the nozzle exit and has a distribution of drop sizes can be associated with probability density functions (PDF). In cases such as flashing jets with high storage pressure conditions, the result is more likely a high-pressure spray where neither the droplet sizes nor their distribution in the dense spray near the nozzle could be quantified experimentally up to now. Thus the droplet size distribution must be guessed and adjusted until the measured drop sizes in the far field of the nozzle are similar to the simulated ones. This is a common practice in many CFD packages that are used in automotive industry. OpenFOAM Lagrangian solvers employ a distribution function for the liquid jet injection process. This assumption may lead to severe variations between the modelled and measured spray quantities but can be used as an alternative to the mono-disperse injection of the Blob model. Various distributions are proposed in the literature for the size distribution. For instance, the Rosin-Rammler distribution is used in standard OpenFOAM spray classes. The droplet size distributions are made based on the minimum and maximum diameter of the droplets and are divided into a number of intervals with each interval specified by a mean diameter.

$$F(x) = 1 - e^{-(\frac{x}{d})^n} \tag{3.33}$$

$$f(x) = -\left(\frac{n}{x}\right)\left(\frac{x}{d}\right)^n e^{-(\frac{x}{d})^n} \tag{3.34}$$

The first equation is the cumulative distribution function and the second one is the probability density function. The n-parameter is a measure of the spread in particle sizes, where a higher value reduces the spread. A typical value of $n = 3$ is used in this study. Here d is the mean particle size of the distribution. It corresponds to the average droplet size of the PDF. This value has to be specified in the model. The χ^2 distribution is also popular in the literature for spray applications but is not studied in this research in favour of the Rosin-Rammler distribution.

3.7.2 Secondary break-up

Break-up models for secondary atomisation have been developed in the 1980s implementing empirical correlations depending on Weber and Ohnesorge numbers. These describe the disintegration of already existing droplets into smaller ones due to the aerodynamic forces that are induced by the relative velocity between the droplet and surrounding gas. These forces result in an unstable growing of waves on the droplet surface or of the whole droplet itself and finally lead to its disintegration. The surface tension force, on the other hand, tries to keep the droplet spherical and counteracts the deformation force. The models which are usually used to simulate secondary break-up processes in full-cone as well as hollow-cone fuel sprays are described next.

Taylor analogy model (TAB)

The Taylor Analogy Break-up model (TAB model) proposed by O'Rourke and Amsden (1987), is based on an analogy between a spring-mass system that oscillates in the same way a flowing drop into a gaseous atmosphere oscillates. The force F responsible for the oscillation of the mass m corresponds to the aerodynamic forces acting on the surface of the droplet. These forces are the primary reason for the drop deformation causing its mass to oscillate. Denoting with k_m, d_m the spring-mass constants and x_{dist} the displacement of the mass from the idle state, the restoring force $F_{spring} = k_m \cdot x_{dist}$ acts in the same way the surface tension force opposes to the change in the droplet shape. The damping force $F_{damp} = d_m \cdot \dot{x}_{dist}$ corresponds to the droplet forces due to the liquid viscosity. The second order differential equation of motion for the damped spring-mass-system is

$$\ddot{x}_{dist} = \frac{F}{m} - \frac{k}{m} x_{dist} - \frac{d}{m} \dot{x}_{dist} \tag{3.35}$$

Substituting x_{dist} with the dimensionless deformation $y_{dist} = x_{dist}/C_b \cdot r$ we get the following equation for the droplet deformation

$$\ddot{y}_{dist} + C_d \frac{\mu}{\rho r^2} \dot{y}_{dist} + C_k \frac{\sigma}{\rho r^3} y_{dist} - \frac{C_F}{C_b} \frac{\rho_g u_{slip}^2}{\rho r^2} = 0 \tag{3.36}$$

Solving this second-order equation gives an analytical expression for the deformation of the drop. The rest of the constants have the following values: $C_b = 0.5$, $C_d = 5$, $C_F = 1/3$, $C_k = 8$, and $k_m = 10/3$. The critical Weber number is 6 from experiments (Baumgarten, 2006). The calculation of the droplet size and number is computed by equating the energy on the surface before and after the break-up.

The disadvantage of this model is that among the various possible modes of oscillations that can result in a drop break-up, the TAB model only describes the fundamental mode corresponding to the lowest order spherical harmonic (Equation (3.36)). It is generally considered that it under-predicts droplet sizes of full-cone diesel sprays and underestimates penetration if it is combined with the Blob model. Moreover Polanco et al. (2010) suggest in their review for flashing jets that TAB works properly only for Weber number lower than 100 which is generally low compared to typical internal combustion engines applications in which $We \sim O(10^3)$.

Enhanced Taylor analogy model (ETAB)

The concept of the Enhanced Taylor analogy model (ETAB) is similar as in TAB for the deformation of the droplet. ETAB distinguishes between the Bag and Stripping breakup modes. The model uses the same procedure to explain deformation of droplets and the time required for break-up, but it assumes that the rate of formation of droplets is proportional to their number

$$\frac{\mathrm{d}}{\mathrm{d}t}n(t) = 3K_{br}n(t) \tag{3.37}$$

In this equation the number of droplets at time t is $n(t)$ and K_{br} is a constant that varies depending on the break-up regime

$$K_{br} = \begin{cases} k_1 & \text{if} \quad We \leq We_t, \quad (bag \quad break-upregime) \\ k_2 & \text{if} \quad We > We_t, \quad (strip \quad break-upregime) \end{cases} \tag{3.38}$$

The We_t is the dividing regime which in most of the times is set to 80. Assuming that children droplets with only uniform size are generated during break-up the Equation (3.39) predicts the child droplet size,

$$\frac{r_{child}}{r_{parent}} = e^{-K_{br}t} \tag{3.39}$$

ETAB is an improved model but in general calculates the new droplet sizes to be bigger than the predictions obtained from the TAB model.

Rayleigh-Taylor and Kelvin-Helmholtz models

The break-up is supposed to be due to the growth of some instability waves developing on the liquid surface until they reach to similar scales to those of the injected liquid blob. At the liquid-gas interface, a kinematic discontinuity is imposed, and the balance equations are applied to tangential and normal stresses taking into account surface tension, dynamic pressure and viscous effects. A dispersion equation was obtained by Reitz and Bracco (1986) relating the spatial and temporal growth rate of the instabilities to their wavelengths. The solution of the equation of Reitz and Bracco is a second-degree equation which gives a single maximum in the wave growth rate curve. Among the different wavelengths, the one which grows faster is considered as the one responsible for the break-up, and is the most unstable one: the dimension of this wavelength Λ and the maximum growth rate Ω are then

$$\frac{\Lambda}{r_0} = 9.02\frac{(1+0.45\cdot Oh^{0.5})(1+0.4\cdot Ta^{0.7})}{(1+0.865\cdot We_g^{1.67})^{0.6}} \tag{3.40}$$

$$\Omega\left[\frac{\rho r_0^3}{\sigma}\right] = \frac{0.34+0.38\cdot We_g^{1.5}}{(1+Oh)(1+1.4\cdot Ta^{0.6})} \tag{3.41}$$

The initial droplet radius is r_0 and Ta is the Taylor number, $Ta = Oh\sqrt{We_g}$. Reitz (1987) calculated the new droplet radius after the break-up to be equal to

$$r_{new} = B_0 \cdot \Lambda \tag{3.42}$$

where $B_0 = 0.61$. In order to complete the description of the disaggregation process of the liquid, the progressive diameter reduction of the liquid jet is then evaluated through the following

$$\frac{\mathrm{d}r}{\mathrm{d}t} = -\frac{r - r_{new}}{\tau_{bu}} \tag{3.43}$$

The droplet size r relaxes to the equilibrium value (the radius of the new droplet) at the break-up time τ_{bu}, where $\tau_{bu} = 3.788\cdot r/\Lambda\cdot\Omega$. The Kelvin-Helmholtz (KH) model is based on a first order linear analysis of the Kelvin-Helmholtz instability. This model is appropriate for high injection velocities, where the Kelvin-Helmholtz waves dominate break-up (We > 100). Hence, the wave model is recommended for Weber numbers greater than 100 at the injection point and is appropriate for the striping break-up mode.

Another model for secondary break-up is the Rayleigh-Taylor (RT) model. This model takes into consideration a different type of instability, the Rayleigh-Taylor instability, induced by the acceleration or deceleration normal to the interface of a liquid within a gas flow

field due to different densities. As before, the balance-equations for the surface-equilibrium are applied at the liquid-gas interface, and here again the droplet breakup is related to the instabilities characterised by the fastest growing wavelengths. Based on Taylor (1963), the growth rate and the corresponding wavelength are in this case

$$\Omega = \sqrt{\frac{2}{3\sqrt{3}\sigma}\frac{(a_{acc}(\rho_l - \rho_g))^{3/2}}{\rho_l + \rho_g}} \tag{3.44}$$

$$\Lambda = C_3 2\pi\sqrt{\frac{3\sigma}{a_{acc}(\rho_l - \rho_g)}} \tag{3.45}$$

The acceleration of the droplet a_{acc} is calculated from the flow characteristics and C_3 is a constant of the model typically $C_3 = 1.0 - 5.3$. The model can be used for cases where the relative velocity of the liquid is high and for drag-deceleration instabilities near the nozzle exit. Moving further downstream the disintegration position, the shear flow induced instabilities prevail and the KH model is expected to be more efficient. Consequently, KH and RT models are intrinsically connected and usually coupled together for modelling the primary atomisation and secondary break-up.

CFD for the spray characteristics of flashing jets

The characterisation of the spray properties of flashing jets in the literature is dominated by detailed experiments. Experimental studies describe their observations using empirical or semi-empirical models that use as a basis zero or one-dimensional models. Simplified reduced-dimension methodologies are usually implemented and constitute a popular approach in commercial software offering fast estimations for flashing calculations (Johnson and Woodward, 1991; Yellow book, 2005; HSE, 2002). These simplifications concern both the dense and dilute spray regions. A common practice to tackle the varying thermodynamic effects which play a major role in the emerging jet is the use of reasonable assumptions for the release process. The isenthalpic and isentropic assumptions are possible for the expansion region of the flashing jets. In the isenthalpic formulations the change in the kinetic energy is small compared with the enthalpy change. On the other hand, in case of isentropic conditions either the momentum equation is replaced with an entropy equation or the energy equation is substituted in favour of well-established isentropic relationships. This assumption is also implemented in PHAST software. The shortcomings of the isenthalpic and isentropic assumptions are not apparent and there is an ambiguity in the literature regarding the assumption to be made for flashing expansion.

CFD offers three-dimensional reproduction of the experiments and can capture effects and provide information for all the flow quantities but is based on numerical models which also have limitations. The CFD approaches for flashing and cavitation have risen up the last decades since multiphase flows models have become more mature for dealing with the related complex transient phenomena. The most recent state of the art three-dimensional CFD studies for flashing, including the HRM model, are implemented following Schmidt et al. (2010). For instance Moulai et al. (2015) and Duke et. al (2015) used HRM in CONVERGENCE software and successfully calculated the mass flow rate and the liquid penetration. Price et al. (2016) used an evaporation model for simulating flashing jets using Lagrangian particle tracking. In their approach the droplet shape changes due to flashing and they provided validation for the liquid penetration but not for SMD. Characterisation of the spatial scale of the liquid blobs and ligaments is still an ongoing research topic and poses significant challenges due to the multi-scale nature of the process. Nilpueng and Wongwises (2013) investigated flashing jets of varius refrigerants through short-tube orifices for low pressures and observed choking and metastable flow phenomena inside the orifice, indicating that increasing the degree of subcooling and pressure, the metastability region increases. The authors offered correlations for the mass flow rate with respect to pressure but not for the spray characteristics. Janet et al. (2015) performed 3D CFD simulations using the two-fluid model for simulating flashing, investigating the patterns at the internal flow only. Heterogeneous nucleation modelling was included and the performance of various wall nucleation models was tested for the critical flow rate calculation, showing a good agreement for the mixture properties at the axial direction but not for the radial profile. The importance of a CFD model for calculating the critical flow rate was highlighted in the previous chapter, and is discussed extensively in chapter 5 where the perfomance of the developed CFD model is discussed. Other two-fluid Eulerian approaches have been developed by Liao and Lucas (2015a) and Liao et al. (2015b) for poly-disperse bubbly flows considering the modelling of bubble forces and bubble-induced turbulence. In the flashing flow test cases considered by the authors, vapour generation inside nozzles and pipes were presented and bubble coalescence and break-up was studied, giving a comprehensive discussion for the impact of the bubbly flow on the emerging jet. In most cases, three-dimensional numerical studies usually focus on specific effects in flash-boiling sprays due to the complex phenomena underpinning the process assessing the validity of cavitation sub-models for flash-boiling. Wang et al. (2014) simulated cavitating liquid jets using a compressible and equilibrium two-phase flow solver. The developed approach involved the presence of non-condensable ambient air into the two-phase mixture calculations using a hybrid Harten-van Leer-Lax-Contact(HLLC)-Rusanov scheme suitable for high-pressure cavitating liquid jets. The test cases considered by Wang et al. (2014) gave

insights for implementing a phase equilibrium CFD solver to predict internal flow patterns and the results did not include droplet size or velocity predictions. Battistoni et al. (2015) used an Eulerian framework for simulating the effect of non-condesable gas in the mixture for cavitating liquids through nozzles. The authors employed the homogeneous-relaxation-model in a one fluid approach and presented results for the void fraction inside the nozzle to show the non-condensable gas distribution inside the nozzle. The effect of the rapid phase change in the internal flow characteristics was also highlighted by Brusiani et al. (2013) who compared two different cavitation models, the first one using the HRM implemented in OpenFOAM and the second cavitation model was a standard implementation within ANSYS software. Both approaches showed that can properly simulate the critical flow rate and choking but not the velocity distribution at the radial direction which was mainly attributed to the non-condensable gas effects by Brusiani et al. (2013). Only few 3D numerical studies investigate both the internal and external flow of superheated jets (Coldrick, 2016; Desantes et al., 2014; Lu et al., 2014; Som et al., 2015). Som et al. (2015) used Large Eddy Simulations for modelling vaporizing gasoline sprays and the provided liquid penetration predictions were in good agreement with the experiments. Desantes et al. (2014) performed simulations using an Eulerian framework within OpenFOAM providing results for liquid penetration. The developed approach employed Fick's law for modelling the mixing associated to the liquid atomisation process, and the results showed that the method can give reasonable predictions for the liquid core but over-predicts the spray angle in the vicinity of the nozzle exit. The test cases considered in the simulations by Desantes et al. (2014) were for diesel sprays. Results and useful insights regarding the liquid penetration and velocity profiles for flashing gasoline sprays can be also found in Weber and Leick (2014). Coldrick (2016) modelled flashing propane jets using a Eulerian-Lagrangian approach. The droplet motion was modelled using Lagrangian particle tracking and tests were performed for superheated propane flowing through nozzles with $L/D = 10$. The results presented by Coldrick (2016) included velocity and temperature profiles for the two-phase jet which were in good agreement with the available experimental data. The assumption of the homogeneous equilibrium was used from Coldrick (2016), with the predictions for velocity having similar trends with Allen (1998). No results for the Sauter mean diameter or the radial profile of the velocity and the spray angle were presented (some practical CFD guidelines for flashing jets are also included in (Coldrick and Webber, 2017). Lu et al. (2014) presented a fully Eulerian 3D CFD method using interface tracking for modelling the primary atomisation of flashing jets. The concept of surface density which will be discussed in detail in chapter 6, was employed for characterising the liquid structures emerging downstream the nozzle exit. Lu et al. (2014) used LES and employed a compressible framework allowing, according to the

authors, the solver to simulate the two-phase jet in both inside and outside the nozzle. The results presented from Lu et al. (2014) regarded qualitative predictions for the liquid volume fraction but did not include any spray characteristics or any special treatment for the thermal non-equilibrium of the process. Baldwin et. al (2016) considered thermal non-equilibrium effects for 3D simulations of similar applications than in Lu et al. (2014) (flashing gasoline jets) using also a compressible Eulerian approach. The authors did not provide results for the spatial chacterisation of the liquid ligaments and droplets or the spray angle and velocity.

According to the author's knowledge, no three-dimensional CFD models for flashing jets validated against SMD experiments and velocity are reported in the literature which is one of the contributions of this thesis.

3.8 Results for Lagrangian modelling of flashing jets

Some preliminary results are demonstrated in this section for assessing the capabilities of OpenFOAM software. The Lagrangian solver SprayFOAM of OpenFOAM® (Weller et al., 1998) was used for simulating the dispersion of a propane flashing jet. The test case is based on the HSE experiments of Allen (1998). These are one of the first well-documented data of flashing jets in the literature. The configuration is relatively simple: A storage vessel connected to a nozzle release system. The nozzles tested are cylindrical with diameter $D = 4mm$ and length $L/D = 10$. The domain used for the simulations is shown in Fig. 3.18. Different meshes were tested for the simulations. The results shown here were obtained using a 800000 hexahedral cells with a cell size equal to 0.1mm at the inlet with a cell expansion ration equal to 5. A second order unbounded scheme was used for the advection terms. For the advection terms containing the turbulence model quantities, a second order upwind biased scheme was used. A Gauss scheme with a linear surface normal gradient scheme was used for the diffusion terms. The inlet pressure and velocity values are dictated by the mass flow rate at the injection position and had fixed values in the rest of the domain. Zero gradient boundary condition was imposed at the walls for pressure and velocity was treated as no-slip. The PIMPLE algorithm was used as a basis for the pressure-velocity coupling and typically up to five PIMPLE iterations were used for the simulations here.

The liquid propane kept in the storage vessel passes by the transfer line to the nozzle and releases to the atmosphere in typical ambient conditions ($1bar$, $293K$). The physical and geometrical parameters are summarised in Table 3.1.

The data extracted from the measurements regarded the axial velocity and droplet size distribution at the centreline and different positions downstream the nozzle exit. Due to the measurement technique and data manipulation (for instance, caused by multiple diffractions

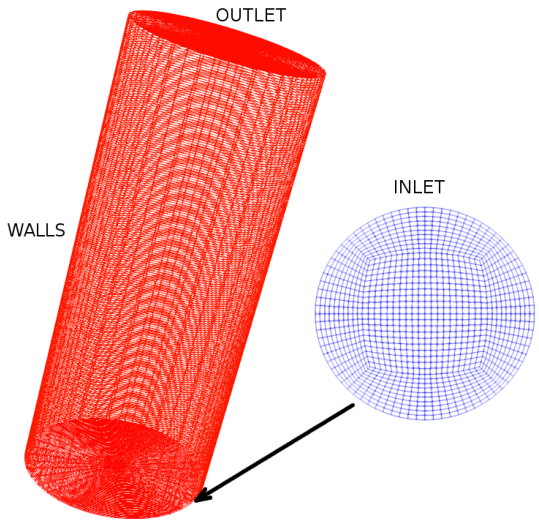

Fig. 3.18 Domain used for the CFD simulations of the Allen (1998) experiment.

in the particle sizer) Allen (1998) raised some uncertainties regarding the accuracy of the observed droplet sizes. Although these uncertainties, the experiments provided useful data on the size distribution trends and jet behaviour at the radial and axial direction which can be employed for CFD codes preliminary validation.

Table 3.1 Parameters for simulating the propane experiments of Allen (1998).

Physical and geometrical parameters	
Working fluid	Propane
Nozzle diameter	4 mm
L/D	10
Injection pressure	6 bar
Injection temperature	288 K
Mass release rate	0.11 kg/s
Co-flowing air	1.3 m/s

The equations solved were similar to the ones described in the section 3.3 of this chapter. Lagrangian approaches are based on additional assumptions for the internal flow. The regime for the fluid flowing within the nozzle prior to the jet release is unknown. The hypothesis for the flow at the nozzle exit, which here is assumed to be pure liquid is dictated from the needed input for the sub-models in the particle tracking approach. Given the mass flow rate and the injection time, the user defines the injection position and method, typically generated at randomly selected points at the injection patch. Having calculated the number of new parcels to inject and the total volume, the injected volume, the volume fraction and

the number of the particles are specified. The three latter are iterated over the number of new parcels assuming spherical droplets. The Blob Sheet atomisation model of Han et al. (1997) is used for the primary atomisation. The injected blobs resemble the liquid sheet which emerges to the atmosphere due to pressure difference. The droplets injected with a large droplet diameter, break-up at a distance $l_{break-up}$ (break-up length) which is a function of the fluid flow characteristics

$$l_{break-up} = B \cdot \sqrt{\frac{\rho_l \sigma \cdot ln(\eta/\eta_0) h \cdot cos(\theta\pi/360)}{(\rho_g \cdot U_{rel})^2}} \tag{3.46}$$

where h is the liquid sheet thickness and η is the wave amplitude when the sheet breaks up, given an intial value η_0. The parameter $ln(\eta/\eta_0)$ was taken to be equal to 12 in Han et al. (1997). Both KH-RT and TAB model are tested and the latter one showed better performance ($We < 100$). A model for flash vaporisation of Zuo et al. (2000) already implemented within OpenFOAM was used. The sub-models used for simulating the experiments are listed in Table 3.2. The O'Rourke collision model O'Rourke (1981) gives the calculated collision probability that two particles collide. If this probability is high enough the particles will collide regardless their direction. Assuming that two parcels are in a computational volume cell V_{cell}, then the collision frequency is

$$p_{12} = \frac{N_{min}\pi}{4V_{cell}}(D_{min} + D_{max})^2 u_{rel} \tag{3.47}$$

where N_{min} is the number of particles in the smaller parcel with diameter D_{min} which is distributed homogeneously in volume V_{cell} with the parcel with diameter D_{max}. The observed droplet position and velocity are plotted in Figures 3.19- 3.22. The averaged position of the liquid parcels at a given position are shown for the CFD simulations. The results are presented using the same data analysis as in Allen (1998). More details for the data collection and visualisation can be found in Allen (1998). Parcels with particle diameter larger than $5.8\mu m$ (Malvern system output limit of the experimental equipment) are plotted. The present calculations where performed in a 12-core personal workstation and the solution took approximately 5 days.

The velocity in the centreline is in good agreement with the experiments. Moving further away the nozzle exit, the jet intact core starts to disintegrate due to the instabilities acting on the jet. The velocity at the jet centreline in the experiment appears to increase slightly in the so-called expansion area, but on the simulation, the trend is rather constant, exhibiting a small difference between the measured data and the CFD results (less than 6 percent). A difference between flashing and non-flashing jets is that contrary to the former, a constant

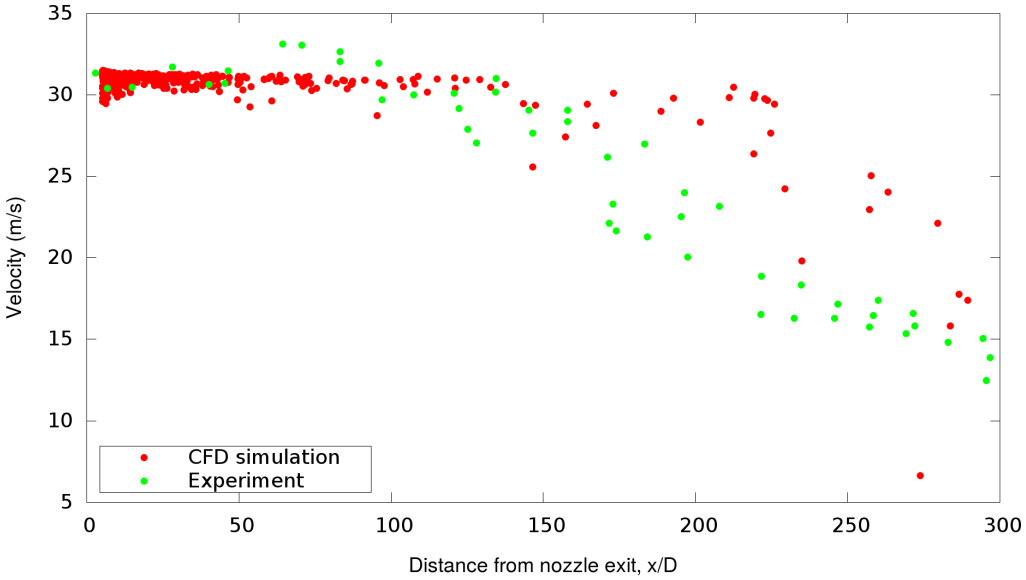

Fig. 3.19 Droplets at the centreline and their axial velocity. Comparison of CFD results with data from Allen (1998).

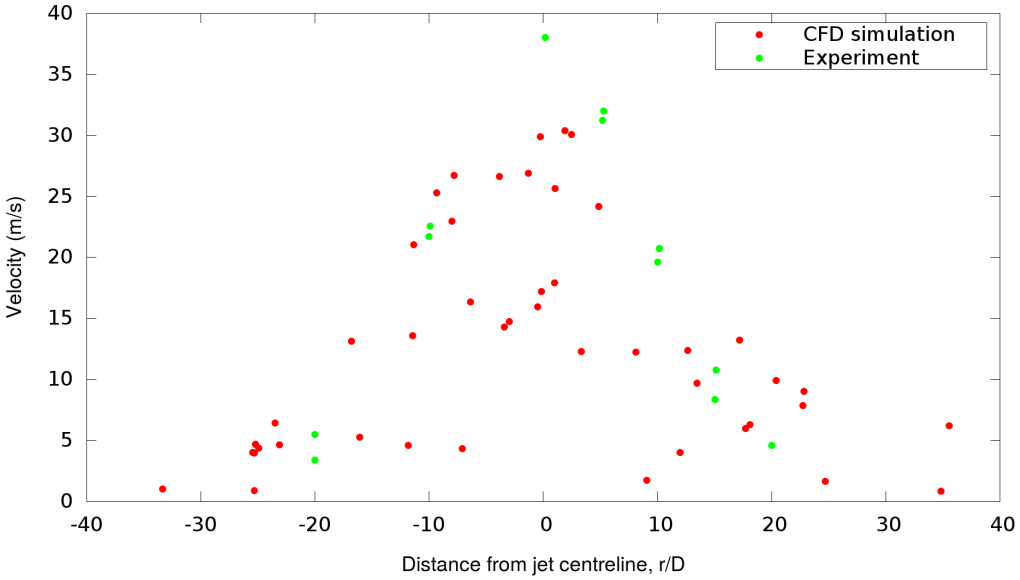

Fig. 3.20 Radial distribution of droplets and their lateral velocity at 300 mm distance from the nozzle exit. Comparison of CFD results with data from Allen (1998).

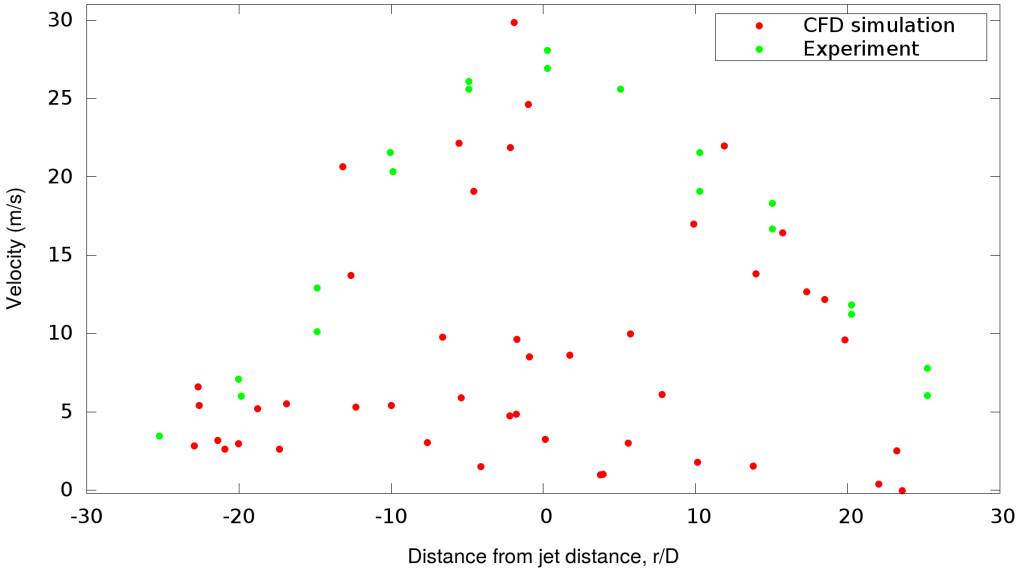

Fig. 3.21 Radial profile of the droplets and their lateral velocity at 500 mm distance from the nozzle exit. Comparison of CFD results with data from Allen (1998).

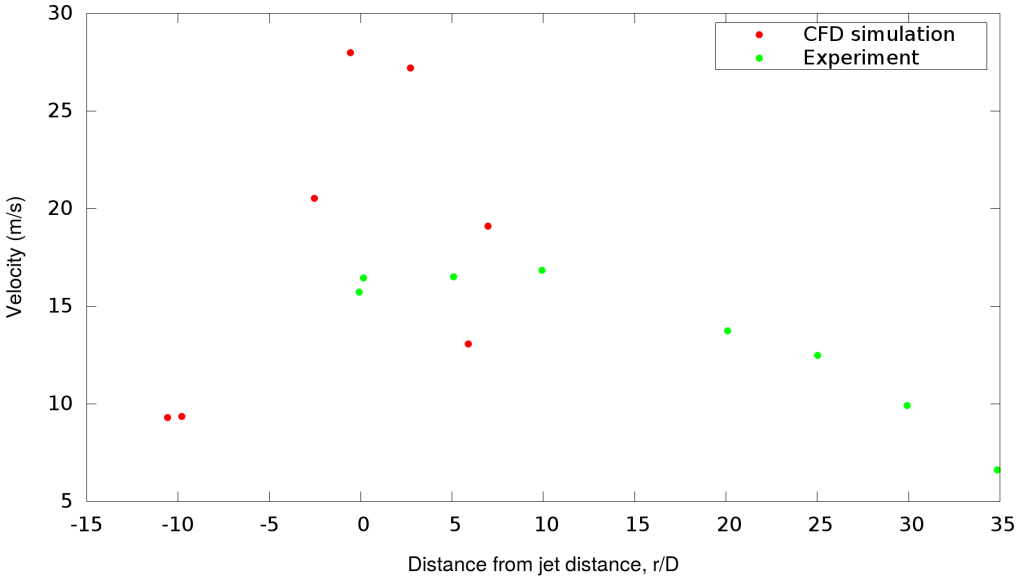

Fig. 3.22 Radial distribution of the particles and their lateral velocity at 1028 mm distance from the nozzle exit. Comparison of CFD results with data from Allen (1998).

Table 3.2 Numerical set-up for simulating Allen (1998) experiments.

Sub-models for the Lagrangian approach	
Injection model	Cone
Primary atomisation	Blob method
Secondary break-up	TAB model
Heat transfer	Ranz Marsal with Bird correction
Phase change model	Zuo et al. 2000
Stochastic collision model	O'Rourke

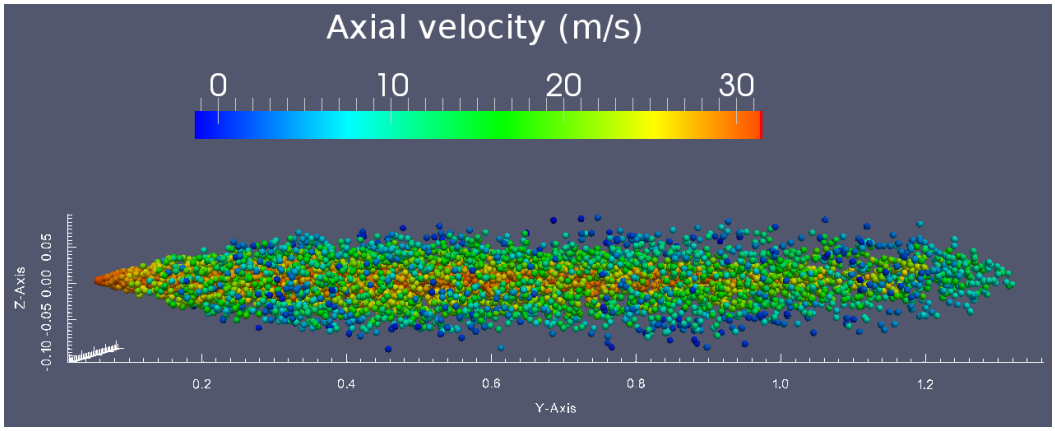

Fig. 3.23 Droplet size bands for Allen (1998) experiments.

centreline velocity is excepected at the first stages of the atomisation, in the potential core region. There is an ambiguity if propane flashes inside or outside and if the L/D parameter impacts on the velocity trend. Yildiz (2005) showed also nearly constant axial velocity for flashing $R134A$ but for smaller $L/D = 2$ and higher superheat degrees, up to $40K$ whereas here $\Delta_{sh} = 7K$. Nevertheless, according to Allen (1998) the axial velocity is possible to be constant in the expansion region thus this difference is reasonable. Fig 3.23 shows an instant caption of the axial velocity when steady state is reached. A decreasing velocity behaviour commonly met in both single-phase iso-thermal jets and flashing jets is observered at the entrainment region of the jet. Like in iso-thermal jets, the entrained mass flow is larger further downstream the nozzle exit and causes the axial velocity profile to decrease (Polanco et al., 2010). The same mechanism causes the centreline velocity drop in non-flashing jets.

The spray particle cloud profile and the lateral velocities of the droplets are shown in Figs 3.20- 3.22 which were post-processed with the aid of a fellow PhD student M. Macchi whose help is greatly appreciated. The jet radial velocities seem to follow a characteristic bell shape (or Gaussian to be more precise) for all the chosen positions downstream the nozzle exit. The maximum values are in good agreement for the $x = 300mm$ and $x = 500mm$, but a significant

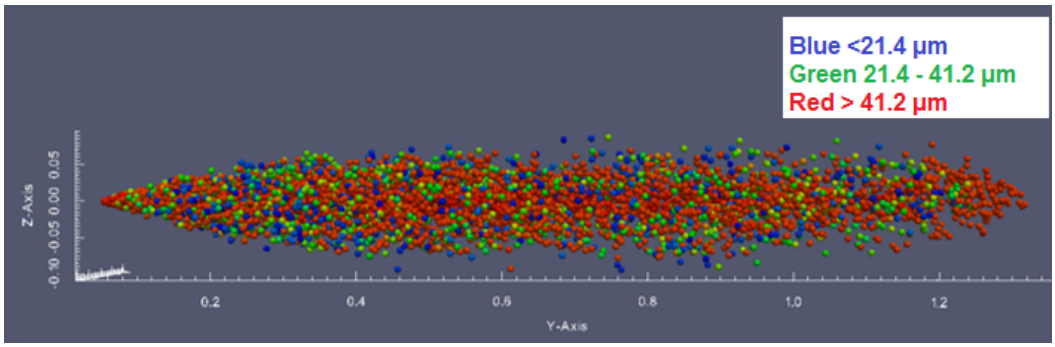

Fig. 3.24 Droplet size bands for Allen (1998) experiments.

variation is observed for the $x = 1080mm$ position. The radial velocity profile is commonly met in both single phase iso-thermal jets and superheat jets. Due to the vena contracta effect, the velocity of the liquid core has a conical shape which maintains along the jet direction. The jet spreads in the radial direction in all the cases in Figs 3.20- 3.22 giving a Gaussian shape similar to the one in non-flashing jets (Abramovich, 1963).

Droplet size measurements were also provided by Allen (1998). Due to limitations analysing the data, the results were presented in three bands: the first band included droplets with diameter less than $21.4\mu m$, in the second one were the particles with diameter between $21.4\mu m$ and $41.2\mu m$ and the third size band included all the droplets with size more than $41.2\mu m$. An illustration of the three size bands is shown in 3.24. Direct comparison between the experimental data and the CFD prediction cannot be made since it is not clear which characteristic diameter is provided. In Figure 3.24 the Sauter mean diameter is shown. If we assume that the diameter provided by the author of the experiments is equal to the SMD, then large differences with the simulated values are admitted. Interpreting the experimental data, there was a significant change in the smaller droplet size band approximately at 700 mm, suggesting that this is possibly the point at which the majority of the propane droplets have been entirely converted to vapour. This might be an indication of the relatively large deviation in axial velocity at the position $x = 1080mm$. In general, the predicted SMD from SprayFOAM solver were usually outside the observed first two ranges ($0 - 21.4\mu m$, $21.4 - 41.2\mu m$). One possible explanation could be the flash vaporisation model used in OpenFOAM. The model of Zuo et al. (2000) is based on the linearised instability sheet atomisation model and was developed for pressure swirl atomisers. The model assumes that a hollow-cone spray with a thin surface is produced during the jet dispersion and that the rate of heat is conducted using the effective thermal conductivity. A simple one-dimensional temperature equation is considered, neglecting the bubble nucleation/growth effect on the heat transfer within the liquid sheet.

3.9 Concluding remarks

The most important modelling ideas for liquid atomisation and sprays are discussed in this chapter. The different approaches in finite volume methods are classified depending if they are in a Eulerian or Lagrangian framework. The concept of liquid blobs is a useful concept for realistic industrial applications with sprays. The most important models for primary atomisation and secondary break-up are presented and the majority of them is already included in standard OpenFOAM software for modelling the dynamics of injected parcels. Preliminary results obtained from the existing implementations in OpenFOAM show that the velocity fields in the dilute spray regions can be predicted adequately but the insufficient description in the dense part of the spray manifest the need of an alternative modelling approach for heat and mass transfer within a Euler framework.

The fundamentals of liquid atomisation and sprays are also presented in this chapter. The necessary definitions for describing the liquid fragmentation into droplets are included here. The process of liquid fragmentation comprises of the primary atomisation into blobs and ligaments and the secondary break-up of the liquid structures into smaller droplets. The regimes in flashing jets are discussed although a complete classification for flashing jets is still to be established in the literature. The reason for this difficulty lies in the wide range of the associated parameters which are the geometry, superheat degree and pressure among others. A list of some important experiments for flashing jets is also included.

Chapter 4

Numerical modelling of multiphase flows

Numerical simulation of a physical process is an intermediate step between the analytical solution and the experiment. In the world of Fluid Dynamics, everything can be described with equations which approximate the reality. Usually, the Navier-Stokes equations are employed and together with sub-models, constitute the system one needs to solve to predict the flow in time and space. Since the analytical solution of this system of equations is possible to very few cases, the solution of the equations is based on numerical approximations which approach the exact of the solution with an error. The purpose of scientist is to minimise this error in the most efficient and accurate approach. The backbone of numerical modelling of fluid motions is the pure mathematical modelling which express, with a certain limit, the mechanisms that make the fluid move, change in shape e.t.c. In this chapter, we explore briefly such models and their logic for characterising multiphase flows. The discussion about their formalism is headed towards two immiscible fluids but can be extended for generalised realism. Other major aspects of numerical modelling of multiphase flows are discussed, e.g. the scale of resolving the physical domain for turbulence and the pressure-velocity coupling which is the cornerstone of CFD for pressure-based approaches.

4.1 Problem formulation

There are two different approaches for representing the two-phase spray flows in CFD. These two approaches are: the Eulerian method, where the spray is considered as a continuum across the whole flow domain, and the Lagrangian method, where the droplet trajectories are tracked through the domain. In the Lagrangian particle tracking approach, the gas phase is usually represented using the Eulerian approach but the liquid spray is modelled by a number of discrete computational particles.

Fluid dynamics problems are usually expressed via the Navier-Stokes(NS) equations or in the case of inviscid flows, the Euler equations. In both cases, the fluid flows expressed with a system of non-linear partial differential equations. This non-linearity of the equations is because of the spatial acceleration of the fluid which remains the basic reason for this complexity of NS. Even though the works of the mathematical and engineering community, NS still remain unresolved except for some special cases which have an analytical solution (2D parallel flow in channels, Couette flow e.t.c). While the solution of Navier-Stokes with given boundary conditions remains impossible, the uniqueness of the solution is still an open problem.

Here no attempt of deriving the NS equations is made but a rather brief contextualisation is induced in order to be easier for the reader to track the methodology developed in the next chapters.

4.1.1 Navier-Stokes equations

Here, we provide the governing equations for multiphase flows with interface modelling. The framework detailed in this chapter leads to the problem formulation for two compressible immiscible fluids. The phase change will be discussed latter. The mass and momentum equations for a fluid in time and space following Prosperetti and Tryggvason (2009) are

$$\left\{ \frac{\partial \rho}{\partial t} + u_j \frac{\partial \rho}{\partial x_j} \right\} + \rho \frac{\partial u_j}{\partial x_j} = 0 \tag{4.1}$$

$$\rho \left[\frac{\partial u_i}{\partial t} + u_j \frac{\partial u_i}{\partial x_j} \right] = -\frac{\partial p}{\partial x_i} + \frac{\partial \tau_{ij}}{\partial x_j} + \rho f \tag{4.2}$$

where $u_i(x,t)$ represents the i-th component of the fluid velocity at a point in space, x_i, and time, t. Also $p(x,t)$ represents the static pressure, $\tau_{ij}(x,t)$, the viscous (or deviatoric) stresses, and ρ the fluid density (instantaneous quantities are considered for now). Also, the Einstein summation convention has been employed [1]. In the second equation, the subscript i is a free index which takes on the values x, y, z for the three dimensions in space. Hence, the momentum equation is a set of two or three equations (for 2D or 3D problems correspondingly) which express Newton's second law written for a continuum in a spatial reference frame. Together they relate the rate of change of momentum per unit mass (ρu_i) which is a vector quantity, to the contact and body forces (ρf). On the LHS of the momentum equation, the outer product of the velocities is formally written via the dyadic sign $\otimes$ which is neglected in this thesis for brevity:

[1] Einstein summation convention: repeated indices in a single term are summed over x, y, and z.

$$u_i u_j = u_i \otimes u_j \tag{4.3}$$

the result of this operation is a tensor. The Stokes hypothesis is used in this study which states that the bulk viscosity is zero. This leads to the argument that the second viscosity of the fluid is equal to $-2/3\mu$. Stokes hypothesis cannot be validated or refused till today due to the difficulty to measure the second viscosity. Experiments, indicate that it still remains valid but only for monoatomic gases Prangsma et al. (1973). For most of the applications for Newtonian fluids, the deviatoric stress tensor is given by

$$\tau_{ij} = 2\mu S_{ij} - \frac{2}{3}\mu \delta_{ij} S_{kk} \tag{4.4}$$

From its definition $\tau_{kk} = 0$. The strain rate tensor is

$$S_{ij} = \frac{1}{2}(\frac{\partial u_i}{\partial x_j} + \frac{\partial u_j}{\partial x_i}) \tag{4.5}$$

From its definition, $S_{kk} = \partial u_k / \partial x_k$. The dynamic viscosity of the fluid is μ and δ_{ij} denotes the Kronecker symbol. In case of incompressible flow, $S_{kk} = 0$ and the deviatoric stress tensor reduces to

$$\tau_{ij} = 2\mu S_{ij} \tag{4.6}$$

4.1.2 Incompressible flow equations

Usually in multiphase flow modelling the pure atomisation process is studied under the incompressible assumption, where both the liquid and the gas are considered incompressible where the speed of the flow is much lower than the speed of sound ($M << 1$) in the domain. This hypothesis leads to the following reduced equations for the mass and momentum respectively

$$\frac{\partial u_j}{\partial x_j} = 0 \tag{4.7}$$

$$\rho \left[\frac{\partial u_i}{\partial t} + u_j \frac{\partial u_i}{\partial x_j} \right] = -\frac{\partial p}{\partial x_i} + \frac{\partial}{\partial x_j} \left(2\mu S_{ij} \right) + \rho f \tag{4.8}$$

In this thesis we mainly focus on the compressible formulation since we are interested in the flow inside the nozzle and downstream the nozzle exit where the jet vaporises and a significant amount of liquid becomes vapour. For detailed and simplified incompressible studies of atomisation the reader refers to Navarro-Martinez (2014); Pringuey (2012).

4.2 Pressure-velocity coupling

Once the problem is formulated, the equations must be solved iteratively. Regarding the way the flow parameters are updated, there are two generic strategies for iteratively solving the NS equations: the density-based and the pressure-based. The density-based strategy solves the set of equations such as continuity, momentum, and energy in a coupled manner. It's slower and memory intensive to solve because it solves all equations in one iteration. The pressure-based approach solves them in a segregated approach: first, it decouples the equations, then it solves the pressure-velocity coupling problem with applying various models. The density-based solver originally designed for high speed compressible flows. The pressure-based approach was designed for in-compressible and mildly compressible flow. Here, a segregated pressure-based approach is used for the development of a new solver. During the solution procedure, the discretised momentum equation leads to an equation that generally does not satisfy the continuity equation. Hence, a pressure correction has to be made in the solver prior to moving to the next time-step employing an coupling algorithm. Among the pressure-velocity coupling algorithms, three are the most commonly used in CFD:

- **SIMPLE**
- **PISO**
- **PIMPLE**

The first one, the Semi-Implicit Method for Pressure-Linked Equations (SIMPLE) algorithm was developed by Patankar (1980) for steady state problems and the discretised momentum equation and pressure correction equation are solved implicitly, while the velocity correction is solved explicitly. PIMPLE is a merger of the SIMPLE and PISO. The PISO algorithm (Pressure implicit with splitting of operator) was proposed by Issa et al. (1986) originally for solving compressible unsteady flows with large time steps. The matrix version of the momentum equation can be written as

$$AU = H(U) - \nabla p \tag{4.9}$$

Here A, H are matrices which contain all the terms of the momentum equation apart from the pressure gradient. The matrix $H(U)$ is updated using the latest velocity field U. The momentum correction for the new pressure can be given from

$$U = \frac{1}{A}(H(U) - \nabla p) \tag{4.10}$$

Then applying the continuity equation a correction for the pressure can be obtained. For instance, in the case of incompressible formulation $\nabla U = 0$ the above reads

$$\nabla \cdot \left(\frac{H(U)}{A} \right) = \nabla \frac{1}{A} \nabla p \tag{4.11}$$

At the n-th outer iteration, the algebraic equation to solve for a variable ϕ, at a central point P can be written in the matrix notation as

$$A_P \phi_P^{(n)} + \sum_{Nb} A_{Nb} \phi_{Nb}^{(n)} = Q_P \tag{4.12}$$

In the early outer iterations, instabilities might be induced due to potential large changes in Φ. In OpenFOAM both SIMPLE and PISO are subject to under-relaxation of the solution during each iteration. The new variable used in the iterations is

$$\Phi^{(n+1)} = \Phi^{(n)} + \lambda_\Phi (\Phi^{(pred)} - \Phi^{(n)}) \tag{4.13}$$

where λ_Φ is the under-relaxation factor, $0 < \lambda_\Phi < 1$. This step aims to boosting the diagonal term for the linear solver and iterate until convergence. Velocity can be relaxed in all the three major pressure-velocity algorithms. For pressure and the final iteration under-relaxation is not recommended. The values are typically stored at the cell-centre. The fluxes are also corrected using the interpolated values of A, H and pressure gradient at the cell faces

$$\phi^{corr} = S_f \cdot U_f = S_f \cdot \left[\left(\frac{H(U)}{A} \right)_f - \left(\frac{1}{A} \right)_f (\nabla p)_f \right] \tag{4.14}$$

The schematics of the SIMPLE and PISO is shown in the (Figure 4.1).

4.3 Resolved and under-resolved Scales

As far as numerical simulations' capabilities are concerned, great progress has been made recently including direct numerical simulation (DNS) of multiphase flows with interface capturing methods. Application of DNS to atomisation has led researchers to fathom the mechanisms of the process Lebas et al. (2009), Duret et al. (2012) and Duret et al. (2013). However, this type of simulations is too demanding regarding CPU resources making DNS prohibiting for practical industrial applications. A consensus has emerged to stress the necessity of a modelling approach that can be combined with DNS result to achieve advanced simulations for spray dynamics. New DNS results confirm the need to overtake the usual

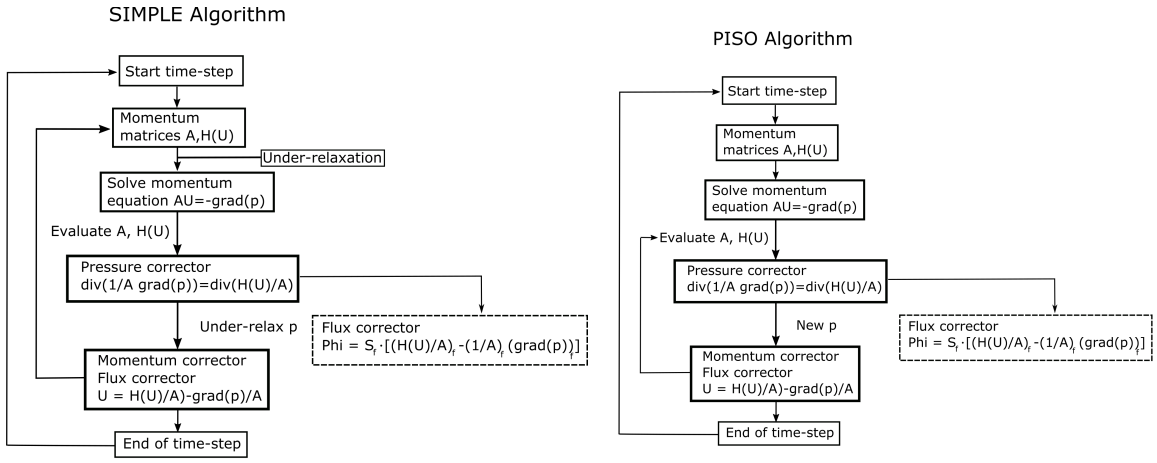

(a) SIMPLE.

(b) PISO.

Fig. 4.1 SIMPLE and PISO algorithms for pressure-velocity coupling.

assumption of "blobs hypothesis" where the injection is studied only downstream the channel exit with the discrete elements approach ignoring the flow history. This strong simplification can be avoided by replacing traditional droplet diameter by more general notion such as the liquid-gas surface density. Within this framework, it is possible to reproduce DNS result through a modelling approach that can be carried out in a much larger computational domain, up to a complete engine combustion chamber, for example with Reynolds-Averaged Navier-Stokes (RANS) method and with Large Eddy Simulation (LES). Such models rely on experiment and DNS result for validation and development.

4.3.1 Reynolds-Averaged Navier-Stokes (RANS)

Modelling and simulation of dispersed flows is challenging due to the existence of a wide range of length scales. This multi-scale nature of atomisation introduces a fundamental challenge to numerical simulations. A pathway to a comprehensive modelling is still to be found. The exact mechanisms of turbulence in multiphase flows are still under extensive study by experimentalists and CFD engineers. Changes in the mean Eulerian velocity due to the particles generated during the break-up can influence the mean strain field and turbulence produced in the system. The wake interaction of the dispersed phase and its contribution to the carrier-phase might be significant. Hibiki and Ishii (2000) showed that the wake entrainment contribution could be important to bubbly-to-slug transition. Acceleration of the carrier-phase behind solid droplets smaller than the Kolmogorov micro-scale η is reported by Sato et al. (1995) although it remains uncertain if the same stands for liquid droplets dispersed in a gaseous environment. Small particles moving through a gas flow seem that

they do not affect the flow. Increasing the particle size of the order of the Kolmogorov scale (which might be $\mathcal{O}(100)mum$ may lead to significant turbulence dissipation. As particle size increases, the effect of particle wakes plays a significant role, first decreasing the turbulence dissipation and eventually causing large turbulence augmentation.

For high Reynolds number flows containing a large number of particles, direct solution of the Navier–Stokes equations including a correct specification of the boundary conditions on each particle and resolution of all scales of the flow would require more computer resources that will be available for some time. Therefore, approximate models are required to represent either the particle-scale motions or the energy-containing turbulent scales. For spray simulations in the traditional RANS CFD modelling approaches, it should be understood that due to the probabilistic approach of the spray motion and the finite grid size of the calculations, many limitations are present. In a practical simulation, many droplets are contained within a given grid volume with a characteristic scale less than. The modelling assumptions, which determine the flow behaviour within each computational element, are thus very important. The limitations on grid size also affect the modelling of heat transfer, momentum exchange, and droplet phenomena at solid surfaces, e.t.c., therefore fine numerical resolution is important for reproducing the structure of sprays. RANS approach employs a time-average regarding turbulence, and consequently, only the mean statistics are predicted. Only an average turbulence length-scale and time-scale can be identified, but no eddy structures or dynamics are reproduced. RANS has been successful for modelling sprays and atomisation (De Luca et al., 2009; Lyras et al., 2017b; Saha et al., 2016; Vallet and Borghi, 1999). Internal flow simulations within nozzles and channels are also proven capable of simulating the two-phase mixture characteristics (Lyras et al. (2018a,b); Salvador et al. (2017)). Especially for the development of the non-spherical droplets model of $\Sigma - Y$ Vallet and Borghi (1999) used RANS as the main framework to construct an interface description where turbulence stretching is considered in the creation/destruction of the liquid/gas interface (more details on this on Chapter 6).

4.3.2 Large Eddy Simulation (LES)

Eddy-resolved simulations, a general family of methods that LES belongs in, predict at least some of the individual spatio-temporal features of the turbulent eddy structures (e.g., at least some of the turbulent eddies are resolved within the computational mesh). In the same group belongs the Direct Numerical Simulations (DNS) approach where turbulence is described for all eddy-containing wave numbers (spatial frequency), i.e., up to the wave number constrained by viscosity, but DNS is not considered in this research and will not be discussed further. In LES, the larger eddies, contain most of the energy, are mainly responsible for transporting

the conserved properties, and vary depending on the flow. Regarding the smaller scales (eddies), these are regarded as universal and less important and should be easier to model. Consequently, turbulence is only resolved up to some cut-off wave number $(1/\Delta)$, beyond which a sub-grid scale is employed. Also, hybrid RANS-LES techniques have been used, wherein only the separated flow regions are treated with an LES approach while attached flow regions are treated with a RANS approach. Scale separation in LES is predicated on Kolmogorov's theory for turbulent flow scales. Apart from the energy-containing range of scales, we have the universal equilibrium range. The universal equilibrium range can be divided to the: inertial range and dissipation range. The dissipation range of scales contains the smallest scales of turbulence (associated with Kolmogorov length scale η). The Kolmogorov micro-scale is defined as $\eta = (\frac{\nu^3}{\varepsilon})^{1/4}$. The inertia range lies in between the energy containing scales and the small scales where viscosity effects play a major role in the dissipation of the flow.

Filtering

In the context of LES for compressible flows, equations are filtered for simplification. In turbulent flows, the field properties become random functions of space and time. Hence, ll the primitive variables Φ like pressure and velocity, must be expressed as the sum of the mean $\bar{\Phi}$ and fluctuating parts Φ' (time or Reynolds averaging). Since here the flow is studied in the compressible, instead of the Reynolds average, the density-weighted filtering, known commonly as Favre filtering (also known as mass-weighted filtering) is employed to avoid the appearance of additional SGS terms when the compressible flow governing equations are filtered. Each variable Φ is split into an averaged $\bar{\Phi}$ and a fluctuating part Φ''. The Favre-averaged value, $\tilde{\Phi}$ is then

$$\tilde{\Phi} = \frac{\overline{\rho\Phi}}{\bar{\rho}} \tag{4.15}$$

The resolved part of each variable, except pressure, is the $\tilde{\Phi}$ and its difference with average value gives the fluctuating part, $\Phi'' = \Phi - \tilde{\Phi}$ resulting to simpler experessions for the conservation laws because of the interesting properties of the operator[2].

Regarding the spatial filtering, since only the large scale components of the total field are needed, a filtering operation for this field is applied. The filtered quantity is obtained by applying a filtering function $G()$ given by the following convolution product

$$\tilde{\bar{\Phi}} = \int_V G(x - x_i)\Phi(x_i, t)\mathrm{d}x \tag{4.16}$$

[2]In contrast to Reynolds averaging, the average of the Favre fluctuation is not zero: $\bar{\Phi''} \neq 0$, but $\rho\bar{\Phi''} = 0$

Typically, the box filter and the Gaussian are used successfully in various engineering problems. The box filter is used for this study and reads in one-dimensional notation

$$G(x-x_i) = \begin{cases} \frac{1}{\Delta} & \text{if } |x-x_i| \leq \frac{\Delta}{2} \\ 0 & \text{if otherwise} \end{cases} \tag{4.17}$$

The filter Δ is calculated using the local mesh resolution, which for 3D domains reads

$$\Delta = \sqrt[3]{\Delta x \Delta y \Delta z} \tag{4.18}$$

Some examples of LES applied to atomisation have been presented by various authors for typically small domains of some millimetres (Irannejad and Jaberi, 2014; Navarro-Martinez, 2014; Pringuey, 2012). Usually, the jet that is studied is injected as blobs or directly from an inlet patch and LES resolves the eddies utilising a sub-grid scale model accounting for energy flux at the unresolved scales and the proper representation of the SGS stress tensor. Due to the fine grid resolution needed in LES, this approach is applied for the early stage of primary atomisation, offering a more detailed description of the near injection fluid motion, rather than for simulating the entire atomisation process.

4.4 Liquid/gas Interface tracking

The study of multi-fluid and multi-phase systems has a great interest in academia and industry. In case of immiscible fluids, e.g. liquid and gas, usually, the two-phases co-exist forming interfaces which significantly change in time and space. A typical example of liquid-gas interface is the free-stream flows, ocean waves or a non-evaporating jet. Regarding cavitating jets, more challenging flow regimes like bubbly or annular are likely to exist, and hence it is possible to have interfaces non only at the free surface of the jet but also within the liquid bulk Figure 4.2. There are two types of interface tracking in CFD, e.g. the explicit and implicit approaches. In this section, only some of the most popular methods are described. Additional methods for interface tracking that are less applicable in simulating atomisation, such as the immersed boundary (IBM) and boundary integral (BI) methods or those that do not belong in the above classification like mess-less methods (e.g. smoothed particle hydrodynamics, SPH) are present in the literature for atomisation.

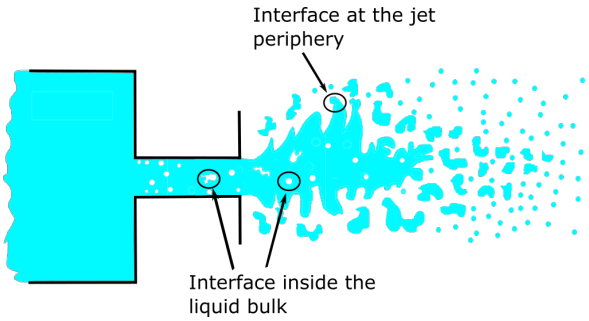

Fig. 4.2 Illustration of the liquid/gas interfaces forming in a jet when boiling occurs.

4.4.1 Explicit approaches

The most popular explicit method for capturing the interface in multiphase flows is probably the front-tracking method. The interface is represented by a moving front with a connected set of points, which forms a moving internal boundary. The governing equations are solved on a fixed grid but the phase boundary is represented by a moving front, consisting of connected marker points. The capillary forces are represented by the CSF model that will be described in the next section, and interpolated to the fixed grid. After calculating the velocity of the sharp interface, the moving front is advected in space. The method was first introduced by Glim et al. (1986) and was extended in 3D by Unverdi and Tryggvason (1992). Applications of the method for atomisation have been presented in Tryggvason et al. (2001).

Moving mesh methods also fall into the category of explicit calculation of the interface. The Arbitrary Lagrangian-Eulerian Method (ALE) by Hirt et al. (1974) is the most important one. ALE method adopts a finite difference mesh with vertices that move arbitrarily avoiding the mesh to become highly distorted which might lead the computations to diverge. In the ALE approach, the convective terms are solved separately from the other terms and each computational time-step has a Lagrangian phase and a Eulerian phase. In the Lagrangian phase, the computational mesh moves with fluid velocity, so the convection terms are not solved. In the rezoning phase, the vertices of the computational mesh are moved back to their original locations, and the convective fluxes are computed.

4.4.2 Implicit methods for calculating the interface

In this class of methods, a fixed mesh is used in all the calculations, and the interface is tracked using a scalar field advected in space. The scalar field (marker) has to be intrinsically connected to the absence or presence of the liquid phase. These methods are easily extended in three dimensions but might require fine meshes to resolve the interface. The same limitation stands for the front-tracking methods. The most commonly cited implicit methods are the

Volume-of-Fluid method (VOF) and the Level-Set method which are going to be described next.

Volume-of-Fluid (VOF) method

This method captures the interface through solving the transport of the marker function in the computational domain. The marker function typically used in commercial software is the volume fraction of the liquid phase. The volume fraction represents the volume occupied by the liquid phase in space within the computational cell. In two dimensions the marker function is the surface area (Figure 4.3). In its simplest form, VOF assumes that the volume occupied inside a computational cell of arbitrary shape can be occupied by liquid or gas. The volume fraction in case of dispersed flows is not a continuous and cannot be defined at one point. Its formal definition (in numerics or experiment) for the continuous phase is,

$$\phi = \lim_{\delta V \to V_o} \frac{\delta V_\phi}{\delta V} \tag{4.19}$$

where δV_ϕ is the volume of the continuous phase inside the cell. The limit V_o is a volume introduced here to ensure a stationary average of the volume fraction accounting for the variations in the volume due to the dispersed phase, for instance bubbles (Crowe, 2005). Similar expression can be induced for the definition of the volume fraction of the gaseous phase. Each computational cell is assigned a value for liquid volume fraction between 0 and 1. Hence, it is,

$$\phi = \begin{cases} 0 & \text{for liquid} \\ \in (0,1) & \text{at the interface} \\ 1 & \text{if gas} \end{cases} \tag{4.20}$$

The method has the advantage that is mass-conservative for each phase, and the change of topology is implicit which means that no special operations are necessary for interface reconnection or break-up. After advecting the volume fraction, the surface can be locally reconstructed. Various methods can be used for reconstructing the interface in the Volume-of-Fluid method. The most popular are the simple line interface calculation (SLIC), the piecewise linear interface calculation (PLIC) and the piecewise parabolic interface calculation. These are employed for the curvature calculation locally. The disadvantage of this method is that the curvature has to be calculated properly, otherwise inaccurate curvature might result in spurious oscillations. This poses a limitation the radius of curvature not to be less than the order of the grid size (at the sub-grid scale). VOF method has been implemented

in all major software, and many VOF implementations exist in the literature regarding the application of the method in cavitation and atomisation. In the most recent detailed numerical studies, (Edelbauer, 2017; Ishimoto et al., 2008; Srinivasan et al., 2010) have used VOF for both processes offering descriptions of the cavitating jets emerging from nozzles. No applications of Volume-of-Fluid or Level-Set are reported for simulating flashing jets. A different Volume-of-Fluid approach implemented in this thesis will be described in the next chapter.

Level-Set (LS) method

The Level-Set formulation is utilised transporting a continuous function like in Volume-of-Fluid method. LS has been developed at Osher and Sethian (1988) as an alternative to the Volume-of-Fluid method. The method gives an accurate representation of the liquid-gas interface and the interfacial normal and curvature. One common characteristic of this method and VOF is that the user does not interfere in the method no matter the complexity of the geometry since both VOF and LS adjust naturally to any topological changes. One of the main differences of those two is the transition from the liquid to gas which in Level-Set method occurs gradually instead of the Volume-of-Fluid where the interface exists in a one-cell layer in between the two phases. The marker function in Level-Set is a function $\chi(x,t)$ which represents the interface between the liquid and the gas. Depending on whether a given point (x,t) belongs in one phase or the other, $\chi(x,t)$ is defined as

$$\chi(x,t) = \begin{cases} +d, & \text{x} \in \text{liquid} \\ -d, & \text{x} \in \text{gas} \end{cases} \tag{4.21}$$

We have defined here the function χ to be positive in the liquid and negative to the gas phase (Figure 4.3). Level-Set function is then a distance function that is defined wherever an interface exists. The distance function is advected from,

$$\frac{\partial \chi}{\partial t} + u \cdot \nabla \chi = 0 \tag{4.22}$$

where u is the velocity field. The above equation can be solved using any high order scheme for hyperbolic systems of the (essentially non-oscillatory) ENO schemes family or Runge-Kutta Liu et al. (1994). Although the distance function is advected well for $\chi = 0$, it tends to fail remaining an actual distance function. Consequently a re-initialisation step is required

for the χ-equation. This is achieved by solving the following Eikonal equation,

$$\frac{\partial \chi_d}{\partial \tau_d} = \mathrm{sgn}(\chi)(1 - |\nabla \chi_d|) \tag{4.23}$$

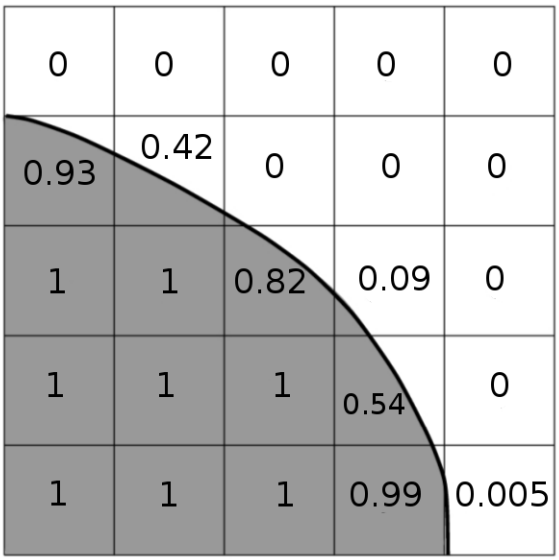

(a) VOF:The liquid volume fraction is the marker.

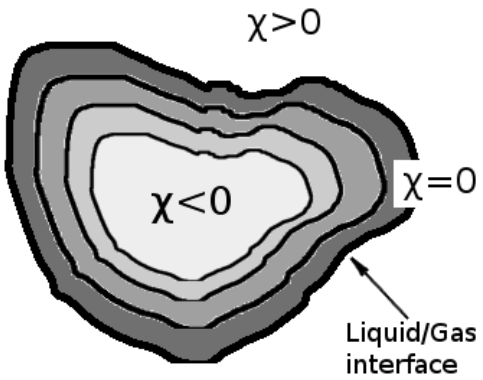

(b) LS:The marker function is the distance.

Fig. 4.3 Schmatics of Volume-of-Fluid and Level-Set methods for tracking the interfaces.

where χ_d is the new corrected distance function, and χ the old value used for initialisation, $\chi_d(t=0) = \chi$. The sign function, $sgn()$ is defined as,

$$sgn(\chi) = \begin{cases} -1, & \text{for } \chi < 0 \\ 0, & \text{for } \chi = 0 \\ 1, & \text{for } \chi > 0 \end{cases} \tag{4.24}$$

Here τ_d is a fictitious time-step which can be associated to the grid resolution (here we consider $\tau_d = 0.1\Delta x$. The re-initialisation equation can be solved in steady state and ideally converges to $\nabla \chi_d = 1$. Despite its efficiency in calculating the interface, Level-Set method has the shortcoming that mass conservation is not guaranteed. This barrier can be overcome with coupling the method with the Volume-of-Fluid approach which is conservative, and the Level-Set which is highly accurate. This idea was implemented first by Bourlioux (1995) and Sussman and Puckett (2000) giving a new method, the coupled Level-Set-Volume-of-Fluid a.k.a. CLSVOF method. Olsson and Kreiss (2005) has developed a conserved level-set method which has shown the ability to conserve mass. This has been the basis of different

variations of the Level-Set method which has been used in liquid atomisation (Desjardins, 2008; Pringuey, 2012).

4.5 Numerical capabilities and OpenFOAM

OpenFOAM software was originally developed by Henry Weller at Imperial College in London Weller et al. (1998). This is a computational fluid dynamics code written in C++ offering a large range of capabilities. The most important feature is that, unlike other commercial CFD codes, the software gives free access to the user to read, understand and modify its code giving the opportunity to develop utilities for pre/pro-processing, meshing, data analysis. The user has the ability to modify the code and develop new solvers for high performance for solving the specific problem owing to the demands of industry which need taylor-maybe CFD solutions appropriate for the complex physics of the application and rather than codes which despite their documentation remain black-boxes. OpenFOAM uses finite-volume numerics on arbitrary shaped unstructured meshes and therefore can handle complex geometries easily. Other important features are its parallelisation and turbulence modelling. Over the years, even though the OpenFOAM team has split, the distribution of the code is still free to anyone for use and contribution and has improved a lot minimising any bugs existed in the first versions, utilising new solvers and tools. In particular, for this research, both the foundation version and the extended version have been used.

Some of the capabilities of OpenFOAM software were described in this chapter briefly focusing on the methods and models that are related to the contribution of this research. In this way it is easier for the reader to understand the novel implementations in the next chapters. To this direction, the PISO/PIMPLE algorithms and the VOF method which are modified next allowing to track the differences with the standard OpenFOAM. No changes in the numerical schemes and turbulence models are implemented and consequently are not described in this chapter. A discussion in each chapter of simulations in included for the discretisation schemes for the varius advection, diffusion and interpolation terms and turbulence models that were employed.

4.6 Concluding remarks

The chapter addresses the fundamentals of the most important numerical aspects of the methodology that has been developed in this thesis. In addition to the compressible Navier-Stokes equations, interface tracking is also included in the momentum equation, and a discussion for the interface tracking techniques is included since a different Volume-of-Fluid

approach implemented in this thesis will be described in the next chapter. The developed methodology employs a pressure-based approach where the equations for the fluid motion are solved in a segregated approach. The pressure-velocity coupling algorithm is an integral part of the methodology, and the most popular ones are discussed. Based on the standard PIMPLE algorithm, new modifications for simulating flashing will be proposed in the next chapter.

Chapter 5

Development of a method for modelling flash-boing in three dimensions

Modelling and simulating the rapid pressure drop inside nozzles is a significant challenge because of the complexity of the multiple associated phenomena. In this chapter, a novel methodology is discussed for calculating the phase change within various nozzle geometries undergoing rapid pressure drops developed in the frame of the open source Computational Fluid Dynamics (CFD) code OpenFOAM. A new solver is developed called FlashFOAM in a compressible framework, that accounts for the inter-phase heat transfer with the Homogeneous Relaxation Model (HRM). The work describes the development of a pressure equation within a different formulation than in other studies. The surface forces due to liquid-gas interfacial instabilities are modelled here in a novel coupling of HRM with the volume of fluid method giving rise to a conservative method for modelling primary atomisation. This new pressure equation is validated with published experimental measurements. A validation series dedicated to long nozzles is included for the first time. Novel additional tests for the flow characteristics and vapour generation in cryogenic liquid cases are included showing that the solver can be employed to gain some new insights into the physics of the flow regimes of sudden depressurising cryogenic liquids. The dependency of the geometry of the nozzles, pressure and sub-cooled degree on the vapour generation have been analysed including the effect of turbulence on the nozzle flow avoiding the laminar flow scenarios of previous validation studies. The validation study has demonstrated that FlashFOAM can be used to simulate flash boiling scenarios accurately and predict the properties of flash atomisation.

5.1 Multiphase mixtures inside channels

Flashing is a complex process involving multiphase flows that usually occurs during the sudden depressurisation of a fluid stored under high pressure and high temperatures. Typical industrial scenarios involve accidental releases through cracks in pipes and vessels. Other applications include fuel spray atomisation during injection in internal combustion (IC) engines and loss of coolant accidents in nuclear power plants. In all these cases, the release results in a spray at the nozzle exit which disperses following turbulent mixing, aerodynamic breakup and droplet collisions. The whole process of flashing is not entirely understood experimentally, but in general, its stages are divided into nucleation, bubble growth, and atomisation Oza (1984). Flashing can occur either inside or outside the nozzle depending on the local pressure and geometry among others, and the vapour generation leads to interfacial interactions that eventually influence the spray properties.

5.1.1 Critical mass flow rate calculation

A key aspect of flashing is bubble nucleation. The flashing phenomenon may happen in the case of a superheated or a sub-cooled liquid following either an isothermal or an isobaric process which corresponds to a metastable state where liquid and vapour co-exist. Flashing inception starts when, inside the saturation dome, the liquid exists in a metastable state. Bubble formation and growth in two-phase mixtures within nozzles have a significant impact on the atomisation and the spray dynamics. Depending on the vaporisation rate and conditions the flow pattern might be bubbly, slug or annular. Sher et al. (2008) and Park and Lee (1994) provided a detailed regime analysis. They also successfully predicted the mass flow rate and the resulting jet dispersion. A successful modelling strategy must be able to capture the changes in the primitive flow variables and consequently the mass flow rate inside the channel. As long as the pressure gradient tends to minus infinity within the channel, Mach number increases towards the sonic condition, when the flow is characterised as critical. The study of this condition is a major topic in cavitation and flashing and is thoroughly examined in this chapter. Different modelling strategies have been developed for simulating flashing flows inside pipes. If the bubble distribution is such that there is no or very little relative velocity (slip velocity) between the two phases, then the flow can be considered homogeneous and if the slip velocity cannot be ignored the flow is separated. Homogeneous Equilibrium Model (HEM) is the most common critical flow model which assumes zero slip velocity. It assumes that mass, momentum and energy transfer between the phases happens rapidly enough so that equilibrium is reached. The HEM model seems to work very well in non-isentropic liquid expansion cases and long pipes where the flow has sufficient time to

reach equilibrium Salvador et al. (2017). However, the predicted mass flow rates can be very large compared to experiments, and in cases of short nozzles where there is not sufficient time for vapour generation to reach equilibrium, the difference between the prediction and the exact value can be 25% according to Schröder and Vuxuan (1987). An improvement was proposed by Fauske (1962) taking into account the slip (velocity) ratio, $\mathscr{S}$, estimating that the maximum mass flow rate is achieved at $\mathscr{S}^{1/2}$ using momentum balance at the nozzle exit. Along the same direction, Moody (1965), using an energy balance, proposed that the maxima of mass flow rate occur at $\mathscr{S}^{1/3}$. Deviations with the actual experimental critical mass flow rates exist using these models, with the calculated values being usually higher than in HEM, and with unphysical values for $\mathscr{S}$. In the models of Fauske and Moody, mass flow rate estimation is treated in the same way for short and long nozzles e.g. by extracting from a formulation that includes only the thermophysical properties of the fluid which are usually stagnation pressure and degree of superheat (or sub-cooling). Zaloudek (1964) and Xu et al. (1995) among others showed that the geometry could play an important role in the case of depressurisation inside pipes. In such cases, the above mentioned models fail to predict the experimental mass flow rates resulting in under-predictions, which can be attributed to the underlying assumption of thermodynamic equilibrium, which is a convenient approach that leads to a set of equations that under certain circumstances can be solved for the multiphase flow across the nozzle. For example, in HEM one might obtain a one-fluid formulation suitable for small-scale cavitating flows. The latter is commonly used in some open source CFD codes (Karrholm (2008)).

One of the most widely known and among the oldest models for thermal non-equilibrium in two- phase critical discharges was proposed by Henry (1970) who considered the flow as frozen and hence no phase change occurs, a concept that could be valid for small flow time-scales like within short nozzles. The non-equilibrium is handled with a coefficient which is a function of the fraction of the equilibrium vapour. Downar-Zapolski et al. (1996) proposed the Homogeneous Relaxation Model (HRM) which accounts for the non-equilibrium vapour generation. The model estimates the rate of change of the local vapour quality. The concept of the relaxation term which has its origin back to Einstein (1920) work for sound propagation in dissociated gases and others, expresses a physical reality, i.e. the instant vapour mass fraction would relax to the equilibrium value over a proposed time-scale. The values of the time-scale are linked to the interphase mass transfer in a way that will be described in the next section. The model might have a behaviour similar to the frozen flow model or the HEM depending on whether the time-scale for relaxation is high or low. Although older modelling approaches were based on an 1-D thinking, when moving to multidimensional modelling,

the HEM and HRM are in reality only homogeneous on the sub-grid scale level, which is less restrictive than 1- D.

5.1.2 Mass, momentum and energy equations

The following equations of mass and momentum are solved in a fully Eulerian framework. The liquid and vapour phases are considered to have the same velocity. The enthalpy equation is dropped in isenthalpic simulations. The compressible formulations used follow that of Prosperetti and Tryggvason (2009),

$$\frac{\partial}{\partial t}\int \rho \mathrm{d}V + \oint \rho u \cdot n ds = 0 \tag{5.1}$$

$$\frac{\partial}{\partial t}\int \rho u \mathrm{d}V = -\oint (\rho u \otimes u)\cdot n ds - \oint \tau \cdot n ds - \int p \mathrm{d}V + \int F_\sigma \mathrm{d}x \tag{5.2}$$

The differential form for the above is then

$$\frac{\partial \rho}{\partial t} + \frac{\partial \rho u_j}{\partial x_j} = 0 \tag{5.3}$$

$$\frac{\partial \rho u_j}{\partial t} + \frac{\partial \rho u_i u_j}{\partial x_j} = -\frac{\partial p}{\partial x_i} + \frac{\partial \tau_{ij}}{\partial x_j} + F_\sigma \tag{5.4}$$

An equation for energy is added to the solver. Including enthalpy into the calculations, the energy equation becomes

$$\frac{\partial \rho h}{\partial t} + \frac{\partial \rho u_j h}{\partial x_j} = \frac{Dp}{Dt} + \frac{\partial}{\partial x_j}\left(a_{eff}\frac{\partial h}{\partial x_j}\right) + \tau_{ij}\frac{\partial u_i}{\partial x_j} \tag{5.5}$$

The last term is the shear heating, $\tau : (\nabla \otimes u)$ expressing the irreversible energy in the system by viscous dissipation. This term is only significant in cases of large velocity gradients (Bird (1960)). Additionally, an equation for tracking the mixture is solved

$$\frac{\partial \rho \gamma}{\partial t} + \frac{\partial \rho u_j \gamma}{\partial x_j} = \frac{\partial}{\partial x_j}\left(\frac{\mu_t}{Sc_t}\frac{\partial \gamma}{\partial x_j}\right) \tag{5.6}$$

The variable γ denotes the liquid and vapour phase in a computational cell. The non-condensible gas (air) is then defined as $1-\gamma$. The present method takes into account three phases, liquid, vapour and non-condensible gas. The liquid and the gaseous phases are considered immiscible. The computational cell contains non-condensible gas when $\gamma \neq 0$.

5.1.3 Volume-of-Fluid method (VOF)

In cases of sudden depressurisation through pipes, cavities are generated at the sharp inlet corners extending up to the nozzle exit. The surface forces due to the liquid-gas interfacial instabilities are modelled here. A VOF method to capture the interface between the liquid and gas phases is implemented. Resolving the surface forces is important in many situations including cases of cavitating cryogenic liquid (Ishimoto et al. (2008)). VOF methods can resolve the inter-phase dynamics offering an explicit update for the evolution of liquid-gas mixture inside the nozzle. The method can aid the understanding of the cavitating/flashing jets mechanism. Previous methods of coupling HEM with VOF are reported (Srinivasan et al. (2010)). Here the HRM is coupled with VOF in a novel formulation. A different VOF approach from the one that is already embedded in OpenFOAM , has been adopted in the present study. Instead of solving a transport equation for liquid volume fraction, ϕ_l, the liquid mass fraction is employed after solving the equation for the vapour quality with the use of the HRM (equations are solved in a segregated approach). The liquid volume fraction is then updated offering a compressible VOF formulation (Jiang et al. (2010)). In this approach, inside a computational cells both the liquid, its vapour and the ambient air can be present. The advantage is that the amount of the vapour is not calculated for a transport equation only, but via the HRM which gives a representation for the interfacial mass transfer at the sub-grid scale. In the present study, the following expression is used,

$$\phi_l = \frac{\gamma(1-x)(\rho_l - (\rho_l - \rho_v)x}{\rho_l} \tag{5.7}$$

The surface tension force needs to be explicitly estimated but the location and shape of the surface between the liquid and gas phase are not explicitly known. The classic continuum surface force (CSF) of Brackbill et al. (1992) is used and represents the surface tension impact as a continuous volumetric force acting within the interface. The force is given by,

$$F_\sigma = \sigma\kappa\nabla\phi_l \tag{5.8}$$

where with σ is denoted the surface tension of the liquid and κ corresponds to the curvature of the interface and is given by,

$$\kappa = -\nabla \cdot \frac{\nabla\phi_l}{|\nabla\phi_l|} \tag{5.9}$$

Regarding the liquid jet atomisation various key factors are usually studied, with traditional CFD codes focusing on the turbulence and aerodynamic break-up neglecting the effect of cavitation. Liquid-gas interface observed inside the nozzle is present in numerous industrial

scenarios with plenty of possible flow regimes. One of the goals of the current work is to point out the occurrence of these interfaces (indicated by the existence of vapour inside the channel) and highlight its importance on the atomisation process. The importance of the liquid-gas interface capturing is also reported for the internal flow and the atomisation region for resolving the break-up process by other numerical studies implementing the VOF method (Edelbauer, 2017; Ishimoto et al., 2008). VOF is capable of revealing more insights in the spray region as well as upstream the nozzle exit allowing the modelling of the primary atomisation and secondary break-up in a volume conservative way.

5.1.4 Thermal non-equilibrium phase change

The vapour mass fraction (denoted as x hereafter) is calculated for both the internal flow and the atomisation region. Introducing the transport equation in a compressible framework with a mixture density ρ and a velocity field u_j it is given as,

$$\frac{\partial \rho x}{\partial t} + \frac{\partial \rho u_j x}{\partial x_j} = \Gamma \tag{5.10}$$

The term Γ stands for the vapour generation rate. Vapour mass fraction is changing through time and space and needs to be modelled for closure. Following Downar-Zapolski et al. (1996), as first approximation, x can be assumed to relax towards an equilibrium value, x_{eq} at a time-scale Θ that is locally dependent on pressure. The HRM is written in the following way,

$$\Gamma = -\rho \left(\frac{x - x_{eq}}{\Theta} \right) \tag{5.11}$$

This is first order approximation to Γ using Taylor series expansion. This formulation attains an exponential tendency for the system from an initial state x_0 to equilibrium through time,

$$x = x_{eq}(1 - e^{-\frac{t}{\Theta}}) + x_0 e^{-\frac{t}{\Theta}} \tag{5.12}$$

The idea of the relaxation to equilibrium has been successfully employed before by Einstein (1920) and Bauer et al. (1976) among others and expresses a physical reality for the complex interfacial mass transfer. The model assumes that the slip velocity is zero. Both isentropic and isenthalpic assumptions can be used for determining x_{eq}. Experimental work of Reinke and Yadigaroglu (2001) indicates a better matching with experimental data is achieved with the isenthalpic condition in cases of sudden depressurisation of superheated liquids. The equilibrium value for the vapour mass fraction can be calculated as,

$$x_{eq} = \frac{h - h_{l,sat}}{h_{v,sat} - h_{l,sat}} \tag{5.13}$$

In this formulation, $h_{l,sat}, h_{v,sat}$ are the saturated enthalpies of liquid and vapour state. The time-scale for the model is calculated as,

$$\Theta = \Theta_0 \alpha^{-0.257} \psi^{-2.24} \tag{5.14}$$

The non-dimensional pressure ψ is equal $(p_{sat} - p)/p_{sat}$. The time-scale Θ_0 is a constant of the model, $\Theta_0 = 6.51 \times 10^{-4}[s]$ and the void fraction α is calculated from the local densities as,

$$\alpha = \frac{\rho_l - \rho}{\rho_l - \rho_v} \tag{5.15}$$

where ρ_l and ρ_v are the liquid and vapour densities. The dimensionless pressure denoted with ψ is defined as,

$$\psi = \left| \frac{p_{sat} - p}{p_{sat}} \right| \tag{5.16}$$

Equations (5.14) and (5.16) have been derived from Downar-Zapolski et al. (1996) for water jets at initial pressure up to $10bar$. It is interesting that this correlation has been used and proven to work for other superheated liquids Lyras et al. (2018b) adding to the universality in this formulation. For pressures above $10bar$ the relaxation time can be written as,

$$\Theta = \Theta_0 \alpha^{-0.54} \psi^{-1.76} \tag{5.17}$$

The constants of the model change accordingly so that $\Theta_0 = 3.84 \cdot 10^7[s]$ and

$$\psi = \left| \frac{p_{sat} - p}{p_{crit} - p_{sat}} \right| \tag{5.18}$$

In their work, Downar-Zapolski et al. (1996) observed that for small pressures, the time-scale Θ takes values of the order of 1 s at the beginning, and monotonically decreases as the void fraction α and the non-dimensional pressure ψ increase. For the value $\alpha = 0.25$ signalled at high-gradient change in the relaxation time graph, where $\Theta \cong 0.1s$ and the transition for bubbly to plug regime is expected according to the authors observations.

5.2 Pressure-velocity coupling

The concept of the pressure equation is to create an equation that encapsulates all the processes involved in the fluid flow motion. The algorithm of Lee et al. (2009) and Schmidt et al. (2010) has been used as a basis. Since density is a function of pressure, temperature and quality, $\rho = \rho(p,h,x)$. Following Bilicki and Kestin (1990), the material derivative of density becomes

$$\frac{D\rho}{Dt} = \left(\frac{\partial\rho}{\partial p}\right)_{h,x}\frac{Dp}{Dt} + \left(\frac{\partial\rho}{\partial h}\right)_{p,x}\frac{Dh}{Dt} + \left(\frac{\partial\rho}{\partial x}\right)_{p,h}\frac{Dx}{Dt} \tag{5.19}$$

The continuity equation reads,

$$\frac{\partial\rho}{\partial t} + \frac{\partial\rho u_j}{\partial x_j} = 0 \tag{5.20}$$

Knowing that $\nabla\cdot(\rho u) = u\cdot\nabla\rho + \rho\nabla\cdot u$, combining with the continuity equation we get,

$$\frac{D\rho}{Dt} + \rho\frac{Du_i}{Dx_i} = 0 \tag{5.21}$$

Combining equations (5.21) and (5.19) we get

$$-\rho\frac{\partial u_i}{\partial x_i}\frac{D\rho}{Dt} = \left(\frac{\partial\rho}{\partial p}\right)_{h,x}\frac{Dp}{Dt} + \left(\frac{\partial\rho}{\partial h}\right)_{p,x}\frac{Dh}{Dt} + \left(\frac{\partial\rho}{\partial x}\right)_{p,h}\frac{Dx}{Dt} \tag{5.22}$$

Now, writing (5.4) in its discretised form for a fixed control volume V (i.e. cell) that is bounded by an arbitrary number N_f of cell faces. Given the surface area of a cell face S_f, its normal vector n_f and the definition of a face flux $\phi_f = \rho_f(u_f\cdot n_f)S_f$, the momentum equation can be written as

$$\frac{\Delta\rho u}{\Delta t}V + \sum_f^{N_f}\phi_f u_f = \sum_f^{N_f}(\tau\cdot n)_f S_f - \sum_f^{N_f}p_f n_f S_f + \sum_f^{N_f}(F_\sigma)_f S_f \tag{5.23}$$

The index in velocity is omitted for the sake of brevity. The discrete momentum equation (5.23) can be transformed into a linear system of equations that, for each computational cell center P surrounded by N_{nb} neighbouring cells, obtains a form:

$$a_P u_P + \sum_{nb}^{N_{nb}} a_{nb}u_{nb} = \text{RHS} \tag{5.24}$$

where the dimensions of the system have been changed due to a division by cell volume V_P. The right-hand-side (RHS) of the equation contains the source contributions arising from the discretisations of the transient, convection and diffusion terms and the pressure gradient. For convenience, the contributions are split into velocity and pressure-dependent parts RHS $= \mathbf{rhs}(u) - \nabla p$, keeping in mind that

$$\tau = \nabla \cdot 2\mu D - \mu(\nabla \cdot u)I \qquad \text{where} \qquad D = \frac{1}{2}[\nabla \otimes u + (\nabla \otimes u)^T] \tag{5.25}$$

and $\nabla p = (1/V)\sum_f^{N_f} p_f n_f S_f$. Here, $\mathbf{rhs}(u)$ denotes the terms in RHS that depend on velocity. Using short-hand notation the momentum equation can be written in a matrix notation according to Jasak (1996)

$$a_P u_P = H(u_j) - \frac{\partial p}{\partial x_i} + F_\sigma \tag{5.26}$$

where the index for velocity is included for the operations. In this formulation, a_P is the diagonal coefficients tensor for a cell P and $H(u_j)$ is the coefficient matrix for all the neighbours of p including other source terms except for pressure gradient. Solving for u_P gives

$$u_P = \frac{1}{a_P}H(u_j) - \frac{1}{a_P}\left(\frac{\partial p}{\partial x_i}\right) + \frac{1}{a_P}F_\sigma \tag{5.27}$$

Here, the velocity u_P is the velocity at the cell centre, which can be substituted with u_j without any confusion. Using (5.27) directly to (5.28) a matrix equation for pressure is obtained

$$\rho\frac{\partial}{\partial x_j}\left(\frac{1}{a_p}H(u_j)\right)_f - \rho\frac{\partial}{\partial x_j}\left(\frac{1}{a_p}\frac{\partial p}{\partial x_i}\right) + \rho\frac{\partial}{\partial x_j}\left(\frac{1}{a_p}F_\sigma\right) + \left(\frac{\partial \rho}{\partial p}\right)_{h,x}\frac{Dp}{Dt} + \left(\frac{\partial \rho}{\partial h}\right)_{p,x}\frac{Dh}{Dt} + \left(\frac{\partial \rho}{\partial x}\right)_{p,h}\frac{Dx}{Dt} = 0 \tag{5.28}$$

The operator $()_f$ stands for the interpolation to the cell faces. In cases of air entrainment to the mixture another term can be added to this last equation. Introducing an indicator function γ for the mixture (liquid and its vapour) ($\gamma = 1$ for no air and $\gamma = 0$ in case of no mixture) and substituting the HRM expression the pressure equation becomes

$$\rho\frac{\partial}{\partial x_j}\left(\frac{1}{a_P}H(u_j)\right)_f-\rho\frac{\partial}{\partial x_j}\left(\frac{1}{a_P}\frac{\partial p}{\partial x_i}\right)+\rho\frac{\partial}{\partial x_j}\left(\frac{1}{a_P}F_\sigma\right)+\left(\frac{\partial\rho}{\partial p}\right)_{h,x}\frac{Dp}{Dt}+\left(\frac{\partial\rho}{\partial h}\right)_{p,x}\frac{Dh}{Dt}$$
$$+\left(\frac{\partial\rho}{\partial x}\right)_{p,h}\left(\frac{x-x_{eq}}{\Theta}\right)+\left(\frac{\partial\rho}{\partial\gamma}\right)\frac{D\gamma}{Dt}=0 \tag{5.29}$$

The operator $()_f$ implies interpolation in the cell faces. This equation is used for the pressure update (without the pressure gradient correction) and includes the effects of the surface tension, thermal non-equilibrium and multiphase mixing as proposed by Lyras et al. (2018a). In cases of spray modelling, an additional term for thermal expansion is incorporated. For the derivation of this equation we used the work of Schmidt et al. (2010). The new term added in this thesis are the surface tension and multiphase mixing terms. Additionally the term for thermal expansion that was neglected from the Schmidt and co-workers is modelled here. This pressure equation makes no use of any equation of state. In fact, the material derivative expression is the EOS-equivalent for the two-phase mixture that takes into account thermal non-equilibrium at the pressure update. Since the HRM term is straightforward now, a few remarks about the other terms of the RHS of Equation (5.29) follow next for better understanding their contribution in the pressure calculation

Pressure term - Compressibility

The term which accounts for the transmission of the pressure waves is directly related to the compressibility via the following

$$\left(\frac{\partial\rho}{\partial p}\right)_{h,x}\frac{Dp}{Dt} \tag{5.30}$$

The first term in the above expression is the compressibility of the mixture, Ψ, which following the one -fluid approach, is takes values between the single-phase values. The compressibility of the $k-$phase is calculated from the speed of sound from

$$\Psi_k=\frac{1}{c_k^2} \tag{5.31}$$

The speed of sound in two-phase mixtures varies significantly across the domain and consequently the mixture compressibility also changes in case the flow becomes bubbly. Following Brennen (2013) Ψ is expressed via a simple weighted average which ensures that $\Psi_l<\Psi<\Psi_v$,that is

$$\Psi=(1-x)\Psi_l+x\Psi_v \tag{5.32}$$

For low Mach number flows, the pressure variations are $O(M^2)$ and the acoustic waves can be neglected. The term $\left(\frac{\partial \rho}{\partial p}\right)_{h,x}$ can be eliminated from the pressure equation.

Enthalpy term - Thermal expansion

The starting point to model the effect of the temperature change on density is the harmonic average of mixture density

$$\frac{1}{\rho} = y\left(\frac{x}{\rho_l} + \frac{1-x}{\rho_v}\right) + (1-y)\frac{1}{\rho_g} \tag{5.33}$$

Assuming that the vapour is following the ideal gas law and that thermal expansion effects are experienced only by the gas phase

$$-\frac{1}{\rho^2}\frac{\partial \rho}{\partial T} = -\frac{xy}{\rho_v^2}\left(\frac{\partial \rho_v}{\partial T}\right) - \frac{1-y}{\rho_g^2}\left(\frac{\partial \rho_g}{\partial T}\right) \tag{5.34}$$

Assuming the ideal law

$$-\frac{1}{\rho^2}\frac{\partial \rho}{\partial T} = -\frac{xy}{\rho_v^2}\left(\frac{-p}{RT^2}\right) - \frac{1-y}{\rho_g^2}\left(\frac{-p}{RT^2}\right) \tag{5.35}$$

which becomes

$$-\frac{1}{\rho^2}\frac{\partial \rho}{\partial T} = -\frac{xy}{\rho_v T} - \frac{1-y}{\rho_g T} \tag{5.36}$$

Finally the term in Equation (5.29) becomes

$$-\frac{1}{\rho^2}\frac{\partial \rho}{\partial T}\frac{DT}{Dt} = -\frac{xy}{\rho_v T} - \frac{1-y}{\rho_g T}\frac{\rho}{T}\frac{DT}{Dt} \tag{5.37}$$

The term $\frac{DT}{Dt}$ is included in the equation in an explicit way. In cases of adiabatic simulations, the term can be neglected.

Surface tension term

The surface tension term contribution is employed when the surface tension between the two-phases is important and can be written as

$$\rho\frac{\partial}{\partial x_j}\left(\frac{1}{a_P}F_\sigma\right) = \rho\frac{\partial}{\partial x_j}\left(\frac{1}{a_P}(\sigma\kappa)_f(\nabla\phi_l)_f^{\perp}|S_f|\right) \tag{5.38}$$

where the operator $()_f^{\perp}$ denotes the normal at the face of the cell.

5.3 Weighted properties in one-fluid approach

The term $\frac{\partial \rho}{\partial p}$ is the isenthalpic compressibility of the mixture and is the weighted average of the liquid and vapour compressibilities, Ψ_l, Ψ_v respectively, updated from the liquid and vapour speed of sound, c_l, c_v. For water these are almost constant, otherwise analytical expressions are used for single phases. Similar to the compressibility, density and viscosity of the mixture are also calculated as the weighted average of the single phases, following the one-fluid approach. Both the harmonic and mean average have been tested and implemented in the solver. For instance, the mean average for density is,

$$\rho = \gamma((1-x)\rho_l + x\rho_v) + (1-\gamma)\rho_g \tag{5.39}$$

The liquid and vapour densities in the mixture are related to pressure via the following equations,

$$\rho_k = \rho_{ref} + \Psi_k(p - p_{ref}) \tag{5.40}$$

where, ρ_{ref}, p_{ref} are used as a reference state for the densities. The rest of the mixture properties are calculated as in Lyras et al. (2018a).

5.4 Reynolds-Averaged Navier-Stokes (RANS)

Turbulence is modelled using the Reynolds-averaged Navier–Stokes (RANS) approach. Each variable Φ is decomposed to an averaged part $\bar{\Phi}$ and a fluctuating part Φ''. The mass weighted Favre averaged is $\tilde{\Phi} = \overline{\rho\Phi}/\bar{\rho}$. The continuity, momentum and energy equations can be written as,

$$\frac{\partial \bar{\rho}}{\partial t} + \frac{\partial \bar{\rho}\tilde{u}_j}{\partial x_j} = 0 \tag{5.41}$$

$$\frac{\partial \bar{\rho}\tilde{u}_i}{\partial t} + \frac{\partial \bar{\rho}\tilde{u}_j\tilde{u}_i}{\partial x_j} = \frac{\partial \bar{p}}{\partial x_i} + \frac{\partial R_{ij}}{\partial x_j} + F_\sigma \qquad \text{,where} \qquad R_{ij} = \overline{\rho u_i'' u_j''} \tag{5.42}$$

$$\frac{\partial \bar{\rho}\tilde{h}}{\partial t} + \frac{\partial \bar{\rho}\tilde{u}_j\tilde{h}}{\partial x_j} = \frac{D\bar{p}}{Dt} + \frac{\partial}{\partial x_j}\left(a_{eff}\frac{\partial \tilde{h}}{\partial x_j}\right) + \overline{\tau_{ij}\frac{\partial u_i}{\partial x_j}} \tag{5.43}$$

Additionally, the equation of the fuel mass fraction $\tilde{\gamma}$ is solved in order to include non-condensible gas effects. This is,

$$\frac{\partial \bar{\rho}\tilde{\gamma}}{\partial t} + \frac{\partial \bar{\rho}\tilde{u}_j\tilde{\gamma}}{\partial x_j} = \frac{\partial}{\partial x_j}\left(\frac{\mu_t}{Sc_t}\frac{\partial \tilde{\gamma}}{\partial x_j}\right) \tag{5.44}$$

The eddy or turbulent viscosity is defined as $\mu_t = \rho C_\mu k^2/\varepsilon$. The turbulent kinetic energy k and the turbulence energy dissipation ε are then calculated as,

$$\frac{\partial \bar{\rho}\tilde{k}}{\partial t} + \frac{\partial \bar{\rho}\tilde{u}_j\tilde{k}}{\partial x_j} = \frac{\partial}{\partial x_j}\left(\frac{\mu_t}{Pr_k}\frac{\partial \tilde{k}}{\partial x_j}\right) - R_{ij}\frac{\partial \tilde{u}_j}{\partial x_i} - \bar{\rho}\tilde{\varepsilon} \tag{5.45}$$

$$\frac{\partial \bar{\rho}\tilde{\varepsilon}}{\partial t} + \frac{\partial \bar{\rho}\tilde{u}_j\tilde{\varepsilon}}{\partial x_j} = \frac{\partial}{\partial x_j}\left(\frac{\mu_t}{Pr_\varepsilon}\frac{\partial \tilde{\varepsilon}}{\partial x_j}\right) - C_{1\varepsilon}\frac{\tilde{\varepsilon}}{\tilde{k}}R_{ij}\frac{\partial \tilde{u}_j}{\partial x_i} - C_{2\varepsilon}\bar{\rho}\frac{\tilde{\varepsilon}^2}{\tilde{k}} \tag{5.46}$$

The constants $C_{1\varepsilon} = 1.6$, $C_{2\varepsilon} = 1.92$, $C_\mu = 0.09$ and the classical Boussinesq eddy viscosity assumption are used. The SST-$k-\omega$ model of Menter (1993), which is expected to perform well in the near wall regions and used successfully by Liao and Lucas (2015a) for flashing inside long converging-diverging nozzle, has also been tested. The k-ε model was used for RANS in this chapter unless is specified otherwise for the cases that the SST-$k-\omega$ was employed.

5.5 Numerical implementation

The segregated approach has been used as the general framework for the present work. The equations are solved sequentially with the finite volume method. The described model has been developed within the framework of the open source CFD code OpenFOAM® (Weller et al., 1998). The solver can handle unstructured polyhedral meshes of arbitrary shape. All variables are stored in the centre of the control volumes. Splitting equations of conservation laws lagging inter-equation coupling terms is sufficient in many cases for subsonic and sonic flows. For the cases tested here, it is very likely to reach the choking conditions while transversing the pressure spectrum of the available experimental data. Since source term coupling plays an important role in the solution, a predictor-corrector step is used. The combination of the SIMPLE (Semi-implicit method pressure-linked equations) and the PISO (Pressure-Implicit with Splitting of Operators) algorithm is used to evaluate pressure. First, the discretised density equation is solved together with the quality equation. The finite difference representation of the convective and diffusive momentum fluxes, in order

to increase stability and accuracy, is split into the diagonal and non-diagonal parts. The discretised momentum equation is solved implicitly using the old pressure p^* and density,

$$a_P u_i^* = H(u_i) \tag{5.47}$$

The solution of this equation yields to a predicted velocity u_i^*. Following Issa et al. (1986) and employing the continuity equation, a pressure equation is constructed based on Eq. (17), which comprises the derivative of density with respect to the quality and the HRM term for the phase change as described in the previous section. Solving the Equation (5.29) gives the new pressure p^{**} .The solution is relaxed using the standard procedure explained in Patankar (1980). An under-relaxation factor of 0.4 is used for the current simulations for pressure. The new fluxes F are obtained after the non-orthogonal corrections from the following,

$$F = \left[\left(\frac{H(u_j^*)}{a_P} \right)_f - \left(\frac{1}{a_P} \right)_f \left(\frac{\partial p^{**}}{\partial x_i} \right)_f \right] \cdot S_f + \left(\frac{1}{a_P} \right)_f (\sigma\kappa)_f \left(\frac{\partial \phi_l}{\partial x_i} \right)_f |S_f| \tag{5.48}$$

where S_f is the face area vector. When the pressure equation is satisfied the above formulation is guaranteed to be conservative. The corrected velocity denoted with u_i^{**} is obtained explicitly from,

$$u_i^{**} = \left(\frac{H(u_j^*)}{a_P} \right)_f - \left(\frac{1}{a_P} \right) \left(\frac{\partial p^{**}}{\partial x_i} \right) + \left(\frac{1}{a_P} \right)_f (\sigma\kappa)_f \left(\frac{\partial \phi_l}{\partial x_i} \right)_f |S_f| \tag{5.49}$$

The PISO iterations used for the present work were no more than ten. After the latest pressure correction, the new velocity field is used to update the fluxes with the pressure gradient and the tensors $H(u_i^*), a_P$ so that Courant numbers larger than one can be accommodated. In this case, typically up to five PIMPLE iterations were needed and the CFL values were up to 2.5. The fluxes were calculated by interpolating the old values of velocity at the cell faces using a TVD scheme (Jasak et al., 1999). Regading the TVD schemes of OpenFOAM, the limited linear differencing scheme which is a bounded second order offered smooth convergence. The van Leer limiter TVD scheme was also proven to be efficient. A second order accuracy scheme that uses the least squares distance calculation for all neighbour cells was used for the gradient terms. The material derivatives added to the model introduce asymmetry, so a preconditioned bi-conjugate gradient method was used for velocity. The pressure boundary conditions are supposed to be fixed values for the inlet and a method that does not reflect waves described by Poinsot and Lelef (1992) was employed. Finally, fixed values for the inlet velocity and zero gradients for the exit velocity were imposed.

The single-phase properties were evaluated using the National Institute of Standards and Technology (NIST) database Linstrom and Mallard (2017). Important parameters like p_{sat} and σ that depend on pressure and temperature are included to the solver as exponential functions and averaged as in Eq. (18) following the one-fluid approach (Wen et al., 2013). The properties of the two-phase mixture inside the nozzle varied between the single phase values and a minimum value for pressure 1kPa was imposed for numerical purposes. The speed of sound of the mixture might also differ significantly across the computational domain. Vapour speed of sound is lower than the liquid speed of sound. For pure liquid the speed of sound limits to c_l and in case of bubbly cavitation is expected to be much lower than the single-phase.

5.6 Results and discussion for flashing water through nozzles

5.6.1 Validation

Different test cases for validation are investigated and presented in this section. Typical experimental apparatus for flash boiling experiments consists of a high-pressure storage vessel, a flow passage and a low-pressure plenum. The initial conditions are either superheated or sub-cooled. Inlet pressure is an important parameter since the local pressure decreases as the liquid approaches the nozzle exit. At some point, it drops below the local saturation pressure where flashing is initiated. The properties of water for the liquid and vapour phases (speed of sound, viscosity heat capacity e.t.c.) were almost constant or changed in a linear manner, for the experiments considered here, and were taken from Wagner and Pruß (2002) and IAPWS (1994). All the experiments considered for validation here were free of any dissolved gases prior to injecting the jet through the nozzle and the friction pressure drop was zero and consequently the validation scenarios have to do mainly with homogeneous nucleation. The experiments of Xu et al. (1995) are considered first. The experiments involved two- phase critical releases of pressurised water in sharp-edged tubes. The channel connecting the high and low-pressure domains has length L = 4.0 mm and diameter D = 4.05 mm. Initially the pressure is kept constant at 40 bar (4 MPa) and tests with different sub-cooling degrees are performed. The outlet pressure is 6.84 bar (0.684 MPa). An axisymmetric representation of the flow domain was used, using quadrilateral meshes of 24000 cells. The shape of the domain is shown in Fig. 5.1 Finer and coarser meshes with 60000 and 120000 cells were also used and results were found to be insensitive to grid resolutions. The present calculations for the fine meshes were performed in a 12-core personal workstation and the fine mesh solution

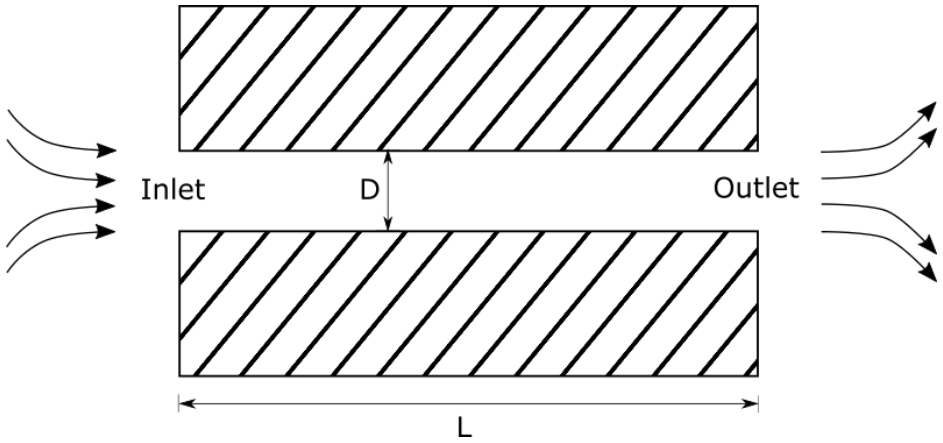

Fig. 5.1 Schematic of the flow domain for the experiments of Xu et al. (1995). Lyras et al. (2018a).

took approximately 1.5 days. Results for the calculated mass flow rates per area a.k.a. mass velocity are shown in Fig. 5.2 The mass flux is not derived from an explicit formulation: instead, it is given as the product of the mass- averaged velocity with the mixture density. The simulations are from the case of sub-cooling of 40^oC (313.16 K) up to the superheated case. In the latter case, the mass flux becomes minimum in both experiments and simulations and the results are in good agreement with the data with a difference less than 5 percent. An instantaneous axisymmetric contour of the density and void fraction is shown in Fig. 5.3 for the case of zero sub-cooling. It is evident that the vapour generation begins at the nozzle inlet, right after the geometry changes. This vapour annulus surrounding the liquid core is also reported for cases of low L/D by Henry (1970) and is also pronounced in cases of cavitation. The critical mass flow rates slightly increase by increasing the sub-cooling of the liquid in the storage conditions. Flow separation is observed downstream the inlet corner. In Fig. 5.4 the predicted mass flow rates are shown for a higher stagnation pressure of 160 bar (16 MPa). The pattern for the dependency on the sub-cooling is similar to the case of 40 bar (4 MPa) inlet pressure. The observed trends for these two cases imply that for small L/D the sub-cooling degree of the inlet liquid is less influential on the critical mass flow rates. On the contrary, this is not the case for larger L/D ratios where Xu et al. (1995) showed that for nozzles with ratios equal or larger than 9.68 the critical mass flow rates of the pressurised water gradually change, following a steeper trend up to liquid with a sub-cooling degree equal to 40^oC. Similar trends are also captured in the present study. Turbulent phenomena are expected to have impact on the mass flow rate at the exit but it is hard to quantify this dependency especially for small L/D where no dedicated studies exist for flashing. As shown in Fig. 5.4 the predictions for $k-\varepsilon$ and $SST-k-\omega$ are in good agreement with the measurements. Fig. 5.5 shows the velocities at the inlet and outlet of the nozzle for some of the cases

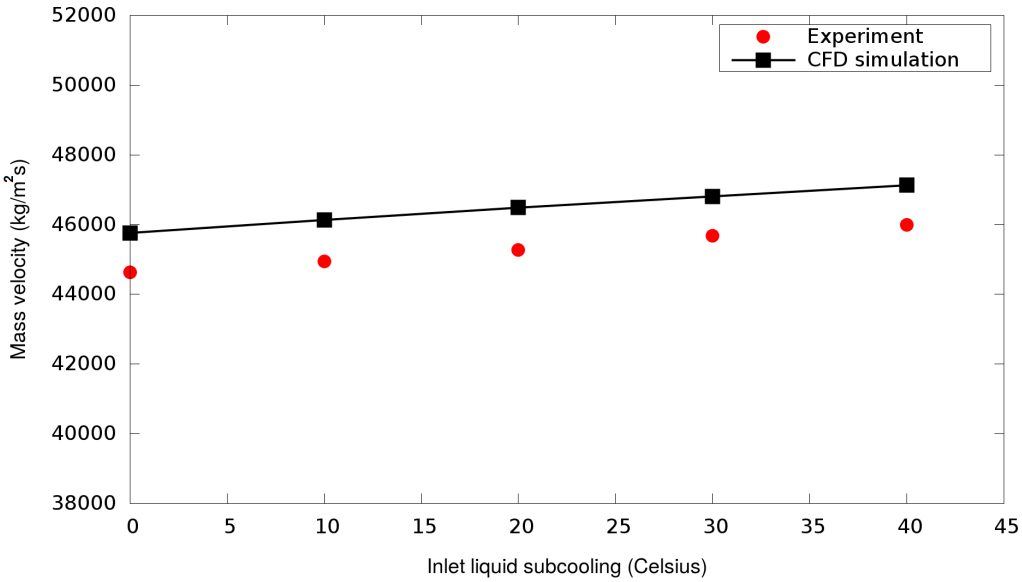

Fig. 5.2 Predicted mass flow rates per area for initial pressure equal to 40 bar compared to experimental data of Xu et al. (1995). Lyras et al. (2018a).

presented along the radial direction (R = D/2 is the radius of the pipe). The characteristic parabolic velocity profile, common in single phase flows, is encountered here. At the centre of the pipe (r/R = 0) the velocity has its maximum value. Moving towards the nozzle walls, the axial velocity gradually decreases reaching its minimum at the wall boundary. Since the pressure drops along the axial direction, the downstream velocities are higher than the upstream with a ratio upstream-to-downstream velocity equal to approximately 0.63. The observations stand both for sub-cooled and saturated flows, where velocity slightly changes. The peaks in the upstream velocities arise naturally due to the initiated cavitation caused by the flow separation shear layer at the low pressure area near the nozzle entrance.

The results presented so far are for flows with various sub-cooling degrees up to the saturated state. It is interesting to see how the presented method performs in only saturated inlet conditions. The results for the mass velocity for different initial pressures keeping the same nozzle as before are demonstrated in Fig. 5.6. As soon as the single-phase liquid core starts to flow towards the exit, the pressure drops, following a trend that will be discussed in more details next, resulting in a two-phase jet at the end of the nozzle. The flashing inception is triggered when the jet pressure drops below the local saturation pressure. As mentioned in the experimental work used here for validation, the metastability of the flow starts at this point. The exact point where the flashing starts is non-trivial to determine, and there is no general model to predict it in the literature without limiting assumptions. The results are in good agreement, with a CFD-to-experiment difference generally less than 7 percent. The

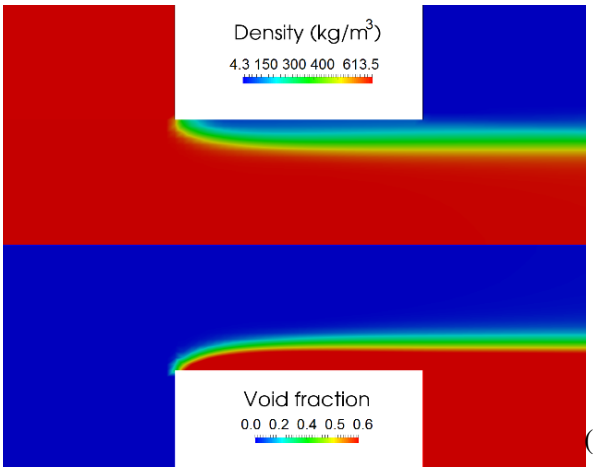

(a) Density and void fraction.

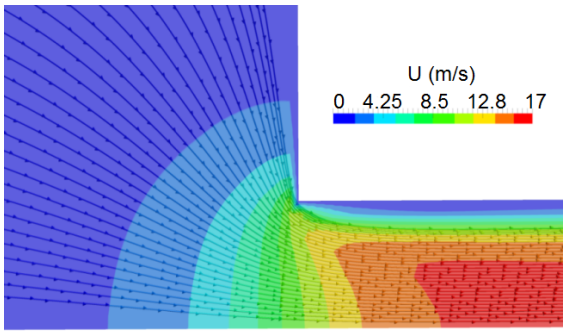

(b) Velocity contours and approximate streamlines.

Fig. 5.3 Predicted instantaneous contours of the mixture density, void fraction and velocity profile for the case of 40 bar at the saturated conditions with same configuration as in the experiment of Xu et al. (1995). Lyras et al. (2018a).

calculated void fraction is shown in Fig. 5.7. The void fraction is smaller in the centreline but increases closer to the wall as the result of the flow separation at the nozzle inlet. A qualitative perspective can be obtained from the void fraction, the pattern of which is more likely to change with increasing the ratio L/D as will be illustrated later. In all cases, the void fraction growth can be divided into three regions with respect to the distance from the centreline of the nozzle: from 0 to r/R equal to 0.15 it is almost constant, then increases on a log scale and from r/R between 0.8 and 1R grows fast to values that were usually around 0.45 in the nozzle inlet and close to the limit of unity at the nozzle end. In Fig. 5.8 the density distribution is shown for different inlet pressures. The density is subject to large variations at the nozzle exit. The large pressure gradient near the nozzle exit attenuates the counter-flow of the non-condensible gas and prevents the recirculation at the exit. Due to the high pressure and temperature, the flow is likely to choke. For the saturated cases choking occurred. Fig. 5.8 shows the density distribution for different inlet pressures. The patterns at the choking plane appear to be similar at the exit.

The test cases presented indicate bubble formation not only at the nozzle walls but also at the liquid bulk as reported also by Levy and Sher (2010). In the absence of impurities and wall roughness we focus on the homogeneous nucleation. In the work of Avedisian (1985) and Hutcherson et al. (1983) the homogeneous transition is explained in detail. The liquid pressure and temperature for a given mixture composition seem to play significant role in nucleation. Adopting the concept of departure diameter as the limit in bubble diameter above which the bubble leaves the nozzle wall (Hutcherson et al., 1983) we can interpret the effect

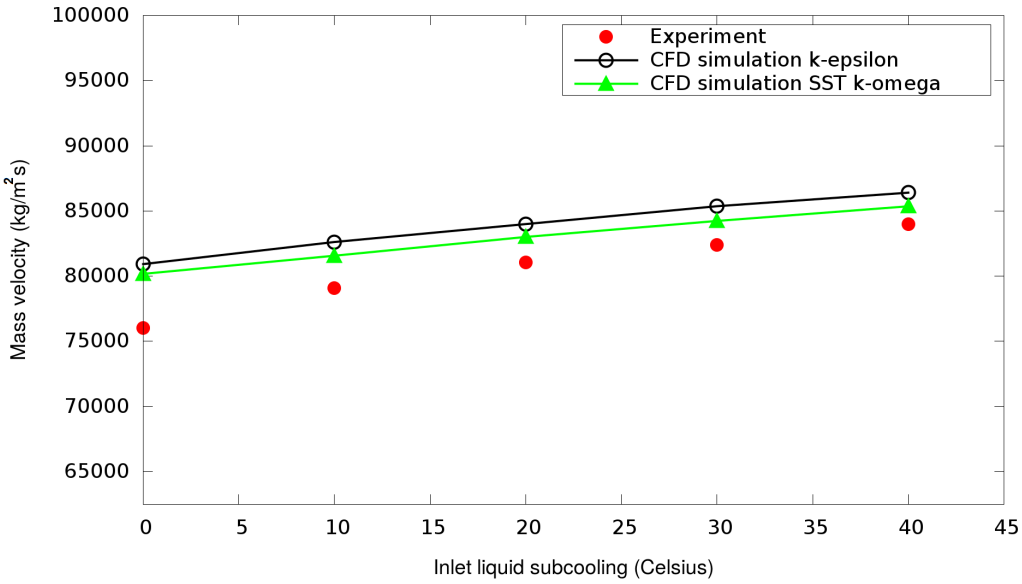

Fig. 5.4 Predicted mass flow rates per unit area for initial pressure equal to 160 bar compared to experimental data of Xu et al. (1995). Lyras et al. (2018a).

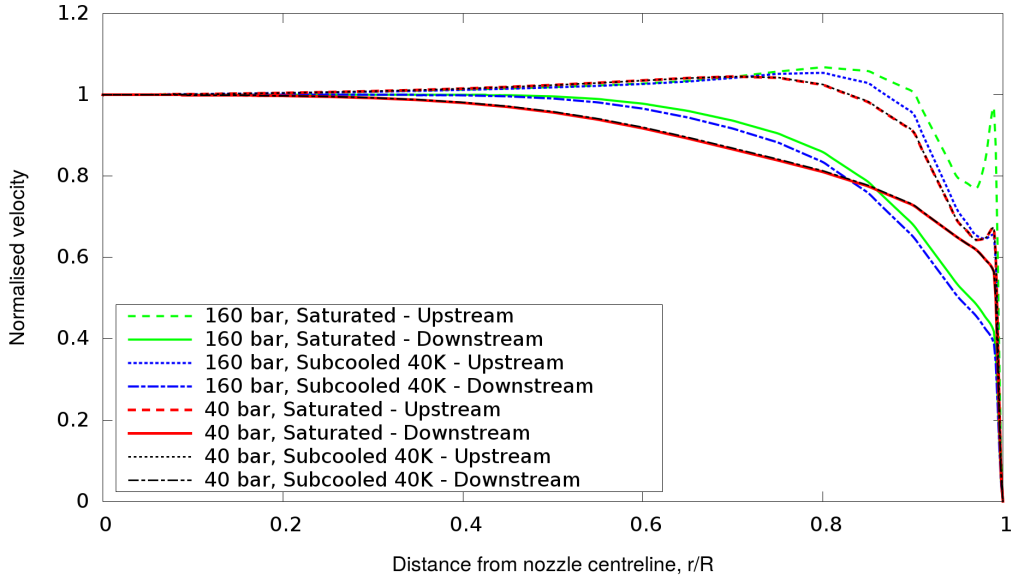

Fig. 5.5 Predicted velocities for different inlet pressures and temperatures upstream-downstream the nozzle, Lyras et al. (2018a).

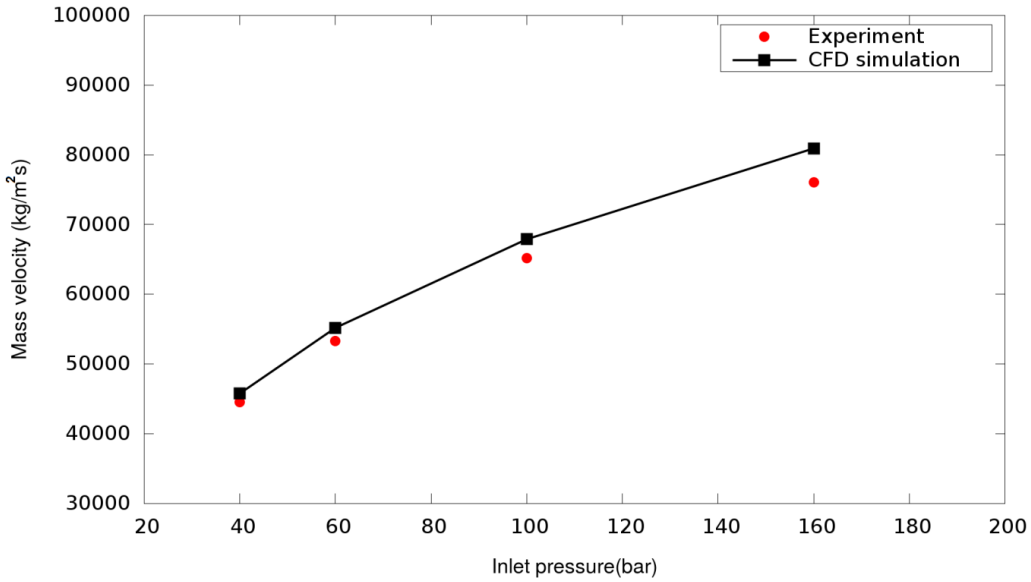

Fig. 5.6 Predicted mass flow rates per area for saturated stagnation conditions and different initial pressures up to 160 bar compared to experimental data of Xu et al. (1995). Lyras et al. (2018a).

of the superheat degree variation on bubble nucleation. Specifically for water, increasing the initial temperature, the surface tension of the vapour decreases with a consequent decreasing for the departure diameter for the bubble. Furthermore, the waiting time τ_{dep} for critical size nucleus to form is proportional to the number of critical vapour nuclei that form per unit volume and time, J and the volume of the liquid. In the homogeneous nucleation theory, J depends on various factors including the superheat degree and surface tension of the vapour. Since $\tau_{dep} \sim 1/JV$ it is evident that increasing the temperature, the waiting time also changes. Avedisian (1985) showed that for water this time-scale decreases, with the nucleation rate increasing significantly after 570K. This limit is locally exceeded here inside the nozzle and is more evident in higher pressure cases (Fig. 5.4) giving a rise to the nucleation rate and hence the vapour mass fraction values (Fig. 5.7).

5.6.2 Turbulence and geometry impact on jet hydrodynamics

The ratio of the nozzle length to diameter may also play a crucial role in the flashing affecting bubble nucleation and atomisation. There are no strict limits as to whether the flow will exhibit internal or external flashing mode. Following HSE (2002) review for flashing releases, one should expect the internal mode to be more likely to occur inside large nozzles although there is an uncertainty for short tubes. For nozzles with small L/D tested here, internal flashing occurs as well. The methodology developed in this study takes into account

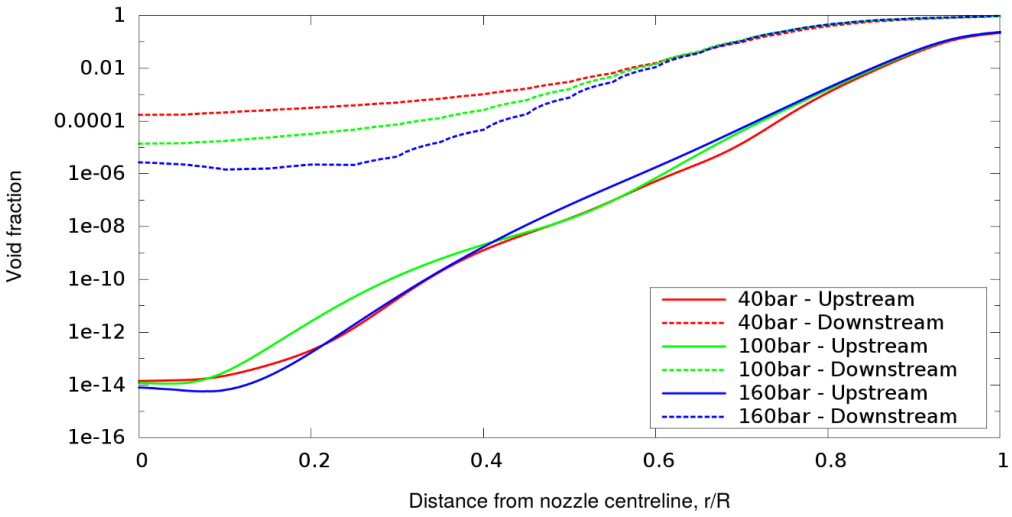

Fig. 5.7 Predicted void fraction in logarithmic scale for the upstream and downstream positions of the nozzle and various inlet pressures of initially saturated conditions. Lyras et al. (2018a).

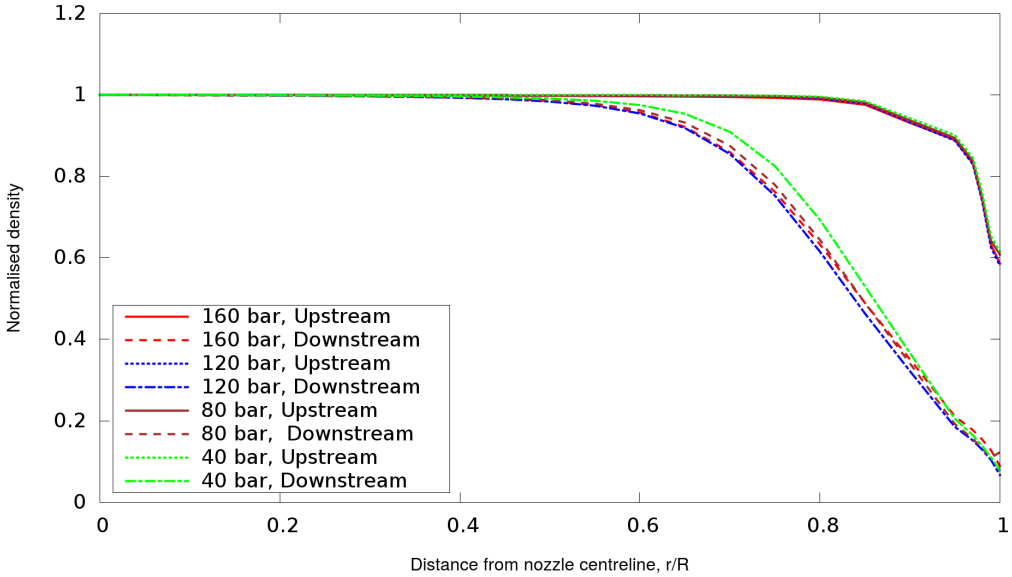

Fig. 5.8 Predicted normalised density for various inlet pressures of initially saturated conditions. Lyras et al. (2018a).

different parameters that could influence the correct mass flow rate calculation such as the compressibility and turbulence effects.

Pressure gradients are always present during liquid flow through the pipe, which cannot be a-priori estimated. A small pressure gradient may play a significant role in the momentum transport. Radial pressure gradients in turbulent pipe flows have been previously reported and seen that are an increasing function of Reynolds number. According to Iciek (1980) for long sharp-edged orifices of L/D > 5 turbulence is expected to be generated before the nozzle exit. On the other hand, for smaller L/D ratios, the inertial forces are likely to dominate viscous forces. A transition from laminar to turbulent regime is possible to occur in these cases, exhibiting a larger effect of L/D on the flow regime.

Since the validated numerical investigations for nozzles with large L/D ratios employing the HRM is scarce, a second series of simulations is included in the present study. Park et al. (1997) performed experiments for various nozzle lengths for flashing water released to nearly atmospheric conditions using different inlet liquid pressures and sub-cooled degrees. They investigated the critical mass flow rates using various L/D. Here the case of L/D = 29.4 is studied. The fluid flows through a pipe with diameter D = 3.4mm and length L = 100mm using a similar shape apparatus as in the previous experiment. In Fig. 5.9 the calculated mass velocity is plotted against the initial liquid temperature for constant inlet pressure equal to 10 bar (1 MPa). Three meshes of 30000, 62500 and 250000 were tested using the same boundary conditions as before except for the fixed pressure and temperature. The computational mesh was refined close to the nozzle walls so that the liquid/gas interphase is resolved and the mesh resolution is considered significantly smaller than the interfacial curvature radius. The present calculations for the fine mesh were performed in a 12-core personal workstation and lasted approximately 2 days. The saturated temperature is 180^oC (453.16 K). This corresponds to the lowest mass flow rate shown in the graph. The mass flow rate follows the same trend as in the case of the sharp-edged orifice demonstrated before, only in this case the evaporation rate has more impact on the critical mass flow rate, hence a steeper mass flow rate curve.

The pressure distribution within the pipe has also been studied. In flashing cases, the pressure drop is expected to be high and can be close to 50 percent of the initial storage pressure (Xu et al., 1995). In Fig. 5.10 the predicted pressure across the pipe is shown for two different initial temperatures. The first case is for the saturated state and the second one for a sub-cooling degree equal to 11^oC. The stagnation pressure for both cases is 15 bar (1.5 MPa). In both cases, the same pattern is observed, which is the rapid pressure drop in the sharp inlet corner where the flow separates, and phase change starts. It is worth mentioning that the pressure at that point is, in both the experimental and numerical study, above the

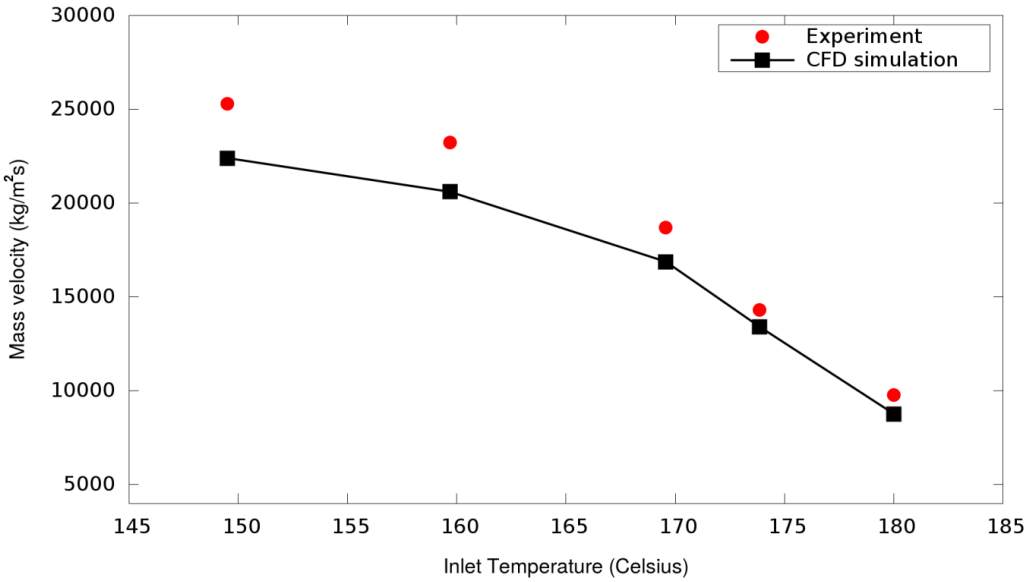

Fig. 5.9 Predicted mass flow rates per area for different initial temperatures compared to experimental data of Park et al. (1997). Lyras et al. (2018a).

local saturation which implies that flashing is triggered downstream of the corner. Another interesting finding providing newer insights is that the pressure drop is generally higher in the sub-cooled case, meaning that the pressure along the pipe is more likely to be higher compared to the saturated inlet for the same initial pressure. The pressure difference in the case of sub-cooling degree of 11^oC is approximately one bar within the pipe up to the position which corresponds to the 85 percent of the pipe length, L.

The relationship of pressure distribution with respect to the stagnation pressure of the liquid is investigated next. In Fig. 5.11 the cases of inlet pressures of 15 bar and 10.15 bar are compared for the case of initially sub-cooled water at 169^oC (442.16 K). Surprisingly, the pressure drop downstream the inlet corner is the same in both cases, and the pressure profile is almost the same after the position of 5 percent of the pipe length. This can be interpreted that the pressure distribution within the nozzle is more sensitive in the sub-cooling degree than the initial pressure at the inlet, at least for nozzles with the relatively large length-to-diameter ratio. In Fig. 5.12 are shown the results for pressure along the nozzle for the case of 10 MPa and for different meshes, coarse, fine and finer. In general, the solution did not depend on the mesh resolution inside the channel giving predictions with good agreement with the experiment. Increasing the L/D ratio, the mixture has more time to fully develop inside the nozzle. The effects of turbulent mixing become more important and the change in flow regime from pure liquid to bubbly is enhanced. Testing the water jet at 15 bar of Park et al. (1997) keeping the same diameter but for L/D equal to one, an indication for the L/D impact

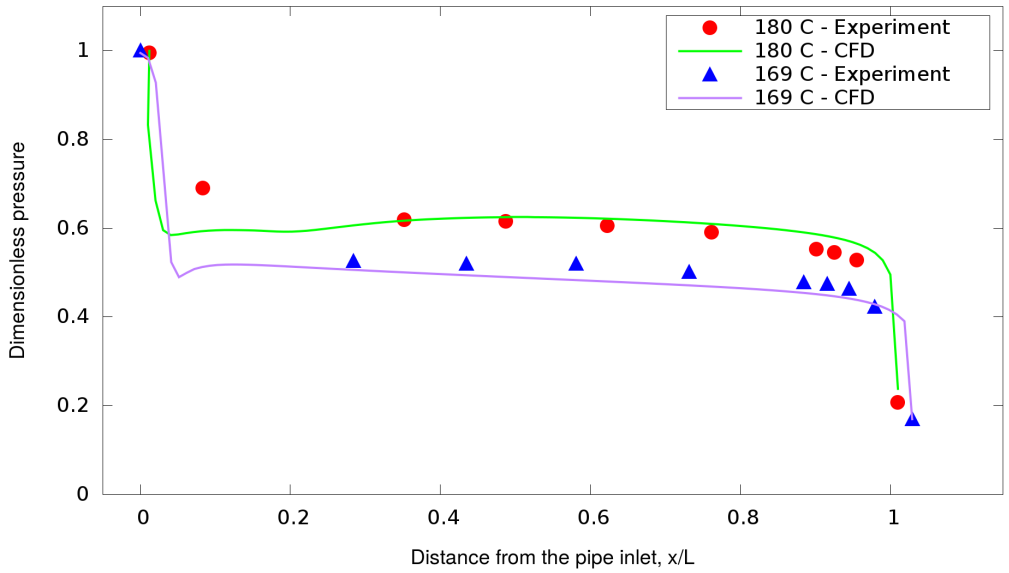

Fig. 5.10 Predicted pressure distribution along the pipe for different inlet temperatures for L/D=29.4 compared to experimental data of Park et al. (1997). Lyras et al. (2018a).

on the regime can be obtained. In Fig. 5.13 the void fraction for both cases has a similar trend with a larger minimum value and almost double for L/D = 29.4. Results of Fig. 5.7 demonstrate a smaller void fraction at the centreline for larger pressures with the one at 40 bar (4 MPa) to be $O(10^4)$ times smaller. Nevertheless the diameter in Fig. 5.13 was 3.4 mm and not the same as in the case illustrated in Fig. 5.7 (D = 4 mm).

5.7 Results for cryogenic liquids

5.7.1 Validation for liquid nitrogen

Numerical simulations concerned a series of NASA experiments by Simoneau (1975) involving Liquid Nitrogen flowing through sharp-edged orifices. The schematics of the experiments are shown in Fig. 5.14. Liquid nitrogen was released from a high-pressure storage vessel with pressures above nitrogen saturation point. The flows are simulated as axisymmetric. This experimental work is one of the very few flashing experiments where two-phase liquid nitrogen is the working fluid and provided the dataset to test the model for different cryogenic scenarios rather than the trivial water channel flows usually considered in other experiments. The nozzle diameter was D = 0.358 cm and L/D = 0.19. The small length to nozzle diameter ratio was kept the same for all the test cases considered in the present study. The tests covered a wide range of temperatures, from 0.75 to 1.035 times the critical temperature (126.3 K),

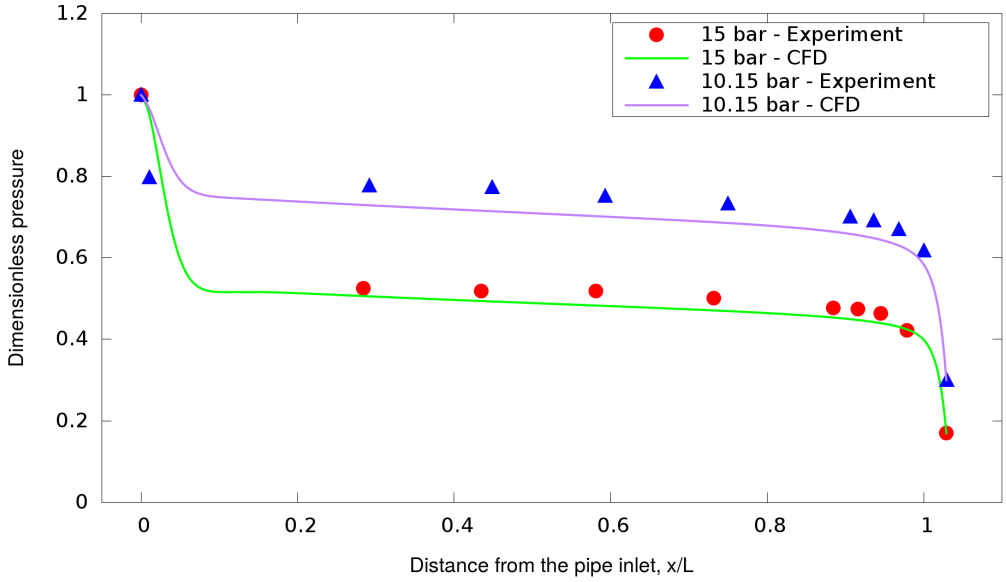

Fig. 5.11 Predicted pressure distribution inside the pipe for 169.4^{o}C and different initial pressures compared to experimental data of Park et al. (1997). Lyras et al. (2018a).

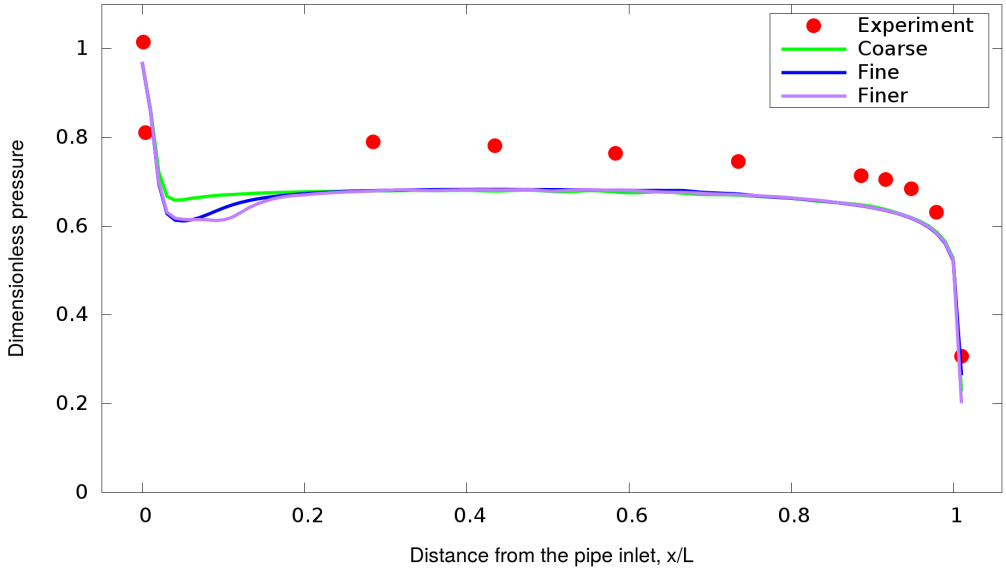

Fig. 5.12 Mesh sensitivity analysis for pressure calculation, for three different meshes of 30000, 62500 and 250000 cells. The inlet pressure was 10 MPa.

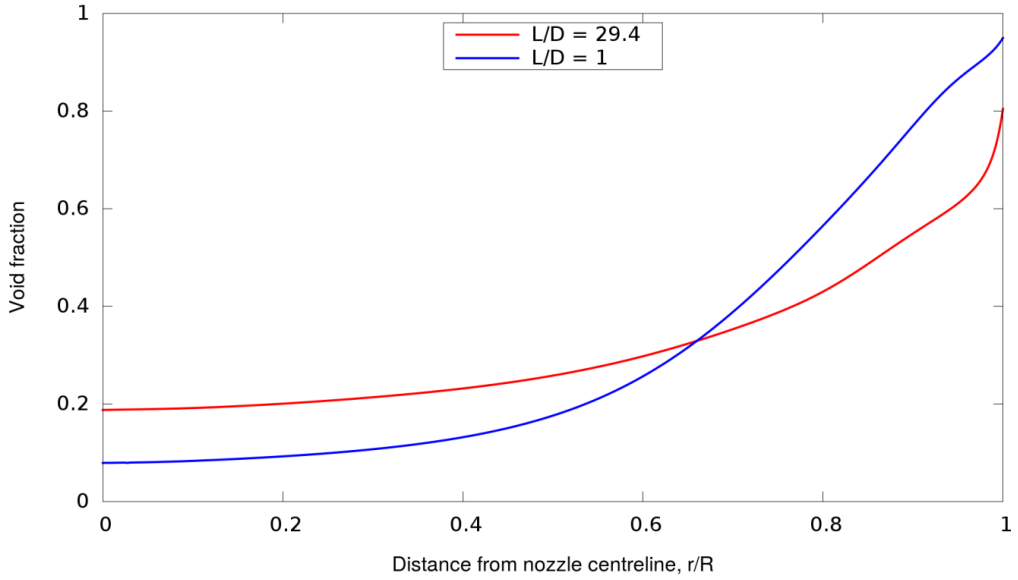

Fig. 5.13 Predicted void fraction for inlet pressure equal to 15 bar and different L/D for water flow. Lyras et al. (2018a).

and the pressures were slightly above and up to two times the critical pressure (33.958 bar). In Table 5.1 the inlet and outlet conditions are shown. Three series of experiments corresponding to different initial temperatures are considered here and the measured properties are denoted by in and out for inlet and outlet respectively. Due to the pressure difference on both sides of the orifice, the liquid flows, and at some point, the liquid pressure drops below the saturation pressure initiating the flashing process. The maximum flow rates were measured at both upstream and downstream orifices with the difference between the two found to be less than 1.75 percent for all the experiments. Here, the upstream data are used for comparison.

Fig. 5.15 shows the mass flow rate per unit area for constant stagnation temperature equal to approximately 95.1 K and various inlet pressures. The temperature at the outlet varied from 83.2 K for the lowest stagnation pressure at 8 bar up to 91.7 K for the maximum stagnation pressure of 67.2 bar. The mass flux was calculated from the mixture density averaged by the vapour mass fraction and velocity. The mass flux is minimum at the lowest pressure and increases in a rather parabolic manner up to the critical pressure. This dependency should not be attributed to choking which is less likely to occur in small tubes and L/D without any strict limits. The experimental observations were in line with this argument at least for sub-cooled stagnation conditions. The predicted mass fluxes linearly increase for inlet pressures greater than the critical pressure and achieve the highest value at the highest inlet pressure 67.2 bar. Similar trends occur when increasing the inlet temperature to 110.1 K (Fig. 5.16) and 119.4 K (Fig. 5.17). The mass flow rates show an increasing pattern by raising the inlet pressure

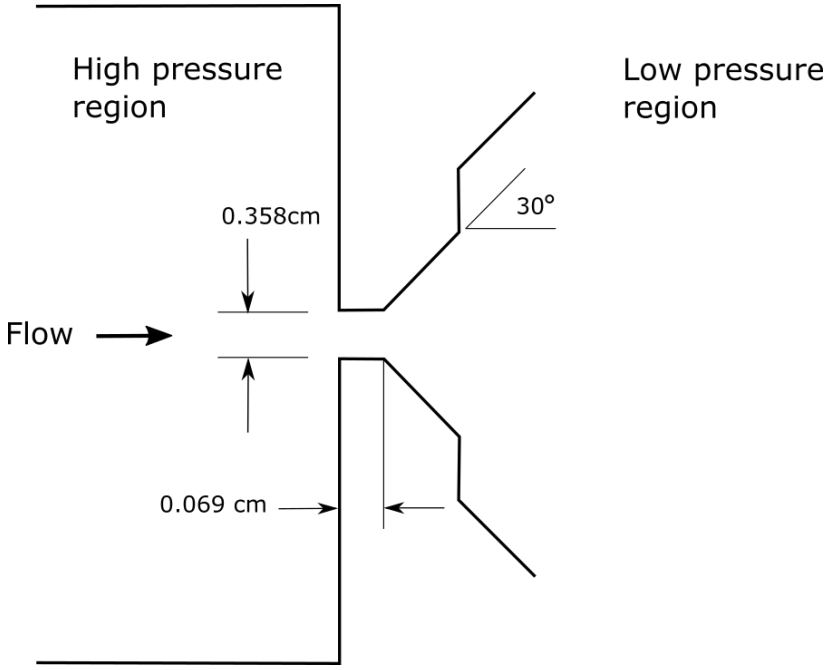

Fig. 5.14 The schematics of the experiments (reproduced from Simoneau (1975). Lyras et al. (2018b).

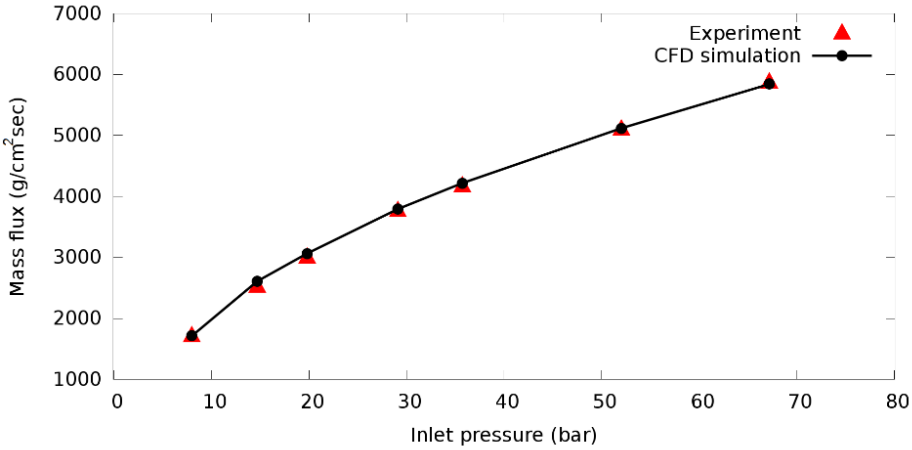

Fig. 5.15 Mass flux for different pressures at an inlet temperature of 95.1 K compared to NASA experiments, Simoneau (1975). Lyras et al. (2018b).

Table 5.1 Inlet and outlet flow properties for the three different series of simulations.

Test case	Inlet		Outlet		Flow
	T_{in}(K)	P_{in}(bar)	T_{out}(K)	P_{in}(bar)	(Re $\times 10^6$)
95.1K	95.0	8.0	83.2	1.9	0.82
	95.2	14.7	86.1	2.4	1.20
	95.2	19.8	87.1	2.7	1.42
	95.0	29.1	88.2	3.1	1.75
	95.2	35.7	89.2	3.3	1.93
	94.9	52.0	91.0	3.9	2.3
	95.1	67.2	91.7	4.1	2.61
110.1K	110.2	16.8	89.70	3.40	2.48
	110.2	22.30	87.80	2.9	2.11
	110.0	31.0	89.70	3.40	2.48
	110.1	41.70	91.10	3.80	2.86
	110.3	55.50	92.70	4.40	3.27
	110.2	67.10	93.50	4.60	3.56
119.4.1K	119.4	25.6	86.30	2.50	2.12
	119.5	30.4	88.20	3.0	2.57
	119.5	34.70	89.70	3.40	2.92
	119.4	39.0	90.40	3.70	3.17
	119.3	45.0	91.70	4.10	3.46
	119.4	54.80	93.0	4.60	3.87
	119.3	67.80	94.5	5.0	4.21

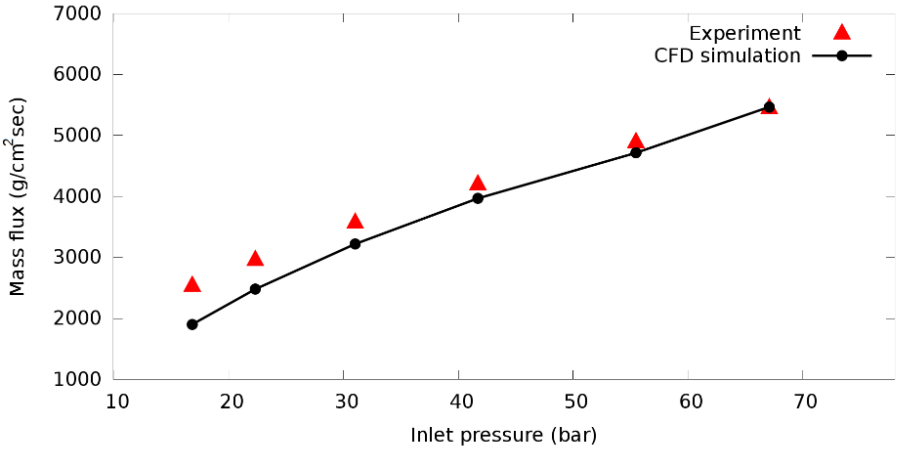

Fig. 5.16 Mass flux for different pressures at an inlet temperature of 110.1 K compared to NASA experiments, Simoneau (1975). Lyras et al. (2018b).

with a linear behaviour as before for pressures above the critical one. The inlet temperature is shown to have a significant impact on the dynamics of the jet and consequently the mass flow rate. The difference between the CFD results and the experimental data remained in most of the cases investigated less than 5 percent and always below 8.5 percent. For the same pressure and geometry, the flow rate decreases as the inlet temperature increases. Higher stagnation temperature manifests the density to be more sensitive to pressure change and smaller average density, thus smaller mass flux. As mentioned above, the formulation for the HRM were initially proposed for water. The good agreement achieved here suggests that the formulations are also suitable for jets of cryogenic nitrogen. The correlation for the time-scale Θ influences the vapour mass production rate as shown in Equation (5.11). The better predictions of the mass flux for lower inlet temperatures compared to the ones for T_{in} =119.4 K might be an indication of the need for alternative correlations for liquid nitrogen. Additionally, simulations using a different correlation for Θ (valid for pressures below 10 bar for water) resulted in better mass flux predictions in some cases for low pressures at T_{in} =119.4 K. The flow is highly turbulent with $O(\mathrm{Re})\sim 10^6$. In all cases, the Reynolds number increases with the increase of the inlet pressure. Simulations' results presented in Figures 5.16, 5.17 and 5.18 show that k-ε can accurately simulate flows of cryogenic jets through sharp-edged orifices.

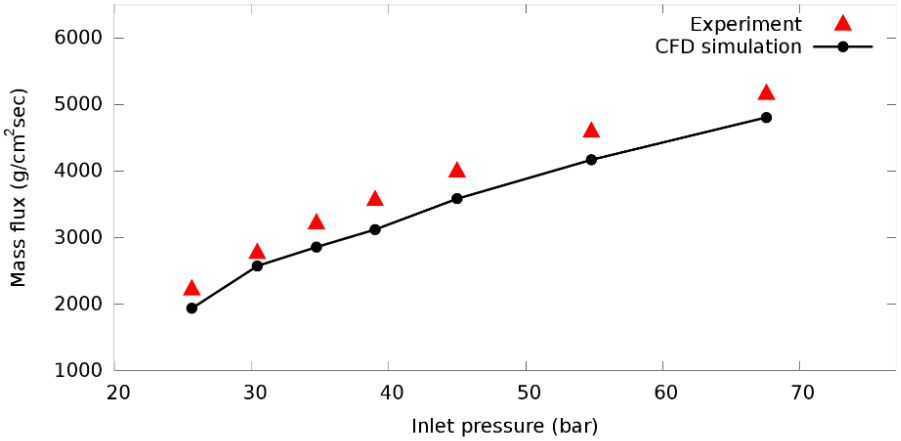

Fig. 5.17 Mass flux for different pressures at an inlet temperature of 119.4 K compared to NASA experiments, Simoneau (1975). Lyras et al. (2018b).

Metastable jet

As mentioned before, flashing jets of cryogenic liquids are usually assigned to metastability and are subject to nucleation at different stages and regimes. Here, the metastability refers to the phase change that drastically occurs to the liquid jet. Studies in nozzles indicate that the initiation of this phase change is possible inside the nozzle Hervieu and Veneau (1996) and is usually pronounced in long nozzles (large L/D). For short nozzles or orifices uncertainties may exist implying that geometry might have less influence. As reported in the NASA experiment Senda et al. (1994) considered in the present study, the flashing jet vaporises within the orifice leading to an alteration of the flow regime and the measured flow coefficient. In the present numerical simulations, the metastable jet exists inside the orifice and phase change starts at the tip of the inlet corners. This phase change, which results in vapour generation, is also reported in the literature for different geometries and seems that does not dependent on the working (Newtonian) fluid. Although, for outlet pressures greater than the saturation pressure, a single-phase jet is expected according to the experiment and for pressures lower than the saturation pressure the jet vaporises. It is interesting to track the velocity inside the orifice and examine how it changes until it emerges in the low-pressure region. In Figure 5.18 the axial velocity is shown at the upstream and downstream orifices for different inlet temperatures at approximately the same pressure. The results shown correspond to half of the domain (symmetric to the flow stream axis). The flow along the orifice radius R (R = 0.179 cm) follows a similar trend in all cases. The upstream velocities are very close to each other and have the maximum value at the centreline of the

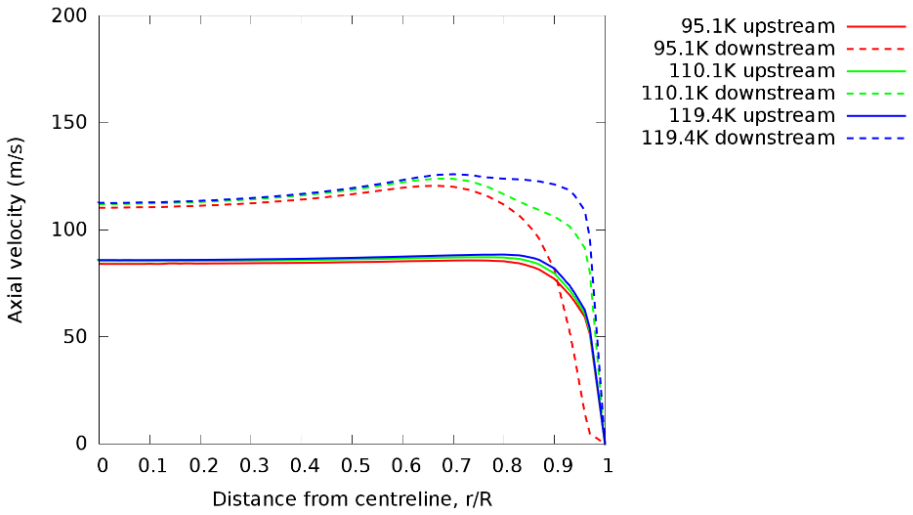

Fig. 5.18 Axial velocity versus radius for different temperatures and for the highest inlet pressure for each case (see Table 5.1). Lyras et al. (2018b).

jet (r/R = 0). As soon as the jet flows towards the exit, nucleation takes place decreasing the mixture density, and higher velocity occurs with a maximum value at approximately 70 percent of the orifice radius. The velocity finally minimises to zero due to the no-slip condition. In Figure 5.19 the full domain is considered offering a general overview of the jet at the downstream orifice. Keeping the inlet temperature constant and varying the pressure, the axial velocity changes correspondingly giving a parabolic-like profile. The peaks of the velocity indicate that vapour is present in the mixture along with the radial direction.

5.7.2 Additional tests for cryogenic liquids

The developed model has been applied to predict the flashing of cryogenic liquids flowing through short pipes. Such applications of the model is another novel aspect of the current work. An additional series of tests was carried out for outlet pressure (end of nozzle) equal to 1 bar (1 MPa). Liquid nitrogen and R134A (1,1,1,2-tetrafluoroethane), which were initially in saturated conditions at 815 bar (0.81.5 MPa) in the storage vessel, are considered. The computational domain is similar to the one in Fig. 5.1. Two dimensional simulations were conducted for qualitative comparisons. Different mesh refinement levels were used for these simulations with the dimensionless wall distance, being around 300, 200, 100, and 10 (the present calculations for the fine mesh took approximately 2.5 days). The diameter (D = 2 mm) of the nozzle is kept constant and the length-to-diameter ratio L/D is equal to 2. The simulations were isenthalpic inside the nozzle. The physical parameters for liquid nitrogen including the saturation properties were taken from Span et al. (2000). The surface

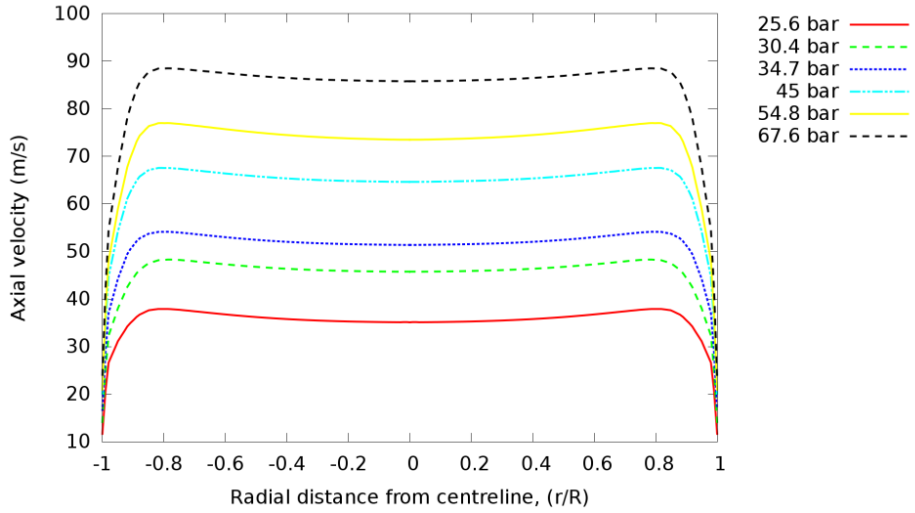

Fig. 5.19 Axial velocity for different pressures at an inlet temperature of 119.4 K. Lyras et al. (2018b).

tension for the sub-critical region decreases linearly with increasing temperature and under the constant temperature assumption can be considered constant, calculated from Lemmon and Penoncello (1994). Likewise for vapour pressure which is a function of temperature. The sub-cooled and saturated properties of R134A were calculated from Tillner-Roth and Baehr (1994) except for the surface tension which was taken following Okada and Hihashi (1994). The axial velocity at the upstream and downstream positions presented in Fig. 5.20 is divided by the maximum one for simplicity and plotted with respect to the whole nozzle diameter (r/R = 0 denotes the centre of the circular profile). The axial velocity is smooth close to the position of the maximum velocity at r/R = 0 but gradually changes when moving closer to the walls. The change in the velocity gradient occurs at almost the same distance for all the liquids at the downstream position. In the upstream case, the velocity profile becomes non-monotonic a bit further away from the wall and the velocity profile follows the patterns shown in Fig. 5.5. The same patterns appear in Winklhofer et al. (2001) where the cavitation gas exists in the shear layer enhancing the velocity peak. It is interesting that the patterns in velocity within the nozzle are similar for cryogenic and non-cryogenic fluid. The void fraction is expected to have its maximum in the recirculation zone close to the wall and becomes minimum at the centreline. Fig. 5.21 shows this trend for the void fraction. The centreline void fraction can vary in the position r/R = 0 and the difference in the volume occupied by the vapour is more extensive for the three liquids at the nozzle exit with a correspondingly different regime. One of the advantages of the presented methodology is that it can offer an estimation for the thickness of the vapour layer formed in the walls. The numerical formulation in the HRM and Equation 5.14 in particular, were extracted for

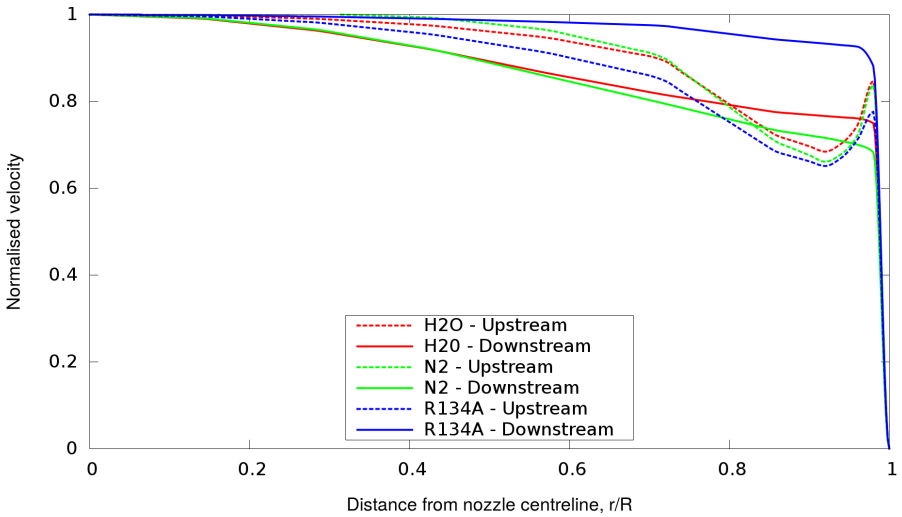

Fig. 5.20 Normalised velocity for liquid nitrogen, R134A and water at atmospheric releases for inlet pressure 8 bar and L/D = 2. Lyras et al. (2018a).

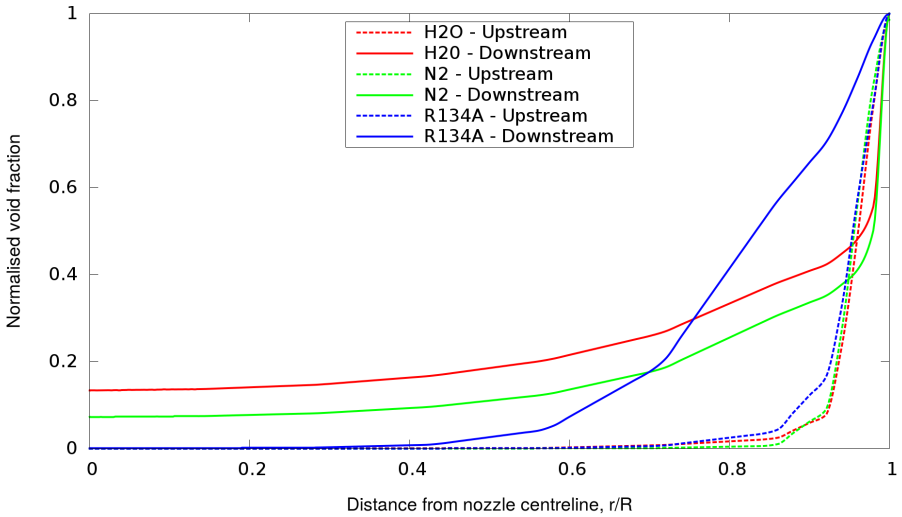

Fig. 5.21 Void fraction versus the distance from the centreline for the three liquids. Lyras et al. (2018a).

water in the original form of the model by Downar-Zapolski et al. (1996). Therefore, testing this formulation for other liquids can be a challenge for predicting the complex physics of the interfacial mass transfer. Previous studies for JP8 fuel (Lee et al. (2009)) and CO_2 (Wen et al. (2013)) have tested its performance for different scenarios. Without dedicated experimental studies for extrapolating constants for the particular fluid, the uncertainty still remains. Nevertheless, results for liquid nitrogen (Lyras et al., 2018b) using the constants presented here and the numerical framework used in Wen et al. (2013) for the pressure update, indicate that the HRM can be successfully used for calculating the mass flow rate of other fluids than water.

Another key-parameter of the presented model is the assumption of zero difference between the velocities of the two phases. The slip velocity is expected where the two phases have different densities. Inside the nozzle liquid and vapour co-exist. The pressure gradient is likely to accelerate the vapour more than liquid. Consequently, the effect of slip velocity is more pronounced to maximise at the nozzle exit (Bar-Kohany and Sher, 2004a). The velocity ratio according to Moody (using the kinetic energy balance), expressed with the liquid, gas specific volumes v_l, v_g as, $\mathscr{S} = (v_g/v_l)^{1/3}$ changes accordingly to the specific volume differences and might become larger than one. For liquid nitrogen and R134A the values of $\mathscr{S}$ are expected to be lower than in water since the liquid specific volume of water is usually more than double compared to the other two fluids. Qualitatively, the conclusions do not change if the expression of Fauske is used for $\mathscr{S}$. Bar-Kohany and Sher (2004b) associated the slip velocity with the choking condition. In their work, for non-choked flow at the nozzle exit, slip velocity is non-zero but can be neglected. They conclude that slip velocity becomes significant when the flow is choked. In the case studies presented here, the flow is choked which indicates that slip might not be negligible. Additionally, evaluating the slip velocity within nozzles and channels, Henry and Fauske (1971) report that for long constant ducts the velocity ratio between liquid and vapour should be expected to be no more than 1.5. This change in the single-phase velocities tends to attenuate with increasing pressure. Hence, according to the authors, the hypothesis of equal velocities for both phases is adequate for the pressure limits in Fig. 5.20. For higher pressure, this result is expected to be reasonable as well.

5.8 Concluding remarks

The new methodology for simulating flashing jets is developed in this chapter. The new solver developed here uses a new pressure equation for coupling pressure and velocity in the PIMPLE algorithm. This novel pressure equation includes the contribution of phase change,

surface tension, thermal expansion and compressibility in the pressure change. The newly added terms are described and the new solver FlashFOAM is tested. A detailed validation is presented for both short and long nozzles for flashing water and liquid nitrogen jets where experimental data are available. Additional series of simulations are demonstrated for a wide range of initial pressures and temperatures. Moreover, extra tests for R134A were carried out showing the capability of this novel coupling of the new pressure equation with the HRM and interface tracking methods to simulate cryogenic fluids. FlashFOAM is capable of simulating flashing and the impact of bubble nucleation on the flow for liquids initially either sub-cooled or saturated. The mass flow rates at the validated cases are close to those observed in the experiments. The predictions confirmed experimental findings that indicate a two-phase jet at the nozzle exit which continues evaporating downstream.

Chapter 6

Modelling liquid jet atomisation: application in superheated jets

This chapter describes a novel methodology for the atomisation of flashing jets. The method is utilised using the ELSA approach introducing the concept of surface density. In ELSA, the liquid is tracked indirectly by the Σ-equation and liquid structures of arbitrary shape can be identified overcoming the limitation of the spherical droplets assumption in Lagrangian methods. As part of the developments in the current PhD thesis, the Σ-equation is modified introducing an additional source term for evaporation that couples the HRM and ELSA for both dense and dilute spray region. The new solver HRMSonicELSAFoam developed was tested for cryogenic liquids and water. Results are presented for the characterisation of the liquid droplets' Sauter mean diameter and other important spray characteristics such as velocity and spray angle. Except for the validation, investigations for shedding light on the dependency of the nozzle geometry and the superheat degree on the spray dynamics is presented in a multi-dimensional approach for flashing jets.

6.1 Surface equations for two-phase flows

The characterisation of liquid atomisation can be considered as the problem of describing the small liquid volumes of arbitrary shape in the three-dimensional space. In two-phase flows (liquid and gas) the two fluids are separated by an interface. The presented method in this research considers liquid-gas cases, although the same method applies to two immiscible fluids e.g. two liquids (Lhuillier, 2003). The interface that separates two fluids is a two-dimensional surface in the three-dimensional space. The representation in space and time of

this surface can be done using either the vector position $\vec{x} = (x, y, z)$ or the surface coordinates x_1, x_2 as (Aris, 1962)

$$\vec{x} = \vec{x}(x_1, x_2, t) \quad \text{or} \quad F(\vec{x}, t) = 0 \tag{6.1}$$

where F is a geometrical constraint. The phase indicator function can be defined via a Heaviside function $H()$ (following Prosperetti and Tryggvason (2009)) as

$$x_l(\vec{x}) = 1 - x_g(\vec{x}) = H(F(\vec{x}), t) \tag{6.2}$$

For each phase k, liquid (l) or gas (g), $x_k = 1$ if and only if $\vec{x}$ lies inside phase k and by convention $x_k = 0$ if the point is outside. For any point, in time and space, the unit normal vectors at the interface pointing towards phase k are opposite vectors

$$\vec{n_g} = -\vec{n_l} = \frac{\nabla F}{|\nabla F|} \tag{6.3}$$

The velocity at the surface point x_1, x_2 is then

$$\vec{w} = \left(\frac{\partial \vec{x}}{\partial t} \right)_{x_1, x_2} \tag{6.4}$$

This is the common velocity the two fluids have on the two sides of the interface. Since the function F becomes zero at the interface, its material derivative is zero

$$\frac{\partial F}{\partial t} + \vec{w} \cdot \frac{\partial F}{\partial x_j} = 0 \tag{6.5}$$

From equations 6.3-6.5 it is clear that every velocity field with the same normal component will produce the same motion of the interface. Using the normal unit vectors, this normal velocity is equal to

$$\vec{w} \cdot \vec{n}_l = -\vec{w} \cdot \vec{n}_g = \frac{\partial F / \partial t}{|\nabla F|} \tag{6.6}$$

This is also called the normal placement speed of the interface and is the component responsible for the interface motion. Recalling the definition of the phase indicator x_k, for each phase k

$$\nabla x_l = -\nabla x_g = \delta(F) \nabla F \quad \text{and} \quad \frac{\partial x_l}{\partial t} = -\frac{\partial x_g}{\partial t} = \delta(F) \frac{\partial F}{\partial t} \tag{6.7}$$

where $\delta()$ is the Dirac function. From equations 6.5-6.7 the topological equation for each phase k can be derived

$$\frac{\partial x_k}{\partial t} + \vec{w} \cdot \nabla x_k = 0 \tag{6.8}$$

This is equivalent to the transport equations for the liquid and the gas phases derived in the previous chapters. The phase indicator and the normal vector are explicitly calculated from the function $F(\vec{x},t)$. Using the above formulations the definition of the local instantaneous interfacial area concentration (or fine-grained surface density) δ_I is derived

$$\delta_I \equiv -\vec{n}_k \cdot \nabla x_k = \delta(F)|\nabla F| \tag{6.9}$$

This definition is employed from Kataoka et. al. (1986); Lhuillier (2003); Marle (1982); Morel (2007). The knowledge of $\delta_I, \vec{n}_k$ and the normal velocity gives the description of the interface. The Dirac-like function δ_I is of major importance for the interface topology and can be used to calculate the interfacial forces. Decomposing the interfacial forces to its tangential and normal component, the total interfacial force is then

$$\delta_I[(I - \vec{n}\vec{n}) \cdot \nabla\sigma - \sigma(\nabla \cdot \vec{n})] \tag{6.10}$$

where the normal vector $\vec{n} = \vec{n}_l = -\vec{n}_g$ is used interchangeably.

6.1.1 An equation for the local instantaneous interfacial area concentration

Because of the complex motion of the interface, the instantaneous interfacial area concentration exhibits significant spatial variations. We are not interested in the value at one point $\vec{x}$ but instead, in its average in a volume V. This average is the global instantaneous interfacial area concentration defined as the volume average of δ_I

$$S_V(\vec{x},t) = \frac{1}{V}\int_V \delta_I \mathrm{d}v = \frac{1}{V}\int_S \mathrm{d}s \tag{6.11}$$

where the last integral denotes the amount of surface S within a volume V. In order to construct an equation for the surface evolution through time we need to fathom to the nature of the relationship between the normal vector and velocity field at the interface and the surface area. The velocity at the surface can be decomposed as

$$\vec{w} = (\vec{w} \cdot \vec{n})\vec{n} + \vec{w_\perp} \tag{6.12}$$

The vector $\vec{w_\perp}$ is the tangential component and is the projection of the velocity vector which is perpendicular to the normal vector, $\vec{w_\perp} = (I - \vec{n}\vec{n}) \cdot \vec{w}$. The surface divergence of the velocity at the interface is

$$\nabla_s \cdot \vec{w} = (\vec{w} \cdot \vec{n}) \nabla_s \cdot \vec{n} + \nabla_s \cdot \vec{w}_\perp \tag{6.13}$$

Following Morel (2007) and using the Leibniz integral rule for an arbitrary function $f(s,t)$

$$\frac{\mathrm{d}}{\mathrm{d}t} \int_S f(s,t) \mathrm{d}s = \int_S \left(\frac{\partial f(s,t)}{\partial t} + f(s,t)(\vec{w} \cdot \vec{n}) \nabla_s \cdot \vec{n} \right) \mathrm{d}s + \int_C f(\nabla_s \cdot \vec{w}_\perp) \mathrm{d}c \tag{6.14}$$

Since $\nabla_s \vec{n} = \nabla \vec{n}$, the ∇_s operator can be substituted hereafter in the last equation[1]. Equation (6.14) can be used to describe the change of a surface in time, $S(t)$ within a constant volume enclosed in a ∂v which remains constant through Fig. 6.1. Gurtin et al. (1989) has offered an extension of equation 6.14 assuming that the tangential component is equal to zero

$$\frac{\mathrm{d}}{\mathrm{d}t} \int_{S(t)} f(s,t) \mathrm{d}s = \int_{S(t)} (f_n + f(s,t)(\vec{w} \cdot \vec{n}) \nabla \cdot \vec{n}) \, \mathrm{d}s - \int_{C(t)} f(\vec{w} \cdot \vec{n}) \frac{\vec{n} \cdot \vec{N}}{\sqrt{1 - (\vec{n} \cdot \vec{N})^2}} \mathrm{d}c \tag{6.15}$$

The first term on the RHS contains f_n which is the normal time derivative of the function $f(s,t)$. This is normal to the boundary of the volume and is the inner vector of the gradient of function f with the appropriate direction. The second integral on the RHS is over the curve $C(t)$ which is the intersection curve of the surface S and the boundary of the constant volume, ∂V. The vector $\vec{N}$ is the unit normal vector of ∂V. The LHS of equation (6.15) is nothing else but the temporal discretisation of S. Setting $f = 1$ the normal time derivative vanishes and the result is a relationship for the unsteady surface evolution

$$\frac{\mathrm{d}S}{\mathrm{d}t} = \int_{S(t)} (\vec{w} \cdot \vec{n})(\nabla \cdot \vec{n}) \mathrm{d}s - \int_{C(t)} (\vec{w} \cdot \vec{n}) \frac{\vec{n} \cdot \vec{N}}{\sqrt{1 - (\vec{n} \cdot \vec{N})^2}} \mathrm{d}c \tag{6.16}$$

The two integrals on the RHS are taken over the surface, the first one, and the intersection C, the second one. Both of these, change in time. On the LHS of equation (6.16) the global instantaneous interfacial area concentration definition can be used, which is the volume averaged value of δ_I. In this case we have for the local instantaneous interfacial area

[1] $\nabla_s \vec{n} = (I - \vec{n}\vec{n}) : \nabla \vec{n} = \nabla \vec{n} - \vec{n}\vec{n} : \nabla \vec{n}$. The later using index notation is equal to $-n_i n_j n_i, j = -n_j (n_i n_i)_{,j}/2 = 0$, since $n_i n_i = 1$

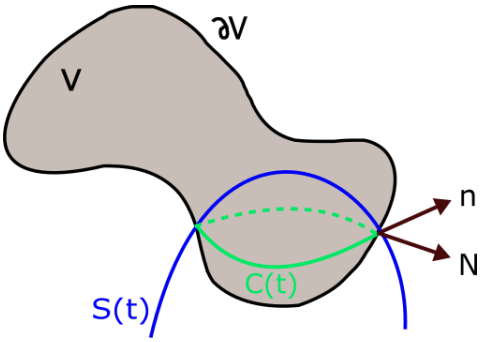

Fig. 6.1 Surface $S(t)$ enclosed inside a volume V with their intersection $C(t)$.

concentration (see Morel (2007)),

$$\frac{\mathrm{d}}{\mathrm{d}t}\int_V \delta_I \mathrm{d}v = \int_V (\vec{w}\cdot\vec{n})(\nabla\cdot\vec{n})\delta_I \mathrm{d}v - \int_{\partial V}(\vec{w}\cdot\vec{n})(\vec{n}\cdot\vec{N})\delta_I \mathrm{d}s \tag{6.17}$$

In this formulation the surface integral is transformed to a volume integral and the line integral is considered in the boundary ∂V and can be also transformed to a volume integral using the divergence theorem

$$\int_{\partial V}(\vec{w}\cdot\vec{n})(\vec{n}\cdot\vec{N})\delta_I \mathrm{d}s = \int_V \nabla\cdot[(\vec{w}\cdot\vec{n})\delta_I\vec{N}]\mathrm{d}v \tag{6.18}$$

The equation (6.17) becomes

$$\frac{\partial\delta_I}{\partial t} + \nabla[\delta_I(\vec{w}\cdot\vec{n})\vec{n}] = \delta_I(\vec{w}\cdot\vec{n})\nabla\cdot\vec{n} \tag{6.19}$$

From equation (6.13) one gets $(\vec{w}\cdot\vec{n})\nabla\cdot\vec{n} = \vec{w} - \vec{w}_\perp$. The equation for δ_I now becomes

$$\frac{\partial\delta_I}{\partial t} + \nabla\cdot[\delta_I(\vec{w}-\vec{w}_\perp)] = \delta_I(\vec{w}\cdot\vec{n})\nabla\cdot\vec{n} \Rightarrow \frac{\partial\delta_I}{\partial t} + \nabla\cdot(\delta_I\vec{w}) = \delta_I\vec{w}_\perp + \delta_I(\vec{w}\cdot\vec{n})\nabla\cdot\vec{n} \tag{6.20}$$

provided that $\nabla\cdot(\delta_I\vec{w}_\perp) = \delta_I\nabla_s\cdot\vec{w}$ from Marle (1982). From equation 6.13 follows that

$$\frac{\partial\delta_I}{\partial t} + \nabla\cdot(\delta_I\vec{w}) = \delta_I\nabla_s\cdot\vec{w} \tag{6.21}$$

By definition of the tangential component of the velocity vector, it is $\nabla_s\cdot\vec{w} = (I-\vec{n}\vec{n}) : \nabla\vec{w}$. Using simple algebra we get (Lhuillier, 2003)

$$\frac{\partial\delta_I}{\partial t} + \vec{w}\cdot\nabla\delta_I = -\delta_I\vec{n}\vec{n} : \nabla\vec{w} \tag{6.22}$$

Both of the last two equations are important for developing a proper equation for the evolution of surface density in two-phase and reactive flows. They both use the microscopic velocity $\vec{w}$.

6.1.2 The Σ-equation

Following Ishii (1975) and Delhaye (1976), the ensemble average of δ_I is equal to the integral of the fine-grained surface density over a volume V with surface S which is equal to the surface density Σ

$$\Sigma(\vec{x},t) =< \delta_I >= \frac{1}{V}\int_V \delta_I \mathrm{d}V = \frac{S(\vec{x},t)}{V} \tag{6.23}$$

In cases of zero mass flux at the interface (zero reaction rate) the velocity $\vec{w}$ in equation 6.8 is equal to the fluid velocity u_j. Integration of equation (6.23) yields an equation for the surface density

$$\frac{1}{V}\int_V \frac{\partial \delta_I}{\partial t}\mathrm{d}V + \frac{1}{V}\int_V u_j \cdot \frac{\partial \delta_I}{\partial t}\mathrm{d}V = \frac{1}{V}\int_V \delta_I n_i n_j : \frac{\partial u_i}{\partial x_j}\mathrm{d}V \tag{6.24}$$

Using the definition of Σ in equation (6.24) the Σ equation is retrieved

$$\frac{\partial \Sigma}{\partial t} + u_j \cdot \frac{\partial \Sigma}{\partial x_j} = -\Sigma n_i n_j : \frac{\partial u_i}{\partial x_j} \tag{6.25}$$

Because of the complex motion of the interface, the associated quantities responsible for the description of Σ such as the interfacial stress or the interfacial orientation tensors need to be averaged. Hence the notation for Σ stands for the average in space hereafter. The RHS is highly anisotropic in low *Re* but becomes isotropic for high Reynolds numbers. In their model for surface flame density, Candel and Poinsot (1990) modelled this term using equation (6.22). The flame front separates the fresh unburned gas with the burnt gas. The velocities on each side k, denoted as u_k, only have different normal components which are used to explicitly calculate the mass flux $\dot{m}$ along the flame interface, $\dot{m} = \rho_k(\vec{w} - u_k)\cdot\vec{n}$,

$$\frac{\partial \langle \delta_I \rangle}{\partial t} + \nabla \cdot (\delta_I \vec{w}) = -\nabla \cdot \left\langle \delta_I \frac{\dot{m}}{\rho_k}\vec{n} \right\rangle + \langle \delta_I (I - \vec{n}\vec{n}) : \nabla u_k \rangle + \left\langle \delta_I \frac{\dot{m}}{\rho_k}\nabla_s \vec{n} \right\rangle \tag{6.26}$$

In case of turbulent flows, the Σ−equation is then written as

$$\frac{\partial \Sigma}{\partial t} + \nabla \cdot (\Sigma \bar{u}) + \nabla \cdot (\Sigma \left\langle u_k' \right\rangle_s) + \nabla \cdot \left(\Sigma \left\langle \frac{\dot{m}}{\rho_k}\vec{n} \right\rangle_s \right) = \Sigma(\nabla \cdot \bar{u} - \langle \vec{n}\vec{n} \rangle_s : \nabla \bar{u}_k) + \Sigma \left\langle \nabla \cdot u_k' - \vec{n}\vec{n} : \nabla u_k' \right\rangle_s + \Sigma \left\langle \frac{\dot{m}}{\rho_k}\vec{n} \right\rangle_s \tag{6.27}$$

This is the flame surface density equation in combustion proposed by Candel and Poinsot (1990). It is worth mentioning that the second and third terms of the LHS represent the convection by the mean and the fluctuating velocity field. The RHS contains the stretching terms due to these velocity fields (first and second term) and the last one is the curvature contribution.

In terms of liquid atomisation Vallet and Borghi (1999) proposed the following equation for Σ

$$\frac{\partial \bar{\Sigma}}{\partial t} + \frac{\partial \bar{\Sigma} \tilde{u}_i}{\partial x_i} = \frac{\partial}{\partial x_i}\left(D \frac{\partial \bar{\Sigma}}{\partial x_i}\right) + (A + \Xi)\bar{\Sigma} - \Upsilon \bar{\Sigma}^2 \tag{6.28}$$

where D is a diffusion coefficient. The equation contains two time-scales, $1/A$ and $1/\Xi$ which correspond to two different surface production time-scales and a destruction constant Υ which has the units of velocity. The A term represents the production of the mean interfacial surface due to mean flow stretching and the mean velocity gradients. Vallet et al. (2001) employed the standard k-ε model to induce a proper time-scale using the corresponding time-scale in the production term (shown in the previous chapter). The first coefficient reads

$$A = c_A \frac{\widetilde{u_i' u_j'}}{\tilde{k}} \cdot \frac{\partial \tilde{u}_i}{\partial x_j} \tag{6.29}$$

where c_A is a constant of the model, usually $c_A = 1$. Stretching due to turbulence on the liquid-gas interface is given via the term Ξ. Assuming homogeneous isotropic turbulence the term is written as

$$\Xi = c_\Xi \frac{\tilde{\varepsilon}}{\tilde{k}} \tag{6.30}$$

which is nothing else but the integral characteristic scale in k-ε turbulence model multiplied by a constant c_Ξ and usually it is $c_\Xi = 1$. The destruction of the interface can be assumed to occur due to one mechanism (for instance coalescence). The probability for one interface to exist inside a finite volume is equal to $\bar{\Sigma}$. Hence, the possibility for two interfaces to interact is proportional to $\bar{\Sigma}^2$. The coefficient Υ is then calculated assuming that after the interaction, liquid droplets form, which in this equilibrium state have interface $\bar{\Sigma}_{eq} = 3\bar{\rho}\tilde{Y}/\rho_l r_{eq}$, where $\tilde{Y}$ is the density-weighted mean value of the liquid mass fraction and r_{eq} is a characteristic length scale whose physical meaning will be discussed later. The destruction term is then derived from (Vallet et al., 2001)

$$\Upsilon = \frac{\Xi \rho r_{eq}}{3\bar{\rho}\tilde{Y}} \tag{6.31}$$

6.2 Eulerian-Lagrangian-Atomisation model

The work of Vallet et al. (2001) gave rise to a new family of Eulerian methods for simulating atomisation and sprays, the so-called ELSA model. The model has been extensively tested for spray injection in the automotive industry. It is used here to predict the characteristics of the liquid structures in the dense and dilute parts of the spray. It is important to point out that one of the innovative ideas introduced in ELSA, is the mean liquid-gas interface density Σ for describing the spray whose definition is not limited to the assumption of spherical droplets which is standard practice in many Lagrangian methods in commercial and open-source software. The interface density can be considered as the amount of spatial surface of liquid per unit volume at a given position. Hence Σ has units of inverse length, m^{-1}. In finite volume methods, the volume is the control volume as shown in Fig. 6.2. A key point to remember is that Σ is zero in pure liquid and gas and behaves in a Dirac-function-type manner. We have seen that the Σ-equation can be written like a typical transport equation on the LHS and contains all the potential contributors that might alter the liquid-gas interface. Before demonstrating the final form of the surface density, we should provide a closure for the diffusion coefficient, in the same manner the diffusion term is treated in the y-equation at the previous chapter. The first term in equation (6.28) is

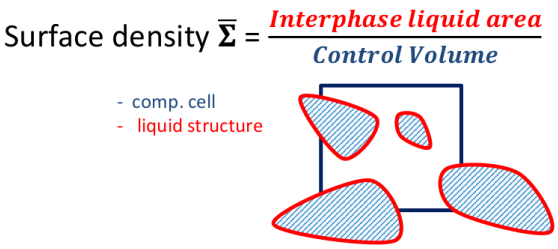

Fig. 6.2 Surface density at a control volume. Bold red colour inside the computational cell indicates the liquid surface and the bold blue line is the control volume in a 2D projection.

$$D\frac{\partial\bar{\Sigma}}{\partial x_i} = \frac{\mu_t}{Sc_t}\frac{\partial(\bar{\Sigma}/\rho)}{\partial x_i} = \frac{\nu_t}{Sc_t}\frac{\partial\bar{\Sigma}}{\partial x_i} \tag{6.32}$$

The ELSA model has been originally developed and validated in RANS and is proven to model accurately the turbulent mixing. It has been modified since its first appearance. Here we use as a basis the formulation proposed by Menard et al. (2006). The model was modified by Lebas et al. (2009) and the Σ equation can be written as,

$$\frac{\partial \bar{\Sigma}}{\partial t}+\frac{\partial \tilde{u_j}\bar{\Sigma}}{\partial x_j}=\frac{\partial}{\partial x_j}\left(\frac{\nu_t}{Sc_t}\frac{\partial \bar{\Sigma}}{\partial x_j}\right)+\Psi\left(S_{init}+S_{turb}\right)+\left(1-\Psi\right)\left(S_{coll}+S_{2ndBU}\right)+S_{vap} \quad (6.33)$$

The model consists of several source terms on the RHS, which are associated with different processes that might have an impact on the atomisation. This approach extends the original model considering different and more mechanisms which can potentially alter the interface evolution. The source terms can be calculated via different approaches. Here they are split for the dense and dilute part of the spray using an indicator function Ψ which is equal to one if the liquid mass fraction, $\tilde{Y_l}$ is between 1 and 0.5 and is zero for cells with a liquid mass fraction less than 0.1. The indicator function can be written as a function of the liquid volume fraction, ϕ_l, where $\phi_l=\bar{\rho}\tilde{Y_l}/\bar{\rho_l}$ as,

$$\Psi(\phi_l)=H(\phi_l-0.1)H(\phi_l-0.5)+(H(\phi_l-0.1)-H(\phi_l-0.5))(2.5\phi_l-0.25) \quad (6.34)$$

where $H()$ is the Heaviside step function. In an analogy of the Σ-equation of Vallet and Borghi (1999), a primer approximation for the terms on the RHS is to write them in the form

$$S=\frac{\bar{\Sigma}}{\tau_\Sigma}\left(1-\frac{\bar{\Sigma}}{\bar{\Sigma}_{eq}}\right) \quad (6.35)$$

where Σ_{eq},τ_Σ are an equilibrium value for the interface and the time-scale of the corresponding process. A shortcoming of this restoration equilibrium model is that it is not well defined when no perturbations are present since at rest $\Sigma_{eq}=0$ which implies that for a finite time-scale τ_Σ the surface will be destroyed infinitely fast. A minimum initial amount of interface has to be assumed that exists in order to evolve Σ. By the definition of Σ, this minimum interface has to be proportional to the inverse of the integration kernel which can be also associated to the characteristic turbulent spatial scales. The term S_{init} corresponds to the minimum liquid-gas surface produced in the atomisation process and is larger where the gradient of liquid mass fraction is higher. The following expression is used from Lebas et al. (2009),

$$S_{init}=2\frac{\mu_t}{Sc_t}\frac{6\bar{\rho}}{\rho_l\rho_g l_t}\frac{\partial \tilde{Y_l}}{\partial x_i}\frac{\partial \tilde{Y_l}}{\partial x_i} \quad (6.36)$$

This expression is used in cases where $\phi_l(1-\phi_l)<0.001$. Otherwise the second fraction in equation (6.36) is equal to $\frac{Y_l(1-Y_l)}{l_t}$. In the previous equation, ρ_g is the density of ambient gas (still air in the present study) and l_t is the turbulent length scale. In k-ε turbulence model $l_t=C_\mu^{3/4}\frac{k^{1.5}}{\varepsilon}$. The $SSTk-\omega$ model has been also used in this study giving in general good agreement with experiments and was proven to be stable enough, especially for the long

pipes. Although the combination of ELSA formulation with k-ε turbulence model is quite common in the literature, the specific rate of dissipation can be easily induced as follows,

$$l_t = C_\mu^{3/4} \frac{k^{1/2}}{\omega} \tag{6.37}$$

where C_μ is a constant equal to 0.09. S_{turb} is the term responsible for the production or destruction of the interface density due to stretching caused by turbulence and collisions/coalescences in the dense part of the spray. It is assumed that interface will be created or destroyed due to turbulence until Σ reaches an equilibrium value, Σ^*_{turb}. The turbulent time-scale τ_t for this process, in case of RANS, is equal to k/ε for the k-ε turbulence models and for the k-ω models it is $\tau_t = 1/\omega$. In LES the turbulent time-scale is

$$\tau_t = ||S_{ij}||^{-1} \tag{6.38}$$

Considering a Weber number equal to one at the equilibrium, the source term is then calculated as,

$$S_{turb} = \frac{\bar{\Sigma}}{\tau_t}\left(1 - \frac{\bar{\Sigma}}{\Sigma^*_{turb}}\right) \tag{6.39}$$

At the dilute part of the spray, the liquid structures are treated in a Lagrangian manner. The source term for the surface creation/destruction due to collisions in the dilute areas is written in a similar way as in equation (6.35). Regarding the collision time-scale τ_{coll} based on the particle collision theory is $\tau_{coll} = L^3_{coll}/S_{eff}u_{coll}$, where L_{coll} is the mean free path and S_{eff} the cross-section of collision. These can be both estimated from the flow field. Finally, the collision time-scale is calculated according to Lebas et al. (2009) as,

$$\tau_{coll} = \frac{1}{\bar{\Sigma}\sqrt{\frac{2}{3}\tilde{k}}} \tag{6.40}$$

where $\tilde{k}$ is the turbulent kinetic energy. Hence, the collisions source term is equal to,

$$S_{coll} = \frac{\bar{\Sigma}}{\tau_{coll}}\left(1 - \frac{\bar{\Sigma}}{\Sigma^*_{coll}}\right) \tag{6.41}$$

The additional equilibrium term Σ^*_{coll} is calculated via an equilibrium Weber number,

$$We^*_{coll} = \frac{\rho_l u^2_{coll} D_{32}}{\sigma_l} \tag{6.42}$$

Where σ_l is the surface tension of liquid. The characteristic collision velocity u_{coll} is calculated via,

$$u_{coll} = \sqrt{\frac{2}{3}\tilde{k}} \tag{6.43}$$

The diameter D_{32} is the characteristic size of the droplet, equivalent to the Sauter mean diameter and equals to,

$$D_{32} = \frac{6\bar{\rho}\tilde{Y}_l}{\rho_l \bar{\Sigma}} \tag{6.44}$$

The equilibrium Weber number, We^*_{coll} is taken equal to 12 which corresponds to a diameter D^*_{32}. Following a correction for the SMD proposed by Lebas et al. (2009), a new droplet diameter is obtained which is then used and the Σ^*_{coll} is now calculated replacing into equation (6.42). The next term to model in equation (6.28) is S_{2ndBU}, which comprises the surface production due to secondary break-up and is updated using an expression like the restoration equilibrium equation. The time-scale τ_{2ndBU} of the break-up is calculated using the experimental work of Pilch and Erdman (1987). This is a characteristic time where the liquid droplet will break-up due to Rayleigh-Taylor or Kelvin-Helmholtz instabilities and is given by,

$$\tau_{2ndBU} = T_{2ndBU}\frac{D_{32}}{u_{rel}}\sqrt{\frac{\rho_l}{\rho_g}} \tag{6.45}$$

where the relative velocity between the two phases, u_{rel} can be computed using the Reynolds stresses (Lebas et al. (2009)) as,

$$u_{rel} = \frac{R_{jl}}{\tilde{Y}_l(1-\tilde{Y}_l)} \tag{6.46}$$

T_{2ndBU} is the total dimensionless characteristic time of drop break-up defined as the time when the drop and its fragments no longer break-up and is given by (Pilch and Erdman (1987))

$$T_{2ndBU} = \begin{cases} 6(We-12)^{-0.25}, & 12 \leq We \leq 18, \\ 2.45(We-12)^{0.25} & 18 \leq We \leq 45, \\ 14.1(We-12)^{0.25} & 45 \leq We \leq 351, \\ 0.766(We-12)^{0.25} & 351 \leq We \leq 2670, \\ 5.5 & We \geq 2670 \end{cases} \tag{6.47}$$

The equilibrium Weber number for the secondary break-up is equal to,

$$We^*_{2ndBU} = 12(1+1.077Oh^{1.6}) \tag{6.48}$$

and assuming the effect of viscosity negligible, the Ohnesorge number can be considered zero, hence $We^*_{2ndBU} = 12$. The equilibrium Σ^*_{2ndBU} is obtained and S_{2ndBU} is updated.

Superheated jets

Finally, the last term in equation (6.28) is S_{vap}, which is responsible for the change in interface density due to evaporation. This term is usually omitted in the literature since there is no available model valid for all the spray regions. In cryogenic superheated liquids such as Liquefied Natural Gas (LNG) or in many refrigerants, evaporation could be important. Accepting the classical view, drop evaporation dominates dilute sprays in the same way break-up dominates dense sprays. Hence S_{vap} might have a contribution to the equation for Σ comparable to the other terms on the RHS of (6.28). The contribution of this term can be split into a dense and dilute part, e.g $S_{vap} = S_{vap,den} + S_{vap,dil}$. The distinction to dense and dilute contribution for the evaporation source term is proposed here for the first time since different conditions for the dense and dilute regions are acknowledged Faeth (2002). In the dilute region, the liquid structures that occur in the flow can be considered to be spherical droplets. Then it is

$$S_{vap,dil} = f_{v,s}\frac{\bar{\Sigma}^2}{\rho} \tag{6.49}$$

The logic behind this formulation is that the term $f_{v,s}$ is the mass transfer due to vaporisation per surface and is multiplied with the surface per area and surface per volume. The mass flux at the surface of a droplet of radius r_s is $f_{v,s} = m_v/4\pi r_s^2$, where m_v is the mass vaporisation rate typically taken from a droplet evaporation model. From Abramzon and Sirignano (1989) one gets $m_v = 2\pi\rho_g D_{32}\mathfrak{D} ln(1+B_M)Sh^*$, where $B_M = Y_l/(1-Y_l)$ is the mass transfer number (Spalding number). The modified Sherwood number, Sh^* depends on the flow characteristics, $Sh^* = Sh^*(Re,Sc)$ and is a function of Sherwood, Reynolds and Schmidt numbers. The modified Sh^* is calculated as in Abramzon and Sirignano (1989)). Substituting the expression of D_{32} we get

$$S_{vap,dil} = -\frac{\mathfrak{D} Sh^* ln(1+B_M)}{6Y_l}\left(\frac{\rho_l\rho_g}{\rho^2}\right)\bar{\Sigma}^3 \tag{6.50}$$

The above expression has units $[1/ms]$. It is important to mention that this formulation depends on the drop evaporation model expression that is used in each case. For instance, if one includes the extra term $(Y_l - Y_\infty)$ the Y_l in the denominator vanishes. Ignoring the vapour film around the droplet, we can assume $Sh = Sh^*$ and the vaporisation model of Spalding (1953) can be retrieved. In the dilute region of the spray, we expect that evaporation on the drop surface leads to surface reduction alongside with the droplet radius decrease justified by

the D^2-law. Consequently, a minus sign is included on the RHS of the above formula. Finally, it is worth-mentioning that the terms containing Y_l in equation (6.50) form a function of Y_l that tends to 1 for $Y_l \to 0$ which means that the term scales to $K\bar{\Sigma}^3$, where $K = \mathfrak{D}Sh^*/6$. The constant K can take a wide range of values depending on the flow. For instance, for $Re = 10^5$ and $Sc = 1$ calculating Sherwood number as $Sh = 2 + 0.552Re^{1/2}Sc^{1/3}$, $Sh = 176.55$ which for water at 25^oC, $\mathfrak{D} = 0.282 \cdot 10^{-4} m^2/s$ and one takes $K = 8.3 \cdot 10^{-4} m^2/s$. Typical values for $\bar{\Sigma}$ are $\mathscr{O}(10^5)$ down to $\mathscr{O}(10^2)$ for smaller ligaments which means that $K\bar{\Sigma}^3$ could have a lower limit of $\mathscr{O}(10^2)$.

Regarding the dense part, $S_{vap,den}$, a simple correlation is introduced here, originally proposed in Lyras et al. (2017a),

$$S_{vap,den} = \frac{\bar{\Sigma}}{\Theta}\left(\frac{x_{eq}\rho_{eq}}{\rho} - x\right) \tag{6.51}$$

where the "eq" index stands for the thermodynamic equilibrium of each illustrated variable. Since in the primary atomisation region, the liquid core is likely to remain in a metastable condition it is postulated that the relaxation time-scale might be appropriate in (6.51). The time-scale Θ can be used regardless the boiling mechanism one might assume for the numerical simulation, e.g. homogeneous or surface boiling.

The evaporation source term is then summarised as

$$S_{vap} = \Psi\left[\frac{\bar{\Sigma}}{\Theta}\left(\frac{x_{eq}\rho_{eq}}{\rho} - x\right)\right] + (1-\Psi)\left[-\frac{Kln(1+B_M)}{Y_l}\left(\frac{\rho_l\rho_g}{\rho^2}\right)\bar{\Sigma}^3\right] \tag{6.52}$$

The Σ-equation can now be written as

$$\frac{\partial\bar{\Sigma}}{\partial t} + \frac{\partial\tilde{u}_j\bar{\Sigma}}{\partial x_j} = \frac{\partial}{\partial x_j}\left(\frac{\nu_t}{Sc_t}\frac{\partial\bar{\Sigma}}{\partial x_j}\right) + \Psi\left(S_{init} + S_{turb} + S_{vap,den}\right) + (1-\Psi)\left(S_{coll} + S_{2ndBU} + S_{vap,dil}\right) \tag{6.53}$$

The full form of the surface density equation with all the terms is now

$$\begin{aligned}\frac{\partial\bar{\Sigma}}{\partial t} + \frac{\partial\tilde{u}_j\bar{\Sigma}}{\partial x_j} = \frac{\partial}{\partial x_j}\left(\frac{\nu_t}{Sc_t}\frac{\partial\bar{\Sigma}}{\partial x_j}\right) + \Psi\left[\frac{Y_l(1-Y_l)}{l_t} + \frac{\bar{\Sigma}}{\tau_t}\left(1 - \frac{\bar{\Sigma}}{\bar{\Sigma}^*_{turb}}\right) + \frac{\bar{\Sigma}}{\Theta}\left(\frac{x_{eq}\rho_{eq}}{\rho} - x\right)\right] \\ + (1-\Psi)\left[\frac{\bar{\Sigma}}{\tau_{coll}}\left(1 - \frac{\bar{\Sigma}}{\bar{\Sigma}^*_{coll}}\right) + \frac{\bar{\Sigma}}{\tau_{2ndBU}}\left(1 - \frac{\bar{\Sigma}}{\bar{\Sigma}^*_{2ndBU}}\right) - \frac{Kln(1+B_M)}{Y_l}\left(\frac{\rho_l\rho_g}{\rho^2}\right)\bar{\Sigma}^3\right]\end{aligned} \tag{6.54}$$

The developed method is implemented within the open source CFD code OpenFOAM (Weller et al., 1998). Typically a second order bounded scheme is used to solve this equation together with a van Leer limiter. The method presented in the previous chapter for calculating the

pressure is naturally coupled with the modified version of ELSA model proposed here. The vapour mass fraction equation is solved prior to the surface density equation calculating the mass fractions and the related source terms in Eq.(6.53). The HRM and modified ELSA are coupled for the first time with interface tracking to simulate superheated liquid jet atomisation. The PIMPLE algorithm, combination of the PISO and SIMPLE algorithms, (Ferziger and Peric, 2001) is used to couple pressure and velocity in a segregated manner. After calculating x the matrix $H(u_j)$ which contains all the terms the momentum equation, except for the gradient of pressure, is updated and is used to calculate the fluxes without the contribution of ∇p. The pressure equation is solved including the contributions of surface tension, thermal non-equilibrium e.t.c. and a new velocity field is obtained which will be relaxed (under-relaxation factors for pressure, velocity and surface density were within the range of 0.3 to 0.7). In most of the simulations 5 to 8 PISO loops were used with 1 to 3 outer loops for updating the $H(u_j)$ matrix using Courant numbers up to 2.2. Fixed values for pressure and velocity were imposed at the inlet flow with a boundary condition developed by Poinsot and Lelef (1992) for p and zero gradient for u at the low-pressure farfield (two-phase jet outlet). For LES velocity and viscosity boundary conditions are set following Montorfano et al. (2013). A second-order bounded scheme (Jasak et al., 1999) for the convective terms was used for the calculations. The scheme is a blend of upwind and central scheme using a smooth transition between the low order to the second order scheme offering a good trade-off of accuracy and stability. Second order schemes with a linear correction were used for the gradient terms. The variables are stored in the cell centres in a co-located arrangement and they are interpolated at the cell faces. The relationship of HRM, ELSA and interface tracking model are summarised in the following pseudo-code:

```
while (PIMPLE)
solve x-equation (HRM)
solve y-equation
calculate Y_l
If (turbulent):  include turbulence model
solve Σ-equation
If (interface tracking):  calculate volume fraction or distance function
```

6.3 Results and discussion

6.3.1 Short L/D: Yildiz (2005) experiments

Numerical simulations were performed using the series of experiments from the FLIE project Yildiz (2005) investigating flashing releases of R134A (1,1,1,2 – Tetrafluoroethane: $CF_3 - CH_2F$). The experimental domain consists of a high-pressure region where R134A is stored at a pressure above its vapour pressure at ambient conditions (663 kPa at 293.15 K). The liquid passes through a nozzle of diameter D and length L and is released into a low-pressure region which is equal to the atmospheric pressure. The computational domain and its discretisation consisting of 2.0 million hexahedral cells are shown in Fig. 6.3. The curvature at the walls in the nozzle exit is not considered for the present simulations. The liquid core is more dense around the centreline of the jet, which indicates that finer mesh is needed there. The physical parameters for the simulations are shown in Table 6.1. The present calculations were performed in a 12-core personal workstation and the solution took approximately 3.5 days. The cases tested here concern the geometry in which $L = 4$ mm and $D = 2$ mm. Keeping in mind the importance of the flash boiling or the geometry impact on the spray, the flow is simulated inside the nozzle avoiding arbitrary assumptions for the jet inlet in the lower pressure region. The results presented in this subsection are included in Lyras et al. (2017a). Fig. 6.4 illustrates the velocity distribution. The jet is emerging in the atmosphere with a velocity of approximately 32 m/s, which is in good agreement with the experimental observations. The liquid core that is observed in the vicinity of the centreline of the jet has the highest velocity. This is obvious in both inside and outside the nozzle. As long

Table 6.1 Initial conditions and nozzle details for the Yildiz (2005) experiment.

	Physical parameters for simulations
Inlet pressure	800 kPa
Inlet temperature	293.35 K
Outlet pressure	100 kPa
Outlet temperature	298 K
L/D	2
Nozzle diameter	2mm
Superheat degree	47K

as we move along the centreline the jet morphology changes with an enhanced evaporation on its surface. The change in the jet regime at the beginning of the release is clearer in Fig. 6.5.

The liquid core is dense with a high number of liquid ligaments close to the nozzle, and the liquid volume fraction has its highest value, close to one. A few diameters away

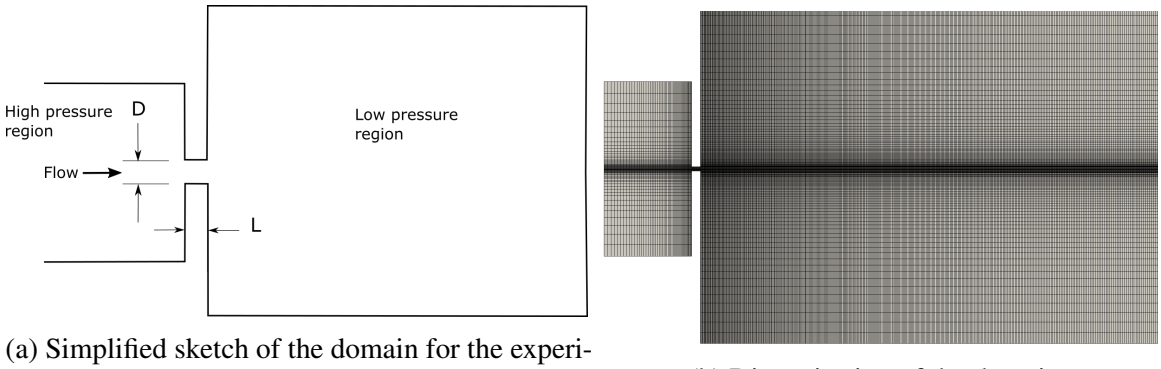

(a) Simplified sketch of the domain for the experiments in Yildiz (2005).

(b) Discretisation of the domain.

Fig. 6.3 Representation of the domain

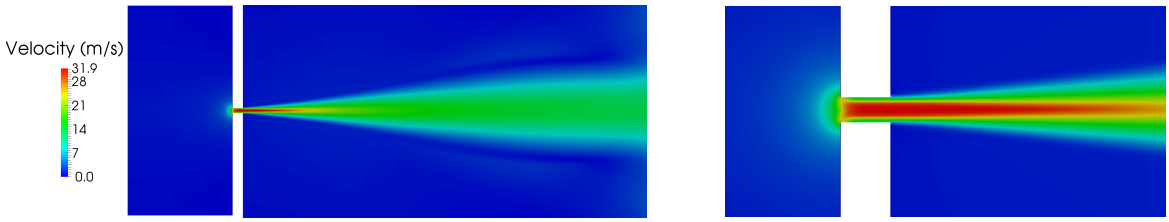

(a) Velocity profile projection for the selected case.

(b) A closer caption of the velocity.

Fig. 6.4 Converged jet velocity, Lyras et al. (2017a).

from the nozzle exit, the liquid volume fraction decreases until it reaches the lowest limit of zero. For a distance up to $200D$, two regions of this decrease can be identified which correspond to different slopes in the graph in Fig. 6.5-b. The same trends are observed in other numerical works (see in Navarro-Martinez (2014)). The bandwidth of these regions is affected by the thermophysical properties and is expected to differ for cryogenic releases and non-evaporating jets. Previous studies in flashing jets indicate a rapid phase change as soon as the local pressure drops lower than the saturation pressure. The initiation of this phase change is more likely to happen within the nozzle for longer nozzles but is also possible for short nozzles with L/D less than seven like here, even in low superheat degrees Simoneau (1975). The jet vaporises within the nozzle, and the flow separation at the sharp inlet corners results in a pressure drop and consequently in phase change (for more details see in Schmidt (1997)). Because of this, the flow becomes two-phase, and the liquid volume fraction decreases close to the nozzle walls as shown in figure Fig. 6.5-b. The same behaviour is observed in the density. Hence, the jet at the nozzle exit, cannot be considered as a pure liquid. Additionally, the method presented in the previous chapter can predict the amount of the vaporised liquid giving a realistic prediction for the jet morphology downstream. Another important parameter for modelling atomisation is the mean interface density and its

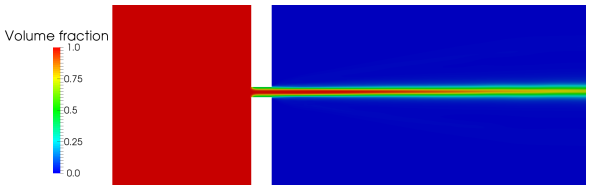

(a) In the whole domain.

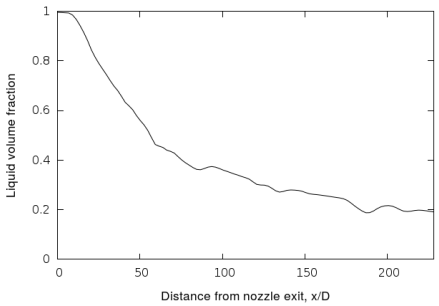

(b) In the centreline of the jet.

Fig. 6.5 Liquid volume fraction for the properties of Table 6.1, Lyras et al. (2017a).

evolution. Σ is calculated via equation 6.28 comprising all the possible processes that could cause an increase or decrease in the liquid-gas interface. The equation is highly non-liner and a second order of accuracy bounded scheme for the convective terms in the Σ-equation is used. A typical distribution of Σ is illustrated in Fig. 6.6. It is expected to be higher closer to the nozzle exit where the initiation term *Sinit* dominates. The source term S_{init} dominates the Σ generation initially and together with S_{turb} are the most important source terms in the primary atomisation region. On the contrary the terms S_{coll}, S_{2ndBU} are less important in the vicinity of the nozzle exit hence Ψ is equal to 1 in this case. The terms S_{coll}, S_{2ndBU} are dominant in the secondary break-up region where droplets are generated due to aerodynamic break-up and collisions. These terms prevail in the $\Sigma-$equation, and Ψ tends to zero for the diluted regions. The terms S_{init} and S_{turb} are expected to be of minor importance in this case. The source term S_{vap} is more important in the primary atomisation, and two/three-dimensional numerical investigations showed that usually is smaller than the other source terms in equation 6.28. From 6.36, the initial interface density is a function of the liquid mass fraction gradient which is greater close to the injection region. After the injection, the jet starts to fragment, and interface is created. Consequently, Σ is increasing. During the primary atomisation, large blobs and ligaments form, which is also reported in Yildiz (2005) in the experiments. After reaching a peak value, Σ starts to decrease rapidly. Some diameters after the peak value, the interface density reduces to $\mathcal{O}(10)$. In this region, apart from the evaporation process, the secondary break-up takes place and causes the large ligaments to burst into smaller droplets which leads to an increase in the interface density. That is why the source term S_{2ndBU} is positive in the Σ-equation. The contribution of the source term due to droplet collisions, S_{coll} is also included in this part of the spray. The droplet size is defined in the regions where the liquid mass fraction and interface density are non-zero. It is calculated as $D_{32} = \frac{6\bar{\rho}\tilde{Y}_l}{\rho_l \tilde{\Sigma}}$ and some two-dimensional results are shown in Fig. 6.6 for the Sauter mean diameter (D_{32}) along the jet centreline. The D_{32} is higher

close to the nozzle exit where the jet is almost pure liquid at the centreline. After almost five diameters, the D_{32} order is of some hundreds of microns. As mentioned before, flashing is a process very efficient in the aerosol industry for producing fine sprays. Hence, the resulting D_{32} values are reasonable and in relatively good agreement with the experimental data from Yildiz (2005). Three-dimensional simulations performed showed that along the radial axis, D_{32} is maximum at the jet centreline and decreases along the radial axis. The axial velocity

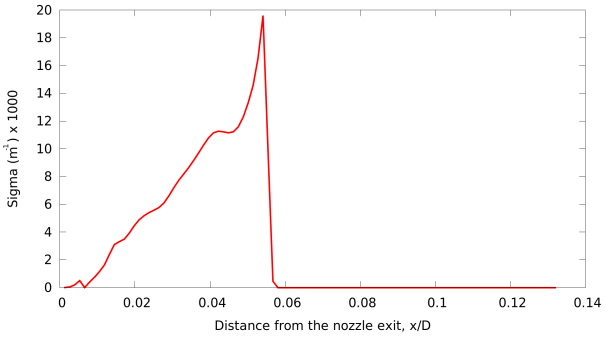

(a) Axial interface density distribution.

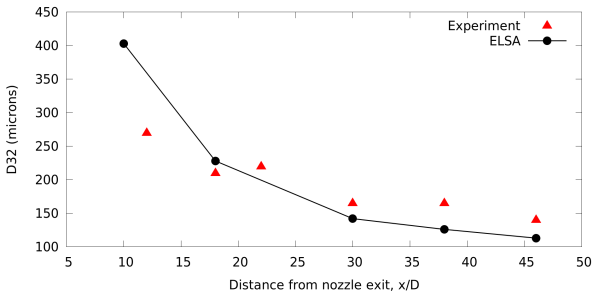

(b) Sauter mean diameter in the centreline of the jet for the modified ELSA compared to Yildiz (2005).

Fig. 6.6 Modified ELSA model simulations, Lyras et al. (2017a).

obtained from the modified ELSA at the primary atomisation region is shown in Fig. 6.7 comparison to the PIV and PDA experimental results. The velocity ranged in the simulations between 32 m/s in the dense region, and 1 m/s in the diluted regions. In the simulations, the peak velocity is observed a few diameters after the jet exits to the atmosphere whereas in the experiments the peak velocity is reported in the region between $10-18D$ as illustrated in Fig. 6.7. The velocity obtained from ELSA model is high and almost constant within this range which is possible according to Yildiz (2005) for the expansion region. The velocity in the modified ELSA decreases with further increasing the distance from the nozzle exit. For example it gets half at $x/D = 110$ Yildiz (2005). The pressure distribution alongside the nozzle is shown in Fig. 6.8-a. The dimensioned pressure is shown here, as presented in the 28th ILASS conference. For the studied release conditions, the vapour pressure is $p_{sat} = 6.63bar$. Non-zero vapour exists inside the nozzle as a result of homogeneous bubble nucleation due to flashing. The patterns of the void fraction inside the nozzle are shown in Fig. 6.8-b. The values at the inlet and outlet of the nozzle are shown for a quantitative comparison. The trends are familiar from the cases simulated in the previous chapter. At nearly $r = 0.8D$ the flow is occupied by a significant amount of gas phase, and the void fraction is more than 0.7 increasing towards the nozzle walls. Regarding the jet behaviour the vapour quality and jet velocity are shown in Fig. 6.9 and Fig. 6.10 respectively. It is evident that both figures follow self-similar patterns moving further away from the nozzle

exit. Since experimental data for the radial profile of velocity are not available, we can only proceed to an analysis of the flashing impact on the jet comparing the axial velocities. The nearly constant axial velocity (only a small increase in axial velocity was reported) at the jet centreline combined with the high superheat degree) shows that flashing effects are not clear in this region ($x/D < 50$). Drastic flow acceleration is not observed in the simulations and the jet seems to continue to evaporate moving further away signalling a phase change and the progressive regime change. In Fig. 6.11 two different captions of the same case in Table 6.1 are shown. The RANS approach is used to model the 3D jet offering an illustration of the jet structure at $x/D = 220$. The liquid fragmentation happens as a result of the fluid flow instabilities that occur on the jet enhanced by the flash-boiling mechanism. The result is the characteristic liquid fragmentation with blobs and ligaments leaving the jet during the primary atomisation process.

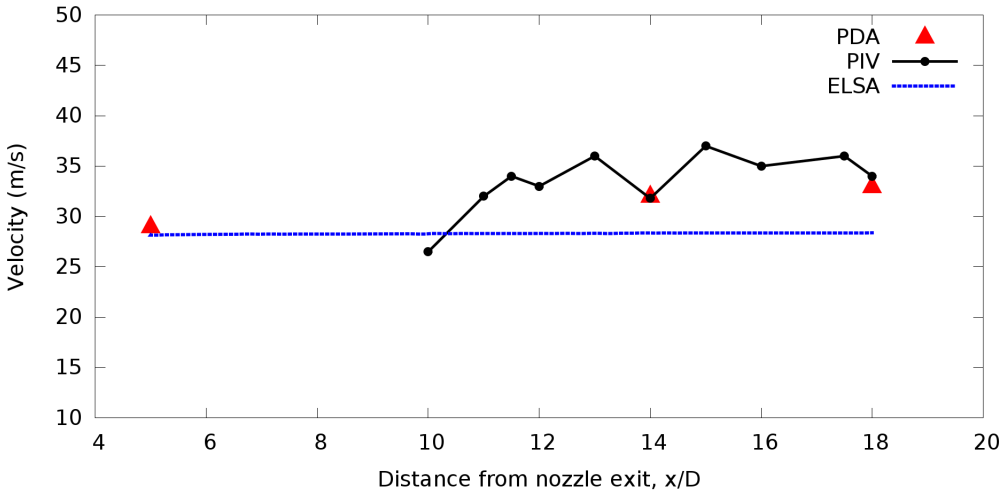

Fig. 6.7 Centreline velocity (Lyras et al. (2017a)) for the new ELSA compared to Yildiz (2005).

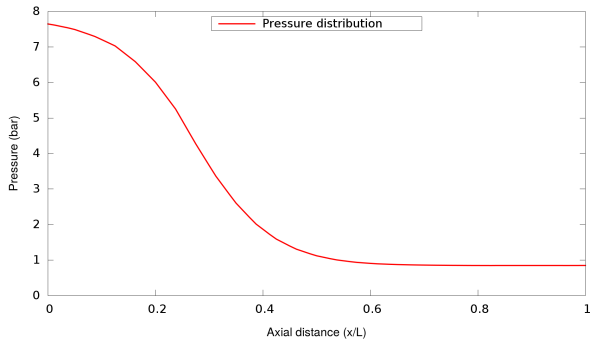

(a) Axial pressure distribution alongside the nozzle.

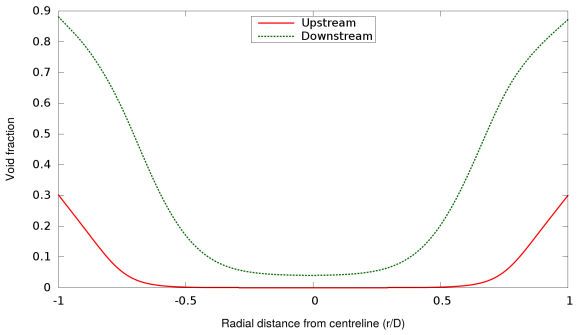

(b) Void fraction at the upstream and downstream locations of the nozzle.

Fig. 6.8 Inside the nozzle flow, Lyras et al. (2017a).

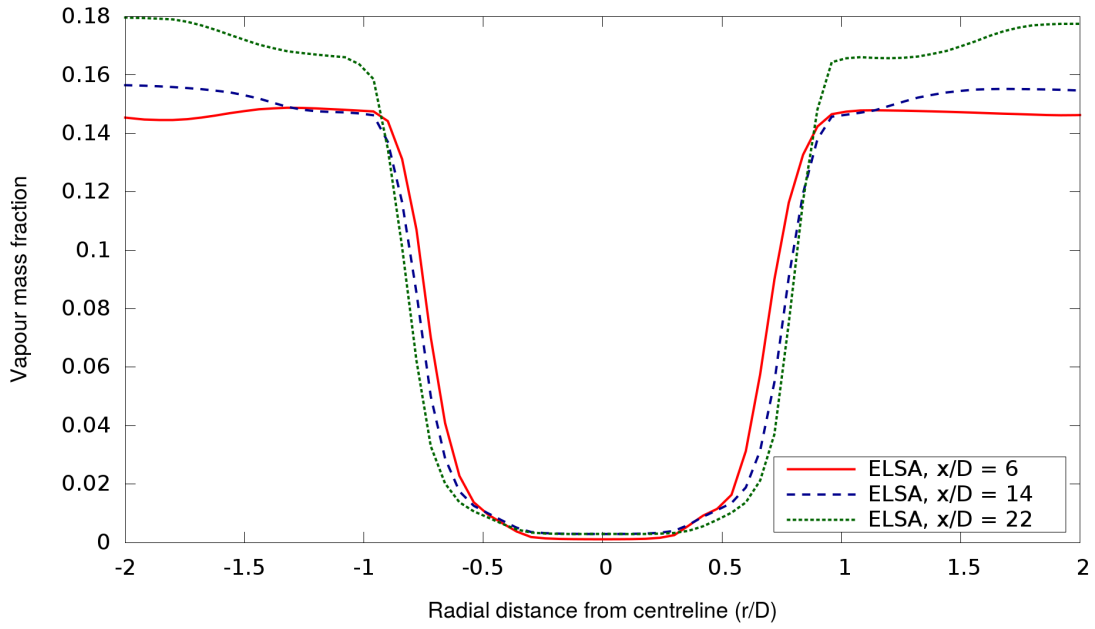

Fig. 6.9 Vapour quality at different locations downstream the nozzle exit, Lyras et al. (2017a).

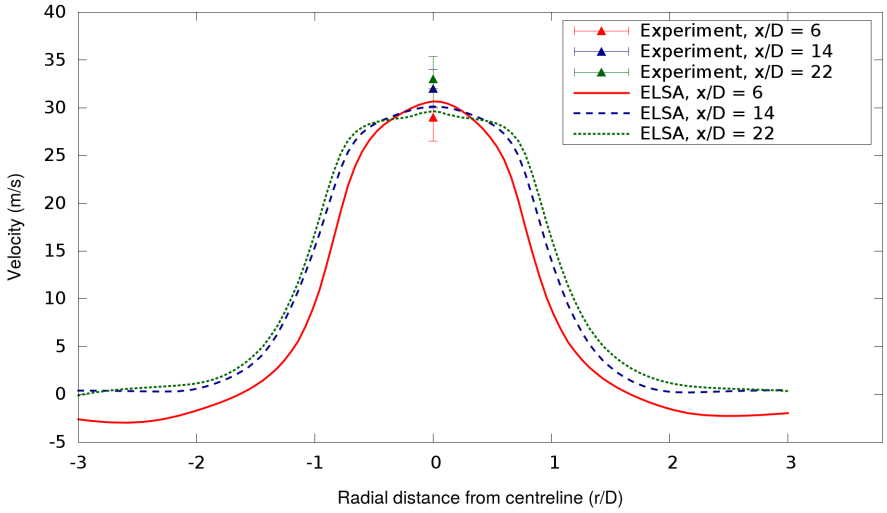

Fig. 6.10 Axial velocity at different locations downstream the nozzle exit, Lyras et al. (2017a).

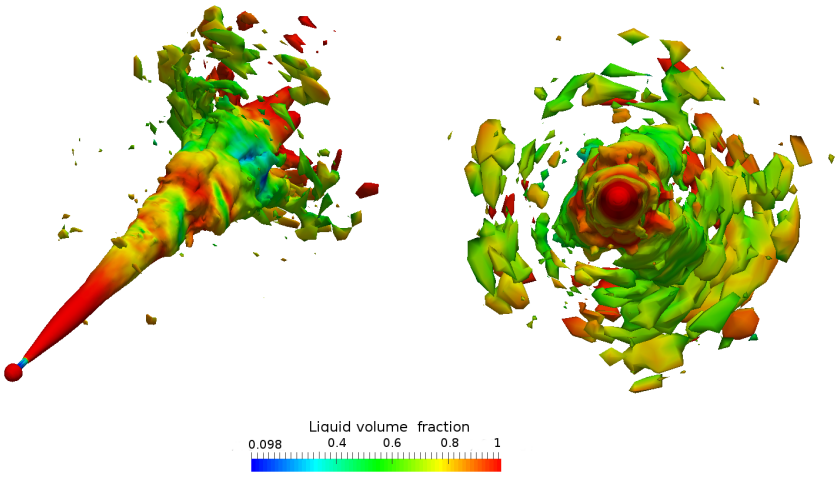

Fig. 6.11 3D representation of the STEP project simulations. The liquid volume fraction is shown from two different angles, Lyras et al. (2017a).

6.3.2 Higher L/D: Zhifu et al. (2012) experiments

The experiments presented before concerned small L/D and a diameter $D = 2mm$. The resulting jet analysis showed that the axial velocity does not change in the vicinity of the nozzle exit. The consequent large values of droplet SMD might be an indication that the jet flashes outside the nozzle. It is of major importance to investigate the changes in the spray

patterns with respect to macroscopic changes. For this reason, the experimental work of Zhifu et al. (2012) has been studied and simulated. In this experiment R134A flows through a long nozzle with $L/D = 78.4$ and diameter equal to $D = 0.81mm$. The domain used for simulations is shown in Fig. 6.12. Different meshes were used with 1.0, 1.5 and 2.0 million cells for RANS calculations and the results were found to be independent of the grid resolution (results from the 1.5 million mesh are shown here which took approximately 3 days). The spray characteristics, the velocity and the Sauter mean diameter at various positions were measured. The flow patterns inside the nozzle were not studied in the experiment. Both RANS and LES framework were used. In Fig. 6.13 an example of small-scale LES simulations is shown for the experiment. The iso-contours of $\tilde{Y}_l = 0.28$ are included to illustrate the very first stages of the liquid jet atomisation. The outlet patches of the simulated domain were far enough, typically in more than $50D$ distance from the jet axis in the radial direction, and at $193D$ from the nozzle exit. RANS results are presented here for validation. The results were taken until steady state reached and any boundary effect at the far-field, downstream the nozzle, has negligible impact. All the physical parameters of the experiment are listed in Table 6.2. The initial pressure was one bar less than in the experiments studied in the previous section. The axial velocity profiles are shown in Fig. 6.14 as a function of the radial distance at two different positions. The axial velocity takes its maximum at the jet centreline in all cases. This is in accordance to the experimental and theoretical studies (Abramovich, 1963) for instance). The same trend is met in single-phase iso-thermal jets in both the potential core and the decay regions where velocity decreases progressively, obtaining a Gaussian shape in the radial direction. An obvious differentiation between the velocity profiles at the two positions occurs for the rate of the velocity decrease moving towards the jet periphery. The results indicate that the distance from the nozzle exit plays a role in the jet dispersion. Axial velocity decreases faster closer to the release point $x = 50mm$ ($x/D = 61.7$), compared to the position $x = 90mm$ ($x/D = 111$) where velocity changes in a smoother manner. This smaller gradient in the largest distance results indicates a more uniform jet morphology in the droplet cloud. The maximum predicted axial velocity at the $x = 50mm$ position is around 35 m/s. The spray velocity starts to increase fast (in the so-called expansion zone) and becomes maximum and then decreases again (entrainment zone). The maximum at the numerical results occurs at approximately x=60mm ($x/D = 60$) whereas in experiments the peak value was observed for a small number of particles in x=40mm ($x/D = 49$). This increase in the axial velocity of the spray was not observed in Allen (1998) and a small increase in Yildiz (2005) was reported. The axial velocity is shown in Fig. 6.15. The jet, after emerging at the low-pressure region, is a dense spray consisting of droplets moving through a vapour cloud, which is a direct consequence of the evaporation mechanism. The acceleration of

the droplets is attributed by the authors of the experiment, to the explosive character of the atomisation of the cryogen. Up to the maximum velocity point, the liquid core might be considered to be practically intact. The velocity starts to decrease due to drag forces which prevail over the inertia forces and govern the droplets' kinematics. From a numerical point of view, this acceleration imposes some major challenges in terms of stability, an under-relaxation procedure for the solution is recommended. The rapid increase and decrease in the axial velocity might cause weakness to the pressure-velocity coupling, and a good choice of turbulence model with near-wall treatment is required from the k-ω family. A second-order bounded scheme (Jasak et al., 1999) for the convective terms was used for the calculations. The scheme is a blend of upwind and central scheme using a smooth transition between the low order to the second order scheme offering a good trade-off of accuracy and stability. Bouncing waves on the walls might also have a major effect on the solution and a proper boundary condition developed by Poinsot and Lelef (1992) was employed. In fact, Fig. 6.15 illustrates all the big challenges of flash atomisation in terms of physics and numerics.

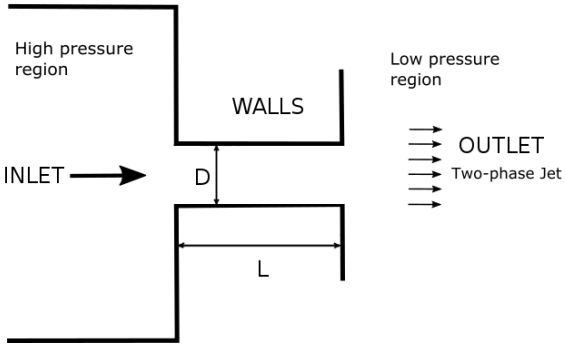

Fig. 6.12 Schematic of the domain used in simulations. The superheated liquid flows through the channel and exits at the low-pressure region as a two-phase jet.

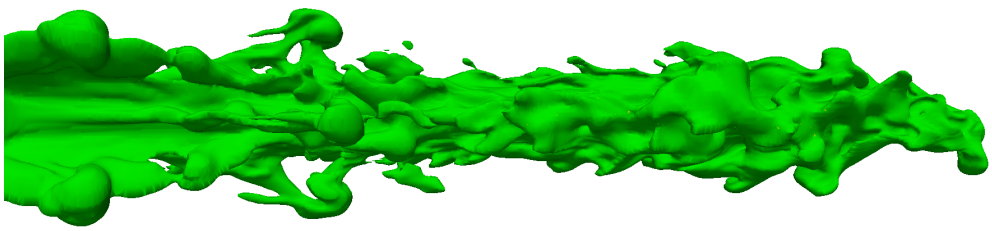

Fig. 6.13 Snapshot of iso-contour $\tilde{Y}_l$ for LES simulations at the first 5mm of spray motion downstream the nozzle exit. A mean cell size equal to $4\mu m$ was used close to the nozzle exit.

Table 6.2 Zhifu et al. (2012) R134A experiments details.

	Physical parameters for simulations
Inlet pressure	700 kPa
Inlet temperature	247 K
Outlet pressure	100 kPa
Outlet temperature	298 K
L/D	78.4
Nozzle diameter	0.81mm
Thermodynamic conditions	Saturated

Regarding the spatial scale of the liquid structures, results for the D_{32} are shown in Fig. 6.16. Quantifying the size of ligaments and blobs that form within the jet is not a trivial task. The limited visibility of the moving particles and the need for non-intrusive measurement techniques makes the experimental characterisation of the mean droplet size extremely difficult. In this experiment, the authors used the phase Doppler Particle Analyzer (PDPA) to measure the spray characteristics. The method uses laser beams that focus on a probe volume and give a signal as soon as a liquid blob passes through. Statistical analysis of the signal gives the SMD which is used for comparison here. Fig. 6.16 shows the radial variations of SMD for $x/D = 61.7$ and $x/D = 111$. The model overestimated the D_{32} closer to the jet centreline and showed good agreement after $1.5D$ distance in the radial direction. This behaviour is reasonable and appears in other numerical studies (see in Vallet et al. (2001)). This can be caused due to the numerical parameters used in the Σ-equation and the source terms in particular. The equilibrium values are also subject to numerical tuning. The difference might also be an indication for changing the HRM constants for R134A. The HRM contribution is both in the pressure update and equation 6.28. A slightly increasing trend in the D_{32} observed in the experiments is also captured from the atomisation model. Fig. 6.16 illustrates the multi-scale character of flash-boiling atomisation. The nozzle length of the experiment was $L = 63mm$. Moving along the nozzle, the flashing inception begins in the internal flow, and one might reasonably assume that at some point the regime transition from pure liquid to a dispersed flow happens. The size of the droplets can be comparable to the nozzle diameter, $\mathcal{O}(10^{-3})m$ initially, and drops due to mechanical and thermodynamic effects to $12\mu m$ at the measured axial positions and becomes $\mathcal{O}(10^{-6})m$ at the radial direction. Hence, the average particle size can be reduced to one thousand times its original size.

The reason for this reduction in spatial scale of the blobs and droplets can be attributed to the explosive character of the atomisation. This character is fundamentally associated with

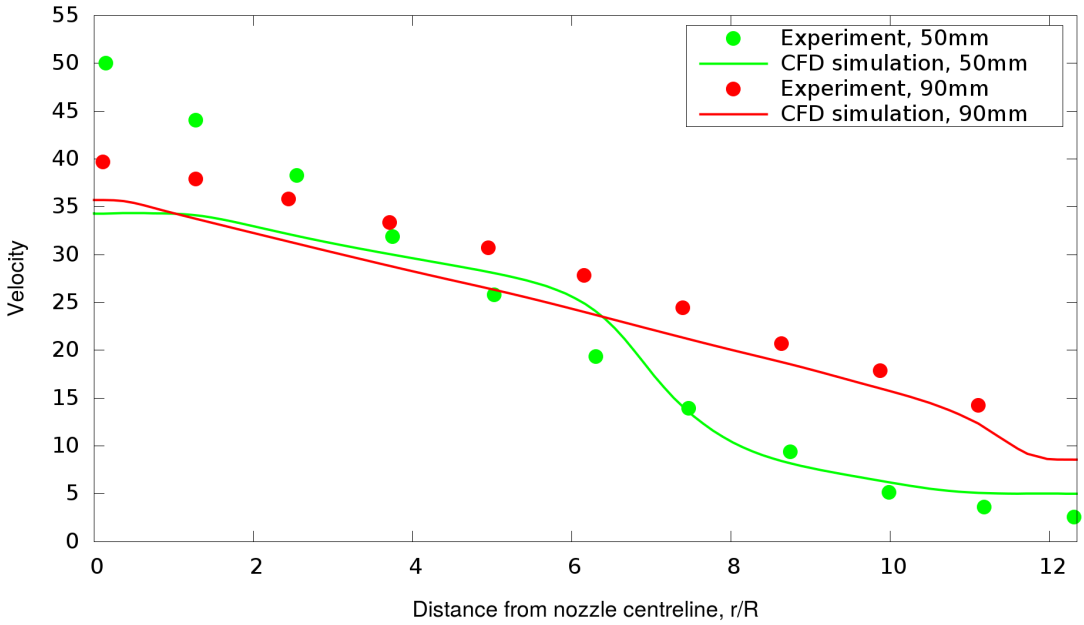

Fig. 6.14 Radial velocity at x=50, 90mm. Comparison with Zhifu et al. (2012).

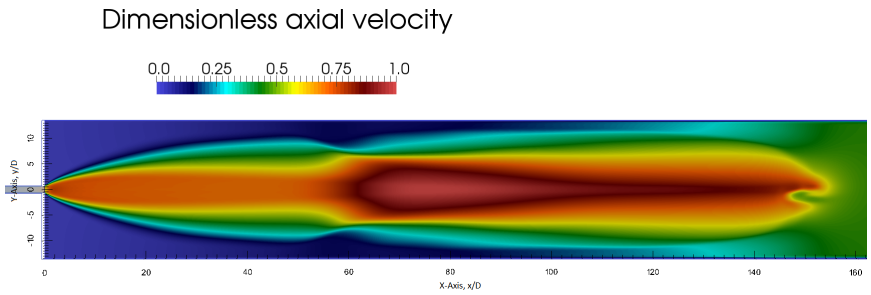

Fig. 6.15 Distribution of dimensionless axial velocity u_x/u_{max} along the normalised distance x/D.

the flashing mechanism which starts inside the nozzle. Results in Fig. 6.16 for D_{32} simulating the same experiment but without considering the internal flow reveal a higher deviation with experiments at $x = 50mm$ but smaller in the $x = 90mm$ position. Exclusion of the internal flow simulation tends to under-predict the SMD at $r/D = 3$ and afterwards for both positions. The droplets emerge to the atmosphere at a temperature higher than the saturation temperature and become locally superheated. This metastable state follows a violent liquid fragmentation (explosive atomisation) with new smaller droplets. Moving further away from the nozzle exit, the flow is expected to become more uniform, with droplet evaporation becoming more important. Droplet evaporation manifests that the smaller droplets moving at the periphery

of the jet become smaller until they are practically negligible. Under these conditions, the mean surface density decreases (Fig. 6.17)

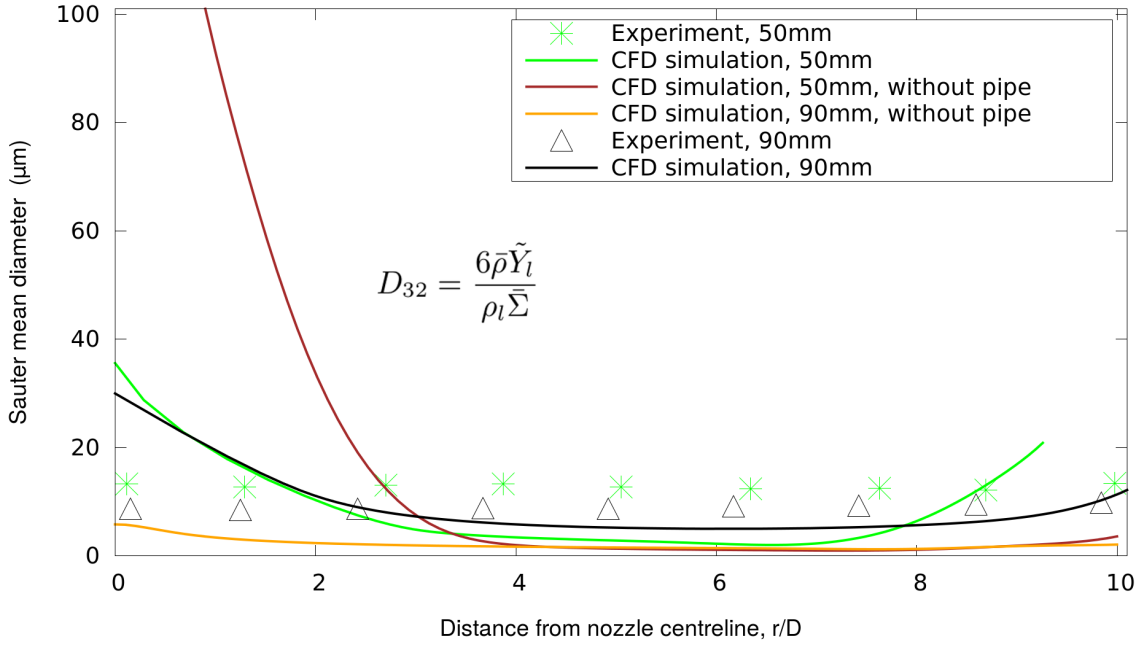

Fig. 6.16 Sauter mean diameter (SMD) at x=50, 90mm. Comparison with Zhifu et al. (2012).

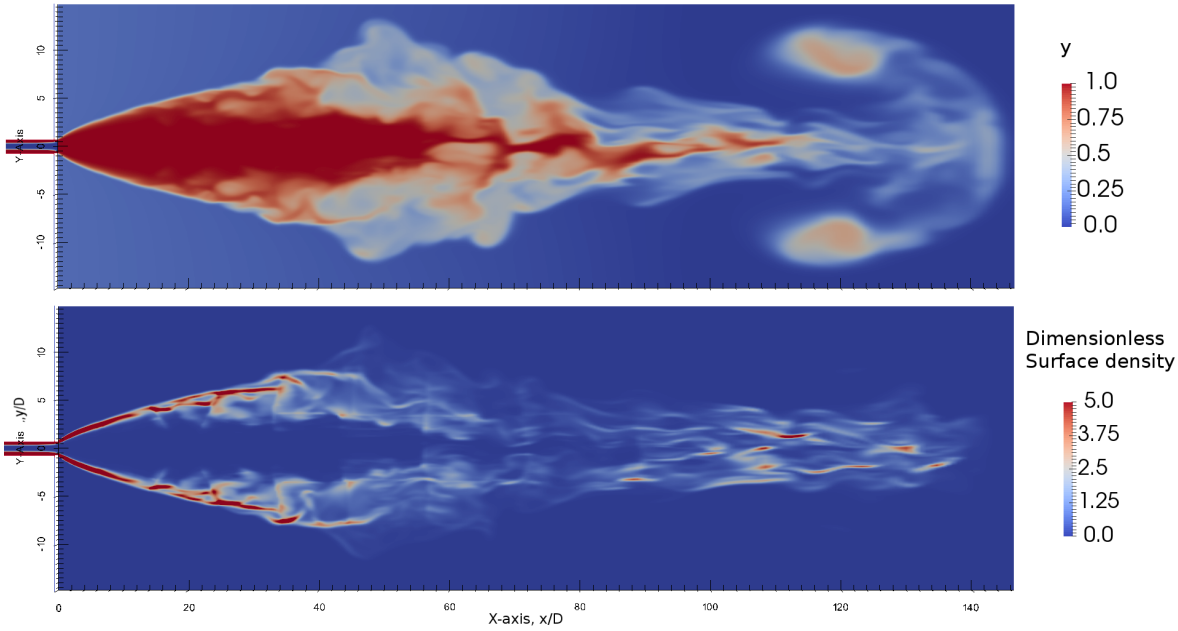

Fig. 6.17 Contours of dimensionless liquid and vapour mass fraction, y and surface density, Σ/Σ_0 along the jet centreline.

which means that the SMD, $D_{32} \propto 1/\bar{\Sigma}$ becomes bigger, hence the increasing trend in Fig. 6.16. In Fig. 6.17 the surface density is shown normalised with a theoretical initial value $\Sigma_0 = 1/\Delta^3$ where Δ is the LES filter used in the simulations. This is the value that Σ will scale with a very fine mesh Navarro-Martinez (2014). This value is expected to be the upper limit for Σ in dilute regions where only small blobs and droplets exist (sub-grid scale). Comparing the results in D_{32} with the experimental findings of Yildiz (2005) one might elucidate the impact of the nozzle geometry on the spray dynamics. The geometry impact is expressed by the length-to-orifice ratio. The average D_{32} in this experiment for a long nozzle was less than $15\mu m$ whereas for an inlet pressure approximately 8bar and a short nozzle with $L/D = 2$ the simulated and measured average droplet size were much higher and remained always greater than $50\mu m$. The nature of the relationship between L/D and SMD was studied by Yildiz (2005). In particular, at $x/D = 110$ the higher values of D_{32} for the longer nozzle were justified from the incomplete atomisation that occurred inside the nozzle for the case of nozzles with larger L/D. Nevertheless, the L/D used in Zhifu et al. (2012) was much larger, and the internal flashing is expected to cause bubble nucleation and bursting earlier, giving in general smaller droplet sizes. A three-dimensional caption of the liquid jet atomisation for shorter $L/D = 4$ using LES with a 15 million cells is presented in Fig. 6.18.

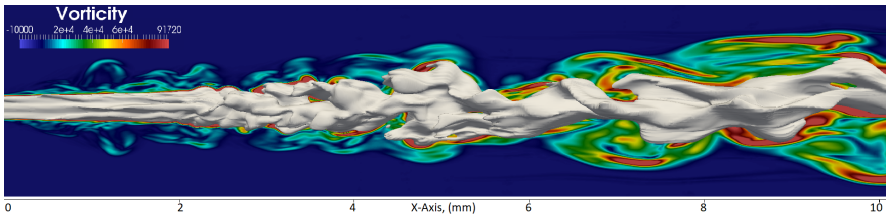

Fig. 6.18 Iso-contour for y=0.47 with the magnitude of vorticity using LES for the first 10mm of the spray. The physical parameters are the same as in Zhifu et al. (2012) but for shorter nozzle $L/D = 4$.

6.3.3 Water experiments, Park and Lee (1994)

The next flashing scenario examined is for water jets flowing through sharp nozzles. The classic experiments of Park and Lee (1994) are considered here. The test cases were for small pressures up to 4bar and initial temperatures up to 125^oC. A long nozzle was used which offers an opportunity to study the internal flashing mechanism in a domain similar to the one in Fig. 6.3. All the major physical properties for the simulations are listed in Table 6.3. LES was tested for simulating the internal flow and the primary atomisation region up to a distance 7D from the nozzle exit using a computational mesh with 17 million hexaedral cells. The Smagorinsky model was used and the sub-grid-scale Reynolds stress, τ^{sgs} is modelled as

$\tau_{ij}^{sgs} - 1/3\tau_{kk}^{sgs}\delta_{ij} = 2\mu_t\bar{S}_{ij}$. The sub-grid-scale eddy viscosity can be derived by dimensional arguments to be equal to $\mu_t = C_S^2\rho\Delta^2 \parallel \bar{S} \parallel$, where $\parallel \bar{S} \parallel = (\bar{S}_{ij}\bar{S}_{ij})^{1/2}$. Here, a low value of the constant $C_S = 0.065$ is used, recommended for channel flows. The calculations were performed using 64 processors and the solution took approximately 2 weeks for converged statistics. Results shown in Fig. 6.19 show the gradual liquid fragmentation though time. The long channel and the low inlet pressure resulted in an increased residence giving time for bubbles to form, burst and collapse signalling a regime change. The growing waves acting on the jet start to influence the jet and the result of these perturbations is evident after some reasonable time, which is expected according to Rayleigh's theory (is more clear here after t=0.0006s). Similar behaviour is observed in the liquid-gas interface in Fig. 6.20. Moving further downstream the nozzle exit, the liquid surface decreases due to large ligaments and blobs shedding to smaller structures. The authors of the experiment investigated a thorough analysis for determining primarily the relationship between the superheat degree and the spray characteristics in low pressure flashing jets. In their study they concluded that for long nozzles bubble nucleation starts at the walls region. They distinguished three regimes for the internal flow: bubbly, annular and slug. They observed that for low superheat degrees the bubbly regime is sustained across the nozzle with bubble formation and growth moving towards the nozzle exit. The bubbles burst outside the nozzle fragmenting the liquid core into ligaments. The intact liquid core becomes shorter with increasing the superheat degree. In this case the bubble nucleation inside the nozzle was reported to be more extensive, predicating a slug or annular regime for the channel flow. During the primary atomisation process in slug regime, the slug bubbles that form from smaller bubbles that collide and coalesce, burst into ligaments. On the other hand, in the annular regime the liquid phase was moved towards the walls and then an enhanced disintegration downstream the nozzle exit due to the interactions with the vapour core gave generally smaller SMD values for the droplets. RANS results for a mesh of 200,000 cells are shown in Fig. 6.21. Both coarser (100,000 cells) and finer (300,000 cells) meshes were used. The present calculations for the fine mesh were performed in a 12-core personal workstation and the fine mesh solution took approximately 2 days. The numerical results in Fig. 6.21 seem to agree with the observations of Park and Lee (1994) that increasing the degree of superheat, the SMD decreases, at least for a constant pressure. Fig. 6.21 illustrates the mean SMD value at the radial direction at distance $x = 50mm$ (x/D=33.3). Results are plotted using the normalised superheat degree

$$\Delta\check{T}_{sh} = \frac{T_{in} - T_{sat}(p_{out})}{T_{sat}(p_{in}) - T_{sat}(p_{out})} \tag{6.55}$$

Small values of $\Delta\check{T}_{sh}$ indicate a non-superheated state of the liquid jet and for $\Delta\check{T}_{sh} = 1$ the liquid boils inside the storage vessel. The results show good agreement for higher superheat degrees. The deviation for $\Delta\check{T}_{sh} = 0.2$ could be associated to the higher residence time inside the channel and the Σ-equation constants. The impact of the initial storage pressure is illustrated in the experimental and numerical results. Bubble nucleation appears to attain a random occurence pattern. Pressure change might also alter the jet stability, with higher pressures leading to a more stable regime (Wang et al., 2017). For the same pressure (p=3bar) increasing $\Delta\check{T}_{sh}$ reduces the SMD. This could be connected to the number of bubbles inside the nozzle which is expected to increase with increasing the superheat degree since the surface tension of the vapour decreases with a consequent decreasing for the departure diameter for the bubble (Hutcherson et al., 1983). Hence, the internal flow becomes more bubbly. In the numerical results, the mean SMD reduces approximately 43 percent of the value for $\Delta\check{T}_{sh} = 0.3$ and in the experiments the mean Sauter mean diameter is 33 percent of the former. On the contrary, keeping the temperature constant, $T_{in} = 110^{o}C$ and decreasing the pressure from 4bar ($\Delta\check{T}_{sh} = 0.2$) to 3bar ($\Delta\check{T}_{sh} = 0.5$) the mean D_{32} decreased approximately $20\mu m$ in the experiment but slightly increases a few microns in the CFD results. The effect of the pressure on the droplet SMD was also studied by Cleary (2008) who suggested that $D_{32} \propto p^{-0.54}$. This suggests that increasing the pressure D_{32} decreases, at least within the limits of the proposed correlation ($L/D < 50$).

Table 6.3 Physical properties for the flashing water experiments of Park and Lee (1994).

	Physical parameters for simulations
Inlet pressure	20-40 kPa
Inlet temperature	110-125^{o}C
Outlet pressure	100 kPa
Outlet temperature	25^{o}C
L/D	72
Nozzle diameter	1.5mm
Thermodynamic state	Saturated

Fig. 6.22 shows the dimensionless spray angle which is the calculated spray angle divided by its maximum value. Both in experiments and CFD the angle is defined as the included angle between the lines connecting the nozzle exit and the points at the spray edge at 20mm (x/D=13.3) downstream the nozzle exit. The angle shows initially an increasing trend increasing the superheat for both cases of 2bar and 3bar. Higher values of superheat correspond to an increment in the number of critical vapour nuclei that form per unit volume and time, J. For higher temperatures, the waiting time for the critical nuclei to form decreases

($\tau \sim 1/J$) giving rise in nucleation rate (Avedisian, 1985) and consequently more vapour appears in jet (see Fig. 6.23). The jet dispersion in the radial direction is wider which indicates that the spray angle is larger. As Park and Lee (1994) point out, the bubbles that form burst and increase the velocity in the radial direction. The spray angle increases until it reaches a maximum and decreases rapidly after. The maximum angle location is not the same for each case. For inlet pressure equal to 2bar it occurs at approximately in $\Delta\check{T}_{sh} \simeq 0.9$ ($T_{in} = 122.5^{o}C$) whereas for the case of 3bar, it occurs at approximately in $\Delta\check{T}_{sh} \simeq 0.65$ ($T_{in} = 120^{o}C$). The spray angle after reaching its maximum starts to decrease due to entrainment effects (see Fig. 6.24). The enhanced atomisation results in a finer spray and the smaller droplets, which are influenced more by drag forces, vaporise until they become negligible or return back to the dense region of the spray. Fig. 6.24 shows the Gaussian shape profile of the radial velocity similar to the ones in single-phase jets. In both flashing and non-flashing jets, the velocity radial profile maintains this shape from the jet centreline and the jet shear layers (Abramovich, 1963).

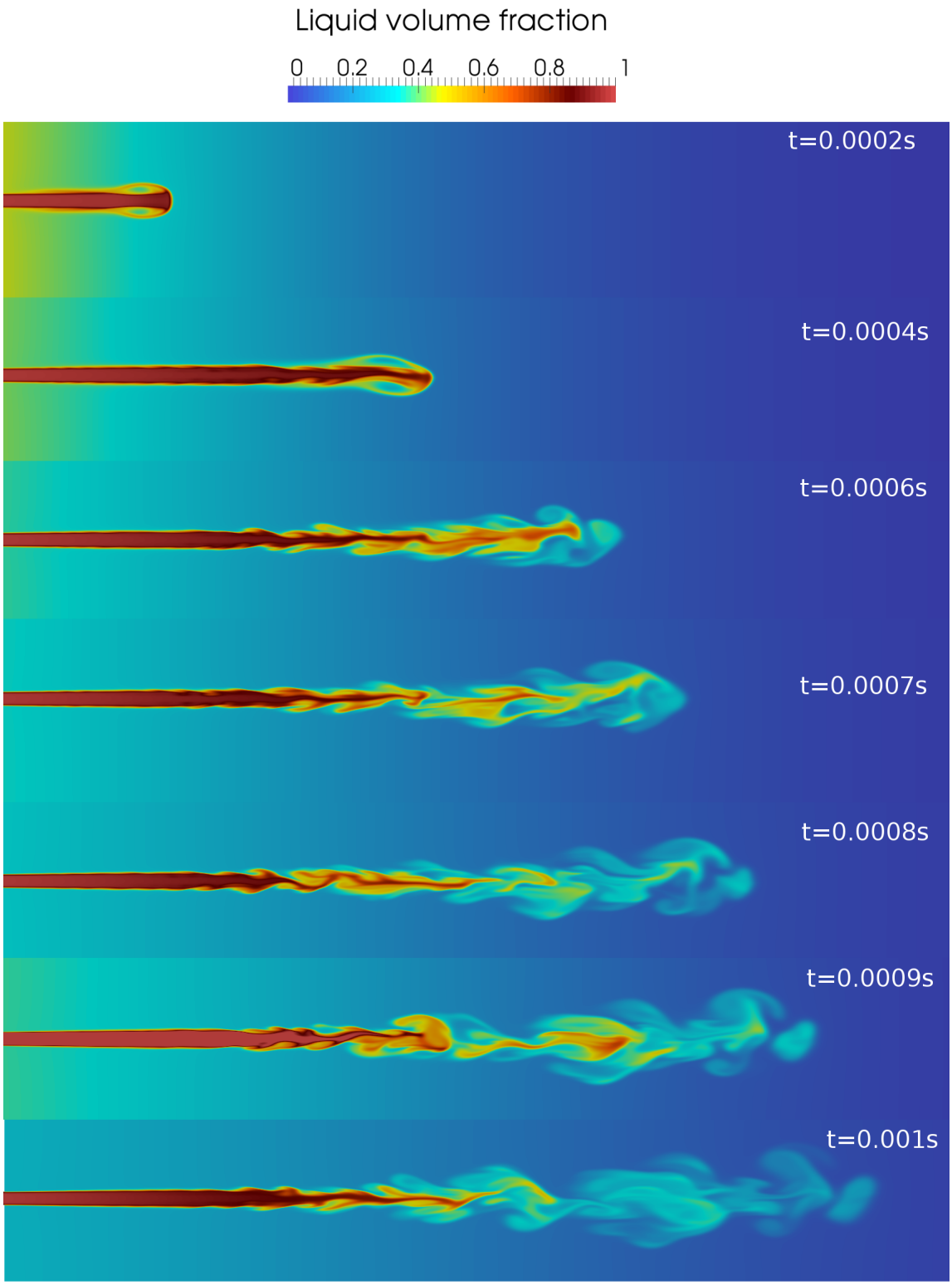

Fig. 6.19 Jet evolution through time for the liquid volume fraction in 3D LES. These are 2D snapshots from the normal plane perpendicular to the jet axis, Lyras et al. (2017b).

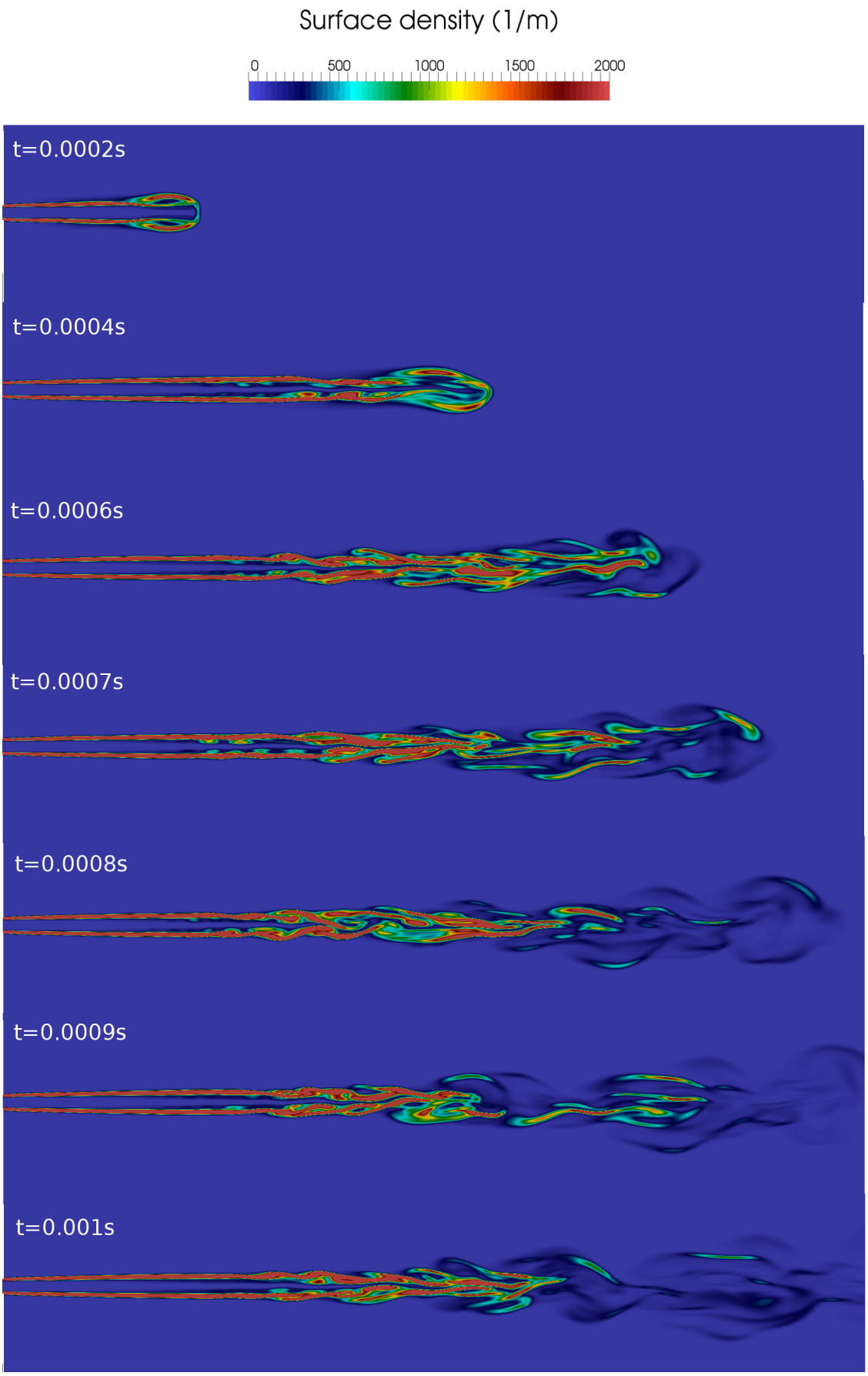

Fig. 6.20 Evolution of Σ with respect to time from 3D LES.

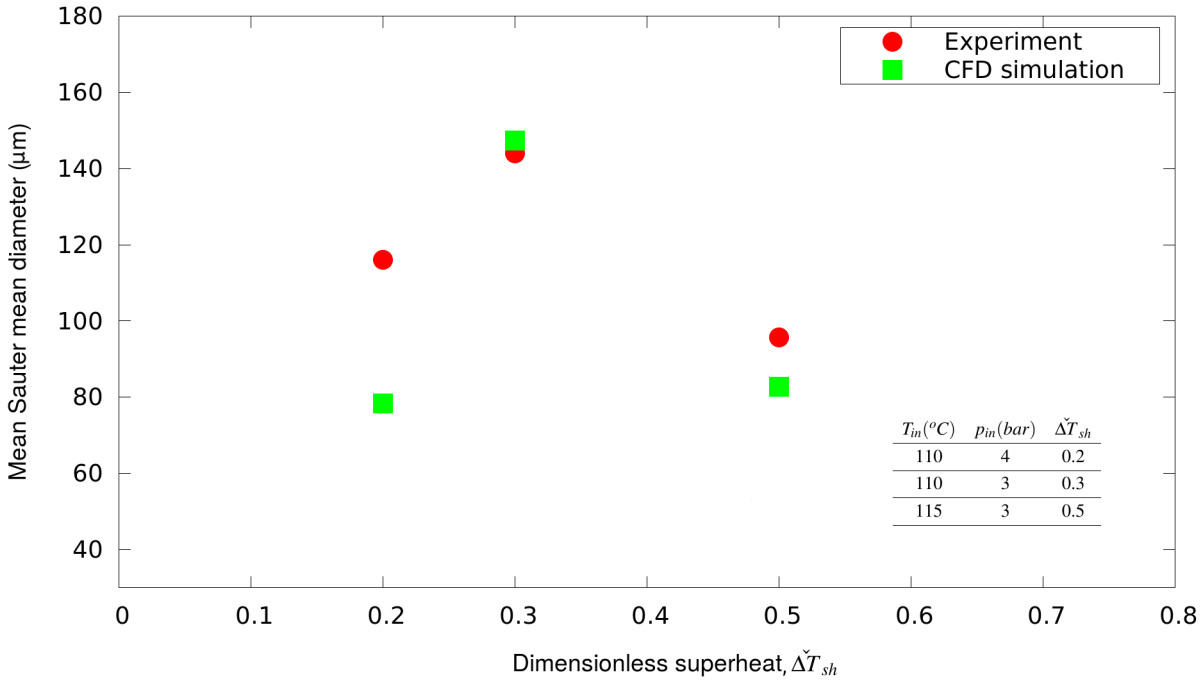

Fig. 6.21 Cross-sectional averaged SMD versus the dimensionless superheat $\Delta\check{T}_{sh}$ at 50mm (x/D=33.3) distance downstream the nozzle exit. Comparison with Park and Lee (1994).

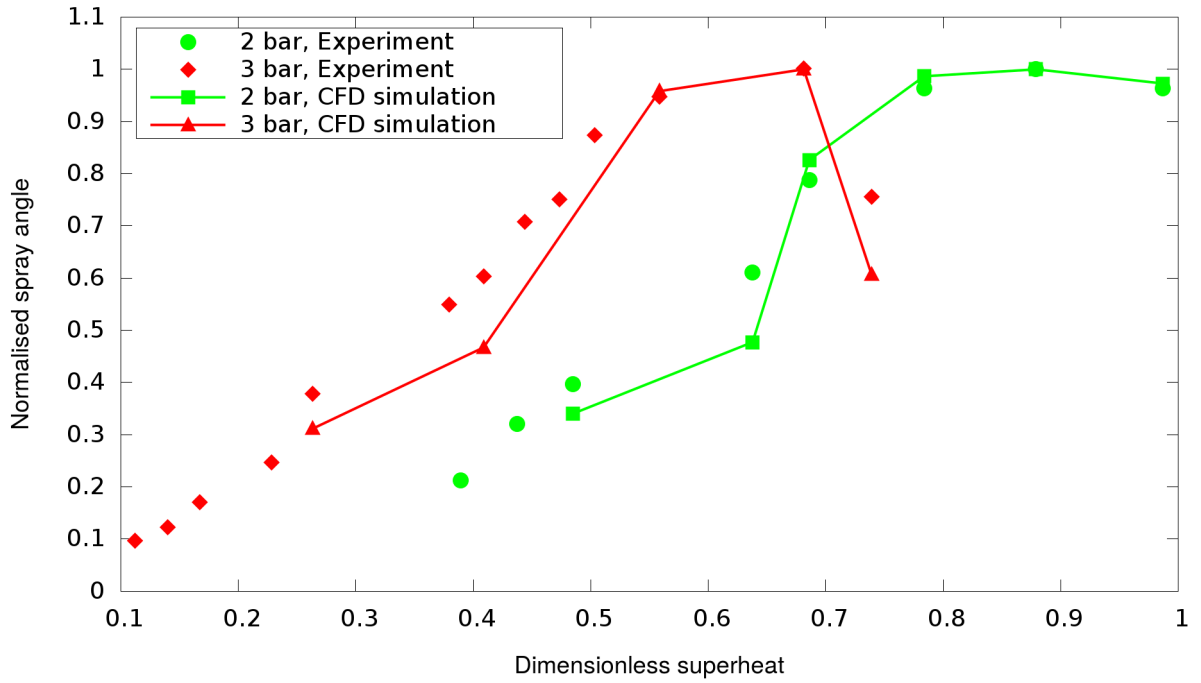

Fig. 6.22 Normalised spray angle with respect to the dimensionless superheat $\Delta\check{T}_{sh}$ at 50mm (x/D=33.3) distance downstream the nozzle exit. Comparison with Park and Lee (1994).

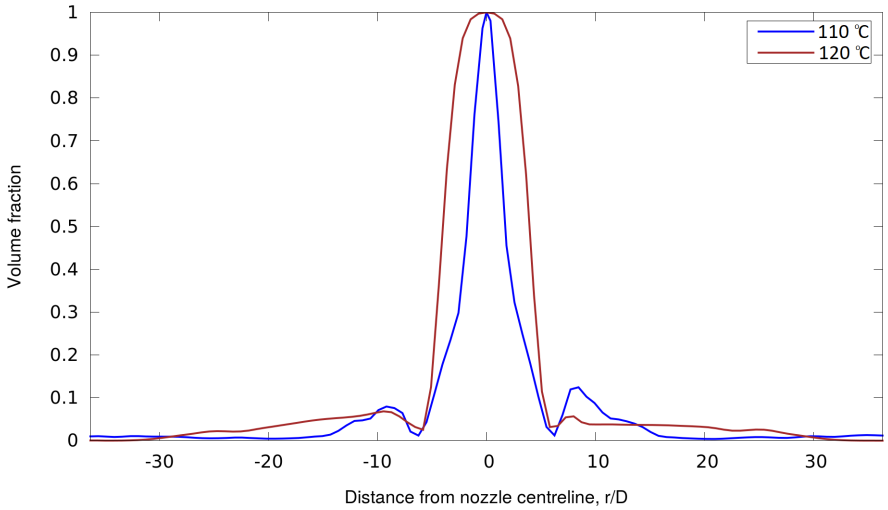

Fig. 6.23 Liquid volume fraction at the radial direction for two different initial temperatures at x=20mm.

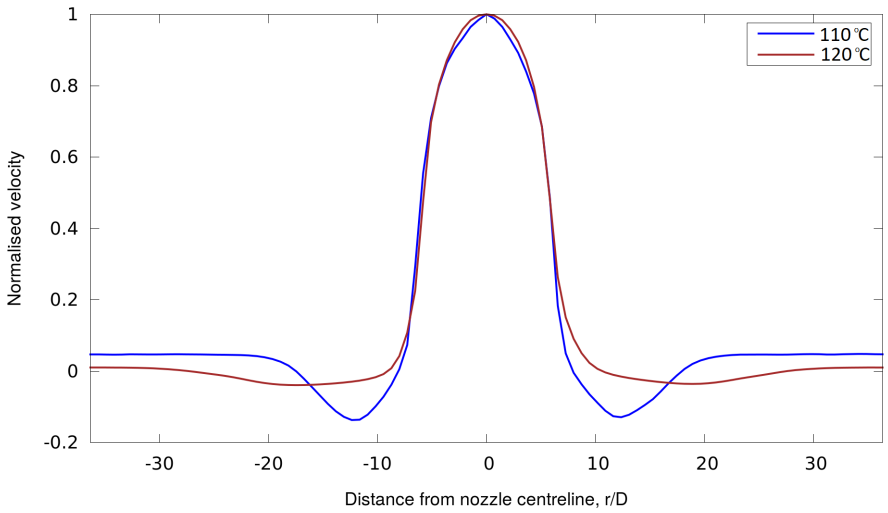

Fig. 6.24 Velocity profile at the radial direction, u_x/u_{max} for two different initial temperatures at x=20mm.

6.4 Application to LNG jets

In this section, an application of the described methodology is presented for the simulation of Liquefied Natural Gas (LNG) releases in the atmosphere in case of an accident like a rupture in a pipeline system or a crack in a storage vessel, valve e.t.c. Since there is no available experimental data in the literature for flashing LNG and LNG spray characteristics,

qualitative results are presented for illustrating the similarities and differences with the previously presented flashing scenarios. Different scenarios are tested here for LNG jets emerging to the atmosphere. Since pressure difference is the driving force for the jet release, the test cases here are divided with respect to the storage pressure to higher and lower pressure.

6.4.1 High pressure LNG jets

First the cryogen (CH_4 : 92%, C_2H_5 : 5%, C_3H_8 : 3%) is assumed to be stored in 30bar and at a low temperature and emerges to a low pressure environment (1bar). The domain is similar to the previous cases in this chapter (see the domain shown in Fig. 6.3) and is 0.6m long. A computational mesh of 3.5 million hexahedral cells was used for the results presented here. The mesh size at the nozzle exit was approximately 0.6mm with a cell expansion ratio equal to 3. The most important parameters of the simulation are shown in Table 6.4. The calculations were performed in a 12-core personal workstation and the solution took approximately 4 days.

A realistic industrial release involves pressure in various operating range and can happen in low (8 bar) or higher pressures (up to 70 bar). LNG is kept stored in very low temperatures under pressure of the order of 110K. When LNG is released in the atmosphere, it interacts with the ambient air which is generally hotter (for instance 293K). LNG starts boiling with a vapour film to be possible to develop in case of structure interactions. From Fig. 6.25 and Fig. 6.26 it is clear that fluid flow instabilities like Kelvin-Helmholtz also occur in the jet with the liquid core maintained close to the nozzle exit as liquid volume fraction indicates. The temperature decreases rapidly and maintains its lower value only at the liquid core. The liquid core appears to be much smaller than the cases of other liquids such as water or R134A. This is also evident in Fig. 6.27 were the normalised Σ indicates the shape of the intact core and obtains its maximum value along in its periphery. The comparison of Σ with y argues that the jet consists of a vapour cloud rather than large ligaments or blobs. In technical terms, the formal definition of a cryogenic vapour cloud is still ambiguous. The vapour produced from cryogenic liquids like LNG are also extremely cold and can be extremely harmful. The vapour might condense the moisture in the surrounding air, creating a highly visible fog. This fog can also be formed around cold equipment when no release of the cold liquid or vapours has occurred. A key thing to remember is that these fog clouds do not define the vapour cloud. They define the area where the vapours are still cold enough to condense the moisture in the air. In fact, the methodology in this thesis treats the ambient air as a non-condensible gas and Fig. 6.25, Fig. 6.26, Fig. 6.27 and Fig. 6.28 give a reasonable representation of the produced vapour cloud. In Fig. 6.29 the axial velocity outside the nozzle exit is plotted

as a function of the distance from the release point to the ambient environment. The axial velocity increases after the release in the expansion region where a continuous break-up of large liquid ligaments is likely to happen. Liquid evaporation of large droplets that form in this region is also likely that happens. After this section, the jet centreline velocity decreases due to the effects of the air entrainment following similar trends with ones in the flashing R134A jets. Fig. 6.29 also offers an opportunity for a qualitative assement of flashing and non-flashing jets. The substantial characterisation of isothermal jets involves the study of the centreline velocity profile. Two main regions that can be observed in isothermal jets are the potential core region where centreline velocity is almost constant and the decay region where the centreline velocity decreases. On the other hand, in flashing jets the centreline velocity increases downstream the nozzle exit in the expansion zone which is evident in the primary atomisation region in Fig. 6.29. Upon reaching a maximum centreline velocity value, the axial velocity decreases as in isothermal jets (entrainment zone).

The dimensionless pressure drop inside the nozzle is shown in Fig. 6.30. This is the calculated pressure divided to the initial storage pressure, 30bar. The pressure starts decreasing right after the channel inlet and at approximately 30 percent of the channel drops below the saturation pressure, 6.63bar. The sharp decrease in pressure follows the slight change after 40 percent until the pressure becomes equal to the ambient pressure. Bubble nucleation starts at the nozzle walls suggesting that the liquid core at the nozzle centreline experiences any changes in a further position as shown in Fig. 6.31 regarding the centreline density. As observed before from other researchers (Reitz, 1990; Wang et al., 2017), the boiling mechanism might start at random locations inside the channel as a result of the pressure and turbulence instabilities. A good of quantifying the phase change into the flow regime is offered in Fig. 6.32,Fig. 6.33 and Fig. 6.34. On the contrary to the axial direction, velocity Fig. 6.32 maintains similar pattern both at the beginning and the end of the nozzle. The changes in the flow regime are more clear in the density and vapour quality at the upstream and downstream locations of the nozzle. The pure liquid starts flowing towards the nozzle exit becomes gradually a two-phase mixture. The amount of vapour in the mixture at the downstream exit is higher both in the near wall region and the jet centreline (r/R=0) as illustrated in Fig. 6.34. The result of the higher vapour in the downstream position is evident in the radial density distribution Fig. 6.33 since the occurrence of the lower density vapour decreases the mixture's density.

Table 6.4 Details for the high-pressure flashing LNG case.

	Physical parameters for simulations
Inlet pressure	3 MPa
Inlet temperature	120 K
Outlet pressure	100 kPa
Outlet temperature	298 K
L/D	2
Nozzle diameter	2mm

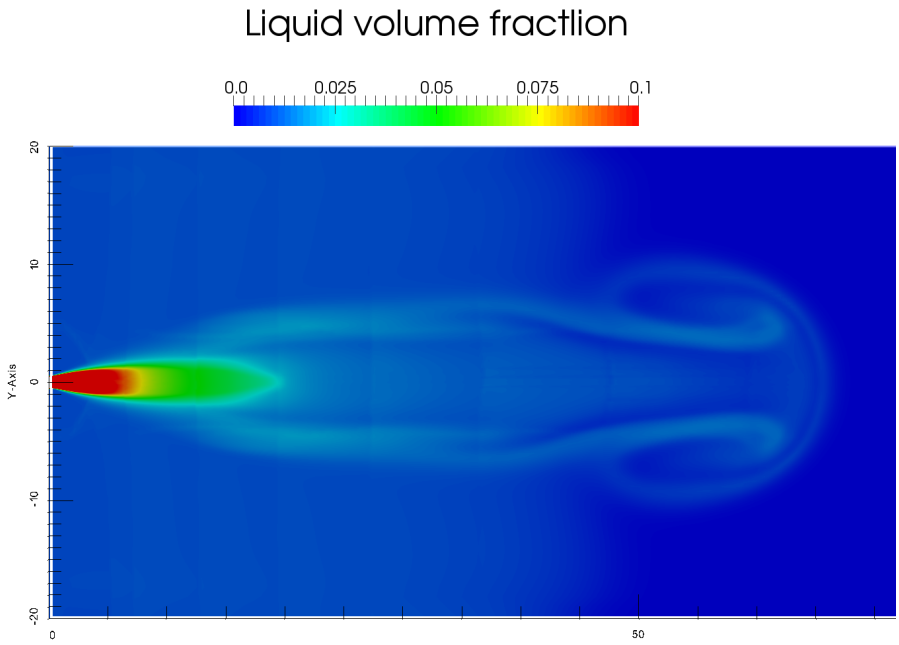

Fig. 6.25 Liquid volume fraction for LNG. Instant caption at t=0.006s.

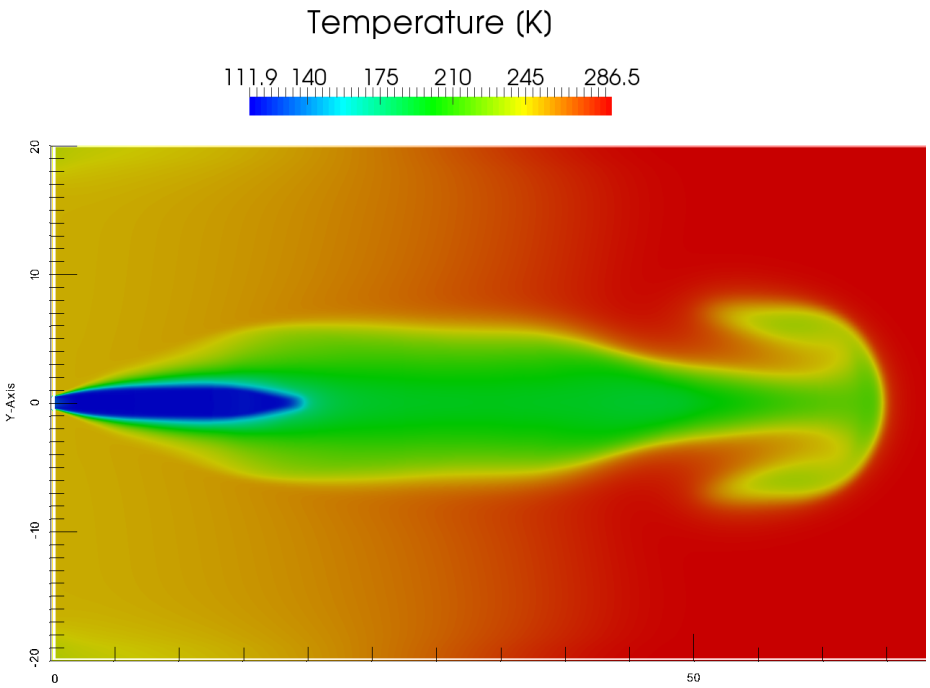

Fig. 6.26 Temperature contour for LNG. Instant caption at t=0.006s.

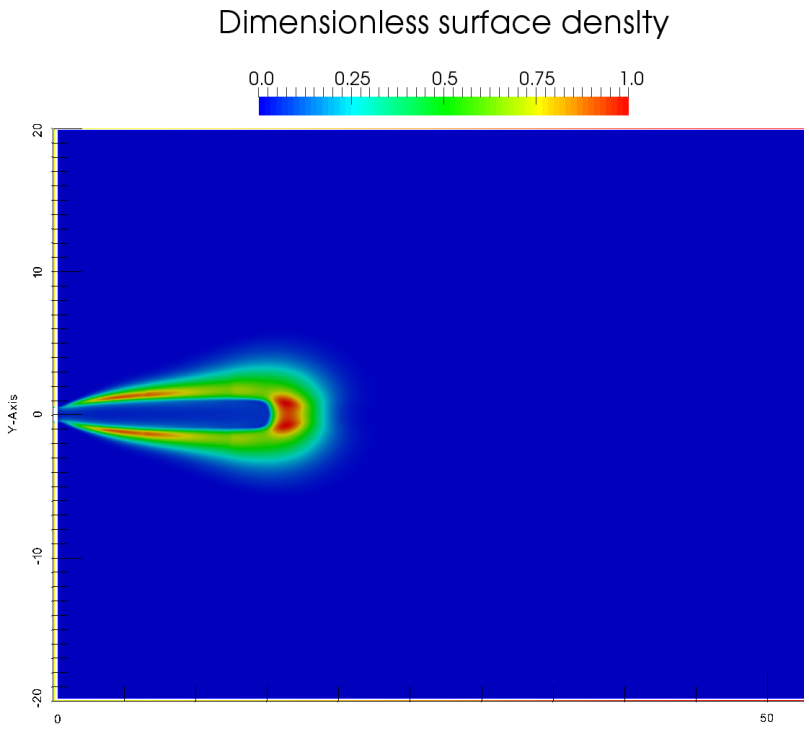

Fig. 6.27 Dimensionless Σ for LNG. Instant caption at t=0.006s.

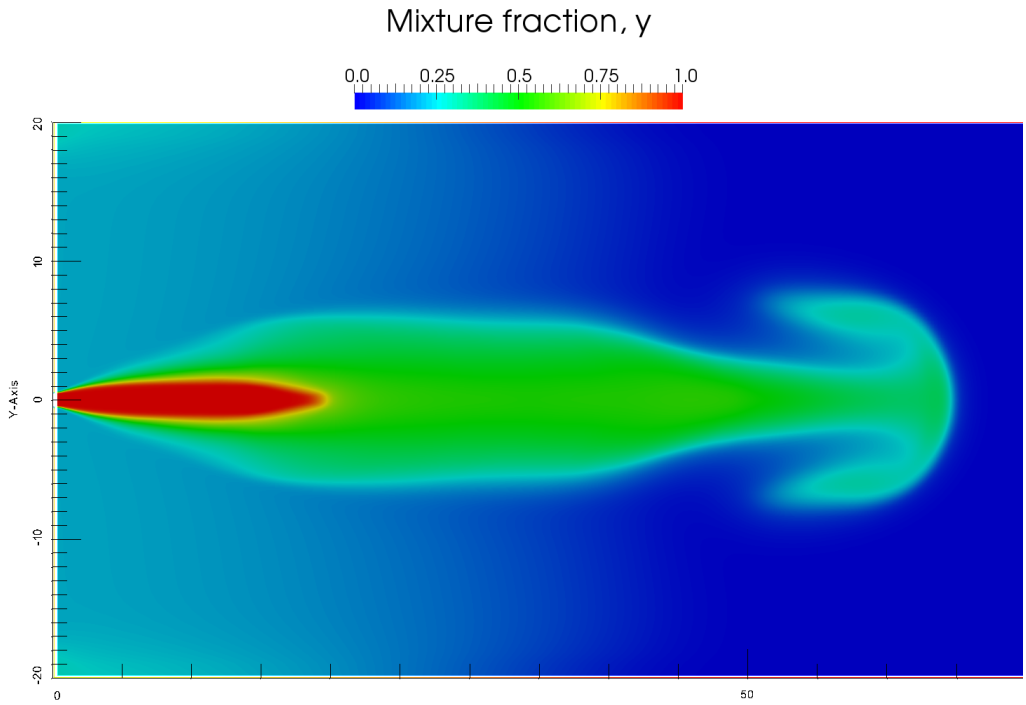

Fig. 6.28 Vapour mass fraction for LNG. Instant caption at t=0.006s.

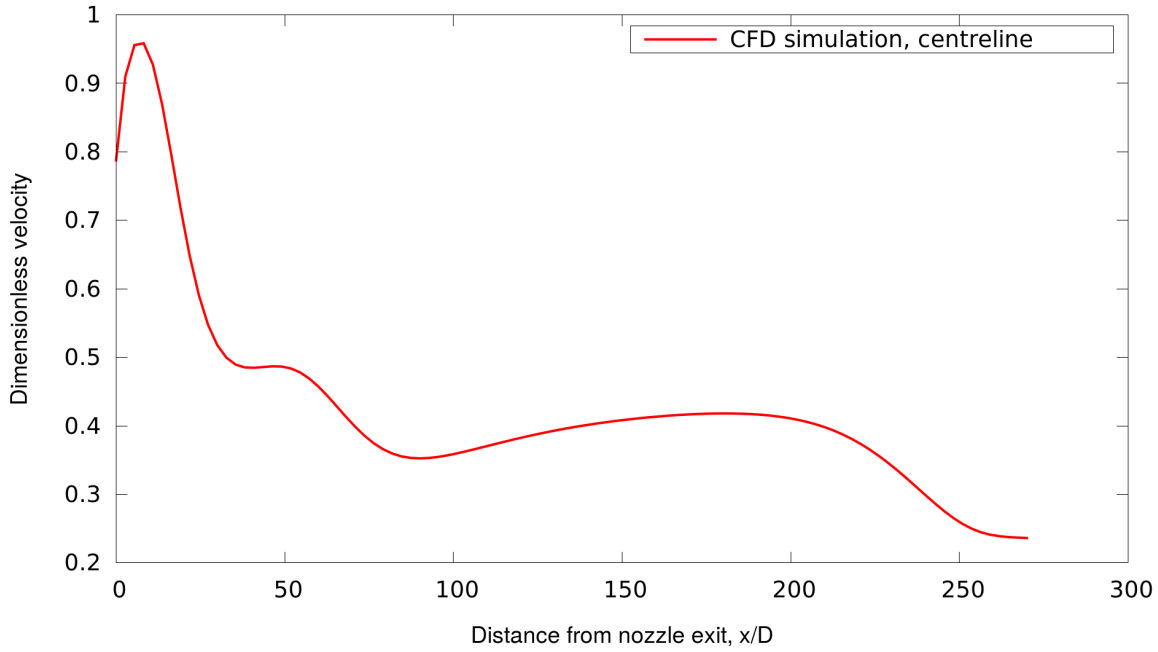

Fig. 6.29 Axial velocity at the jet centreline outside the nozzle exit for high-pressure LNG jet.

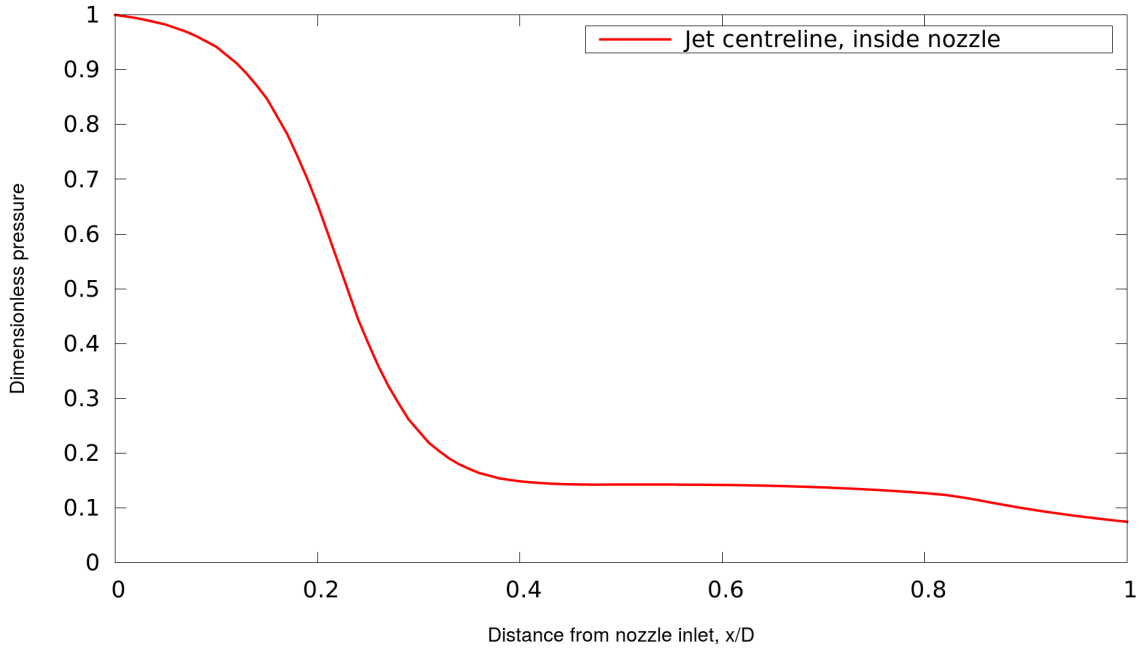

Fig. 6.30 Centreline pressure profile for LNG, along the nozzle.

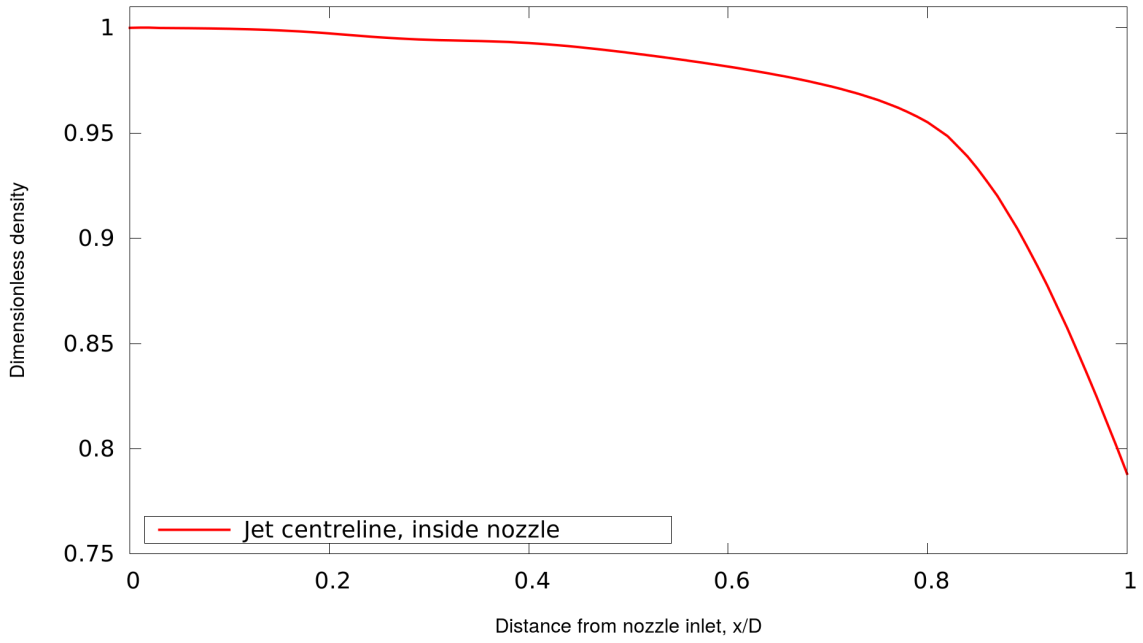

Fig. 6.31 Centreline density profile for LNG, along the nozzle.

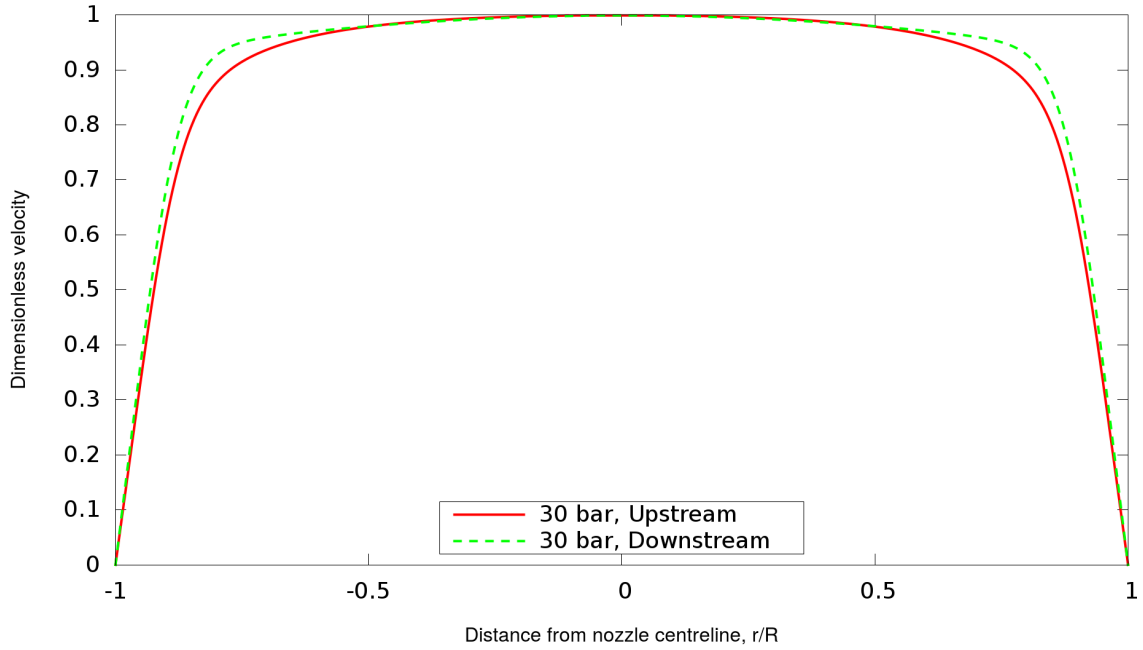

Fig. 6.32 Upstream-downstream velocity profile for high-pressure LNG along the nozzle.

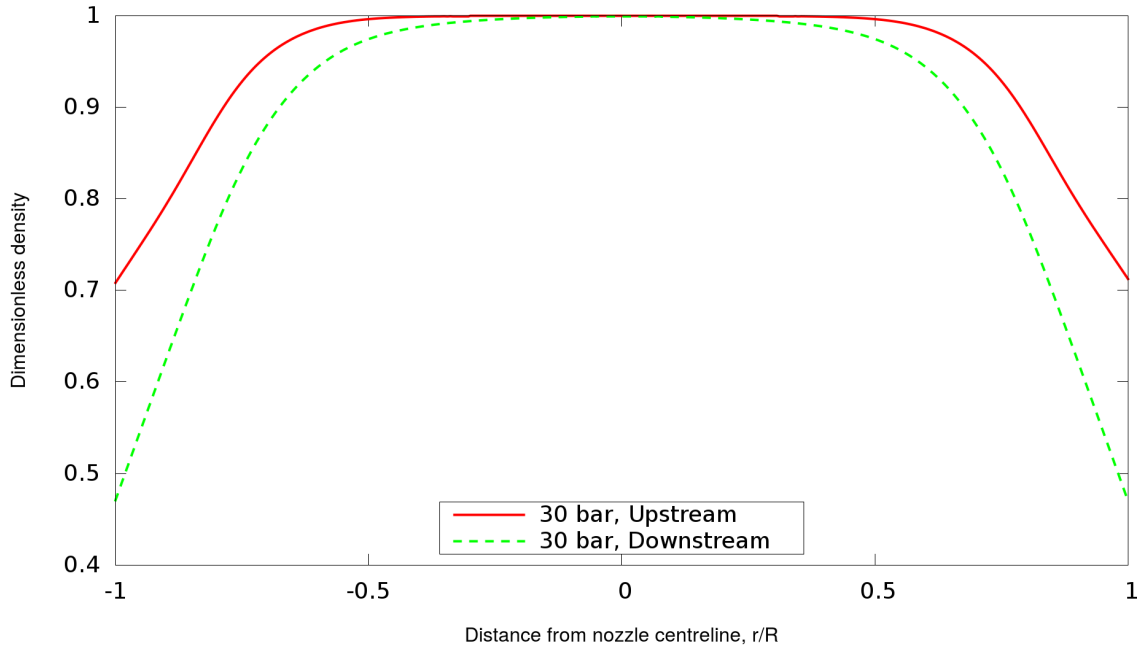

Fig. 6.33 Upstream-downstream density profile for high-pressure LNG along the nozzle.

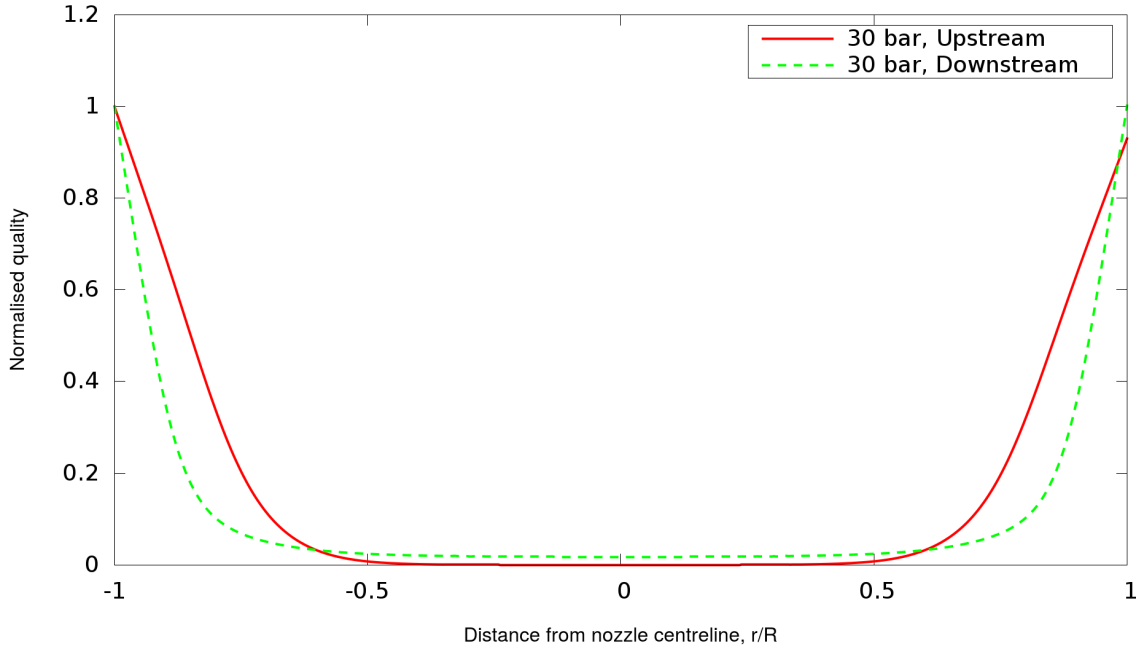

Fig. 6.34 Upstream-downstream quality profile for high-pressure LNG along the nozzle.

6.4.2 Low pressure LNG jets

The second test LNG case presented here concern LNG stored in lower pressure. The nozzle geometry comprises of the cylindrical nozzle of diameter $D = 10mm$ and $L/D = 2$. The fluid is stored at 7.1 bar and at a low temperature 111 K and emerges to a low pressure environment (1 bar). The most important parameters of the simulation are shown in Table 6.5. The cryogen is a mixture of methane, carbon dioxide, ethane and some other hydrocarbons (Table 6.6). The diameter of the channel that LNG flows through is five times larger than the diameter in the high-pressure test case. The results are presented for three different computational meshes allowing for a mesh-sensitivity analysis. The computational meshes included a coarse mesh (37000 cells), a medium size mesh (62000 cells) and a fine mesh (128000 cells). In all the cases a structured grid was used with non-uniform spacing in the near-wall region and the dimensionless wall distance was always less than 200. The present calculations for the medium mesh took approximately 3.5 days. The results here focus on the internal flow patterns since the internal flow is crucial for the jet dynamics and indicative of the phase change process. Fig. 6.35 shows the pressure distribution at the jet centreline inside the channel. The sharp pressure drop is also illustrated in the numerical results presented in Chapter 5. In comparison to the pressure drop in the high-pressure test case, pressure decreases in a more abrupt manner. For instance at x/L=0.2 the dimensionless pressure is

equal to 0.64 and 0.4 in the high and low-pressure case respectively. This difference can be attributed to the larger diameter of the nozzle (Yildiz, 2005). It is difficult to evaluate the influence of the nozzle diameter since the pressure difference in the two cases is essentially different. According to Yildiz (2005) keeping the pressure constant, the flow morphology inside the nozzle might be very different and can additionally alter significantly the droplet size. The velocity profile in the centreline in Fig. 6.36 also appears to change along the channel but with an increasing trend which seems to stabilise around x/L=0.4 where velocity is almost equal to its maximum value. Due to lack of experimental data it remains uncertain whether and in what extent the liquid flashes inside the short nozzle. Radial velocity profiles at the beginning and the end of the nozzle are shown in Fig. 6.37 and Fig. 6.38. Compared to the upstream location, the two-phase jet at the downstream position is illustrated in Fig. 6.38 with a developed flow profile. The flow which separates off the sharp corner at the beginning of the channel signals a pressure drop locally. As noted in Chapter 7 for flashing liquids through channels, this decrease in pressure leads to an increase in the rate of phase change. During the flashing process, the liquid contraction occurs alongside with the pressure drop at the channel inlet (positive velocity divergence), Fig. 6.37. The results in general showed an independence on the mesh resolution with the medium and fine mesh results to be adequately close. Similar to velocity, the internal radial profiles of the mixture density are shown in Fig. 6.39 for the upstream location and in Fig. 6.40 for the downstream position at the channel exit. The majority of the bubble nucleation is more likely that happens in the wall region with bubbles forming due to the change in the channel geometry and pressure drop. The nucleation position is random and depends on the local changes in the nozzle and the nuclei that form in arbitrary positions, grow until the critical radius, R_{crit} which depends on the pressure and temperature fluctuations and eventually alter the two-phase density. The dimensionless mixture density appears to be less for the low-pressure release compared to the high-pressure case in Fig. 6.33. A possible explanation could be the difference in the rate of change in pressure between the two cases (Fig. 6.30 and Fig. 6.35). The pressure in the channel centreline drops earlier and as a result the critical bubble size in the Young-Laplace equation also changes. The flow becomes more bubbly with a consequent smaller two-phase mixture density moving towards the downstream position.

Table 6.5 Properties for the low-pressure flashing LNG simulations.

	Physical parameters for simulations
Inlet pressure	0.71 MPa
Inlet temperature	111 K
Outlet pressure	100 kPa
Outlet temperature	304 K
L/D	2
Nozzle diameter	10mm

Table 6.6 LNG composition for low-pressure simulations.

	Component ($mol\%$)
Methane	88.906
Carbone Dioxide	5.176
Ethane	4.454
Propane	0.961
Nitrogen	0.345
Iso-Butane	0.080
N-Butane	0.068
Iso-Pentane	0.010

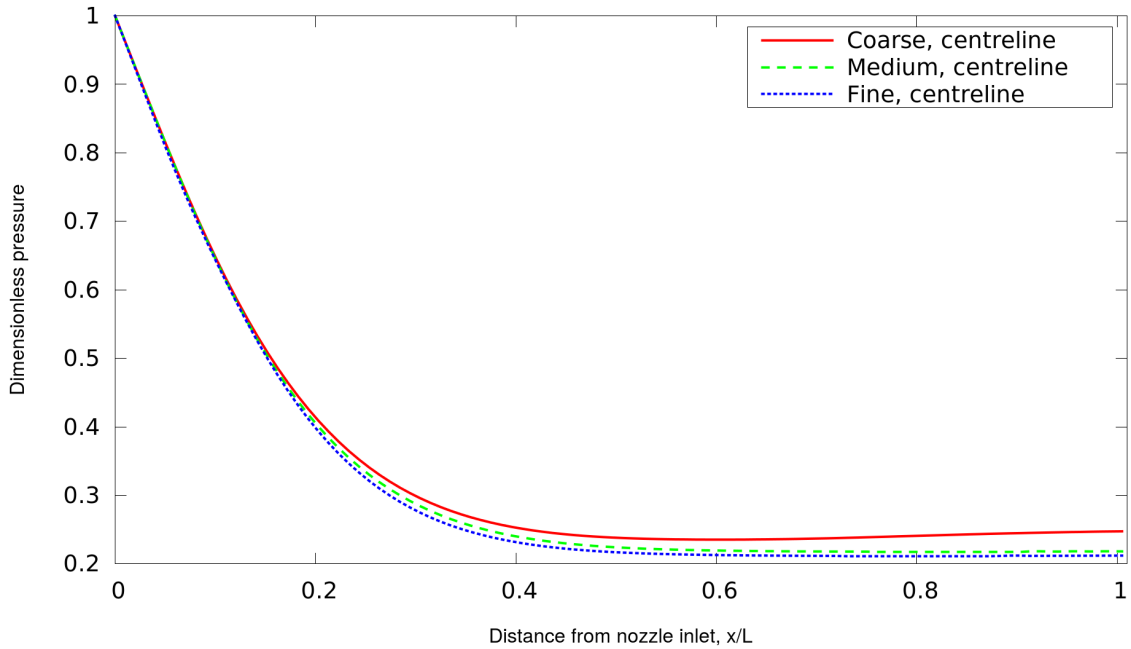

Fig. 6.35 Centreline pressure profile for LNG (coarse, medium and fine mesh).

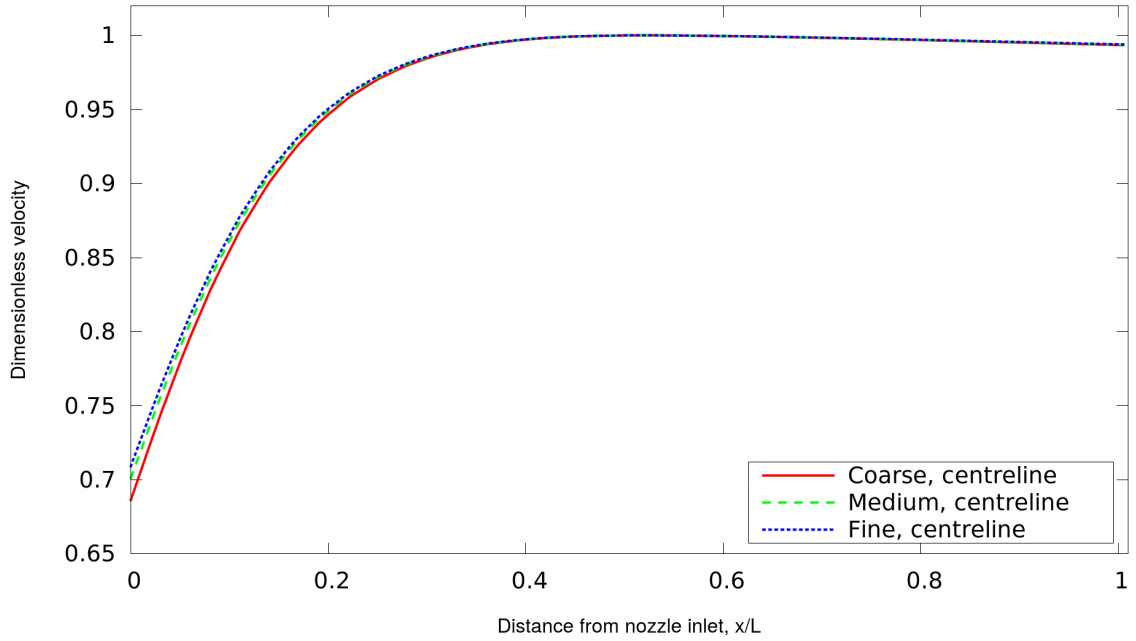

Fig. 6.36 Centreline velocity profile for low-pressure LNG (coarse, medium and fine mesh).

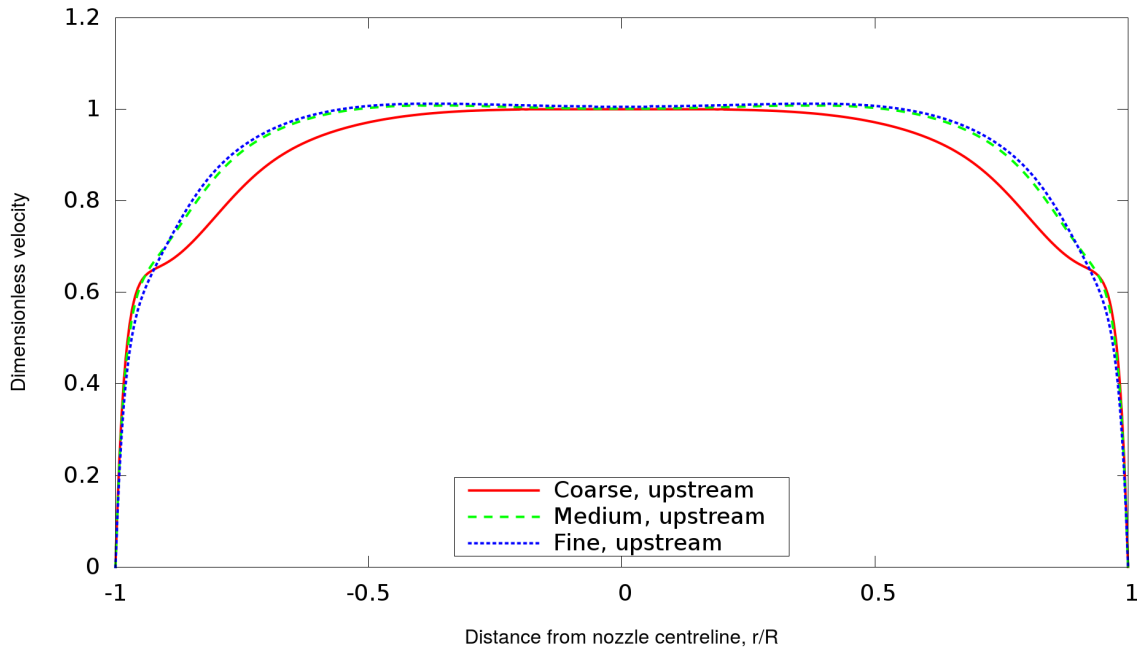

Fig. 6.37 Upstream velocity profile for low-pressure LNG (coarse, medium and fine mesh).

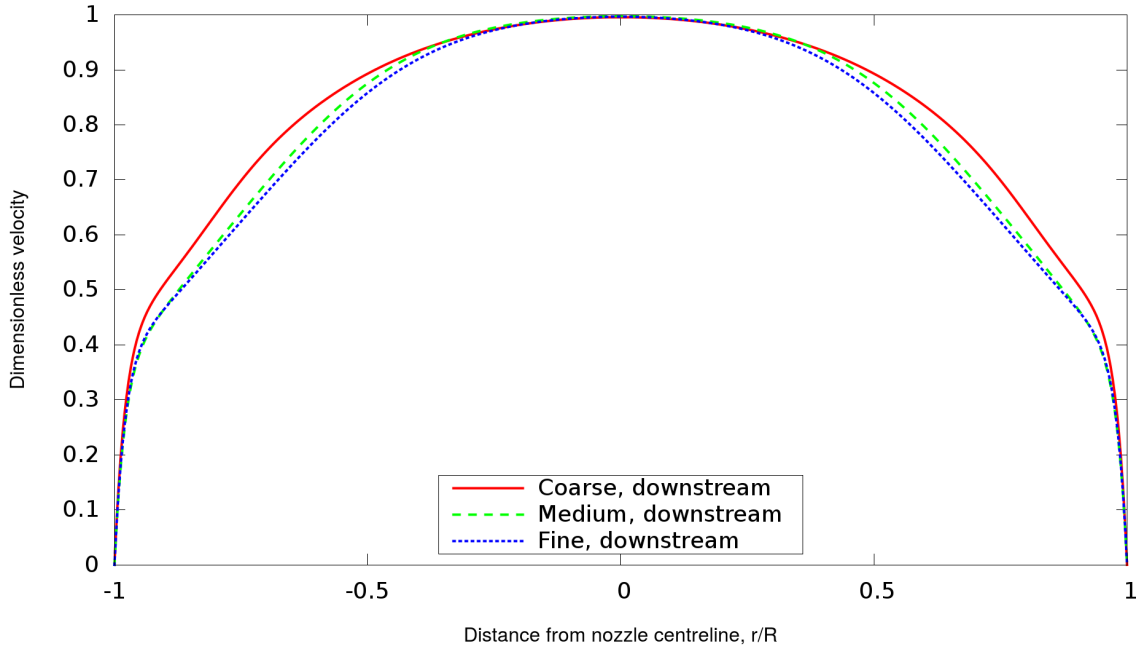

Fig. 6.38 Downstream velocity profile for low-pressure LNG (coarse, medium and fine mesh).

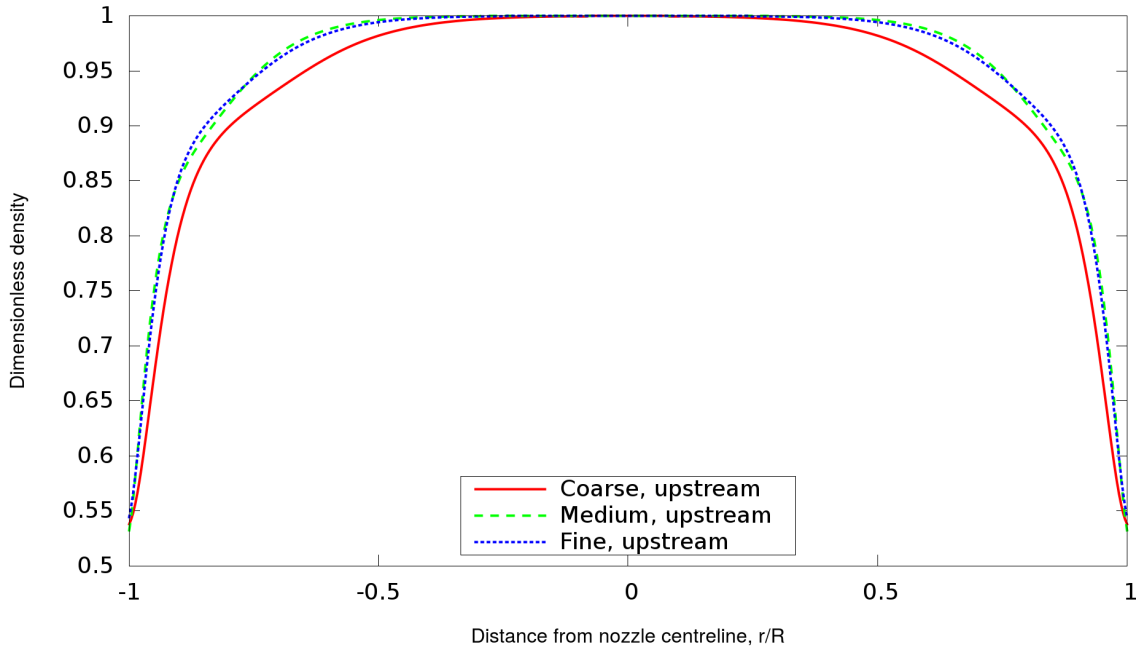

Fig. 6.39 Upstream density profile for low-pressure LNG (coarse, medium and fine mesh).

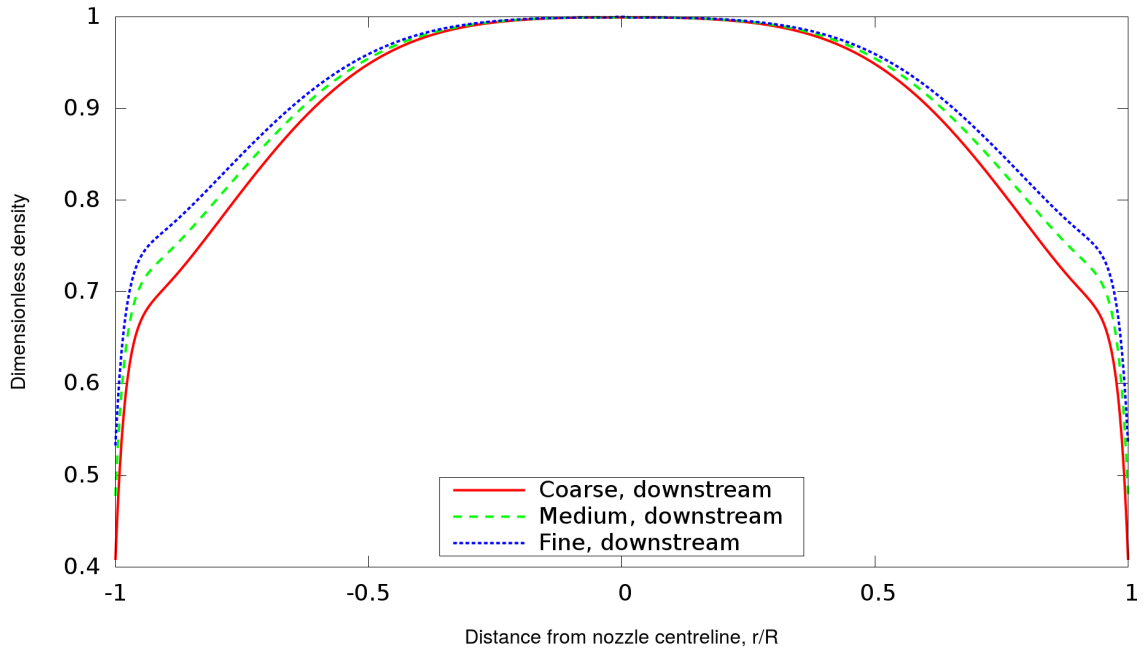

Fig. 6.40 Downstream density profile for low-pressure LNG (coarse, medium and fine mesh).

Since we have presented validation for the developed compressible methodology for flashing water, liquid nitrogen and R134A using velocity, pressure, spray angles and droplet sizes, it is interesting to try to investigate other quantities as well. The concentration of methane is shown in Fig. 6.41 for the centreline of the jet versus the time for three different distances x=1, 2 and 3m from the nozzle exit. The mole fraction is calculated with the one-fluid approach and considering the average of the liquid and vapour phases in order to be consistent with the volume of fluid approach as presented in chapter 5.

The calculation of the vapour mass fraction of methane employs the Homogeneous Relaxation Model which means that the calculations make use of the relaxation time with the exponential constants derived for flashing water. The relaxation time formulation is appropriate for various flashing liquids as presented in this thesis, but might, at some point, be less adequate depending on the working fluid. Thus, the derivation of the HRM for the mole fraction calculations might introduce additional errors for the concentrations of the constituents of flashing jets concerning liquids other than water, such as liquefied natural gas here. This dependency should be expected to be more important in the dense part of the jet.

The trends in Fig. 6.41 show that the mole fraction of methane is initially high, but decreases with increasing the distance downstream the nozzle exit. As it is expected, the concentration obtains its maximum peak value earlier for the positions close to the release point. After reaching a maximum value, the concentrations start to decrease with decreasing

the mass flow rate (valve closes after 147s) and at the end approaches zero. The liquid fragmentation as a result of the growing instabilities on the jet surface is one of the reasons for this drop. As long as the jet disintegrates into the ambient low pressure environment, it disperses along the radial direction. The bubble nucleation occurring in the dense part of the jet is a stabilisation factor for the jet and at the same time a major parameter for the flow regime transformation. Due to the thermodynamic changes within the jet, the liquid core progressively changes to a more bubbly regime causing the liquid mixture mass fraction to reduce, resulting to consequent significant changes in the concentration of methane.

Adding extra transport equations for the concentration could be another way to estimate the mole fractions and would also be scientifically correct but raises two additional challenges. The first one is the need to include additional transport equations including the slip velocity which means that one needs to solve two sets of equations for continuity and momentum changing the structure of the presented methodology since now only one set of equations is solved for continuity, momentum and energy. Moreover, the HRM which is typically implemented in the one-fluid approach in the literature, should be utilised in the context of the two-fluid approach which is a non trivial task. The second challenge would be the source term for the cryogen in the RHS of these transport equations which should include a Fick-like diffusive term and a non-diffusive term specific of the non-equilibrium thermodynamics has not been found yet.

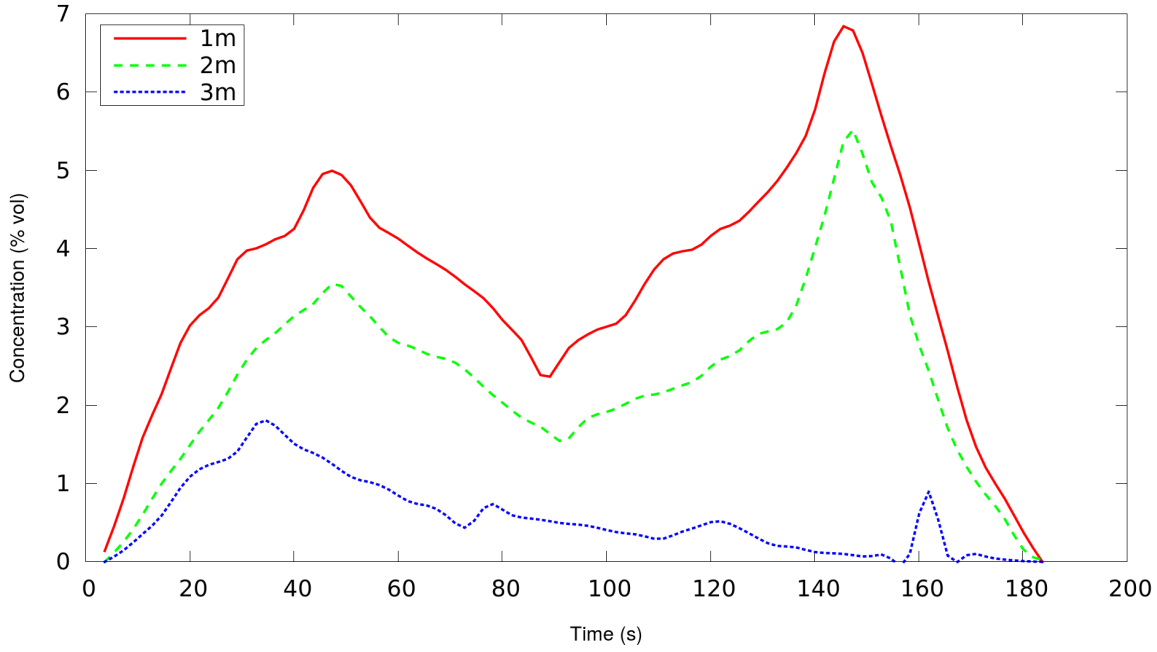

Fig. 6.41 Methane concentrations for three different locations downstream the release point.

6.5 Concluding remarks

A novel method for modelling the atomisation of superheated jets is presented in this chapter. The method is coupled with the new pressure equation presented in the previous chapter constructing a unified approach for modelling superheated jets atomisation considering the flow inside the channel they emerge from. This is a Eulerian approach for modelling the spray motion and employs the liquid-gas interface density concept. Based on the existing ELSA models, a new extension is proposed for the Σ-equation which is appropriate for the dense and dilute spray regions of evaporating sprays. This new Σ-Y model has the capability to simulate all the stages of flashing jets atomisation. A validation series is presented for some important spray characteristics such as the Sauter mean diameter of the droplets, the velocity and spray angle. Different flashing jets scenarios are demonstrated for flashing water, R134A for validation and useful insights for low and high-pressure LNG releases are discussed.

Chapter 7

Conclusion

The current study presents a numerical approach for simulating the atomisation of flashing liquids accounting for the distinct stages, from primary atomisation to secondary break-up to small droplets using the Eulerian-Lagrangian-Spray-Atomisation model coupled with the homogeneous relaxation model and interface tracking techniques. The new pressure equation developed in the previous chapters, is coupled with a new extension of the ELSA model for flashing jets. The new Σ-equation accounts for some of the most important phenomena that influence liquid atomisation. The proposed approach has the advantage of avoiding the unrealistic common assumption of pure liquid at the nozzle exit. It models the change in the regime inside the nozzle treating flashing in a unified approach simulating the metastable jet both inside and outside the nozzle. Important mechanisms such as thermal non-equilibrium, aerodynamic break-up, droplet collisions and evaporation are modelled in a novel atomisation model.

7.1 Main conclusions

A new compressible methodology has been developed to model the atomisation of super-heated jets flowing through nozzles. This is a unified approach for both the internal flow and spray dynamics. The new method has been developed within the frame of the open source CFD code OpenFOAM and can be used to model the rapid phase change within various nozzle and orifice geometries in the scenario of abrupt pressure drops. The methodology is implemented in two new solvers FlashFOAM and HRMSonicELSAFOAM, is capable of simulating flashing and the impact of bubble nucleation on the flow, and is validated using experiments with both sub-cooled and saturated initial conditions. The mass flow rates at the validated cases are close to those observed in the experiments.

The predictions confirm experimental findings that indicate a two-phase jet at the nozzle exit which continues evaporating downstream. The void fraction trends show an annular flow regime. In the presented method the liquid phase is tracked, and uses a novel pressure update. This pressure correction uses the PIMPLE algorithm and includes the effects of flash-boiling, ambient air entrainment and interfacial forces in a new numerical approach for coupling pressure and velocity in flashing. Based on the original model of Schmidt et al. (2010), additional terms are added for obtaining a new pressure equation which is one of the cornerstones in the developed approach for modelling cavitating and flashing jets (FlashFOAM solver). In addition to the Homogeneous Equilibrium Model, extra numerical models such as interface tracking and the Σ-equation (HRMSonicELSAFOAM) are added creating a CFD tool for simulating flash-boiling in three dimensions.

Turbulence modelling is found to play a major role for accurately predicting mass flow rate, and the models have been tested within the Reynolds-Averaged-Navier-Stokes and Large Eddy Simulations (LES) context. Accurate predictions for the internal flow and the primary atomisation are presented. Building on the original implementation of the Σ-Y model, a new extension of the Eulerian-Lagrangian-Spray-Atomisation model is presented. In the new ELSA model, source terms for accounting for the creation/destruction of the interface due to mechanical and thermodynamic effects are used into the modelling strategy. A novel expression for the change in the surface density for cryogenic jets is used here, and is inserted in the Σ-equation. The model for the spray dynamics is thoroughly described together with the pressure equation proposing a new unified methodology to simulate the whole process of liquid atomisation starting from inside the nozzle until the jet shatters to small droplets downstream the nozzle exit.

Further numerical simulations have also been conducted for the investigating flashing of cryogenic liquids. Patterns of the flow characteristics indicate that the heat and mass transfer is important in cryogenic liquids that flash through channels. The thermal non-equilibrium model employs a semi-empirical correlation validated for water data. This correlation has also been tested for cases involving other liquids such as liquid nitrogen, R134A and LNG and found to be adequate for predicting the void fraction. Additional tests for various nozzle geometries, different superheat degrees and storage pressure have been carried out. In particular, validations have been conducted using the cryogenic jets flowing within short orifices and long channels for a large range of pressures studying the patterns of the flowing metastable two-phase jets.

7.2 Achievements

7.2.1 Modelling strategy for flashing within channels and atomisation

An extended literature review for modelling cavitation, flashing and atomisation has been produced. The literature is divided into two main parts, one for studying the internal flow and a second one which is the atomisation and spray mode. Details and basic concepts have been analysed for a better understanding of the motivations. Theories and results of the mathematical models that have arisen even before the establishment of CFD as a numerical tool were presented first, moving progressively towards the most advanced models and sophisticated approaches which extend in three-dimensional space.

The methodology presented here has been developed within the open-source code OpenFOAM which offered the platform to implement a multiphase CFD tool. OpenFOAM is a CFD library written in C++ and freely distributed that allows users to program continuum mechanics solvers and pre/pro-processing tools in a high-level specific language. OpenFOAM programming utilises the Object-Oriented Programming (OOP) paradigm for top-level coding. With this concept, codes are easier to write, edit and modify and the developers can easily share and update shorter codes.

Object-orientation techniques enable the creation of data types that closely mimic those of continuum mechanics. Operator overloading capability in C++ allows using a conventional mathematical notation for tensors and partial differential equations.

The Lagrangian approach implemented in OpenFOAM was identified as a potential framework to simulate flashing jets using the discrete elements method. The approach was thoroughly tested and the associated sub-models were examined. In general, the Lagrangian approach in OpenFOAM gave reasonable predictions for velocity but gave large deviations for the droplet sizes. Apart of the known limitations of these sub-models for primary, secondary break-up, droplets collisions and coalescence, droplet evaporation and rebound, this methodology requires additional assumptions prior to any simulation. This dictates to assume for instance that the liquid jet is injected to the low-pressure region is pure liquid, which as it has been illustrated here, is not generally true. The empiricism in the Lagrangian approach is generally more extensive than in the Eulerian methodology that is developed here.

7.2.2 A novel methodology for modelling flash-boiling inside channels

A new compressible solver has been developed within the frame of open source CFD code OpenFOAM to compute phase change within various nozzle and orifice geometries

experiencing rapid pressure drops. The solver is capable of simulating flashing and the impact of bubble nucleation on the flow, and is validated using experiments with both sub-cooled and saturated initial conditions. The mass flow rates at the validated cases are close to those observed in the experiments. The predictions confirmed experimental findings, that indicate a two-phase jet at the nozzle exit which continues evaporating downstream. The void fraction trends show an annular flow regime.

In the presented method the liquid phase is tracked and uses a novel pressure update. This pressure correction which is in the heart of the PIMPLE algorithm includes the effects of flash-boiling, ambient air entrainment and interfacial forces in a new numerical approach. Turbulence modelling is found to play a major role in accurate predictions of the mass flow rates and the k-ε model appears to be adequate for the geometries presented. The model has been tested within the RANS framework for validation and LES for obtaining more insights.

The two-phase mixture properties are estimated from the pressure calculated from the new pressure equation. The present study attempts to efficiently crystallise flash-boiling factors and vapour generation influenced by thermal non-equilibrium, high-pressure gradients and turbulence. Internal flashing is the most catastrophic scenario which causes severe changes in the flow regime in the channel and was successfully simulated here.

Further numerical simulations have also been conducted for the flashing of cryogenic liquids. Patterns of flow characteristics indicate that the heat and mass transfer is important in cryogenic liquids that flash through pipes. The thermal non-equilibrium model employs a semi-empirical correlation validated for water data. This correlation has also been tested for cases involving other liquids (liquid nitrogen, R134A, LNG) and found adequate for predicting the void fraction. This research aims to fill the gap in the literature for cryogenic flashing liquids presenting a method to simulate 3D flashing cryogenic jets inside channels the numerical tools developed in an open-source environment.

7.2.3 A new holistic methodology for modelling flashing sprays

A Eulerian-Lagrangian Atomisation Spray method implemented within OpenFOAM is presented. Although ELSA traditionally uses RANS as the basic benchmark, here is also implemented in the new code for LES. The model follows the original implementation of Σ-Y model, solving two equations, one for the liquid mass fraction, and another one for the interface density. Source terms for accounting for the creation/destruction of the interface due to mechanical and thermodynamic effects are used in the modelling.

A novel expression for the change in surface density in superheated jets is used here and is inserted in the Σ-equation. The applications of the method include fuel atomisers, accidental releases and other situations of a sudden pressure drop of a superheated/sub-cooled

liquid in a low-pressure environment. Non-evaporating or non-flashing sprays can also be modelled.

The modified ELSA approach, combines the advantages of Eulerian and Lagrangian frameworks and uses explicit formulations for modelling the droplet characteristics like the Sauter mean diameter. To the knowledge of the author, this study corresponds to the first attempt to simulate in three dimensions the atomisation of flashing jets considering the impact of the internal flashing on the spray motion. Preliminary results show that the method can adequately describe the droplet sizes along the jet centreline. It is remarkable that with ELSA small liquid structures can be quantified, even with averaged turbulence statistics. This scale characterisation is extremely important since the nature of the presented releases is multi-dimensional: the size of liquid structures can range from the characteristic scale of the problem, some centimetres, up to some microns which means 10^4 times less. The SMD results had a reasonable agreement and were always of the same order of magnitude.

7.3 Follow-up research

7.3.1 Application

The presented modelling strategy has the potential to capture the underlying physics of the atomisation of liquid jets under flash-boiling, aerodynamic break-up, fluid flow instabilities and turbulence. It has been validated and tested for water and cryogenic liquids. The model can be employed for providing insights for a jet dispersion in process industry where real experiments face limitations due to hazards and large scale of the problem. Especially, the holistic approach described in chapters 5 and 6 could be employed for modelling accidental releases in on-shore and off-shore on-shore terminals.

Regarding the automotive industry applications, this research aspires to lead to the development of new computational tools that will facilitate the cost-effective design of novel injection systems that operate in high pressures such as atomisers and for gasoline direct injection applications. Additional problems in other fields could be modelled with the present approach and the model could be tested in more complex geometries.

7.3.2 Improvements in thermal non-equilibrium model

The thermal non-equilibrium model employs a semi-empirical correlation validated for water data. This correlation has also been tested for cases involving other liquids (liquid nitrogen, R134A) and found adequate for predicting the void fraction. Additional tests for calibrating the HRM parameters for these liquids and different depressurisation regimes in moderate

superheat degrees could be conducted in the future. Coupling HRM with bubble growth models could provide more detailed insights into the physics inside the pipe. This could also be possible with a two-fluid approach and with a careful selection of the additional assumptions that are introduced to the problem. The current work needs to be extended to include the effects of the sub-grid scale turbulence for resolving more accurately the bubble dispersion patterns in the flow.

7.3.3 Extensions/Improvements in spray model

The basis of the spray model is the modified Σ-equation comprising of various source terms that correspond to a different process. Some of these terms include parameters and constants that are induced typically from small-scale DNS-type numerical results. Hence, parametric studies for model calibration for realistic flashing releases would give insights regarding the optimum selection of the numerical constants.

Further research should be made for the implicit/explicit treatment of the source terms in the Σ-Y model and the impact of the turbulence modelling approach on the primary atomisation. Bounded schemes of second-order in space were used in the present study and would be interesting to employ higher order schemes and evaluate the efficiency of the model. Already implemented schemes in OpenFOAM of higher order (third and fourth order) generally failed and implementation of new schemes might be necessary.

7.3.4 Numerical method

An improvement in the boundary condition the far-field downstream the nozzle exit could be beneficial for the solution. The travelling waves that bounce to the walls can be a source of numerical instabilities. Problems could also occur in the pressure-velocity coupling. A better understanding of the implementation within OpenFOAM of the boundary conditions proposed by Poinsot and Lelef (1992) is needed. Careful coupling with other boundary conditions such as zero gradient would be useful for the stability of the solution.

The interface tracking techniques we use are based on the Volume of fluid and Level set. The latter needs to be incorporated using a high order scheme from the WENO family for the re-initialisation equation. VOF was proven to be efficient and accurate. Zalesak's limiters for bounding the solution for the liquid mass fraction was tested without offering much different in the results. Thus there is no need for VOF to implement a multi-dimensional limiter. Improvement of the higher order temporal discretisation schemes in OpenFOAM could be essential since these seem to suffer from instabilities.

The presented study uses the one-fluid approach, and all the properties are averaged to have one single mixture set of equations. The models are naturally implemented in the Eulerian framework and the Navier-stokes are solved using one set of equations for the two phases in a segregated manner. Two-fluid approaches considering that each phase has its own phase velocity could be used as the framework for developing CFD models that consider the slip velocity which for the moment is ignored.

7.3.5 Subcritical-critical jets

The model could be used for modelling jets in critical conditions including real gas effects, for both dense and dilute part of the spray. The jet dynamics at the limit of transition between sub-critical to critical conditions could be investigated. This study could be extremely beneficial in a large range of applications. The suggested numerical strategy has the potential to capture the physics underpinning the phenomena even at the complicated thermodynamic conditions described in this document and therefore can play a crucial role in cases where no experiments have been conducted or these are limited because of the complexity of their hazardous character.

References

Abramovich, G. N. (1963). *The Theory of Turbulent Jets*. M.I.T. Press.

Abramzon B. and Sirignano W. (1989). Droplet vaporization model for spray combustion calculations. *International Journal of Heat and Mass Transfer*, 32:1605–1618.

Alekseev, M. V., Vozhakov, I. S., Lezhnin, S. I. and Pribaturin, N. A. (2016). Simulating compression waves in the outer atmosphere at depressurization of the pipeline with water coolant. *Journal of Engineering Thermophysics*, 25(1):100–125.

Allen, J. T. (1998). Laser-based measurements in two-phase flashing propane jets. Part one: velocity profiles. *Journal of Loss Prevention in the Process Industries*, 11(5):291–297.

Arcoumanis, C., Gavaises, M., and French, B. (1997). Effect of Fuel Injection Processes on the Structure of Diesel Sprays. *SAE Technical Paper 970799*.

Aris, R. (1962). *Vectors, Tensors and the Basic Equations of Fluid Mechanics*. Prentice Hall Inc., Englewood Cliffs, NJ.

Avedisian, C. T. (1985). The Homogeneous Nucleation Limits of Liquids. *Journal of Physical and Chemical Reference Data*, 14(3):695–729.

Baldwin, E. T., Grover, R. O., Duke, D. J., Matusik, K. E., Kastengren, A. L., Powell, C. F., Parrish, S. E. and Schmidt, D.P. (2016). *String Flash-Boiling in Flashing and Non-Flashing Gasoline Direct Injection Simulations with Transient Needle Motion*. ILASS Americas 28th Annual Conference on Liquid Atomization and Spray Systems, Dearborn, MI, May 2016.

Bar-Kohany, T. and Sher, E. (2004a). Subsonic Effervescent Atomization - A Theoretical Approach. *Atomization and Sprays*, 14(6):495–509.

Bar-Kohany, T. and Sher, E. (2004b). Effervescent atomization under sub-sonic and choked conditions - a theoretical approach. *Chemical Engineering Science*, 59(24):5987–5995.

Battistoni, M. and Duke, D. and Swantek, A. and Tilocco, F. Z. and Powell, C. F. and Som, S. (2015). Subsonic Effervescent Atomization - A Theoretical Approach. *Atomization and Sprays*, 14(6):495–509.

Bauer, E. G., Houdayer, G. R. and Sureau, H. M. (1976). A non-equilibrium axial flow model in application to loss-of-coolant accident analysis. The CYSTERE system code. *OECD/NEA Specialist Meeting on Transient Two-phase Flow*, 428(1875):379–397.

Baumgarten, C. (2006). *Mixture Formation in Internal Combustion Engines*. Springer Berlin Heidelberg.

Bayvel, L. P and Orzechowski, Z. C. E. (1993). *Liquid atomization*. Washington, DC Taylor & Francis.

Benajes, J., Pastor, J. V., Payri, R. and Plazas, A. H. (2004). Analysis of the Influence of Diesel Nozzle Geometry in the Injection rate Characteristic. *Journal of Fluids Engineering*, 126(1):63–71.

Bianchi, G. M., Forte, C., Negro S., and Pelloni P. (2008). A 1d Model for the Prediction of Flash Atomization in GDI Multi-Hole Injectors: Preliminary Results. *SAE Int. J. Engines*, 1:1278–1293.

Bilicki, Z. and Kestin, J. (1990). Physical aspects of the relaxation model in two-phase flow. *Proceedings of the Royal Society of London A: Mathematical, Physical and Engineering Sciences*, 428(1875):379–397.

Bird, R. B. (1960). *Transport Phenomena*. John Wiley & Sons, Madison, Wisconsin.

Bourlioux, A. (1995). A coupled Level Set and Volume of Fluid algorithm for tracking material interfaces. *Proceedings of the 6th International Symposium On Computational Fluid Dynamics*, 6:15–22.

Brackbill, J. U. and Kothe, D. B. and Zemach, C. (1992). A Continuum Method for Modeling Surface Tension. *J. Comput. Phys.*, 100(2):335–354.

Brennen, C. E. (2013). *Cavitation and Bubble Dynamics*. Cambridge University Press.

Brusiani F., Negro, S., Bianchi, G. M., Moulai, M., Neroorkar, K. and Schmidt, D. (2013). Comparison of the Homogeneous Relaxation Model and a Rayleigh Plesset Cavitation Model in Predicting the Cavitating Flow Through Various Injector Hole Shapes. *SAE Technical Paper 2013-01-1613*.

Candel, S. M. and Poinsot, T. J. (1990). Flame Stretch and the Balance Equation for the Flame Area. *Combustion Science and Technology*, 70(1-3):1–15.

Cleary, V. M. (2008). *Source Term Models for Superheated Releases of Hazardous Materials*. University of Wales Cardiff, Cardiff.

Coldrick, S. (2016). Modelling Small-scale Flashing Propane Jets. *AIDIC, Chemical Engineering Transactions*.

Coldrick, S. and Webber. D. M. (2017). Evaluation of the DRIFT Gas Dispersion Model Version 3.6.4. *Health and Safety Executive, Research Report RR1100*.

Crowe C. T. (2005). *Multiphase Flow Handbook*. CRC Press.

Delhaye, J. M., (1976). Sur les surfaces volumiques locale et integrale en ecoulement diphasique. C. R. Acad. Sci. Paris, t. 282, Serie A, 243–246.

De Luca, M., Valet, A., and Borghi, R. (2009). Pesticide atomization modelling for hollow-cone nozzle. Atomization and Sprays, 19(8):741–753.

Desantes, J. M., PYRI, R., Gimeno, J. and Marti-Aldaravi, P. (2014). Simulation of the First Millimeters of the Diesel Spray by an Eulerian Spray Atomization Model Applied on ECN Spray A Injector. *SAE Technical Paper 2014-01-1418*.

Desjardins, O. (2008). Numerical methods for liquid atomization and application in detailed simulations of a diesel jet. PhD thesis. Stanford University.

Downar-Zapolski, P., Bilicki, Z., Bolle L. and Franco J. (1996). The non-equilibrium relaxation model for one-dimensional flashing liquid flow. *International Journal of Multiphase Flow*, 22(3):473–483.

Duke, D. J., Battistoni, M., Swantek, A. B., Sovis, N., Kastengren, A. L., Powell, C. F., Som, S. and Schmidt, D. P. (2015). *Validation of Cavitation Simulations in Submerged Nozzles*. ILASS 2015.

Duret, B., Luret, G., Reveillon, J., Menard, T., Berlemont, A. and Demoulin, F. X. (2012). DNS analysis of turbulent mixing in two-phase flows. International Journal of Multiphase Flow, 40: 93–105.

Duret, B., Reveillon, J., Menard, T., Demoulin, F. X. (2013). Improving primary atomization modeling through DNS of two-phase flows. International Journal of Multiphase Flow, 55: 130–137.

Edelbauer, W. (2017). Numerical simulation of cavitating injector flow and liquid spray break-up by combination of Eulerian–Eulerian and Volume-of-Fluid methods. *Computers and Fluids*, 144:19–33.

Edwards, A. R. and O'Brien, C. E. (2013). *Studies of phenomena connected with the depressurization of water reactors. J. Brit. Nucl. Energy Soc.*, 9():125–135.

Einstein, A. (1920). Uber Schallschwingungen in teilweise dissoziierten Gasen. *Sitzung Berl. Akad. Physik Chemie*, 380–385.

Elghobashi1994 S., (1994) On predicting particle-laden turbulent flows. *S. Appl. Sci. Res.*, 52:309–329.

Faeth, G. M, (2002). *Dynamics of secondary drop breakup—a rate controlling process in dense sprays*. Proceedings of the ILASS—Europe 2002, Zaragoza.

Fauske, H. K. (1962). Contribution to the theory of two-phase, one-component critical flow. *Rep.Num. ANL-6633*, 1–180.

Ferziger, J., Peric, M., 2001. Computational Methods for Fluid Dynamics. Springer Berlin Heidelberg.

Gibbs, W. (1961). *The Scientific Papers, Vol. 1.*. Dover Publ. Inc., NY.

Glimm, J., McBryan, O., Menikoff, R. and Sharp, D. H. (1986). Front Tracking Applied to Rayleigh–Taylor Instability. *SIAM Journal on Scientific and Statistical Computing*, 7(1):230–251.

Günther, A. and Wirth, K. E. (1986). Evaporation phenomena in superheated atomization and its impact on the generated spray. *International Journal of Heat and Mass Transfer*, 64:952–965.

Gurtin, M. E., Struthers, A. and Williams, W. O. (1989). A transport theorem for moving interfaces. *Quart. Appl. Math.*, 47(4):773–777.

Han, Z., Parrish, S., Farrell, P. V., Reitz, R. D., (1997). Modeling Atomization Processes Of Pressure Swirl Hollow-Cone Fuel Sprays. *Atomization and Sprays*, 7:663–684.

Hendricks, R. C., Simoneau, R. J. and Barrows, R. F. (1976). *Two-phase choked flow of subcooled oxygen and nitrogen, TN D-8169*. NASA, United States.

Henry, R. E. (1970). The two-phase critical discharge of initially saturated or subcooled liquid. *Nuclear Science and Engineering*, 41:336–342.

Henry, R. E. and Fauske, H. K. (1971). The Two-Phase Critical Flow of One-Component Mixtures in Nozzles, Orifices, and Short Tubes. ASME. J. Heat Transfer, 93(2):179–187.

Hervieu, E. and Veneau, T. (1996). Experimental determination of the droplet size and velocity distributions at the exit of the bottom discharge pipe of a liquefied propane storage tank during a sudden blowdown. *Journal of Loss Prevention in the Process Industries*, 9(6):413–425.

Hewitt, G. and Hall-Taylor, N. S. (1970). *Annular Two-phase Flow*. Pergamon Press, Oxford.

Hibiki, T. and Ishii, M. (2000). Two-Group Interfacial Area Transport Equations at Bubbly-to-Slug Transition. Nuclear Engineering and Design - NUCL ENG DES, 202:39–76.

Hiroyasu, H. (1991). Break-up length of a liquid jet and internal flow in a nozzle. *Proc. 5th ICLASS*, 275–282.

Hirt, C. W, Amsden, A. A., and Cook, J. L. (1974). An arbitrary Lagrangian-Eulerian computing method for all flow speeds. *Journal of Computational Physics*, 14(3):227–253.

Hsiang, L. P. and Faeth, G. M. (1995). Drop deformation and breakup due to shock wave and steady disturbances. *International Journal of Multiphase Flow*, 21(4):545–560.

Hutcherson M. N., Henry R. E. and Wollersheim D. E. (1983). Two-Phase Vessel Blowdown of an Initially Saturated Liquid—Part 2: Analytical. *ASME. J. Heat Transfer.*, 105(4):694-699L.

Iciek, J. (1980). The hydrodynamics of a free, liquid jet and their influence on direct contact heat transfer-I. *International Journal of Multiphase Flow*, 8(3):239–249.

International Association for the Properties of Water Steam (IAPWS) (1994). *Viscosity of thermal conductivity of heavy water substance in Physical Chemistry of Aqueous Systems*. Proceedings of the 12th International Conference on the Properties of Water and Steam, Orlando, FL, 107-138.

Irannejad, A. and Jaberi, F. (2014). Large eddy simulation of turbulent spray breakup and evaporation. *International Journal of Multiphase Flow*, 61:108–128.

Ishii, M. (1975). *Thermo-fluid Dynamic Theory of Two-phase Flow*. Eyrolles. Paris/Scientific and Medical Publications of France, New York.

Ishimoto, J., Ohira, K., Okabayashi, K., and Chitose, K. (2008). Integrated numerical prediction of atomization process of liquid hydrogen jet. *Cryogenics*, 48:238–247.

Issa, R. I., Gosman, A. D. and Watkins, A. P. (1986). The Computation of Compressible and Incompressible Recirculating Flows by a Non-iterative Implicit Scheme. *J. Comput. Phys.*, 62(1):66–82.

Janet, J. P., Liao, Y. and Lucas, D. (2015). Heterogeneous nucleation in CFD simulation of flashing flows in converging–diverging nozzles. International Journal of Multiphase Flow, 74:106–117.

Jasak, H. (1996). Error Analysis and Estimation for the Finite Volume Method with Applications to Fluid Flows. PhD thesis. Imperial College, London.

Jasak, H., Weller, H. G. and Gosman, A.D. (1999). High resolution NVD differencing scheme for arbitrarily unstructured meshes. *International Journal for Numerical Methods in Fluids*, 31(2):431–449.

Jiang, X., Siamas, G. A, Jagus K. and Karayiannis T. G. (2010). *Physical modelling and advanced simulations of gas–liquid two-phase jet flows in atomization and sprays*. *Progress in Energy and Combustion Science*, 36(2):131–167.

Johnson, D. W. and Woodward, J. L. (1999). *Release: a model with data to predict aerosol rainout in accidental releases*. American Institute of Chemical Engineers.

Ju, D., Fang, J., Zhang, T., Qiao, X., Xiao, J. and Huang, Z. (2010). *High-speed shadow imaging in internal flow pattern and macroscopic characteristics of a R134a flash-boiling spray discharged through a vertical twin-orifice atomizer*. *International Journal of Multiphase Flow*, 75:224–236.

Karrholm, F. P. (2008). *Numerical Modelling of Diesel Spray Injection, Turbulence Interaction and Combustion*. Chalmers University of Technology, Goteborg, Sweden.

Kataoka, I., Ishii, M. and Serizawa, A. (1986). Local formulation and measurements of interfacial area concentration in two-phase flow. *International Journal of Multiphase Flow*, 12(4):505–529.

Khodadadi Azadboni, R., Wen, J., Heidari, A. and Wang, C. (2017). Numerical modeling of deflagration to detonation transition in inhomogeneous hydrogen/air mixtures. *Journal of Loss Prevention in the Process Industries*, 49:772–730.

Kitamura, Y., Morimitsu, H. and Takahashi, T. (1986). Critical superheat for flashing of superheated liquid jets. *Industrial & Engineering Chemistry Fundamentals*, 25(2):206–211.

Kolev, N. I. (2011). *Multiphase Flow Dynamics I Fundamentals*. Springer, Germany, fourth edition.

Lamanna, G., Kamoun H., Weigand B. and Steelant J. (2014). Towards a unified treatment of fully flashing sprays. *International Journal of Multiphase Flow*, 58:168–184.

Lebas, R., Menard, T., Beau, P. A., Berlemont, A. and Demoulin, F. X. (2009). Numerical simulation of primary break-up and atomization: DNS and modelling study. International Journal of Multiphase Flow, 35(5): 89–129.

Lee, C. S. and Park, S. W. (2002). A numerical study on fuel atomization characteristics of high-pressure diesel injection sprays. *Fuel*, 81:2417–2423.

Lee, J., Madabhushi, R., Fotache, C., Gopalakrishnan, S. and Schmidt, D. (2009). Flashing flow of superheated jet fuel. *Proceedings of The Combustion Institute - PROC COMBUST INST*, 32:3215–3222.

Lemmon, E. W., Penoncello, S. G. (1994). The Surface Tension of Air and Air Component Mixtures. In: Kittel P. (eds) Advances in Cryogenic Engineering. Advances in Cryogenic Engineering, 39:1927–1934.

Levy, M., Sher, E. (2010). Transition from heterogeneous to homogeneous nucleation in a simple structure flash-boiling atomizer. *Atomization and Sprays*, 20(10):905-907.

Lhuillier, D. (2003). Dynamics of interfaces and rheology of immiscible liquid–liquid mixtures. *Comptes Rendus Mécanique*, 331(2):113–118.

Liao, Y. and Lucas, D. (2015a). 3D CFD simulation of flashing flows in a converging-diverging nozzle. Nuclear Engineering and Design, 292:149–163.

Liao, Y., Rzehak, R., Lucas, D. and Krepper, E. (2015b). Baseline closure model for dispersed bubbly flow: Bubble coalescence and breakup. Chemical Engineering Science, 112:336–349.

Lin, S. P. and Reitz, R. D. (1998). Drop and spray formation from liquid jet. *Annual Review Fluid Mechanics*, 30:85–105.

Linstrom, P. J. and Mallard, W. G. (2017). *Eds., NIST Chemistry WebBook, NIST Standard Reference Database Number 69*. National Institute of Standards and Technology, Gaithersburg MD, 20899.

Liu, X. D., Osher, S. and Chan, T. (1994). Weighted Essentially Non-oscillatory Schemes. Journal of Computational Physics, 115(1):200–212.

Lu, N. X. and Reveillon, J. and Meslem, Y. and Demoulin, F. X. (1994). Modelling Cavitation and Flash Atomization. American Society of Mechanical Engineers, Fluids Engineering Division (Publication) FEDSM, FEDSM2014-21988.

Lyras, K., Dembele, S., Vendra, C. M. R. and Wen, J. (2017a). *Numerical simulation of superheated jets using an Eulerian method*. ILASS-Europe 2017a, Valencia.

Lyras, K., Dembele S. and Wen, J. (2017b). *Modelling flash-boiling atomisation with the homogeneous relaxation model implemented in a fully compressible solver*. 70th Annual Meeting of the American Physical Society Division of Fluid Dynamics, Denver, Colorado.

Lyras, K., Dembele, S., Schmidt, D. P. and Wen, J. (2018a). *Numerical simulation of subcooled and superheated jets under thermodynamic non-equilibrium*. International Journal of Multiphase Flow, 102:16–28.

Lyras, K., Dembele, S., Vyazmina, E., Jallais, S. and Wen, J. (2018b). *Numerical simulation of flash-boiling through sharp-edged orifices*. International Journal of Computational methods and Experimental measurements, 6(1):176–185.

Maksic, S. and Mewes, D. (2002). *CFD-calculation of the flashing flow in pipes and nozzles*. Proc. of ASME FEDSM'02, Montreal, Quebec, Canada.

Marle, C. M. (1982). On macroscopic equations governing multiphase flow with diffusion and chemical reactions in porous media. *International Journal of Engineering Science*, 20(5):643–662.

Menard, T., Beau, P. A., Tanguy, S., Demoulin, F. X. and Berlemont A. (2006). Primary break-up: DNS of liquid jet to improve atomization modelling. Computational Methods in Multiphase Flow III, 50:343–352.

Menter, F. R. (1993). *Zonal Two Equation k-w Turbulence Models for Aerodynamic Flows*. AIAA Paper 93-2906, 23rd Fluid Dynamics, Plasmadynamics, and Lasers Conference, Fluid Dynamics and Co-located Conferences, Valencia.

Miller, R. S. and Bellan, J. (1999). Direct numerical simulation of a confined three-dimensional gas mixing layer with one evaporating hydrocarbon-droplet-laden stream. *Journal of Fluid Mechanics*, 384:293–338.

Montorfano, A., Piscaglia, F., Ferrari, G., 2013. Inlet boundary conditions for incompressible les: A comparative study. Mathematical and Computer Modelling 57, 1640–1647. https://doi.org/10.1016/j.mcm.2011.10.077.

Moody, F. J. (1965). Maximum flow rate of a single component, two-phase mixture. *Journal of Heat Transfer*, (1965):134–142.

Morel, C. (2007). On the surface equations in two-phase flows and reacting single-phase flows. *International Journal of Multiphase Flow*, 30(10):1045–1073.

Moulai, M., Grover, R., Parrish, S., and Schmidt, D. (2015). *Internal and Near-Nozzle Flow in a Multi-Hole Gasoline Injector Under Flashing and Non-Flashing Conditions*. SAE Technical Paper 2015-01-0944.

Mugele, R. A. and Evans, H. D. (1951). Droplet Size Distribution in Sprays. *Industrial & Engineering Chemistry*, 43(6):1317–1324.

Navarro-Martinez, S. (2014). Large eddy simulation of spray atomization with a probability density function method. *International Journal of Multiphase Flow*, 63:11–22.

Nilpueng, K. and Wongwises, S. (2013). Numerical simulation of refrigerants flowing through short-tube orifices during flashing process. *HVAC and R Research*, 19(2):159–174.

Olsson, E. and Kreiss, G. (2005). A conservative level set method for two phase flow. Journal of Computational Physics, 210(1):225–246.

O'Brien, V., (1961). Why raindrops break up- Vortex instability. *Journal of Meteorology*, 18(4):549–552.

Okada, M. and Higashi, Y. (1994). Surface tension correlation of HFC-134a and HCFC-123 in CFCs, The Day After. Proceedings of the Joint Meeting of IIR Commissions B1, B2, E1, and E2, Padua, Italy, 541–548.

O'Rourke, R. J. (1981). *Collective drop effects on vaporizing liquid sprays. PhD thesis*. Princeton University, USA.

O'Rourke, P. J. and Amsden, A. A. (1987). *The Tab Method for Numerical Calculation of Spray Droplet Breakup*. SAE Technical Paper 872089.

Osher, S. and Sethian, J. A. (1988). Fronts propagating with curvature-dependent speed: Algorithms based on Hamilton-Jacobi formulations. Journal of Computational Physics, 79(1):12–49.

Oza, R. D. (1984). On mechanism of flashing injection of initially subcooled fuels. *Journal of Fluid Mechanics*, 106:105–109.

Park, B. S. and Lee, S. Y. (1994). An experimental investigation of the flash atomization mechanism. *Atomization and Sprays*, 4(2):159–179.

Park, C. K., Park, J. W., Chung, M. K. and Chun, M. H. (1997). An Empirical Correlation for Critical Flow Rates of Subcooled Water Through Short Pipes with Small Diameters. *Nuclear Engineering and Technology*, 29(1):35–44.

Patanakar, B. (1980). Numerical Heat Transfer and Fluid Flow. Hemisphere Publishing Corporation.

Pavlov, P. A. (1988). *Dynamics of Superheated Liquid Boiling*. Sverdlovsk:Ural. Otd. Akad. Nauk SSSR.

Pilch, M. (1981). *Acceleration Induced Fragmentation of Liquid Drops*. University of Virginia.

Pilch, M., Erdman, C. A. (1987). Use of breakup time data and velocity history data to predict the maximum size of stable fragments for acceleration-induced breakup of a liquid drop. *International Journal of Multiphase Flow*, 13(6):741–757.

Plateau, J. A. F. (1850). *Ann. Phys.*, 80(1850):566.

Plesset, M. S. and Prosperetti, A. (1977). Bubble dynamics and cavitation. *Annual Review of Fluid Mechanics*, 9:145–185.

Poinsot, T. J and Lelef, S. K. (1992). Boundary conditions for direct simulations of compressible viscous flows. *Journal of Computational Physics*, 101(1):104–129.

Polanco, G., Holdø, A. E. and Munday, G. (2010). General review of flashing jet studies. *Journal of Hazardous Materials*, 173(1):2–18.

Prangsma, G. J., Alberga, A. H. and Beenakker, J. J. M. (1973). Ultrasonic determination of the volume viscosity of N2, CO, CH4 and CD4 between 77 and 300 K. *Physika*, 64(2):278–288.

Price, C., Hamzehloo, A., Aleiferis, P. and Richardson, D. (2016). An approach to modeling flash-boiling fuel sprays for direct-injection spark-ignition engines. *Atomization and Sprays*, 26(2):1–43.

Pringuey, T. (2012). *Large eddy simulation of primary liquid sheet breakup*. University of Cambridge, Cambridge.

Prosperetti A. and Tryggvason G. (2009). *Computational Methods for Multiphase Flow*. Cambridge University Press.

Ramamurthi, K. and Nandakumar, K. (1999). Characteristics of flow through small sharp-edged cylindrical orifices. *Flow Measurement and Instrumentation*, 10:133–143.

Rayleigh Lord, (1892). *Phil. Mag.*, 34:145–154.

Lord Rayleigh, (1917). On the pressure developed in a liquid during the collapse of a spherical cavity. *Phil. Mag.*, 34:94–98.

Reinke, P. and Yadigaroglu, G. (2001). Explosive vaporization of superheated liquids by boiling fronts. *International Journal of Multiphase Flow*, 27(9):1487–1516.

Reitz, R. D. (1978). *Mechanisms of Breakup of Round Liquid Jets. PhD thesis*. Princeton University.

Reitz, R. D. (1987). Modeling atomization process in high-pressure vaporizing sprays. *Atomization and Spray Technology*, 3:309–337.

Reitz, R. D. and Bracco, F. V. (1986). Mechanisms of breakup of round liquid jets. Gulf Publishing Co., Houston. *Encyclopedia of Fluid Mechanics*, 3:233–249.

Reitz, R. D., and Diwakar, R. (1987). *Structure of High-Pressure Fuel Sprays*. SAE Technical Paper 870598.

Reitz, R. D. (1990). A Photographic Study of Flash-Boiling Atomization. *Aerosol Science and Technology*, 12(3):561–569.

Rusche, H. (2002). *Computational fluid dynamics of dispersed two-phase flows at high phase fractions. PhD thesis*. Imperial College London.

Saha, K., Som, S., Battistoni, M. and Li, Y., Pomraning, E. and Senecal, P. K.(2016). Numerical Investigation of Two-Phase Flow Evolution of In- and Near-Nozzle Regions of a Gasoline Direct Injection Engine During Needle Transients. SAE Technical Paper 2016-01-0870.

Sato, Y., Hanzawa, A., Hishida, K. and Maeda, M. (1995). Interactions between Particle Wake and Turbulence in a Water Channel Flow (PIV Measurements and Modelling for Turbulence Modification). Advances in Mulitphase Flow 1995, 27–40.

Salvador, F. J., Jaramillo, D., Romero, J. V and Roselló, M. D. (2017). Using a homogeneous equilibrium model for the study of the inner nozzle flow and cavitation pattern in convergent–divergent nozzles of diesel injectors. *Journal of Computational and Applied Mathematics*, 309:630–641.

Saurel, R., Petitbas, F. and Abgrall, R. (2008). Modelling phase transition in metastable liquids: application to cavitating and flashing flows. *Journal of Fluid Mechanics*, 607:313–350.

Savart, F. (1833). *Ann. Chim.*, 53(1833):337–398.

Schiller, L. and Nauman, A. (1933). Uber die grundlegende Berechnung bei der Schwekraftaufbereitung. *Ver. Deutch Ing*, 44:318—320.

Schmidt, D. (1997). *Cavitation in Diesel Fuel Injector Nozzles*. University of Wisconsin Madison.

Schmidt, D. P. and Corradini, M. L. (2001). The internal flow of diesel fuel injector nozzles: A review. *International Journal of Engine Research*, 2(1):1–22.

Schmidt, D. P., Gopalakrishnan, S. and Jasak, H. (2009). Multi-dimensional simulation of thermal non-equilibrium channel flow. *International Journal of Multiphase Flow*, 36(4):284–292.

Schröder, J. J. and Vuxuan, N. (1987). Homogeneous non-equilibrium two-phase critical flow model. *Chemical Engineering and Technology*, 10:420–426.

Senda, J., Yamaguchi, M., Tsukamoto, T. and Fujimoto, H. (1994). Characteristics of Spray Injected from Gasoline Injector. *JSME International Journal Series B*, 37(4):931–936.

Senecal, P. K., Schmidt, D. P., Nouar I., Rutland C. J., Reitz R. D. and Corradini M. L. (1999). *Modeling high-speed viscous liquid sheet atomization. International Journal of Multiphase Flow*, 25(6):1073–1097.

Sher, E., Bar-Kohany, T. and Rashkovan, A. (2008). Flash-boiling atomization. *Progress in Energy and Combustion Science*, 34:417–439.

Simoes-Moreira, J. R. and Shepherd, J. E. (1999). Evaporation waves in superheated dodecane. *Journal of Fluid Mechanics*, 382:63–86.

Simoes-Moreira, J. R. (2000). Oblique evaporation waves. *Shock Waves*, 10:229–234.

Simoes-Moreira, J. R. and Bullard C. W. (2003). Pressure drop and flashing mechanisms in refrigerant expansion devices. *International Journal of Refrigeration*, 26:840–848.

Simoneau, R. J. (1975). *Maximum two-phase flow rates of subcooled nitrogen through a sharp-edged orifice, TM X-71760*. NASA, United States.

Som S., Wang Z., Pei Y., Senecal P. K., and Pomraning E. (2015). *LES of Vaporizing Gasoline Sprays Considering Multi-injection Averaging And Grid-convergent Mesh Resolution*. ASME 2015 Internal Combustion Engine Division Fall Technical Conference, Houston, Texas, USA.

Spalding, D. B. (1953). *The Combustion of Liquid Fuels*. A Proc. 4th Symp. (Int.) on Combustion, Williams and Wilkins, Baltimore, MD, 847-864.

Span, R., Lemmon, E. W., Jacobsen, R. T., Wagner, W. and Yokozeki, A. (2000). A Reference Equation of State for the Thermodynamic Properties of Nitrogen for Temperatures from 63.151 to 1000 K and Pressures to 2200 MPa. Journal of Physical and Chemical Reference Data, 29(6):1361–1433.

Srinivasan, V., Salazar, A. and Saito, K. (2010). Modeling the disintegration of cavitating turbulent liquid jets using a novel VOF–CIMD approach. *Chemical Engineering Science*, 65:2782–2796.

Sussman, M. and Puckett, E. G. (2000). A Coupled Level Set and Volume-of-Fluid Method for Computing 3D and Axisymmetric Incompressible Two-Phase Flows. Journal of Computational Physics, 162(2):301–337.

Taylor, G. I. (1963). *The Instability of Liquid Surfaces when Accelerated in a Direction Perpendicular to their Planes*. *Cambridge University Press*, 3:532–536.

Tikhonenko, L. K., Kevorkov, L. P. and Lutovinov, S. (1978). An investigation of the local paramters of critical flow of hot water in straight pipes with a sharp inlet edge. *Teploenergetika*, 25:41–44.

Tillner-Roth, R. and Baehr, H. D. (1994). An International Standard Formulation for the Thermodynamic Properties of 1,1,1,2-Tetrafluoroethane (HFC-134a) for Temperatures from 170 K to 455 K and Pressures up to 70 MPa. Journal of Physical and Chemical Reference Data, 23(5):657–729.

Tryggvason, G., Bunner, B., Esmaeeli, A., Juric, D., Al-Rawahi, N., Tauber, W., Han, J., Nas, S., and Jan, Y. J. (2001). A Front-Tracking Method for the Computations of Multiphase Flow. *Journal of Computational Physics*, 169(2):708–759.

Unverdi, S. O. and Tryggvason, G. (1992). A front-tracking method for viscous, incompressible, multi-fluid flows. *Journal of Computational Physics*, 10(1):25–37.

Vallet, A. and Borghi, R. (1999). Modelisation eulerienne de I'atomisation d'un jet liquide. C. R. Acad. Sci. Paris, t. 327, Serie II b, 1115–1200.

Vallet, A., Burluka, A. and Borghi, R. (2001). Development of an eulerian model for the "atomization" of a liquid jet. Atomization and Sprays, 11(6):619–642.

van den Bosch, C. J. H. and Waterings, R. (2005). *Methods for the calculation of physical effects*. TNO, The Hague, Nederlands.

von Kuensberg Sarre, C., Kong, S. C. and Reitz, R. D.(1999). Modeling the Effects of Injector Nozzle Geometry on Diesel Sprays. *SAE Technical Paper 1999-01-0912*.

Wagner, W. and Pruß, A. (2002). The IAPWS Formulation 1995 for the Thermodynamic Properties of Ordinary Water Substance for General and Scientific Use. Journal of Physical and Chemical Reference Data, 31(2):387–535.

Wallis, G. B. (1969). *One-dimensional two-phase flow*. McGraw-Hill, New York.

Wang, Y., Qiu, L., Reitz R. D. and Diwakar R. (2014). Simulating cavitating liquid jets using a compressible and equilibrium two-phase flow solver. *International Journal of Multiphase Flow*, 63:52–67.

Wang, X., Chen, B., Wang, R., Xin, H. and Zhou, Z. (2017). Experimental study on the relation between internal flow and flashing spray characteristics of R134a using straight tube nozzles. *International Journal of Heat and Mass Transfer*, 115:524–536.

Weber, D. and Leick, P., (2015). *Structure and velocity field of individual plumes of flashing gasoline direct injection sprays*. ILASS 2014.

Weirzba, A. (1993). Deformation and Breakup of Liquid Drops in a Gas Stream at Nearly Critical Weber Numbers. *Experiments in Fluids*, 9:59–64.

Weisman, J. and Pei, B. S. (1983). Prediction of critical heat flux in flow boiling at low qualities. *International Journal of Heat and Mass Transfer*, 26(10):1463–1477.

Weller, H. G., Tabor, G., Jasak, H. and Fureby, C. (1998). A Tensorial Approach to Computational Continuum Mechanics Using Object-oriented Techniques. *Comput. Phys.*, 12(6):620–631.

Wen, J., Heidari, A., Xu, B. and Jie, H. (2013). Dispersion of carbon dioxide from vertical vent and horizontal releases—A numerical study. *Proceedings of the Institution of Mechanical Engineers, Part E: Journal of Process Mechanical Engineering*, 227:125–139.

Wen, J., Le Fur, P., Jie, H. and Vendra C. M. (2016). Further development and validation of CO2FOAM for the atmospheric dispersion of accidental releases from carbon dioxide pipelines. *International Journal of Greenhouse Gas Control*, 52:293–304.

Winklhofer, E., Kull, E., Kelz, E. and Morozov, A. (2001). *Comprehensive hydraulic and flow field documentation in model throttle experiments under cavitation conditions*. ILASS—Europe 2001, Zurich.

Witlox, H. W. M. and Bowen P. J. (2002). Flashing liquid jets and two-phase dispersion A review, contract research report 403/2002. *HSE*, (2002).

Xu, J., Chen, T. and Yang, L. (1995). Two-Phase Critical Discharge of Initially Saturated or Subcooled Water Flowing in Sharp-Edged Tubes at High Pressure. *Journal of Thermal Science*, 4(3):193–199.

Yildiz, D. (2005). *Experimental investigation of supeheated liquid jet atomization due to flashing phenomena. PhD thesis*. von Karman Institute, Universite de Bruxelles, Brussels.

Zaloudek, F. J. (1964). Steam-water critical flow from high pressure systems: interim report. *University of Michigan Library, US*

Zhang, Y., Li, S., Zheng, B., Wu, J. and Xu, B. (2015). Quantitative observation on breakup of superheated liquid jet using transparent slit nozzle. *Experimental Thermal and Fluid Science*, 63:84–90.

Zhifu, Z. F., Wu, W., Chen, B., Wang, G. X. and Guo, L. (2012). An experimental study on the spray and thermal characteristics of R134a two-phase flashing spray. *International Journal of Heat and Mass Transfer*, 55(15):4460–4468.

Zuo, B., Gomes, M. A. and Rutland, C. (2000). Modelling superheated fuel spray and vaporization. *International Journal of Engine Research - International Journal of Engine Research*, 1:321–336.

List of Publications

Lyras, K., Dembele, S., Vendra, C. M. R. and Wen, J. (2017a). Numerical simulation of superheated jets using an Eulerian method. ILASS-Europe 2017, Valencia.

Lyras, K., Dembele S. and Wen, J. (2017b). Modelling flash-boiling atomisation with the homogeneous relaxation model implemented in a fully compressible solver. 70th Annual Meeting of the American Physical Society Division of Fluid Dynamics, Denver, Colorado.

Lyras, K., Dembele, S., Schmidt, D. P. and Wen, J. (2018a). Numerical simulation of subcooled and superheated jets under thermodynamic non-equilibrium. International Journal of Multiphase Flow, 102:16–28.

Lyras, K., Dembele, S., Vyazmina, E., Jallais, S. and Wen, J. (2018b). Numerical simulation of flash-boiling through sharp-edged orifices. International Journal of Computational methods and Experimental measurements, 6(1):176–185.

Lyras K., Dembele, S., Vyazmina, E., Jallais S. and Wen, J. Numerical simulation of flash-boiling through sharp-edged orifices. (2018c). 9th International conference for computational and experimental methods in multiphase flows, Tallinn Estonia.

Lyras, K., Dembele S. and Wen, J. Numerical modelling of cryogenic sprays. (2017c). FABIG 92th Technical meeting, Aberdeen-London.